STUDY OF ORGANIC RADICALS THROUGH ANION PHOTOELECTRON VELOCITY-MAP IMAGING SPECTROSCOPY

By

Andrew Robert Dixon

A Dissertation Submitted to the Faculty of the

DEPARTMENT OF CHEMISTRY AND BIOCHEMISTRY

In Partial Fulfillment of the Requirements

For the Degree of

DOCTOR OF PHILOSOPHY

WITH A MAJOR IN CHEMISTRY

In the Graduate College of

THE UNIVERISTY OF ARIZONA

2016

THE UNIVERSITY OF ARIZONA
GRADUATE COLLEGE

As members of the Dissertation Committee, we certify that we have read the dissertation prepared by Andrew Dixon, titled "Study of Organic Radicals Through Anion Photoelectron Velocity-Map Imaging Spectroscopy" and recommend that it be accepted as fulfilling the dissertation requirement for the Degree of Doctor of Philosophy.

_____Date: 22 June 2016
Dr. Andrei Sanov

_____ Date: 22 June 2016
Dr. Oliver Monti

_____ Date: 22 June 2016
Dr. Michael Heien

_____ Date: 22 June 2016
Dr. Michael F. Brown

Final approval and acceptance of this dissertation is contingent upon the candidate's submission of the final copies of the dissertation to the Graduate College.
I hereby certify that I have read this dissertation prepared under my direction and recommend that it be accepted as fulfilling the dissertation requirement.

_____ Date: 22 June 2016
Dr. Dissertation Director: Andrei Sanov

STATEMENT BY AUTHOR

This dissertation has been submitted in partial fulfillment of the requirements for an advanced degree at the University of Arizona and is deposited in the University Library to be made available to borrowers under rules of the Library. Brief quotations from this dissertation are allowable without special permission, provided that an accurate acknowledgement of the source is made. Requests for permission for extended quotation from or reproduction of this manuscript in whole or in part may be granted by the head of the major department or the Dean of the Graduate College when in his or her judgment the proposed use of the material is in the interests of scholarship. In all other instances, however, permission must be obtained from the author.

SIGNED: Andrew Robert Dixon

Acknowledgements

I would first like to thank Dr. Andrei Sanov and his patience; to accept me into his group and allow me to stay was very kind, though I am sure a burden at times. His enthusiasm for deep thoughts and bad jokes taught me a lot of lasting lessons on physical chemistry.

I am very much thankful to my committee members: Dr. Oliver Monti, Dr. Michael Brown, and Dr. Michael Heien. Between conversations and questioning, they managed to get me to the end of my graduate school career and despite my best attempts to foil them.

I was exceptionally lucky to have Dr. Dmitry Khuseynov as my mentor. From navigating the instrument to surviving graduate school, he thought me and I learned as best I could. I had Dr. Lori Culberson, a mentor and the occasional provider of pecan pie, in addition to Dmitry. This team was wonderfully synergistic. When I formally joined the Sanov lab, I could not have asked for a better pair of scientists to learn from.

This work would not have been possible without the support of the members of the department. Most crucial are the founding members of the Hall of Justice, the endearing name of our graduate school house I have shared with Chris Blackstone, my labmate, and Zachary Lachance, our classmate. I have many friends from this department, too numerous to name, but these two gentlemen have come through in flying colors.

In naming some specific friends, I must thank the Heien lab, our next-door neighbors in the Carl S. Marvel Laboratories building, as well as the rest of building inhabitants that wandered through from time to time. Our ‘Zone 2’ family is/was a great

source of comfort and wisdom. Nothing will test chemist's wit like arguing about a graduate student's mental health as metric to measure success, discussing the trends based on empirical data, and predicting what futures might lie ahead over lunch and coffee, complete with graphs. I also apologize for what tools I borrowed and have failed to return, if any. This work would have not been possible without the Heien lab's expertise and expansive tool chest.

Many thanks to the Kevin and Stephen from ChIEF. At some point, I am fairly confident that they will have repaired or rebuilt everything in our laboratory at least once. The Sanov Lab would not survive without them. Equally important are Lee and Ed from the Machine Shop. Many times they were happy to take time out from their day to listen to my incoherent ramblings and turn them into tangible things.

Finally, nothing would have ever happened at the Department of Chemistry and Biochemistry, for me or otherwise, without Lori Boyd. Like most scientists, I am hopeless at any amount paperwork or deadlines. Thankfully Lori is continually aware of the cogs which make graduate school run, and devotes a great deal of time and effort to the students. I was extremely fortunate to have her help, and she made sure that I actually managed to graduate.

Dedication

This work is dedicated first to my family. My brothers Erik and Kyle, without whom I would not have survived. My father, Richard Dixon, who continues to raise what I hope is a good son and one which I know he is proud of. For all of my faults, I am blessed with my family. They mean more than the world to me.

Secondly, I dedicate this tome to my twice-teacher of high-school chemistry, Dan Jewett. Foolishly, he allowed me to attempt my hand at the chemical sciences. If my fortitude can be attributed to family, certainly the opening steps of this endeavor can be attributed to him. His knowledge and enthusiasm left me well-prepared.

Lastly, this is dedicated to my mother, Agnes Dixon. Though she did not see me complete my work at the University of Arizona, she has been with me and will continue to be with me. If I make an impact in this world of any small fraction as she did, I will be pleased to be measured in some meaningful amount in her likeness.

Table of Contents

List of Figures

List of Tables

Abstract

Molecular and cluster anions have been investigated using photoelectron velocity-map imaging spectroscopy to study the nature of electrons in radical species.

We report a negative-ion photoelectron imaging study of benzonitrile and several of its hydrated, oxygenated, and homo-molecularly solvated cluster anions. The photodetachment transition from the unsolvated benzonitrile anion to the $\tilde{X}^1A_1$ state of the neutral peaks at 58 ± 5 meV. The electron affinity (EA) of the lowest excited electronic state of benzonitrile, $\tilde{a}^3A_1$, is determined as 3.41 ± 0.01 eV. The next excited state, the open-shell singlet $\tilde{A}^1A_1$, is found about an electron-volt above the triplet, corresponding to a vertical detachment energy of 4.45 ± 0.01 eV. The step-wise and cumulative solvation energies of benzonitrile anions by several types of species were determined, including homo-molecular solvation by benzonitrile, hydration by 1–3 waters, oxygenation by 1–3 oxygen molecules, and mixed solvation by various combinations of O_2, H_2O, and benzonitrile.

Ethylene has been shown to be a degradation product following the 1-e^- attachment to ethylene carbonate. As a solvent molecule for O_2^-, our photoelectron imaging study shows a relatively small solvation energy of ≤ 0.24 eV for the expected π-π interaction in the $O_2^-(C_2H_4)$ cluster anion. The EA of the $O_2(C_2H_4)$ cluster was measured at 0.69 ± 0.01 eV, while the $X\,^3A'' \leftarrow X\,^2A''$ photodetachment transition shows a 1400 ± 100 cm^{-1} vibrational progression in the 1064 nm spectrum.

Negative-ion photoelectron imaging was used to investigate the substituted carbene derivative of fluoroacetonitrile. We report a closed-shell singlet ground state for the

cyanofluorocarbene, FCCN, with an adiabatic electron affinity EA = 2.081 ± 0.002 eV and a singlet-triplet gap of $\Delta E_{S\text{-}T}$ = 0.42 ± 0.04 eV. The open-shell singlet $^1A''$ state was also observed experimentally. We find that the experimentally measured $\Delta E_{S\text{-}T}$ of FCCN agrees well with the general trend of similar carbenes.

We report preliminary results on the photoelectron imaging of phenylcarbene, cyanophenylcarbene, and chlorophenylcarbene anions. Triplet phenylcarbene is observed to have an EA of ≤ 0.83 eV, considerably lower than the previously indirectly-determined value. Transitions to the singlet and triplet ground state of both cyanophenylcarbene and chlorophenylcarbene are observable, though unidentified bands make full assignment difficult. Cyanophenylcarbene is found to have a triplet ground-state, with a tentative EA of 2.04 eV. Chlorophenylcarbene is found to have a singlet ground-state. The phenyl-group is found to favor the singlet state slightly.

The cyanofluoromethyl radical, FC(H)CN, was estimated to have an EA of 1.53 ± 0.08 eV, by a combination of experimental and theoretical results.. With similar methodology, we report the adiabatic electron affinity of the cyanobenzyl radical, EA(PhCHCN) = 1.90 ± 0.01 eV, and assign an upper limit of the EA for the chlorobenzyl radical, EA(PhCHCl) ≤ 1.12 eV. These values were used to estimate the C-H bond dissociation energy (BDE)s for these substituted methanes. Fluoroacetonitrile was found to have a BDE of DH_{198} = 90.7 ± 2.8 kcal mol^{-1}. The C-H bond dissociation energies at the benzyl-α sites of the phenylmethanes are determined as 80.9 ± 2.3 kcal mol^{-1} for benzyl nitrile and an upper limit of 84.2 kcal mol^{-1} for benzyl chloride. These results are discussed in terms of substituent interactions in a simple MO framework and in relation to other similar molecules, including recently reported results for chloroacetonitrile.

The 532 nm photoelectron spectrum of glyoxal provides the first direct spectroscopic determination of the adiabatic electron affinity, EA = 1.10(2) eV. This assignment is supported by a Franck-Condon simulation of the experimental spectrum that successfully reproduces the observed spectral features. The vertical detachment energy (VDE) of the glyoxal radical anion is determined as VDE = 1.30(4) eV. The EA of methylglyoxal is determined as ≤ 0.8 eV based on the signal-to-noise ratio of the $X\ ^1A'$ ← $X\ ^2A''$ transition, with a VDE = 1.28(4) eV. The EA of the $a\ ^3A''$ ← $X\ ^2A''$ and $A\ ^1A''$ ← $X\ ^2A''$ transitions are determined as 3.28(3) eV and 3.614(5) eV respectively.

The intrinsically short-lived ethylenedione molecule (OCCO) was observed and investigated using anion photoelectron spectroscopy. The adiabatic electron affinity of its $^3\Sigma_g^-$ ground state is 1.936(8) eV. The vibrational progression with a 417(15) cm^{-1} frequency observed within the triplet band corresponds to a trans-bending mode. Several dissociative singlet states are also observed, corresponding to two components of the $^1\Delta_g$ state and the $^1\Sigma_g^+$ state. The experimental results are in agreement with the theory predictions and constitute the first spectroscopic observation and characterization of the elusive ethylenedione molecule.

Two glyoxal derivatives related to the ethylenedione anion ($OCCO^-$), ethynediolide ($HOCCO^-$) and glyoxalide ($OHCCO^-$), were studied. These anions provide access to the corresponding neutral reactive intermediates: the HOCCO and OHCCO radicals. In the HOCCO/OHCCO anion photoelectron spectrum, we identify several electronic states of this radical system and determine the adiabatic electron affinity of HOCCO as 1.763(6) eV. This result is compared to the corresponding 1.936(8) eV value for ethylenedione (OCCO).

Initial attempts were made to detect and observe the dicyanoacetylene anion, $NCCCCN^-$, by photoelectron imaging. While it is believed the experimental design path of H_2^+ abstraction from fumaronitrile is sound, no spectral signature can be assigned to $NCCCCN^-$. Calculations targeting the low-lying transitions from the anion indicate that the molecule should have a significantly positive electron affinity and at least the ground state should be accessible with the currently available laser sources. The cluster ion $O_2(N_2O)^-$ of the same nominal mass as $NCCCCN^-$ is identified as an interfering ion and ideas have been proposed for resolving this difficulty.

Chapter 1: Introduction to the Applications of Gas-Phase Anion Photoelectron Velocity-Map Imaging

The electronic structure of a molecule defines its reactivity and stability, governs the connectivity of the atoms, and the molecule's interaction with other species. In essence, studying the electronic structure is the study of chemical bonding within and outside the molecule. Gas-phase anion photoelectron imaging spectroscopy is a powerful and flexible technique to study interactions of electrons with molecules, molecular electronic structure and intermolecular interactions. It provides a rich set of data to draw from, allowing many aspects of a target species (neutral and anionic) to be studied simultaneously.

There are a great many advantages to studying electronic structure by gas-phase anion photoelectron velocity-map imaging spectroscopy. The investigation of isolated, relatively cold ions provides a framework for the study of chemical bonding with much greater resolution than in condensed phase and therefore with greater clarity. In many cases stable anion species, such as closed-shell anions, may provide access to states that are metastable or highly-reactive. The stability of such anions and the isolation afforded by a vacuum environment allow otherwise fleeting neutral intermediates to be directly observed and therefore characterized spectroscopically.

Anionic species are of great interest in biological,[1] atmospheric,[2-4] and astrochemical systems.[5] In some cases their role is well-known but for many systems, particularly astrochemical ones,[6] there remains an open-field of inquiry. Understanding the energetics and reactivity of anions both isolated and solvated is vital for a complete

picture of these roles. Gas-phase anion photoelectron imaging accesses much of this information by studying the detachment of an excess electron.

Since the detachment process reflects the anion-neutral transition, a wealth of information is obtained for both the neutral and anion species. Direct spectroscopic investigation reveals information about the energetics and angular momentum properties of the electrons. A straightforward utility of anion photoelectron imaging is the determination of the adiabatic electron affinity of the neutral and vertical detachment energy related to the transition from the electronic and vibrational ground-state anion to any number of energetically-accessible neutral states. This in turn can be correlated to the electronic structure of the neutral, changes in molecular structure upon detachment, bonding interactions, intermolecular interactions, and fundamental information about the detached electron. Information related to electron-transfer reactions,[7,8] photovoltaics, and reactivity[9,10] may all be potentially studied via the related anions.

One great boon is that there are many unstable and elusive neutral species of interest for which there exists stable anions. Thus, anion photoelectron imaging offers a way around the need for rapid detection, and with less challenging experimental methods. Radicals are a class of molecules in particular which are well-suited for such studies. Below, a brief description of the technique is given to better highlight its most salient features.

Gas-phase anion photoelectron spectroscopy begins with a (usually) ground-electronic state, vibrationally-cold anion. A linearly-polarized laser pulse interacts with the ion, and assuming photon energy is sufficient, a one-photon interaction occurs which

results in the detachment of an excess electron and a transition from the anion to a neutral electronic state. The final state consists of the resulting neutral core and a (photodetached) free electron wave. This wave is described by the electron's linear and angular momenta, which will generally change based on the photon energy. The electron kinetic energy (eKE), proportional to the square of linear momentum, is measured and by simple algebra the electron binding energy (eBE) is determined. That is, $eBE = h\nu - eKE$. Angular distribution can be determined either by varying the direction of detection in the laboratory frame, or 2D detection methods like velocity-map imaging.

The formation of desired anions is one of the pillars of this approach. On one hand, anions are not trivial to produce, since direct ionization techniques like collision and photoionization yield cations. Furthermore, the neutral species of interest produced must generally have a positive electron affinity. Forming anions of target radicals is not always through an obvious path, nor do reactions in the plasma always have the desired results. Despite this difficulty, there are many advantages to using anions, especially when studying neutrals. Firstly, charged species are very simple to manipulate in the gas-phase. A mass spectrometer is an excellent tool to separate a complex mixture and isolate a charged species of interest.

Secondly, anions are easily solvated by a number of species. Separation in a mass spectrum allows for an examination of dimers, trimers, and solvation shells built one molecule at a time. Such an approach can allow for a detailed map of the energetics of the first few charge-dipole or charge-quadrupole interactions, creating an important bridge between the isolated gas-phase ion and condensed systems.

Thirdly, there are a number of highly reactive species, often reaction intermediates, which are interesting but unstable. The addition of an excess electron can often stabilize these species so that unstable neutrals can be studied by anion photodetachment. The use of an anion is not only beneficial due to the information obtained about the neutral state, but additionally the binding energy for excess electrons is on the order of a few electron volts. This means that an experiment can employ a number of standard laser systems in the near-infrared, visible, and near- and middle-ultraviolet regimes.

The selection rules for photodetachment transitions are not as restrictive as those for a one-photon optical excitation; states of different multiplicity whose electron affinity is within the photon energy window can be accessed in principle.[11] In practice, this is dictated significantly by a Franck-Condon overlap as well as the total photoelectron cross-section for the electronic transition. The result is a photoelectron spectrum that maps out the low-lying electronic states with Franck-Condon profiles which reflect the difference between anion and neutral states. In some cases, mostly with simple molecules, the profile can show significant vibrational progressions.

Photoelectron imaging is relatively new approach to measuring the detached electron, and offers additional information in the form of angular distributions versus a hemispherical analyzer or magnetic bottle detector. While angular information can be obtained with these types of detectors, it presents difficulty in both data collection time and instrument design. The inherent advantage to imaging the detachment is that is information is obtained simultaneously with the energetic information, often producing additional clarity in the examination.

Two-dimensional imaging was first used to study the energetics and angular distributions of photofragments.[12,13] This technique was expanded to study photoelectrons,[14] and made significantly powerful by the introduction of velocity-mapping.[15,16] The key step is that the velocity-map imaging (VMI) condition focuses all photoelectrons of the same velocity to the same positon on the 2-dimentional detector, regardless of their initial position in the ion-laser beam interaction region. This creates a significantly sharper image, which improves the level of precision in the analysis.

Outgoing photoelectron waves are projected onto a 2D position-sensitive detector by the VMI electrode stack. Since there is a 3-dimensional distribution of outgoing electrons, the actual result is a 2-dimensional projection of the real distribution. To recover a more useful data set, a 2-dimentional reconstruction of the wave in the plane of the ion beam and laser beam polarization vector is performed. This is made possible by the fact that the photoelectron distribution is cylindrically symmetric with respect to the laser polarization vector, and the application of the Abel inversion transformation.[17] The resulting reconstruction contains two key data sets. The first is the radial information, which reflects the momentum of the electrons by a Fourier transform into position space. Integrating over all angles, the radial position can be calibrated to eKE by using a well-known detachment (typically O^-). The actual radial distribution can then be converted simply to an eBE spectrum by paying heed to the appropriate Jacobian transformation for the intensity.

As was mentioned previously, additional information comes in the form of the angular distribution. The photoelectron angular distribution (PAD) is representative of the initial angular momentum properties of the detached electron.[18-21] For analysis, a

particular radial width (perhaps associated with a single, resolved vibrational transition) can be integrated as a total intensity as a function of the angle with respect to laser polarization. The resulting curve can be described by a single parameter; this value is referred to as β_2 and indicates a one-photon, linearly-polarized electric field interaction (though for the remainder of this work it will simply called β). β is a function of eKE, and a plot of β vs eKE can reveal information about the nature of the bound electron. In general, it is expected that two electrons originating from different orbitals but detached from identical molecules will yield two different PAD as a function of eKE.[11,22]

Often, identifying the electronic transitions observed in the image is as simple as empirically examining the PADs. PADs are also sensitive to the solvent effects; in some cases the electronic wavefunction remains essentially unchanged while in other cases strong polarization greatly affects the result. Additionally, differing PADs have been successfully used to de-convolute complex spectra into angular components, allowing overlapping features to be more definitively identified.[23] Recently, a model was developed which correctly models the detachment of electrons by the linear combination of atomic orbitals from a single center to approximate molecular orbitals, which further expands the utility in examining PADs.[24]

The following dissertation reflects the study of a varied arrangement of molecules, with a strong focus on unusual neutral radicals and diradicals. There is a particular focus of the π-interaction effects on the stability of these radicals, as reflected in bond dissociation energies, dimerization, and singlet-triplet splitting. Many of the species studied in this work were chosen to begin the development of trends or models related to electronic structure. Others have been chosen from more specific interests,

whether related to materials development, atmospheric, astrochemical, or otherwise in nature.

Much of the work presented here has been previously published in peer-reviews journals; however the following is not a reprinting of these articles. The goal of this dissertation is to collect these published works, along with new and preliminary data, and collectively organize it into more overarching topics for clarity and insight.

Radicals are molecules with at least one nominally unpaired electron. As a result, radicals and diradicals (two unpaired electrons) are considered to be highly reactive species and often appear as intermediate species during chemical reactions. Due to strong electronic effects, many of these species have numerous low-lying multi-reference states. In this volume, many of the radicals and diradicals studied are carbon-centered radicals, either methyl radicals or carbenes. Not only can practical quantitative results be obtained for these systems, but studying them is of fundamental interest in understanding how different substituents affect the stability of certain electronic states or the radical system as a whole.

Further, new theoretical methodologies such as equation-of-motion ionization potential or spin-flip, EOM-XX-CCSD (XX=IP, SF), [25,26] make capturing the complex electronic structures of radicals much more accessible. These methodologies allow for low-cost computations which produce either non-standard references like open-shell singlets or multi-configurational electronic states. Virtually all investigations described in this thesis make use of these newly available methods.

Chapter 2 reviews the instrumentation as well as some minor changes in its maintenance. Included in this is an examination of the current electron gun system used to produce the plasma discharge in which anions are formed. A general design for a new electron gun is discussed.

Chapter 3 and 4 discuss the solvation energy of two different anionic systems: benzonitrile and oxygen. Benzonitrile is a species of varied interest; it has electronic properties that make it a desirable component or functionality in charge-transfer and charge-transport materials. Despite this interest, the previous measurement of its EA was imprecise and indirectly determined. Our interest in it came from our previous work on other cyano containing systems, particularly those with a high degree of conjugation. A successful investigation determined a more precise and very different value for the EA, as well as the splitting between the lowest triplet and open-shell singlet states. Several solvation series were examined, and approximate solvation energies were determined. Most interestingly, a series of homo-molecular clusters are examined. Their electronics show a strong, but mostly non-covalent π-stacking structure, which is explored theoretically using DFT methods. Much of the experimental work was done in tandem with Dmitry Khuseynov, welcomed with the vast amount of information collected. The theoretical investigations, particularly regarding the dimer, were carried out by myself. This whole of this work was published in the Journal of Chemical Physics in 2015.

Chapter 4 is previously unpublished work on the ethylene (C_2H_4) solvating the O_2^- anion. Discovered during the thermal decomposition of ethylene carbonate under somewhat precise conditions, the system presents straightforward electronic structure but unusual geometry. The presence of a defined but solvent-broadened O_2 vibrational

progression, as well as a characteristic excited state transitions, indicate an O_2^- core anion. Calculations on the geometry indicate an unexpected position for the ethylene solvent, an interaction with a single hydrogen which lies between the oxygens. Despite more initially intuitive structures, this geometry agrees well with the experimental results. The π-π interaction is unfavorable in this case, contrasting the homomolecular dimers of benzonitrile. This work was done largely by myself, though several attempts with other similar starting materials were attempted with the help of Chris Xue. At the time of this dissertation, this work is unpublished in a public journal.

Chapter 5 and 6 discusses a class of 'mixed' carbene diradicals. This was prompted by previous work, which focused on singly and homogenously-substituted carbenes. The comparison between chlorocyanocarbene and cyanofluorocarbene in Chapter 5 offers insight for the competing effects present with differing substituent groups. Experimental determinations for their singlet-triplet splitting are presented in conjunction with a theoretical study using the equation-of-motion ionization potential (EOM-IP) and spin-flip (EOM-SF) methodology. While the halogen group stabilizes the singlet group more efficiently, the cyano group leads to π-delocalization and a more stabilized triplet state. These effects are observed to be largely independent in these simple carbenes, leading to intermediate electronic properties and geometries. In Chapter 6, these insights are used to elucidate details about phenylcarbenes: phenylcarbene, cyanophenylcarbene and chlorophenylcarbene. For this dissertation these systems are examined now for the purposes of future work. Limited experimental data is presented, as well as some of the difficulties in conducting the study. Preliminary results include an upper-bound for the electron affinity of phenylcarbene (≤ 0.83 eV), and good agreement

with low-level calculations on the singlet-triplet gap (ΔE_{S-T}) for cyanophenylcarbene and chlorophenylcarbene. Higher levels of theory and more experimental work will be required for these systems.

My part in this work was to perform experimental investigations on chlorocyanocarbene, specifically the production of the related anion, spectroscopic work, and analysis. Once this groundwork was laid, I moved ahead with cyanofluorocarbene and took lead on that investigation. This included the experimental work, most of the theoretical work, and the interpretation of the results in conjunction with chlorocyanocarbene. The cyanofluorocarbene work was published in 2014 in the Journal of Physical Chemistry A, with the previous work on chlorocyanocarbene published earlier in 2013. The phenylcarbene investigation is, at the time of writing, unfinished.

Chapter 7 examines another class of 'mixed' radicals involving the loss of hydrogen from substituted methanes. This study focuses on establishing trends for the observed effects in the stability of a methyl radical based on π-donating and π-accepting substituents which interact strongly with the lone electron in the nominally sp^3-hybrdized orbital. This stabilization is viewed through the bond dissociation enthalpies (BDE) which are calculated using Hess's Law and the newly measure EAs. An examination of the BDEs of these species as compared to similar species shows that both substituent types help to stabilize the radical with respect to the parent methane by acting in a similar matter. Like previous work on related carbenes, the literature contained only information on singly or homogenously-substituted systems. It is observed that in 'mixed' species, the combination of π-donating and π-accepting effects act synergistically (the so-called captodative effect, observed for the first time experimentally for these kinds of radicals).

The result is that several of these ‘mixed’ species have some of the lowest BDEs ever measured for substituted methanes. The cyanohalomethyl radical work was done in conjunction with their respective carbenes, though I must credit Dmitry Khuseynov with managing the difficult task of obtaining a photoelectron image for cyanofluoromethyl radical anion. The phenylmethyl radical experimental work, all theoretical results, and the conclusions in Chapter 4 are largely my own contribution. This work was published in 2014 in Chemical Physics Letters.

Chapter 8 involves the improvement of a previous, indirect measurement of EA from a close-shell neutral molecule, glyoxal (OHCCHO). Glyoxal is the smallest dialdehyde and of importance in atmospheric science, particularly involved in pollution. The anion of methylglyoxal is also investigated, a molecule which has been to shown to act very similarly and is correlated to the same sources and chemistries. Both are the start of a new interest in carbonyl-containing systems. The chapter summarizes a method for easily obtaining glyoxal and methylglyoxal vapor from commercially available solutions, a theoretical investigation into the nature of the glyoxal anion, and the determination of the electron affinities. The results are again more precise than previous determinations and measured directly; they also settle previous studies disagreement between theoretical results and experiments (or lack thereof). This work was down with the help of Chris Xue, who also lead the theoretical work on the nature of the anion.

Chapter 9 is the experimental proof for the existence of ethylenedione, OCCO, a molecule that was only hypothetical for 102 years before it was finally observed. Formally, the molecule is a dimer of carbon monoxide. Theoretical investigations have shown repeatedly that a stable triplet state should exist, though the molecule’s lifetime is

limited due to a singlet-triplet intersystem crossing where the molecule dissociates to the lowest energy configuration – a Van der Waals dimer of CO. By forming the OCCO anion from glyoxal, we successfully observed a transition to several low-lying neutral electronic states, confirming the existence of the stable triplet. Their energy spacing and identities are explored using EOM-IP-CCSD and EOM-SF-CCSD, in good agreement with the experimental results. A key vibrational spacing is identified and measured, as well as the EA, for the triplet state. Modeling of the two-lowest lying electronic transitions creates a completely consistent picture of the spectral profile observed for 532 nm. This work was done with the help of Chris Xue, and the results, sans Franck-Condon simulation of the triplet transition, were published in Angewandte Chemie in 2015.

Chapter 10 serves as a link between Chapters 8 and 9. The singly-deprotonated glyoxal-related species (OHCCO) and its hydrogen-rearrangement product (HOCCO) are not only related to the parent species glyoxal, but to OCCO. Experimental and theoretical evidence is presented showing the simultaneous presence of both species in the ion packet. The EA of HOCCO is measured, and a low-lying doublet state is observed. The detachment profile, along with theoretical calculations, show that this system is the major product formed during H^+ abstraction, and acts as a perturbed OCCO-like species. Using the same methodology, OHCCO is shown to have a geometry and electronic structure more expected for a radical formed directly from gyloxal. This work was performed concurrently with our investigation of OCCO, and published in the Journal of Chemical Physics in 2016, which included the follow-up analysis of OCCO with the complete simulation of the 532 nm included in Chapter 6

Chapter 11 presents the first attempts to detect the dicyanoacetylene anion by anion photoelectron spectroscopy. NCCCCN is a molecular with significant astrochemical interest, as is the resulting anion. In addition to structural similarities to ethylenedione, a first attempt was made to create this anion using the H_2^+ abstraction of fumaronitrile by O^- in an identical method applied to glyoxal. Results for anion photoelectron VMI of the m/z 76 anion packet are inconclusive; detachment from $O_2^-(N_2O)$ is clearly the dominate spectral feature. Suggestions are offered for the experimental methodology to overcome the apparent issues. A theoretical analysis using methodology identical to that applied to ethylenedione anion show that dicyanoacetylene should have a stable anion, with the neutral ground-state having a positive electron affinity of 1.156 eV at the CCSD/aug-cc-pVTZ level of theory and basis. EOM-IP-CCSD results are consistent with previous work on the system. This work is preliminary and unpublished.

The purpose of Chapter 12 is to summarize the major findings of the above investigations, provide insight, and suggest future work to further our understanding in areas like carbenes, radical stabilization, and weak dimer interactions.

Chapter 2: Instrumentation and Normal Operation

Overview

The instrument used for this work is a custom-built differentially-pumped negative-ion Wiley-McLauren mass spectrometer with a single-pass reflectron for photofragmentation and a coupled photoelectron velocity-map imaging assembly. The 4 major parts of the instrument (source chamber, TOF, VMI stack, and reflectron) will be described in more detail separately, along with the vacuum systems. In a general sense, the source chamber is used to produce cooled anions, while the TOF's primary role is to separate the ions so produced for laser spectroscopy or photofragmentation. Photoelectron imaging is performed by the VMI stack, a series of focusing electrodes and a position sensitive detector. The reflectron is used to examine possible mass fragments resulting from laser-ion interaction. For a more detailed description of instrument and the principles of its operation, please refer to the thesis of Terefe G. Habteyes, "Electronic Structure and Photochemistry of Molecular and Cluster Anions via Tandem Time-of-flight Mass Spectroscopy and Photoelectron Imaging," published in 2008.

1. Source Chamber

The front end of the instrument is the large source chamber, connected by a 12" pneumatic gate to a 10" Varian diffusion pump. The pump currently uses Santovac-9 oil, a derivative of Santovac-5 which is significantly cheaper but maintains properties sufficient for the normal operation of the instrument. The diffusion pump is roughed by a Trivac D90A rotary pump. The nominal pressure before experimental procedures begin is 4-7 x 10^{-7} Torr, assuming the unit has pumped down fully. This number is as low as 3 x 10^{-7} Torr, though the practical limit is affected by ambient humidity due to outgassing and permeation. Pressure is measured by both a thermocouple (operating range of 5-200 μTorr) and a filament detector (10^{-4} – 10^{-9} Torr). Carrier gas is introduced by a feedthrough stainless steel port attached to Teflon tubing (0.25″ OD/ 0.17″ ID) using Swagelock fittings. Gas is generally pre-seeded with sample vapor outside the instrument, but sample holders and heaters can all be used inside the source chamber. This is often done when high temperatures are required; the source chamber not only safely contains the heating element but the vacuum insulates the heater and sample, which allows for less power and time to reach target temperatures (provided the target temperature is higher than the current temperature). The Teflon tubing connects to a General Valve Series 99 pulse nozzle, which is triggered at the repetition rate of the laser system employed for the experiment. During nozzle operation, pressures in the source chamber are between 2-5 x 10^{-5} Torr. Argon, oxygen, and nitrous oxide are all commonly employed as carrier gases; trace amounts of oxygen and water are almost always present. The nozzle sits facing the 12" pneumatic gate. Perpendicular to the nozzle is a Southwest Vacuum Devices, Inc. model CE3K5U electron gun. The electron gun uses a tungsten or

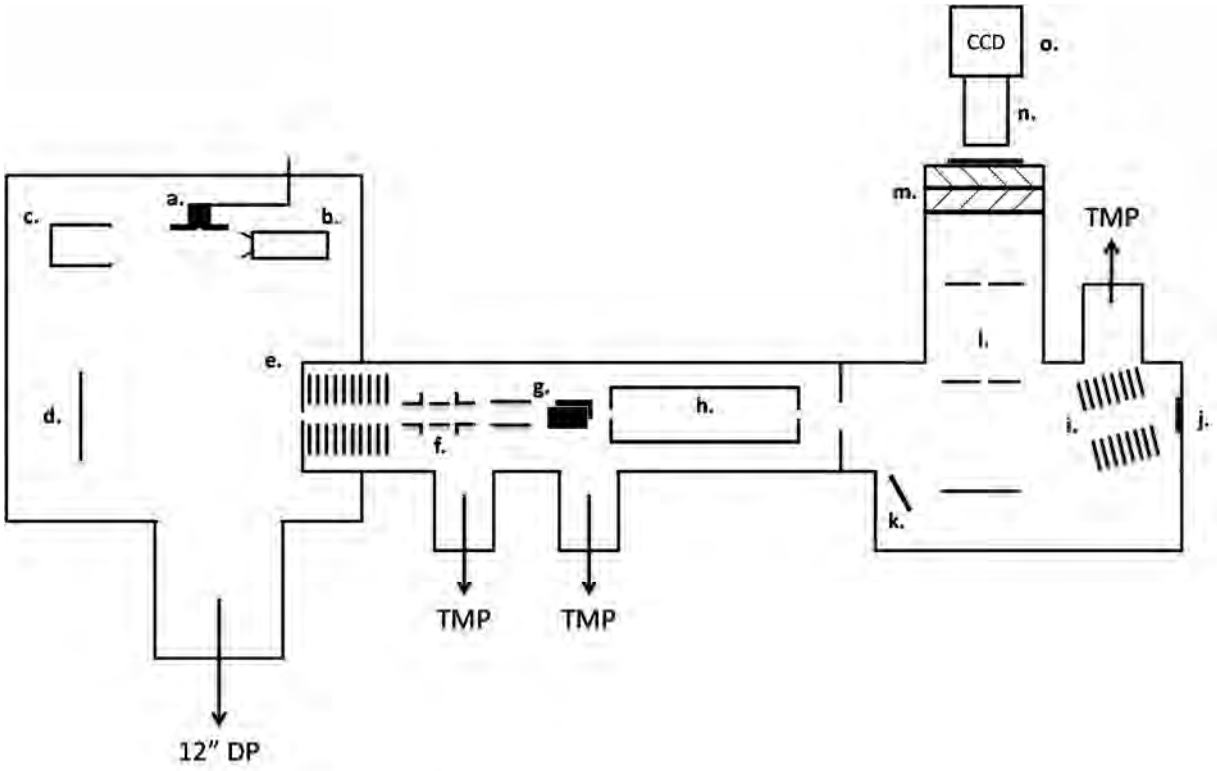

a. General Valve Series 9
b. CE3K5U Electron Gun
c. Faraday Cup
d. Repeller Plate
e. Acceleration Stack Electrodes
f. Einzel Lens
g. X and Y Deflectors
h. Potential Switch
i. Reflectron
j. In-Line MCP
k. Off-line MCP
l. VMI Electrode Stack
m. Dual MCP Assembly, Chevron Configuration
n. Magnifying Lens Attachement
o. CoolSnap Myo CCD

Figure 1. Schematic diagram of the anion photoelectron imaging spectrometer used in this work.

tantalum filament to produce a focused and directed beam of electrons at ~1 keV potential energy. The beam is directed ~4 mm from the nozzle face and terminates into a Faraday cup, electrically isolated from the chamber and grounded instead by a feed-through wire which runs either to ground or to a multimeter to monitor current. Typical currents measured at the cup are 2-7 μA. During the experimental cycle, a portion of gas is expanded into the vacuum. When the gas expansion passes through the electron beam, number density is high enough to produce plasma. As the plasma expands and cools, it travels forward 18 cm where it is then flanked one side by the 4 mm orifice to the TOF section of the instrument and on the other by a pusher plate. The total separation between these plates is 15 cm. Anions can form from a number of ways, with common schemes shown below.

$\sim 1kV\ e^- + M \longrightarrow \sim 1kV\ e^- + M^+ + e^-$	High energy impact forms slow secondary electrons
$e^- + X + M \longrightarrow X^- + M$	Direct slow secondary electron attachment
$e^- + AB \longrightarrow A^- + B$	Dissociative slow secondary electron attachment
$O^- + H_{1+n}C_NRR' \ldots \longrightarrow H_nCRR' \ldots {}^- + OH$	H^+ abstraction from organic molecule by O^-
$O^- + H_{2+n}C_NRR' \ldots \longrightarrow H_nCRR' \ldots {}^- + OH_2$	H_2^+ abstraction from organic molecule by O^-

Not Pictured: Evaporation of solvent molecules during electron attachment or formation of clusters following anion formation

2. Time-of-Flight Region

The anion packet is extracted into the TOF region by a -950 V square pulse. The TOF section of the instrument contains the ion optics and potential switch. It is pumped by two Turbotronik 110C turbomolecular pumps, backed by a single Trivac D16B rotary pump. The nominal pressure in this region is 5-8 x 10^{-8} Torr, and when the experiment is

running it is 5-10 x 10^{-7} Torr. Anions are accelerated by a series of 10 plates, with the final plate at approximately -2.5 kV and each plate stepped down by 1/10 of the voltage. The outer case of the ion optics region is held at the same -2.5 kV potential. Following the acceleration stack, a 3 part einzel lens operating in a decelerating mode is used to focus the ion packet. The first and third pieces are held at -2.5 kV. The second lens component is held at 1 kV. Beyond the Einzel lens, a series of parallel plates are used as deflectors in the vertical and horizontal directions. They are referenced to the case at -2.5 kV. Following the ion optics region sits a 2 ft metal tube which acts as potential switch. As part of the experimental cycle, this tube is held to +5 kV. During this time, no anions may pass beyond the tube. A small time window where the tube is grounded allows ions of a certain range of mass-to-charge ratio (m/z) through. This serves to ensure that only 1 experimental cycle's ion beam is being examined by any of the detectors at any time. Otherwise, very slow ions or very fast ions may interfere with a current experimental cycle.

3. Detection Region

3.1 TOF Detector and Reflectron

Beyond the potential switch, a small pneumatic gate separates the TOF region from the detector region. This region is pumped by a single Turbotronik 1100C turbomolecular pump, backed by a single Trivac D16B roughing pump. When fully pumped down, this region is at 3-4 x 10^{-9} Torr. During experiments, it may reach 5-8 x 10^{-8}, and rarely as high as 1 x 10^{-7} Torr. This region contains the in-line mass spectrometer multichannel plate (MCP), reflectron, off-line MCP, and the VMI assembly.

The in-line MCP sits directly in the path of the incoming ion beam. In front of it lies the reflectron, which is made up of a series of angled plates. Similar the acceleration stack, the final plate is held -4 kV with each successive plate being stepped down by a fraction of -4 kV, with the very first plate at 0 kV referenced to ground. The plates are angled in such a way that anions which are deflected are accelerated toward the off-line MCP, which sits below the initial ion beam path. The off-line MCP and in-line MCP/reflectron sit on either side of the VMI assembly.

3.2 Velocity-Map Imaging Assembly

The VMI is a detector stack which sits perpendicular to the ion beam path. It consists of 3 charged plates and a dual-MCP in a chevron pattern coupled to an external P43 phosphor screen. The bottom electrode is held at a fixed negative potential to extract photoelectrons upward into the VMI stack. A second plate is at ground to screen voltages. The third plate is charged positively to accelerate the incoming photoelectron wavepacket. The voltages of the stack are set to satisfy the velocity map focusing condition, where all photoelectrons of the same velocity strike the same location on the detector regardless of the initial position in the ion packet/laser pulse interaction region. A small screen held at ground screens the dual-MCP voltages. Photoelectron waves which strike the outer MCP collapse to a single position, which cause a current cascade due to the energetic impact. The multiplied signal from the dual-MCP strikes the P34 position sensitive detector; this detector is otherwise uncoupled to the dual-MCP except by a 100-300 ns, 1 kV pulse timed to interrogate only signals related to the

photodetachment event. Practically, this window is aligned to the peak laser intensity. Electrons from the dual-MCP which strike the P34 detector during this window produce a lights pulse. The light is collected by a thermoelectrically-cooled CoolPics Myo CCD with a magnification optic. To collect a full image, this camera integrates over long periods of time.

4. Normal Instrument Operation

4.1 Photoelectron Imaging

Laser light is introduced by either of two 1/10 λ quartz windows, set at an approximate Brewster angle (~54°) for visible light. The windows allow light to strike either the initial ion beam and/or the reflected ion beam (from photofragmentation) in a direction perpendicular to ion beam propagation and the VMI. Pulsed laser light is provided by two major laser systems: a SpectraPhysics LAB-130-50 Nd:YAG and a QuantaRay Surefire II/ND6000 dye laser system.

During a typical experimental cycle, the light pulse is timed to interact with a specific mass-to-charge ratio. The reflectron can be used at this time to identify the correct laser timing. At -4 kV, all initial ions in the beam are reflected away from the in-line MCP. Photodetachment of electrons from an ion packet results in neutral species which continue on to pass uninterrupted to the MCP. Alternatively, the relationship of m/z and laser timing follows a power series relationship, determined empirically by several strong ion signals. Often, strong signals like those related to the carrier gas N_2O or O_2 are used to predict the timing of much weaker signals from other analytes and with surprising accuracy within 20 ns. Detached electrons are projected upward through the

VMI stack and photoelectron signals on the P34 screen are integrated for ~1 million experimental cycles. Between sets of ~4500-9000 cycles, an equivalent set is collected for background by moving the experimental time window to a region containing no ion signal.

4.2 Photofragmentation Experiments

Photofragmentation experiments are performed first by tuning the max voltage of the reflectron so that the m/z of interest is well-focused for the off-line detector. Photofragments are detected at the same time as the parent ion by the following condition:

$$(1)\ \frac{V_F}{V_p} = \frac{m/z_F}{m/z_P}$$

where *V* is the reflectron potential and *m/z* is the mass-to-charge ration of the fragments and parent ion respectively. The time of flight for ions originating from the laser interaction region

has a linear relationship with respect to potential and varies inversely proportional to the mass of the ions. By varying the reflecton voltage based on the ratio of *m/z*, fragments of different masses are made to arrive at the off-line MCP at the same time. Typically, a number of possible fragments are determined by the molecular geometry or cluster type. The reflectron is varied to search for each fragment separately by integrating the off-line MCP signal for 512 seconds, along with a background subtraction performed without the laser interaction. In principal, the off-line MCP signal could be observed in the time

domain while scanning voltages but signal strength is typically too weak to do so practically. As further consideration, ions of m/z very similar to the parent are difficult to observe. When the max voltage magnitude of the reflectron is above that of the initial ion beam (typically about -3.5 kV), all primary ions are reflected. The off-line MCP signal is dominated by a massive background signal (non-photofragment ion) compared to most fragment ions. To allow for background subtraction, the off-line detector must be made less sensitive by reducing voltage, and results in less sensitivity for the already weak fragment signal.

5. Custom-made Electron Gun for Future Work

5.1 Modifications to the CE3K5U Commercial Electron Gun

The currently employed CE3K5U electron gun is a commercial model by Southwest Vacuum Devices that is no longer in production. Modifications are done to the currently available electron gun bodies to replace the filaments, as was done professionally by Southwest Vacuum Devices. The original device includes 3 major parts as labeled in Figure 2: a glass stem, the main electron body, and the ceramic emitter-post assembly, also included separately. The glass stem is designed primarily for use in commercial electron gun applications like CRT monitors and analog oscilloscopes. The tube is hollow, and allows for the stem to be fused into the device, vacuum to be drawn, and then for the stem to be sealed to preserve this vacuum. While it originally functioned as a mechanically stiff connection to the main electron body, the emitter cannot be replaced while the stem is connected. To replace the emitter, the stem is cut off by clipping the

leads. While they can be spot-welded back on later, in practice this has proved less than useful.

The emitter-post assembly is a ceramic disk with two isolated metal leads through it. The assembly is held in the anode cup of the electron gun by tantalum strips spot-welded to the cup and some level of friction. Bending these strips allows for the assembly to be removed. The emitter itself can be a number of metals; the original design of CE3K5U is a 0.020″ thick tungsten wire, spot-welded to the emitter posts. This wire is to be bent in a triangular fashion, with the highest point of the wire between 0.008-0.011″ below the anode cup and directly beneath the emitter hole.

Currently, the conditions used so far make a tantalum emitter much more conducive to the alignment and height adjustment required for a functioning emitter. Tungsten oxide forms during spot-welding, making connections brittle and prone to breaking with any adjustment. Thus, it is more suited to some kind of jig to ensure proper height and alignment. In contrast, 0.025″ tantalum wire is much more malleable and can be manipulated into proper alignment much more easily. A 0.020″ wire has not been tested, but may function more adequately and with less current flow over the emitter. Normal tungsten emitter current is between 2.5-3 amps. This is especially important because there are somewhat large tolerances in emitter post heights; while most emitters are approximately 0.465″ in total height, referenced to the anode cup, measuring each combination of emitter assembly and electron gun body is strongly suggested. In addition, emitter alignment with the emitter hole of the anode cup must be checked multiple times after

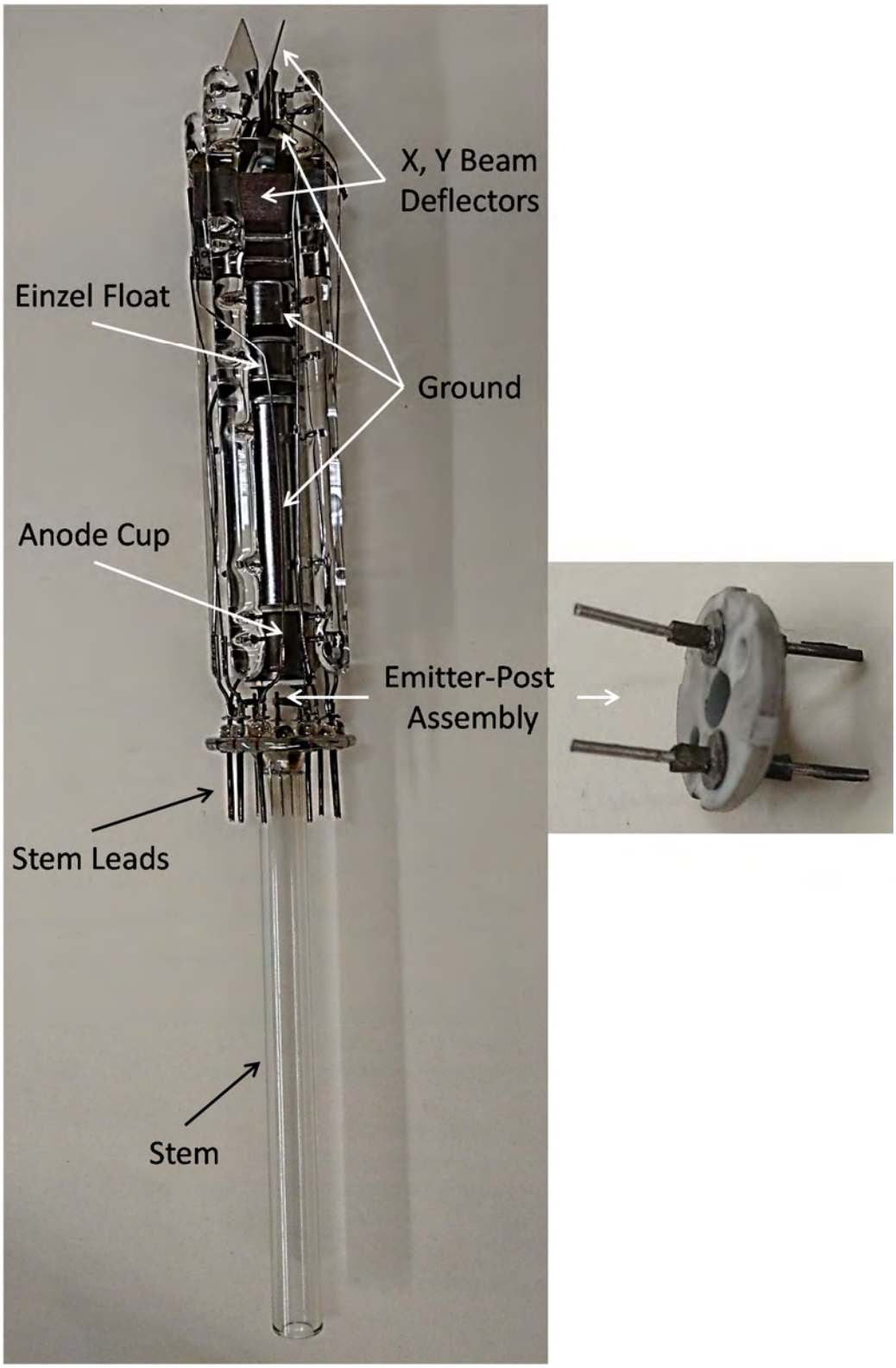

Figure 2. A labeled picture of the Southwest Vacuum Devices CE3K5U Electron Gun with a magnified, separate image of the emitter-post assembly. See text for details.

installation. A secure emitter-post assembly within the cup is strongly desired before installing the gun.

5.2 Preliminary Plans for Custom Electron Gun

The following design is incomplete, but does address some key design requirements for building a custom electron gun. It is a combination of designs including elements from the CE3K5U electron gun, the custom-built electron gun residing in the second anion photoelectron velocity-map imaging spectrometer of the Sanov lab, and the design of a low-voltage, high-current electron gun by Erdman and Zipf.[27] Electrostatic optics should follow the principals discussed in JILA Report #104 and as a first test should be matched with currently-employed voltages.[28]

The schematic for the new gun is shown in Figure 3. While dimensions for the electrostatic optics have been proposed, the following points have yet to be addressed to satisfaction. Firstly, no mounting hardware is included in the design. This includes the mounting of the electron beam deflectors to the respective ground plates. The same issue arises in mounting the anode cup, Einzel lense units, and the grounded plates for the beam deflectors. The general solution is straightforward; Teflon or another insulating material surrounds any screw or all-thread in any place where it must pass through an electrically-isolated part. Plastic washers or nuts can provide stability by being place above and below any pass-through. There are also commercially-available designs for this exact function, though they have yet to be explored.

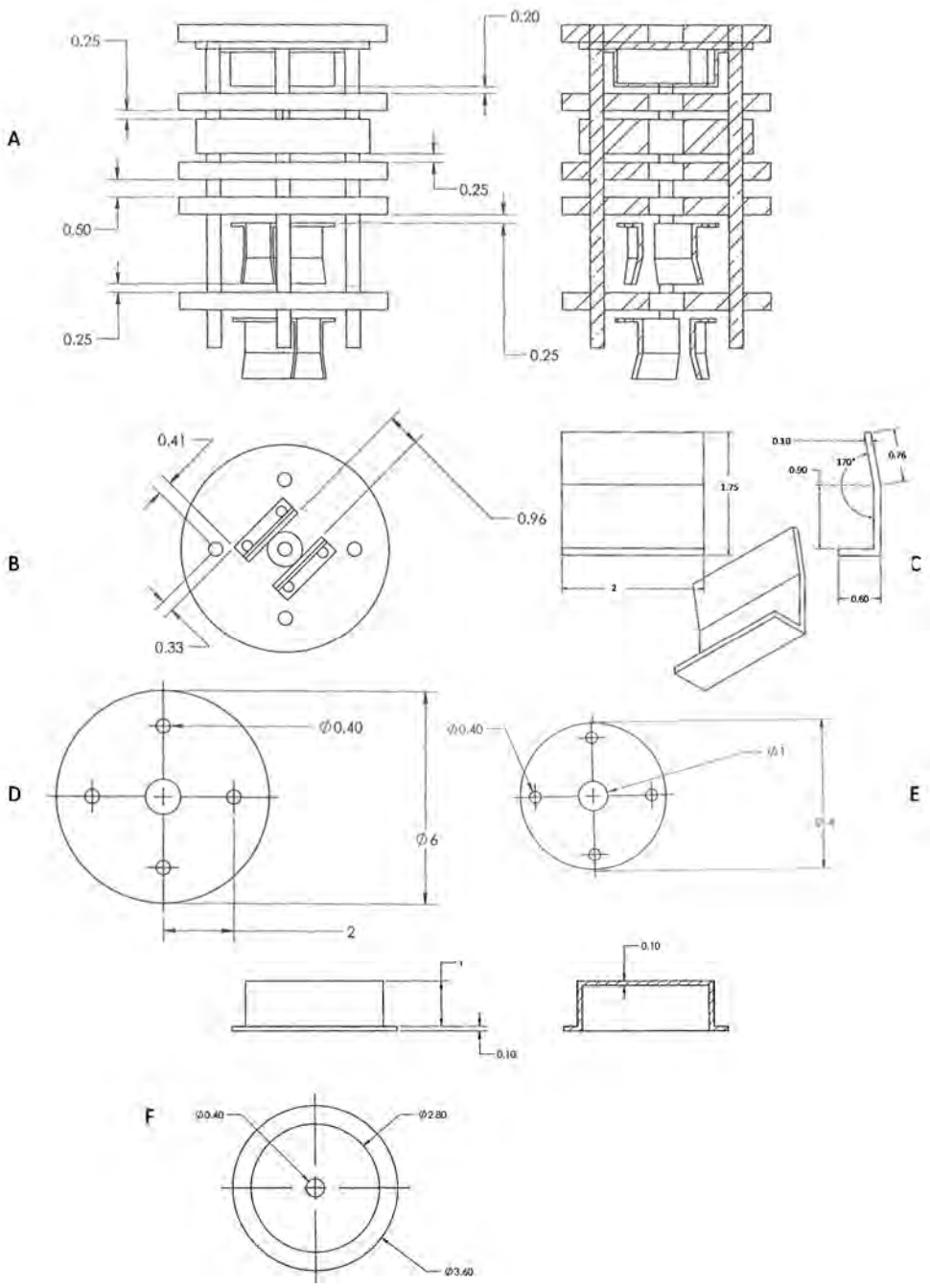

Figure 3. General schematic for a custom-built electron gun in centimeters unless otherwise indicated. Crossed-zeroes indicate a diameter. A) Gun in profile, showing gap distances. B) Dimensions for the X,Y beam deflectors and C) the proper mounting references. D) Einzel lense part dimensions for top, bottom, and E) middle. F) Dimensions for the anode cup.

Secondly, and perhaps most difficult is the attachment of any emitter-posts and the anode cup. The general design allows for the back plate to be removed and replaced in simple fashion. Thus, any emitter replacement can be performed with less difficulty and more precision. The anode cup is drawn with an oversized lip to provide room for mounting hardware; no design has been made for the emitter-posts. One possible solution is to machine the back plate entirely out of MACOR. This would eliminate the need for any insulating hardware required between the anode cup and plate. Feedthroughs to the plate could act as emitter-posts, while the anode cup and the rest of the electron gun body could be secured with all-thread, bolts, and nuts. Throughout the design, no definitive sizes for the mounting hardware have been suggested.

Lastly, no electrical connections have been shown on the design, though in principal they could all be achieved with Kapton-coated wires terminated with washer heads. The actual mounting of the completed gun inside the source chamber of the instrument has been grossly simplified by design. The oversized plates which remain at true ground allow the gun to be placed in any appropriately-sized metal tube. Ideally, a half-cylinder with lips raised up fore and aft of the gun will provide for repeatable and simple mounting with more than adequate air flow to cool the emitter.

Chapter 3: Benzonitrile - Electron Affinity, Excited States, and Anion Solvation Energies

Overview

We report a negative-ion photoelectron imaging study of benzonitrile and several of its hydrated, oxygenated, and homo-molecularly solvated cluster anions. The photodetachment transition from the unsolvated benzonitrile anion to the $\tilde{X}^1A_1$ state of the neutral peaks at 58 ± 5 meV. This value is assigned as the vertical detachment energy of the valence anion and the upper bound of adiabatic electron affinity (EA) of benzonitrile. The EA of the lowest excited electronic state of benzonitrile, $\tilde{a}^3A_1$, is determined as 3.41 ± 0.01 eV. The next excited state, the open-shell singlet $\tilde{A}^1A_1$, is found about an electron-volt above the triplet, corresponding to a vertical detachment energy of 4.45 ± 0.01 eV. These experimental results are in good agreement with ab initio calculations for neutral benzonitrile and its valence anion, but do not preclude the existence of a dipole-bound state of similar energy and geometry. The step-wise and cumulative solvation energies of benzonitrile anions by several types of species were determined, including homo-molecular solvation by benzonitrile, hydration by 1–3 waters, oxygenation by 1–3 oxygen molecules, and mixed solvation by various combinations of O_2, H_2O, and benzonitrile. The plausible structures of the dimer anion of benzonitrile were examined using density functional theory and compared to the experimental observations. It is predicted that the dimer anion favors a stacked geometry capitalizing on the π-π interactions between the two partially charged benzonitrile moieties.

1. Introduction

Benzonitrile (cyanobenzene) is the precursor molecule for numerous cyano-aromatic functionalities, but despite its diverse roles in chemistry, much remains unknown about its electronic properties. Cyano-containing molecules are of interest for their electronic properties and the associated reactivity. Cyano-aromatic functionalities, in particular, are often involved in intramolecular charge-transfer processes as electron acceptor moieties.[7,29] Benzonitrile (C_5H_5CN), on the other hand, has been shown to act a donor in intermolecular charge-transfer transitions.[8]

Many conjugated molecules containing CN functional groups have been investigated as electron-transport systems.[30-32] Among them, benzonitrile has been investigated as a charge-transfer agent on carbon nano-tubes doped with transition metals, where the aromatic ring coordinates with the metal atom.[33] It is also known to form ordered surfaces on metals. Due to its bi-functionality, it can interact with surfaces both with the CN lone pair and the π-conjugated ring.[34-36] This makes it an appealing target for surface chemistry, functionalization, and molecular sensor design.

The chemistry of cyano-containing organics is under investigation in the Titan atmosphere, where both benzene and HCN have been detected.[37] Under temperature conditions matching those on Titan, the formation of benzonitrile from these precursors proceeds rapidly and essentially to completion and has been predicted to occur even at temperatures of interstellar clouds.[37,38]

Despite the importance and relevance of benzonitrile, gaps remain in the knowledge of its most essential properties. Electron affinity (EA) is of utmost importance for electron transfer, particularly for the function of electron acceptors. To this end, even the

nature of the anion is still unclear. Given its large dipole moment (> 4 Debye),[39] the benzonitrile molecule is expected to support a dipole-bound anion[40,41] state, but valence anion states are possible as well. Measurements of electron affinity are the best way to shed light on this issue, but the most recent experimental determination of this property of benzonitrile dates back to 1983. In that work, using electron capture detection, the EA was determined—indirectly—to be 0.26 ± 0.10 eV.[42] Despite the larger uncertainty, this result was in agreement with the 1975 also indirect measurement of EA = 0.256 ± 0.017 eV,[43] and with the subsequent 1992 work that concluded the ground-state anion of benzonitrile was not observable by electron transmission spectroscopy, because it was "bound by a few tenths of an electron-volt".[44]

No direct spectroscopic determination of the electron affinity of benzonitrile exists to this day and only limited details are known about the electronic structure of benzonitrile and its effect on fluorescence and charge transfer.[45] An excited singlet state was found 4.5 eV above the ground state and has been well studied.[46,47] A nearby dark state was suggested by an electric-field induced perturbation study, with some restrictions on its symmetry inferred indirectly.[48] However, this state has not been observed spectroscopically.

We report a photoelectron imaging study of the benzonitrile anion and its clusters with water, O_2, and additional benzonitrile moieties. The detachment energy to the ground state of the neutral, as well as the adiabatic EA of the two lowest-lying excited states are determined from the photoelectron spectra. In addition, we report solvation energies for several solvent molecules and several states of benzonitrile and propose possible structures for the benzonitrile dimer anion which are consistent with the

observed spectra.

2. Experimental and Theoretical Methods

Anion photoelectron imaging experiments were performed using the custom-built instrument described in detail elsewhere.[49] In short, benzonitrile vapor was seeded in argon by passing the carrier over a liquid sample kept at room temperature. The resulting mixture was expanded into the high-vacuum chamber through a pulsed supersonic nozzle (General Valve, Inc., Series 99). The expansion was crossed at a right angle by a 1 keV electron beam. Anions were formed in the resulting plasma via slow secondary electron attachment to neutral molecules and clusters.[50] The anions were then extracted into the Wiley-McLaren mass-spectrometer and separated according to their *m/z* ratios. Anions of selected mass were irradiated with pulsed linearly-polarized light, produced by a Spectra Physics LAB-130-50 Nd:YAG laser. The fundamental or frequency-doubled, tripled, or quadrupled output was used as the source of 1064, 532, 355, or 266 nm radiation, respectively. The ion and laser beams intersected at 90° within the velocity-map[15] photo-electron imaging[17,22] assembly.

The photodetached electrons were projected electrostatically in the direction perpendicular to both the light and ion beams, toward a 40 mm position-sensitive dual microchannel plate detector coupled to a P43 phosphorous screen (Burle, Inc.). Positions of electron impacts on the detector were recorded by a thermoelectrically-cooled charge-coupled device camera (CoolSNAP Myo, Photometrics, Inc.). Images were typically collected for ~10^5-10^6 experimental cycles and were analyzed by reconstructing the original 3D-electron distribution via the inverse Abel transformation[17] implemented in the BASEX software.[51] The resulting radial distributions were converted to

photoelectron spectra using the well-known O^- photodetachment transitions for calibration.[52,53] All spectra presented in this work are plotted with respect to electron binding energy (eBE), calculated as eBE = hν – eKE, where eKE is electron kinetic energy.

Electronic structure calculations were carried out using the Q-Chem 4.0[26] and Gaussian 09[54] software packages. Q-Chem was used for geometry optimizations of benzonitrile and it anion at the couple-cluster theory level (CCSD) with the augmented Dunning's correlation-consistent basis set of double-ζ quality (aug-cc-pVDZ). The optimized structure of the anion was used for calculations of electron detachment energies using the equation-of-motion ionization-potential methodology combined with coupled-cluster theory (EOM-IP-CCSD).[25] In the Franck-Condon simulation of the photoelectron spectrum of bn^-, vibrational modes were treated as independent harmonic oscillators with Duschinky rotations as implemented in the PESCAL 2010 program.[55] Calculations on cluster anions were done in Gaussian. Geometry optimizations for the anion and neutral species employed the M06-2X density functional. Electron affinities (EA) were calculated as the difference in electronic energy (no ZPE correction) for the anion and neutral species calculated at the respective optimized geometries. Vertical detachment energies (VDE) were calculated as the difference in electronic energy (no ZPE correction) for the anion and neutral species, both calculated at the anion geometry.

3. Results

Several types of anionic species containing benzonitrile (bn) were studied in this work: the unsolvated bn^- anions; the hydrated cluster anions of benzonitrile $bn^-(H_2O)_n$, n = 1–3; the oxygenated cluster anions $bn^-(O_2)_n$, n = 1–3; the mixed hydrated-oxygenated

cluster anions $bn^-(H_2O)_n(O_2)$, n = 1–2; the homo-molecularly solvated cluster anions $(bn)_n^-$, n = 2–4; and the corresponding mono-hydrated and mono-oxygenated species, $(bn)_n^-(H_2O)$, n = 2–3 and $(bn)_n^-(O_2)$, n = 2–3.

3.1 Benzonitrile Anion

The photoelectron images and corresponding spectra for the unsolvated benzonitrile anion, bn^-, recorded at 1064, 532, 355, and 266 nm, are presented in Figure 1(a-d), respectively. Band A, appearing in all spectra, corresponds to the lowest-energy photodetachment transition of the anion. Assignment of this band requires the knowledge of the nature of the anion state. For reasons discussed in Section IV, it is assigned as the $\tilde{X}^2B_1 \rightarrow \tilde{X}^1A_1$ photodetachment transition of the valence anion of benzonitrile. We will refer to the $\tilde{X}^1A_1$ ground state of neutral bn, for brevity, as 'the singlet'. Band D, which corresponds to the electron counts appearing near the 1064 nm image center, is attributed to autodetachment.

All spectra in Figure 1 indicate a very small electron affinity of benzonitrile. The position of the first distinct peak of band A in the 1064 nm spectrum indicates a vertical detachment energy of VDE = 58 ± 5 meV. It also defines, with experimental certainty, the upper bound of adiabatic electron affinity, EA ≤ 58 meV. This result contrasts the previous indirect determination of the EA by electron capture, 0.26 ± 0.10 eV.[42]

Compared to 1064 nm (a), the 532 nm spectrum (b) in Figure 1 exhibits a complete loss of vibrational resolution for Band A. The resolution loss is not surprising due to the higher eKE. The 355 nm spectrum (c) reveals another transition, labeled B. This band is

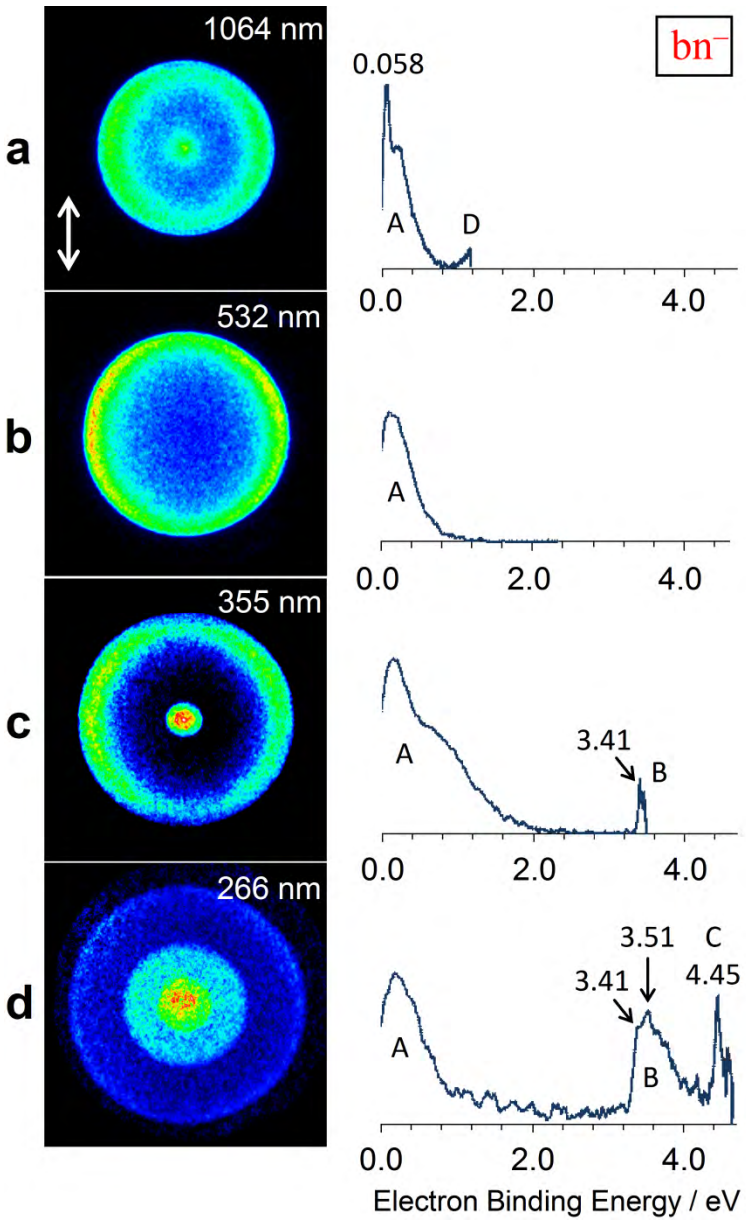

Figure 1. Photoelectron images and spectra of the benzonitrile anion (bn^-) at (a) 1064 nm; (b) 532 nm; (c) 355 nm; (d) 266 nm. Bands A, B, and C are assigned as transitions to the $\tilde{X}^1A_1$, $\tilde{a}^3A_1$, and $\tilde{A}^1A_1$ states of neutral bn, respectively. Band D is autodetachment. The direction of laser polarization is indicated by the double-sided arrow in (a).

observed near the 355 nm image center, but unlike band D it shifts away from the center at a shorter wavelength in (d). As discussed in Section IV, band B is assigned as the $\tilde{X}^2B_1 \rightarrow \tilde{a}^3A_1$ photodetachment transition. The $\tilde{a}^3A_1$ neutral state, which is not accessible via optical excitation from the $\tilde{X}^1A_1$ ground state of benzonitrile, will be referred to simply as 'the triplet'. Band B's onset at 3.41 ± 0.01 eV, prominent at 355 nm in Figure 1(c), as well as at 266 nm in (d), corresponds to the adiabatic electron affinity of the triplet state. The VDE of this band is determined from the 266 nm spectrum, VDE = 3.51 ± 0.01 eV.

In the 266 nm spectrum in Figure 1(d), yet another band (C) appears, assigned as the $\tilde{X}^2B_1 \rightarrow \tilde{A}^1A_1$ photodetachment transition. As justified later, the $\tilde{A}^1A_1$ neutral states of benzonitrile will be referred to as 'the open-shell singlet'. Band C peaks at VDE = 4.45 ± 0.01 eV. Taking into account the 0.058 eV VDE of band A, this value corresponds to a 4.39 eV vertical gap between the $\tilde{X}^1A_1$ and $\tilde{A}^1A_1$ neutral states at the anion geometry. This result agrees well with the previous measurements of the $\tilde{X}^1A_1 \rightarrow \tilde{A}^1A_1$ optical excitation of neutral benzonitrile using UV absorption, observed just above 4.5 eV.[46,47]

Table 1. Observed solvation-induced shifts of band A, corresponding to approximate solvation energies. Band B shifts are also indicated for bn^- solvated by bn or H_2O only (explicitly labeled with letter B). All values are in eV. The numerals and letters in parentheses indicate the datasets (figure numbers), where the reported shifts are observed.

Reference species	Added solvent molecule *		
	bn	H_2O	O_2
bn^-	0.54 (6b,7b) B: 0.42 (3c)	0.32 (2b) B: 0.24 (3b)	0.35 (4b)
$bn^-(H_2O)$	0.45 (8a)	0.28 (2c)	0.30 (4d)
$bn^-(H_2O)_2$	–	0.24 (2d)	0.22 (5c)
$bn^-(O_2)$	0.43 (8c)	0.27 (4d)	0.21 (4c)
$bn^-(H_2O)(O_2)$	–	0.21 (5c)	–
$(bn)_2^-$	0.35 (7c)	0.23 (8a)	0.24 (8c)
$(bn)_3^-$	0.27 (7d)	0.14 (8b)	0.20 (8d)
$(bn)_2^-(H_2O)$	0.26 (8b)	–	–
$(bn)_2^-(O_2)$	0.31 (8d)	–	–

* Heterogeneously solvated cluster anions of the general composition $X^-(Y)_m(Z)_n$, where $Y \neq Z$, can be viewed as resulting either from addition of Y to $X^-(Y)_{m-1}(Z)_n$, or from the addition of Z to $X^-(Y)_m(Z)_{n-1}$. For example, the $bn^-(O_2)(H_2O)$ data presented in Figure 4(d) results in two separate but related entries in the table: H_2O added to $bn^-(O_2)$ and O_2 added to $bn^-(H_2O)$. This analysis does not take into account the structural solvation motifs of these clusters. For example, no consideration is given which solvent molecule is the "primary" (more strongly bound) solvation agent.

3.2 Hydrated and Oxygenated Cluster Anions of Benzonitrile

The photoelectron images and spectra of $bn^-(H_2O)_{1-3}$ cluster anions are presented in Figure 2, with the corresponding unsolvated bn^- data reproduced for reference. The photoelectron images collected at 1064, 532, and 355 nm are presented, but only the 1064 nm spectra are shown, as the trends to be discussed are consistent throughout the spectra at all the wavelengths.

As indicated in the figure, band A in the $bn^-(H_2O)$ spectrum, peaking at eBE = 0.38 eV, is shifted up by 0.32 eV, compared to unsolvated bn^-. This shift corresponds approximately to the solvation energy of the bn^- anion by one water molecule. The magnitude of the interaction is on the lower end of typical hydration energies, but not unusual among other highly conjugated cyano-anions, such as the anions of trans-1,2-dicyanoethylene (fumaronitrile)[56] and tetracyanoethylene.[57] The $bn^-(H_2O)$ system was previously investigated by Maeyama et al. using the structurally-sensitive infrared vibrational autodetachment spectroscopy.[58] Using DFT methods, this cluster was assigned a C_s symmetry structure with the water being singly hydrogen-bound to the CN functionality, the other bond perpendicular to the aromatic ring. While some discrepancies exist between the experiment and theory, our experimental results in Figure 2 are in good agreement with the measurements reported by Maeyama et al.[58] In particular, their adiabatic detachment energy of 0.31 eV is in excellent agreement with the first peak of band A in Figure 2. Their VDE = 0.50 eV is in good agreement with the band A's peak in our higher photon energy spectra (not pictured in Figure 2). The second and third water molecules in $bn^-(H_2O)_2$ and $bn^-(H_2O)_3$ have further stabilizing effects of progressively decreasing magnitudes (0.28 and 0.24 eV, respectively).

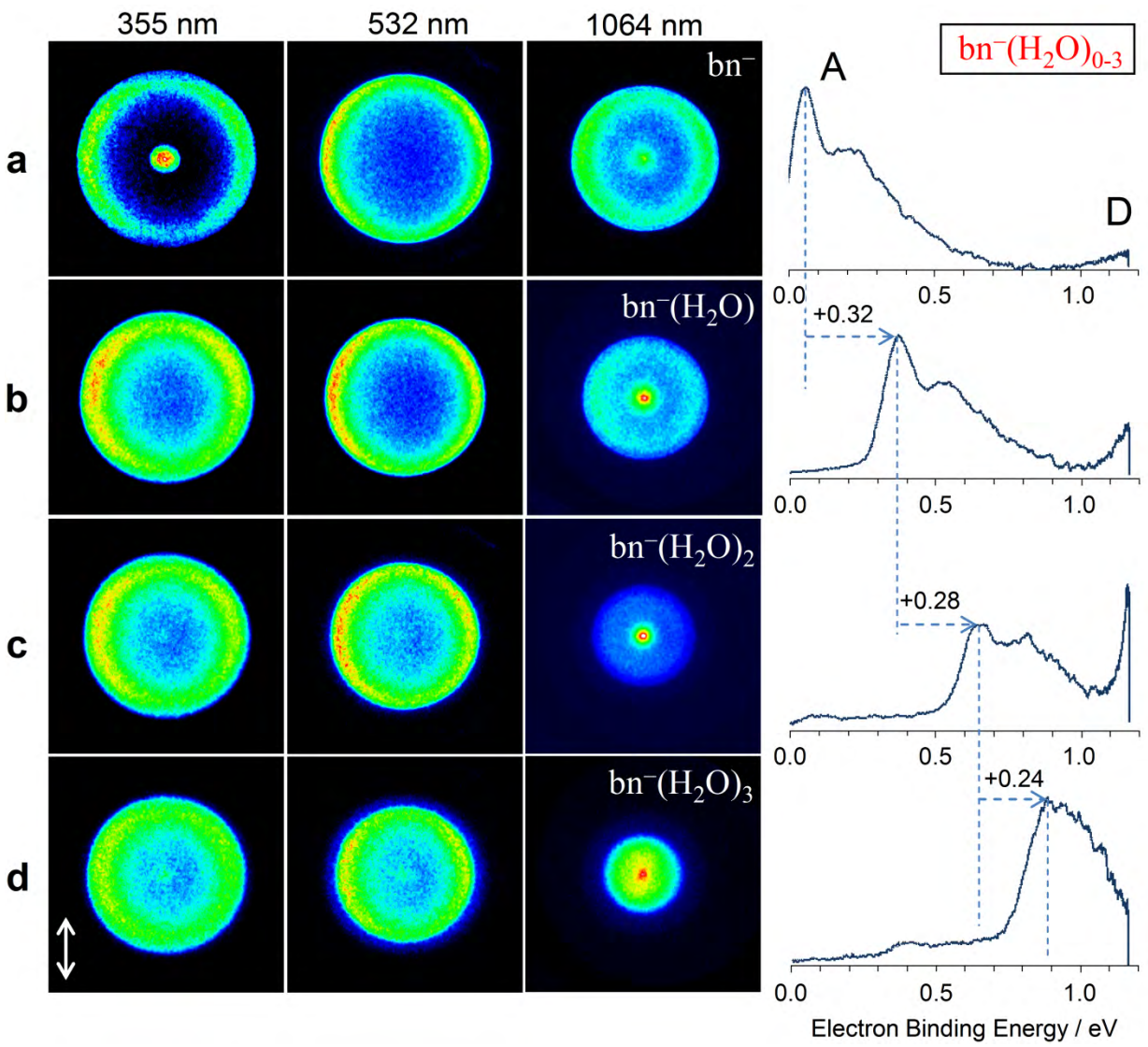

Figure 2. Left to right: 355, 532, and 1064 nm photoelectron images and 1064 nm photoelectron spectra of hydrated bn^- cluster anions: (a) unsolvated bn^- reference, reproduced for comparison from Figure 1; (b) $bn^-(H_2O)$; (c) $bn^-(H_2O)_2$; (d) $bn^-(H_2O)_3$. The direction of laser polarization is indicated by the double-sided arrow in (d). Spectral band shifts calculated based on the VDEs for band A are indicated by dashed horizontal arrows. The values are in eV.

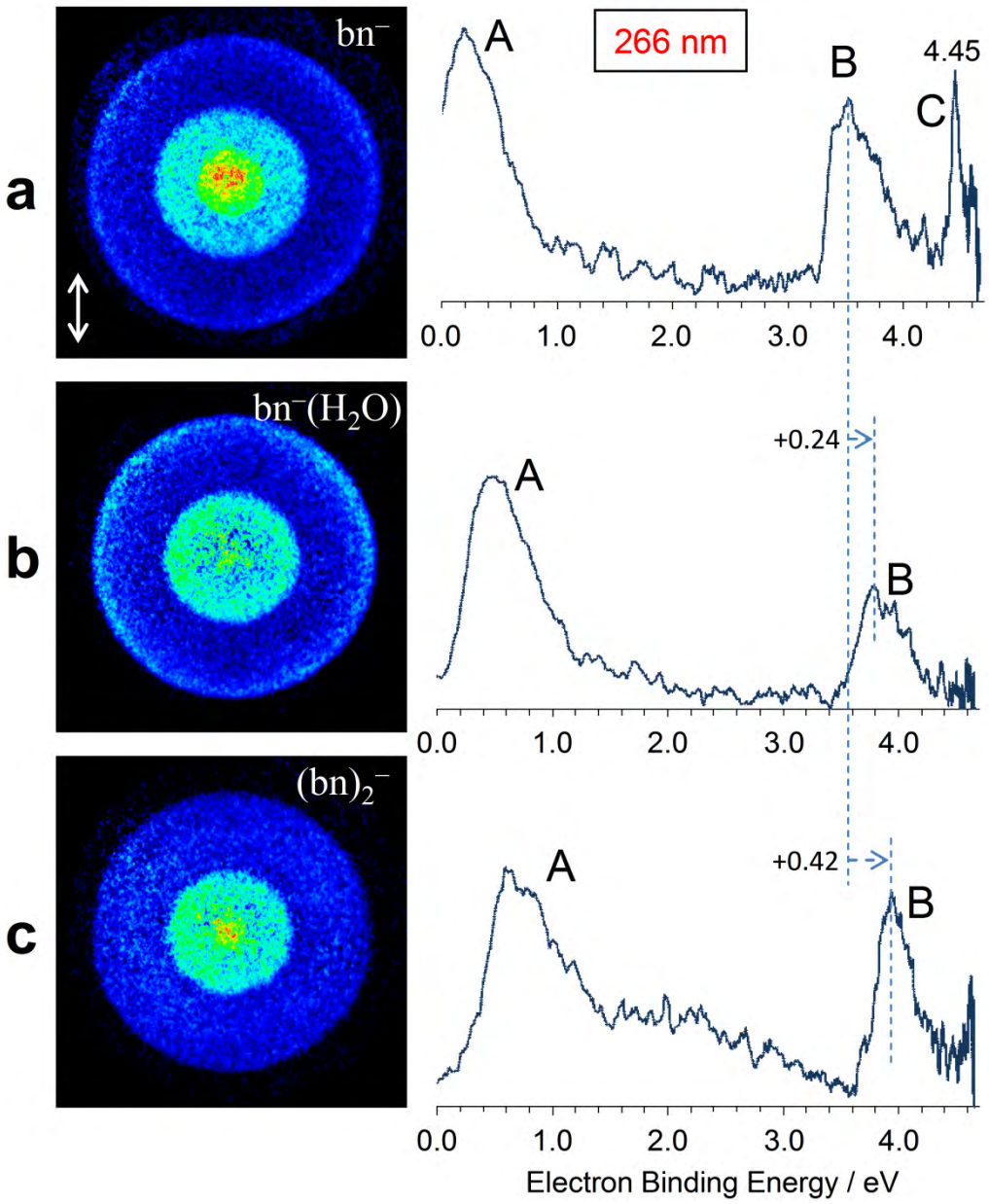

Figure 3. Photoelectron images and spectra of (a) bn^-, (b) $bn^-(H_2O)$, and (c) $bn^-(bn)$ collected at 266 nm. The results of the unsolvated anion (a) are reproduced for reference from Figure 1(d). The direction of light polarization is indicated by the double-sided arrow in (a). The band shifts are in eV.

The monohydrated cluster, $bn^-(H_2O)$ was additionally examined at 266 nm. The photoelectron image and spectrum are shown in Figure 3(b), where the reference bn^- dataset for the same wavelength is reproduced for comparison in (a). Band B in the $bn^-(H_2O)$ spectrum is shifted relative to the bn^- spectrum by 0.24 eV, which is smaller than the corresponding shift for band A, 0.32 eV in Figure 2(b). The difference is indicative of the different interaction strengths between the respective $\tilde{a}^3A_1$ and $\tilde{X}^1A_1$ states of neutral benzonitrile and water molecules. Band C, peaking at 4.45 eV in the bn^- spectrum in Figure 3(a), is shifted beyond the 266 nm photon energy cutoff in the $bn^-(H_2O)$ spectrum 3(b).

Cluster anions of benzonitrile solvated by 1-3 oxygen molecules were also studied. The 1064 nm photoelectron spectra of the $bn^-(O_2)_{1\text{-}3}$ cluster anions are presented in Figure 4(b)-(c), in comparison to the corresponding data for unsolvated bn^- in Figure 4(a). Band A in the mono-oxygenated cluster is shifted by 0.35 eV, which is comparable to (or even slightly greater than) the 0.32 eV shift in the corresponding $bn^-(H_2O)$ data in Figure 2(b). The effect of the second oxygenation in $bn^-(O_2)_2$, however, is only 0.21 eV [Figure 4(c)], smaller than the 0.28 eV effect of adding a second water molecule [Figure 2(c)]. Although mono-oxygenation appears to be slightly more effective than mono-hydration in stabilizing the bn^- anion, the trend is reversed when double-oxygenation is compared to double-hydration (a total of 0.56 eV for the addition of two O_2 molecules vs. 0.60 eV for two H_2Os).

For further comparison, cluster anions of the mixed $bn^-(O_2)(H_2O)_{1\text{-}2}$ composition were also examined. The 1064 nm spectrum of $bn^-(O_2)(H_2O)$ is shown in Figure 4(d). If this cluster is viewed as $bn^-(O_2)$ with an H_2O molecule added, then based on the band

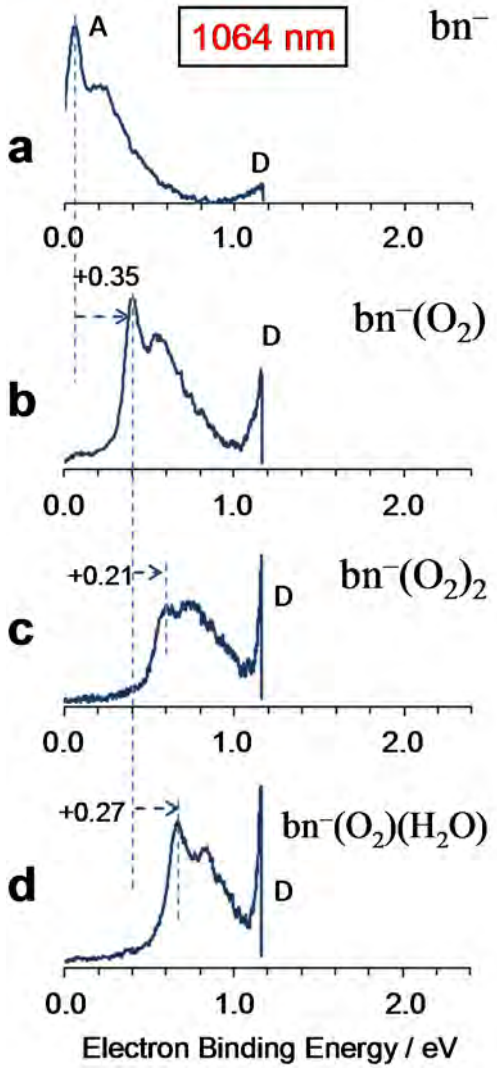

Figure 4. The 1064 nm photoelectron spectra of the oxygenated and mixed hydrated-oxygenated cluster anions of benzonitrile. The results of the unsolvated anion in (a) are reproduced from Figure 1(a). The band shifts are indicated in eV.

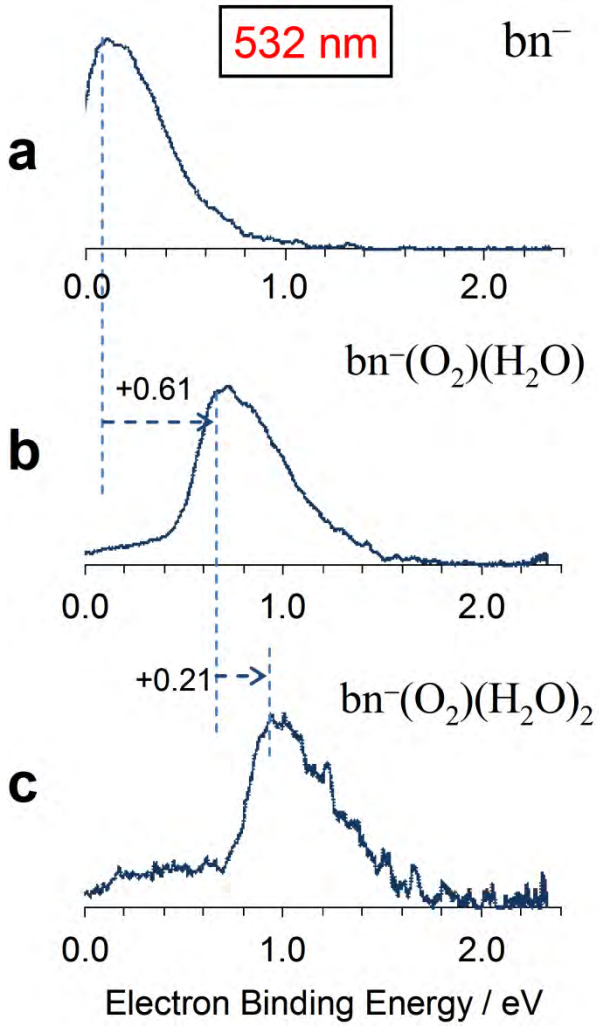

Figure 5. The 532 nm photoelectron spectra of mixed oxygenated and hydrated cluster anions of benzonitrile. The results for unsolvated bn^- in (a) are reproduced from Figure 1(b) for comparison. The band shifts are indicated in eV.

shift in Figure 4 (d) vs. (b), the approximate binding energy of H_2O to $bn^-(O_2)$ is 0.27 eV. This value is similar to the binding energy of H_2O to $bn^-(H_2O)$ in Figure 2(c). On the other hand, if $bn^-(O_2)(H_2O)$ is viewed as $bn^-(H_2O)$ additionally solvated by O_2, then comparison of the data in Figures 2(b) and 4(d)indicates that the approximate binding energy of O_2 to $bn^-(H_2O)$ is 0.30 eV, larger than the 0.21 eV binding energy of O_2 to $bn^-(O_2)$ revealed in Figure 4c. These differences are likely to be due to aggregate many-body effects in solvation, but they also point to different modes of solvation by O_2 or H_2O. This conclusion is intuitive, given that the bn^- is a relative large anion and H_2O is polar, while O_2 is not. Further discussion of possible structures can be found in Section IV C.

The 532 nm photoelectron spectra of $bn^-(O_2)(H_2O)$ and $bn^-(O_2)(H_2O)_2$ are presented in Figure 5, again in comparison with corresponding data for bn^-. The combined 0.61 eV binding energy of O_2 and H_2O in $bn^-(O_2)(H_2O)$ observed at this wavelength is similar to the 0.62 eV cumulative value from O_2 and H_2O in the 1064 nm data in Figure 4. The overall O_2 and H_2O stabilization of bn^- is also comparable to the corresponding values due to either two waters (0.60 eV in Figure 2) or two oxygen molecules (0.56 eV in Figure 4). The addition of a second water to $bn^-(O_2)(H_2O)$ shifts the band in $bn^-(O_2)(H_2O)_2$ by only an additional 0.21 eV [Figure 5(c)], which is similar to the band shift between $bn^-(H_2O)_2$ and $bn^-(H_2O)_3$ in Figure 2(d). Thus, even though different solvent molecules may bind to the anion in different ways, the binding of additional solvents is often less efficient, as it would be in the bulk.

3.3 Benzonitrile Dimer, Trimer, and Tetramer Anions

Perhaps the most intriguing observations in this work reflect on the properties of the homo-molecular cluster anions of benzonitrile, $(bn)_n^-$. The dimer, trimer, and tetramer anions were investigated using 1064, 532, and 355, and 266 nm light. The results for the dimer are presented in Figure 6(b)-(e) and can be compared to the 1064 nm data for the monomer anion in Figure 6(a). Figure 7 shows the 532 nm spectra of $(bn)_n^-$, n = 1–4.

Based on these spectra, particularly the similarity of the 266 nm spectrum of $(bn)_2^-$ in Figures 3(c) and 6(e) and the corresponding spectrum of bn^- in Figure 3(a), $(bn)_2^-$ is best described qualitatively as a monomer-anion solvated by a neutral bn molecule, i.e., $bn^- \cdot bn$. Similarly, the $(bn)_n^-$, n = 3–4 clusters also appear to involve monomer-anion cluster cores, solvated by $(n-1)$ predominantly neutral bn molecules and can be described as $bn^- \cdot bn_{n-1}$. In this picture, the cluster anion photodetachment transitions correspond to those of the bn^- cluster core, shifted by the approximate amounts of solvation-stabilization energy.

The lowest-energy photoelectron band of the dimer (band A) exhibits a stabilization of 0.54 eV relative to the monomer [Figures 6(b-e) and 7(b)]. This large band shift indicates strong but predominantly non-covalent interactions with the bn^- cluster core. The trimer and the tetramer exhibit gradually decreasing sequential solvation energies of 0.35 and 0.27 eV, respectively [Figures 7(c) and (d)]. Band B in the 266 nm spectrum of the dimer [Figures 3(c) and 6(e)] corresponds to the triplet state of bn formed in the photodetachment of the bn^- cluster core. This band is shifted by 0.42 eV, relative to the same band in the bn^- spectrum, in contrast to the 0.54 eV shift of the A band. The decreased solvation-induced shift of band B in $(bn)_2^-$ mirrors the similar effect observed

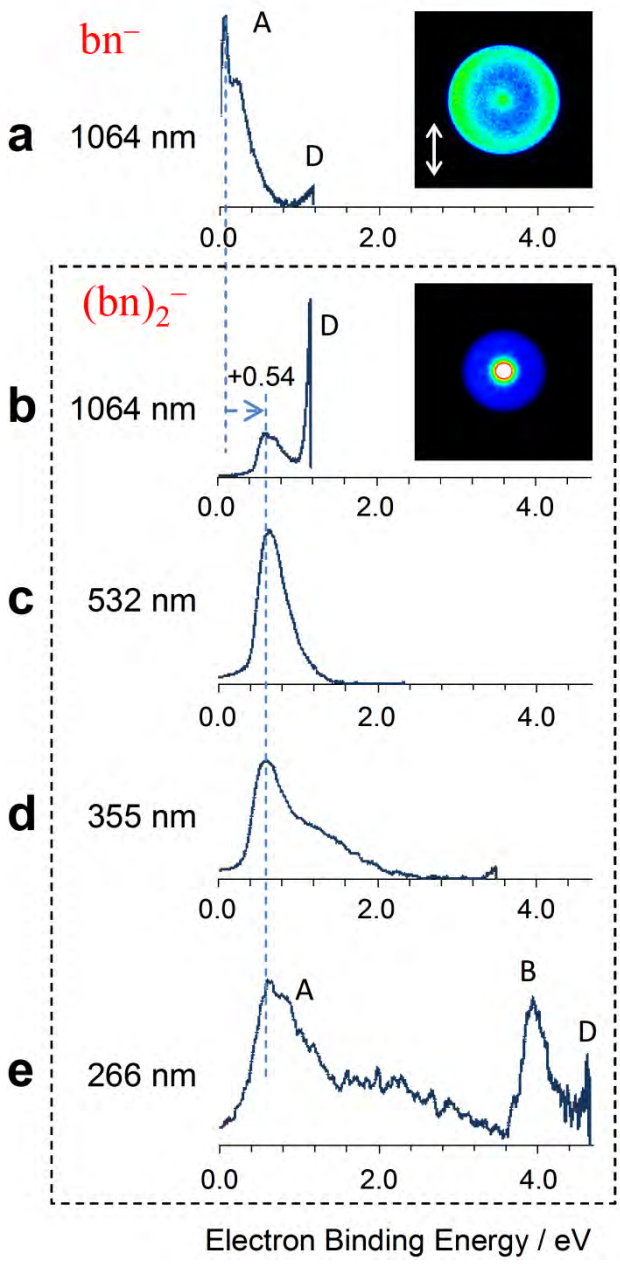

Figure 6. Photoelectron imaging results for the $(bn)_2^-$ dimer anion. (a) The reference 1064 nm data reproduced from Figure 1(a). (b)–(e) The 1064, 532, 355, and 266 nm $(bn)_2^-$ results. The 266 nm $(bn)_2^-$ spectrum of in (e) is from Figure 3(c). The band shifts are indicated in eV.

in the $bn^-(H_2O)$ spectrum [0.24 eV shift for band B in Figure 3(b) vs. 0.32 eV for band A in Figure 2(b)].

The observed band shifts are quite similar to those observed for other substituted aromatics. For example, the dimer and trimer anions of nitrobenzene (nb) were previously studied by photoelectron spectroscopy.[59] Compared to nb^-, the dimer exhibited an approximate band shift of ~0.5 eV and the trimer – an additional ~0.3 eV. These solvation energies compare almost exactly to what is observed here for benzonitrile.

3.4 Hydrated and Oxygenated Dimer and Trimer Anions of Benzonitrile

Figure 8 displays the 532 nm spectra of the $(bn)_n^-(H_2O)$ and $(bn)_n^-(O_2)$, n = 2-3 cluster anions. Arguments similar to those in Section III.C suggest that these clusters are also based on the bn^- monomer-anion cores, and their structures are therefore best described $bn^-(bn)_{1\text{-}2}(H_2O)$ and $bn^-(bn)_{1\text{-}2}(O_2)$.

In particular, the $(bn)_n^-(O_2)$, n = 2-3 photoelectron spectra in Figure 8(c) and (d) are inconsistent with a superoxide-based motif, $O_2^-(bn)_n$, n = 2-3. Similar arguments can also be made with regard to the data presented in Figures 4 and 5 for other oxygen-containing cluster anions studied in the work. The photodetachment of O_2^- has been extensively studied.[60-66] In particular, its 532 nm spectrum obtained under the experimental conditions similar to the present work exhibits resolved vibrational structure, with intensity peaking at an eBE ≈ 1.0 eV.[67] Although the vibrational structure is often lost due to solvation, the assumption of the $O_2^-(bn)_2$ structure of the cluster examined in Figure 8(c) would imply a slightly negative band shift resulting from solvation of the

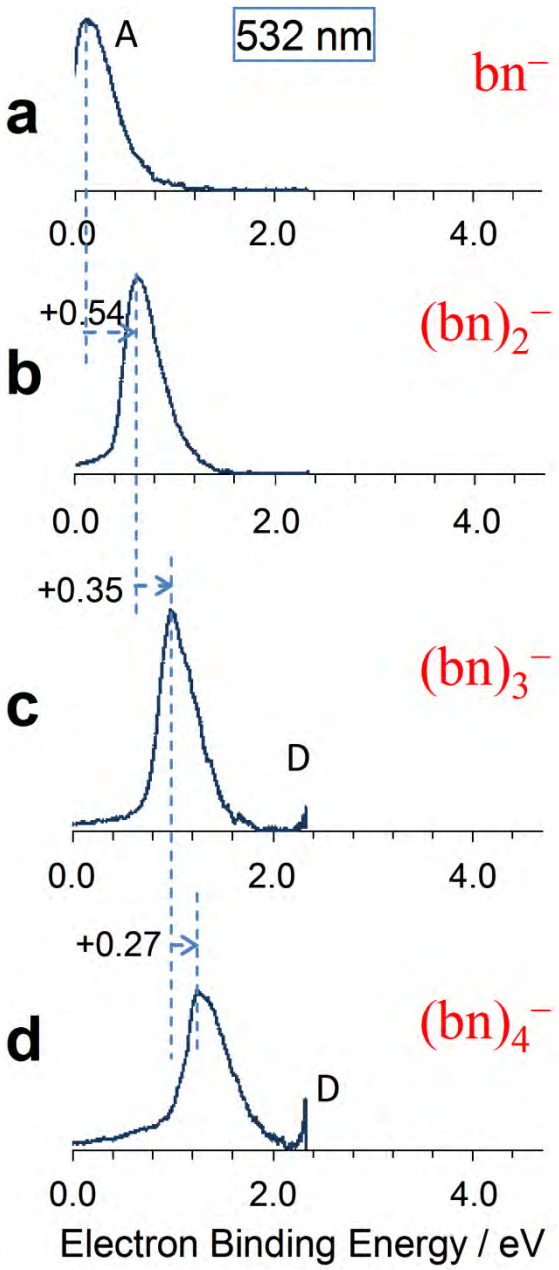

Figure 7. The 532 nm photoelectron spectra of the (b) dimer, (c) trimer, and (d) tetramer anions of benzonitrile. The results in (a) for the monomer anion, bn^-, are reproduced from Figure 1(b). The band shifts are indicated in eV.

O_2^- core by two polar benzonitrile molecules. This assumption is inconsistent with the generally expected energetics of cluster formation. Moreover, band A in the $(bn)_2^-(O_2)$ spectrum in Figure 8(c) exhibits very similar structure to band A in $(bn)_2^-(H_2O)$ photodetachment, Figure 8(a), suggesting the same type of anionic cluster core in both cases.

With that, the origin of the lower-eBE bands (to the left of band A) in the $(bn)_2^-(H_2O)$, $(bn)_3^-(H_2O)$ and $(bn)_3^-(O_2)$ spectra in Figures 8(a), (b), and (d), respectively, is unclear. One may speculate that these bands are due to metastable decay of the parent clusters, resulting in the photodetachment of smaller species. However, detailed analysis and confirmation of this hypothesis are outside the scope of this work.

Based on the observed band shifts, the binding energies of water or oxygen to the benzonitrile dimer and trimer anions are indicated in the respective spectra in Figure 8. All reported solvation energies, approximately determined based on the spectral shifts of band A in benzonitrile cluster anions are summarized in Table 1.

4. Discussion

4.1 Benzonitrile Anion

Two different structures can be proposed for the benzonitrile anion, bn^-: (i) the valence anion ($^2B_1$ electronic state), with the excess electron occupying the lowest vacant valance orbital of benzonitrile, i.e. the $4b_1$ (π^*) orbital shown in Figure 9(b)-(c), and (ii) the dipole-bound anion ($^2A_1$ state), where the diffuse electron is loosely bound to the electrostatic dipole moment of neutral bn. The ab initio calculations for the valence anion, discussed below predict a VDE of 0.047 eV, which is in adequate agreement with

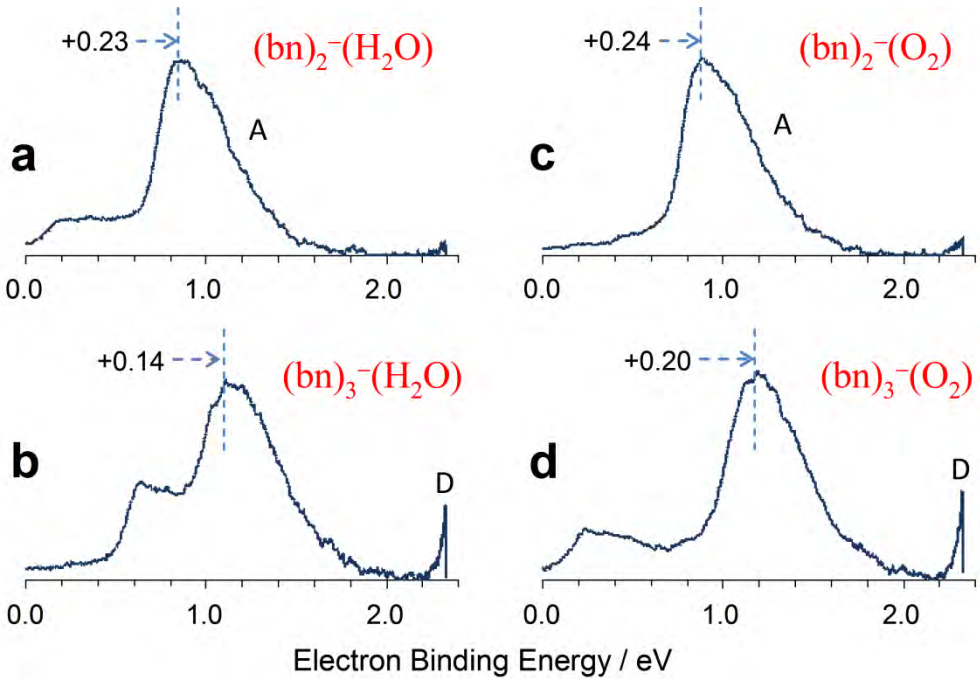

Figure 8. The 532 nm spectra of the hydrated and oxygenated dimer, (a) and (c), respectively, and trimer, (b) and (d), respectively cluster anions of benzonitrile. The observed band shifts are reported in eV with respect to band A of the unsolvated anion.

the observed maximum of band A (0.058 eV). The dipole-bound anion is presently under the theoretical investigation by Kirnosov and Adamowicz and their results indicate a VDE = 0.0186 eV.[39] Although this value is slightly below the experimentally observed band maximum, the small discreapancy alone is not sufficient to draw a definitive conclusion about the qualitative structure of the anions observed in this work.

Hence, bn^- presents an interesting theoretical and experimental problem. The existence of two states is anticipated, with close energetics and similar geometric structures, but very different electronic wavefunctions. Because of the energetic proximity and similar geometries, inter-conversion between the two types of anions is possible and even likely. In particular, the dipole-bound state may serve as a gateway to the valence structure. Similar processes have been hypothesized before, but usually involving valence and dipole-bound states of similar energies, but different geometries, such as in $HCCCN^-$.[68-70] The possibility of such inter-conversion in bn^-, where the two states overlap not only in energy, but also in the configuration space, is both interesting and intriguing. This possible process is under current theoretical investigation.[39]

There are several indications that the transitions observed in this work should be assigned primarily to the valence anion, although the contribution of the dipole-bound bn^- state cannot be ruled out completely based on available data. First, the low-energy band A in Figure 1(a) shows evidence of a vibrational progression, consistent with a perhaps small, but not trivial geometry difference between the valence anion and the neutral. It is less consistent with a dipole-bound anion, because photoelectron spectra of dipole-bound species are dominated by single sharp transitions,[71-73] reflecting almost no equilibrium geometry change of the neutral core upon the photodetachment.

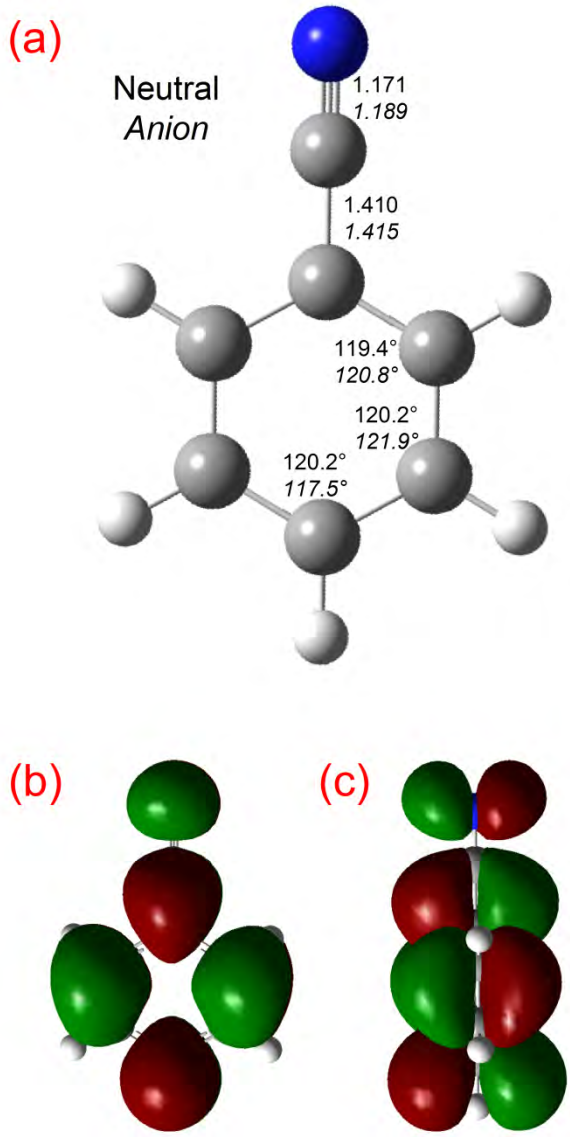

Figure 9. (a) Selected structural parameters of neutral benzonitrile (regular font) and its anion (italic font) optimized with the CCSD/aug-cc-pVDZ method and basis. Both the neutral and anion structures are of C_{2v} symmetry. (b) and (c) The singly-occupied $4b_1$ HOMO of bn^- shown from two different viewing angles.

To quantify this argument, we performed a Franck-Condon (FC) simulation of the lowest-energy photodetachment band of bn^-, assuming the valance-bound anion structure. The valence anion and neutral bn geometries were optimized in Q-Chem at the CCSD level using the aug-cc-pVDZ basis. The resulting structures are presented in Figure 9(a); they are similar to the corresponding B3LYP/6-31+G(d,p) geometries reported by Maeyama et al.[58] Both the anion and neutral structures in Figure 9(a) are of C_{2v} symmetry and, aside from a slight puckering of the ring in the anion, very similar. This is consistent with the experimental VDE of bn^- (Band A) being near the apparent onset of the band.

Next, the vibrational frequencies of neutral benzonitrile in the ground electronic state were calculated in Gaussian using the M06-2X density functional and the aug-cc-pVTZ basis set. The vibrational modes were treated as independent harmonic oscillators with Duschinky rotations, as implemented in the PESCAL 2010 program.[55] The eBEs and intensities of the resulting bn^- photodetachment transitions are shown as a FC stick spectrum in Figure 10, overlapped with the 1064 nm experimental spectrum from the data in Figure 1(a). The eBE of the 0-0 simulated transition was set to the experimentally determined VDE.

The stick spectrum was convoluted with a Gaussian function of a 5 meV full width at half-maximum, intentionally chosen to underestimate the experimental broadening. No anharmonicities or hot bands were included. The convoluted FC spectrum is shown in Figure 10 as a smooth blue line. The simulation clearly captures all of the major features of experimental Band A, including the decline of intensity at ~0.8 eV. Band D in the 1064 nm spectrum, assigned as autodetachment, is not part of the FC simulation. The

agreement clearly shows that the valence anion geometry, rather than the nearly unperturbed structure of a dipole-bound anion, is responsible for the experimentally observed band profile.

The second indication in favor of the valance structure of the anions studied in this work is the persistence of the overall features of band A with solvation. This is particularly clear in the $bn^-(O_2)$ case in Figure 4(b). Band A shifts by 0.35 eV upon the addition of O_2, while its overall spectral structure remains mostly unchanged. In the dipole-bound anion, the attached electron wavefunction is defuse and extended far from the core.[40,41,74] The solvation of such an anion by an O_2 molecule would likely lead to the formation of superoxide,[60,63,66] solvated by bn. The spectrum in Figure 4(b) is not consistent with O_2^-(bn).

The third indication is that past experiments on other systems have indicated that the photoelectron angular distributions in the photodetachment of dipole-bound anions tend to be predominantly parallel to the direction of the laser polarization.[75] This is contrary to the slightly perpendicular angular distributions of band A seen in the photoelectron images in Figure 1, particularly (a)–(c). On the other hand, the observed angular distributions are consistent with the π^* character of the valence anion HOMO ($4b_1$) shown in Figure 9(b)-(c).[21,22]

We therefore conclude that the transitions observed in our experiments are most consistent with the valance structure of the bn^- anion. This conclusion does not preclude the existence of the dipole-bound species, nor does it negate their presence in our experiments. It is possible that the dipole-bound signal is overwhelmed by the valence transitions observed in the same energy range, particularly if the photodetachment

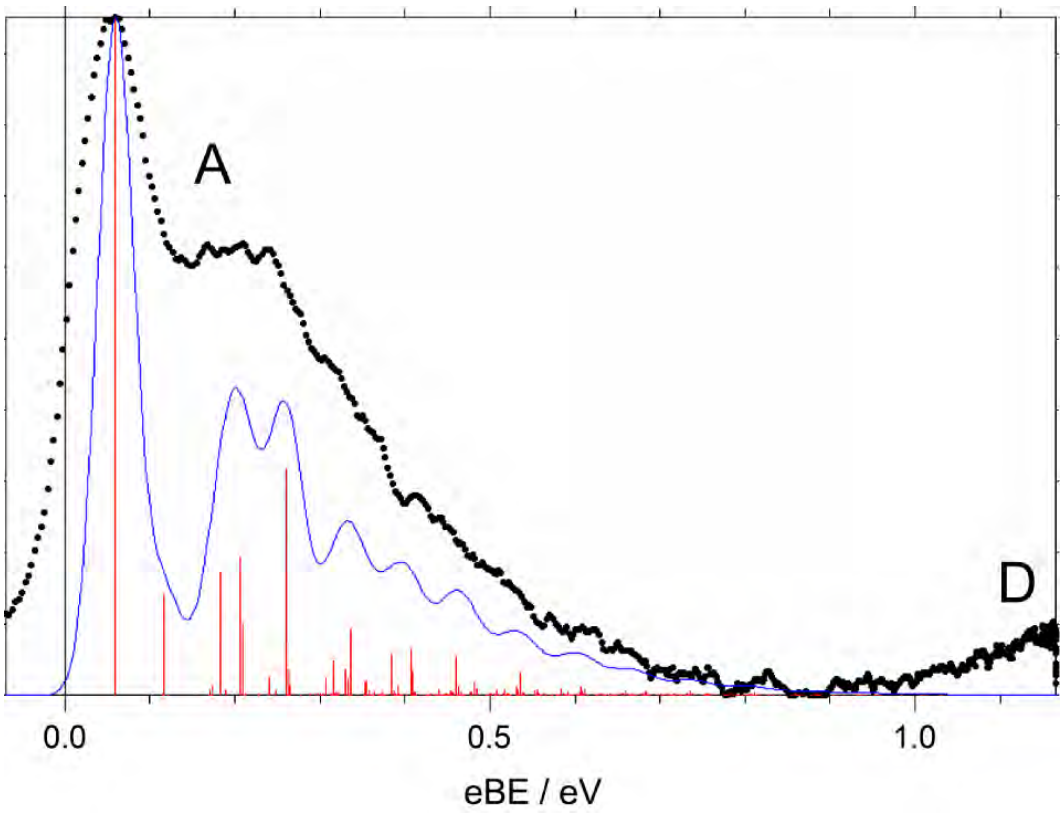

Figure 10. Franck-Condon (FC) simulation of the $\tilde{X}^2B_1 \rightarrow \tilde{X}^1A_1$ photoelectron spectrum of bn^-. Red vertical lines: the FC stick spectrum computed as described in the text. Continuous blue line: the FC stick spectrum convoluted with a Gaussian function (FWHM = 5 meV). Filled symbols: the expanded 1064 nm experimental spectrum from Figure 1(a).

cross-section for the dipole-bound species is smaller than that for the valance anion.

4.2 The Low-Lying Electronic States of Benzonitrile

To aid in the assignment of all observed photodetachment transitions, the bn^- anions and the low-lying electronic states of neutral benzonitrile were investigated using the coupled-cluster and equation-of-motion electronic-structure methods, specifically targeting the photodetachment. All calculations described in this sub-section were carried out using Q-Chem 4.0.[26]

To meet the needs of the EOM calculations, first the anion and neutral geometries were optimized at the CCSD level using the aug-cc-pVDZ basis. As already mentioned in Section IV.A, the resulting structures are shown in Figure 9(a). The ground and excited electronic states of neutral benzonitrile were then accessed with single-point EOM-IP-CCSD calculations starting from the anion reference at the optimized anion geometry. The properties of the resulting neutral states are summarized in Table 2.

The lowest-energy vertical transition corresponds to detachment from the $4b_1$ HOMO of the anion, resulting in the closed-shell singlet neutral state. The calculated transition energy, VDE = 0.047 eV, is in agreement with the experimental value of 0.058 eV for Band A. Photodetachment from HOMO–1 ($3b_1$) yields two neutral states: the lowest triplet, $\tilde{a}\,^3A_1$, and the open-shell singlet, $\tilde{A}\,^1A_1$. The triplet is predicted to lie (vertically) 3.358 eV above the anion, which also compares very well to the observed VDE of Band B, 3.51 eV [Figure 1(d)]. The $\tilde{A}\,^1A_1$ state is predicted to be at 4.281 eV above the anion. For comparison, the experimental VDE of band C is 4.45 eV. The slight discrepancies between the observed detachment energies and the calculated energetics of the $\tilde{a}\,^3A_1$

Table 2. Benzonitrile anion photodetachment transitions and the corresponding neutral states determined using the EOM-IP-CCSD/aug-cc-pVDZ calculations starting from the anion reference and geometry optimized at the CCSD/aug-cc-pVDZ level of theory. The nominal electron configuration of bn^- is $\tilde{X}^2B_1$: …$(8a_1)^2(8b_2)^2(1a_2)^2(3b_1)^2(4b_1)^1$.

Nominal detachment orbital	Neutral state	Predicted VDE / eV	Experimental VDE / eV	Observed transition
α-$4b_1$	$\tilde{X}^1A_1$	0.047	0.058(5)	Band A
β-$3b_1$	$\tilde{a}^3A_1$	3.358	3.51(1)	Band B
α-$3b_1$	$\tilde{A}^1A_1$	4.281	4.45(1)	Band C
β-$1a_2$	$\tilde{b}^3B_2$	4.711	–	–
α-$1a_2$	$\tilde{B}^1B_2$	4.897	–	–

and $\tilde{A}^1A_1$ states are not surprising in light of the complexity of the molecule, the limited double-ζ basis set, and the non-inclusion of triple excitations in the coupled-cluster calculations. These limitations notwithstanding, the predicted vertical gap between the $\tilde{a}^3A_1$ and $\tilde{A}^1A_1$ states of bn, 0.923 eV, is in remarkable agreement with the difference between the experimental VDEs of band B and C: ΔVDE = 0.94(2) eV.

Photodetachment from HOMO–2 ($1a_2$) yields a higher-lying pair of triplet and open-shell singlet states: $\tilde{b}^3B_2$ and $\tilde{B}^1B_2$. The predicted transition energies, 4.711 and 4.897 eV, respectively (Table 2), fall outside the experimental energy range. With that, all observed spectroscopic features are accounted for by theory.

4.3 Solvated Benzonitrile Cluster Anions

The overall appearance of band A in the photoelectron spectra remains largely unchanged upon the addition of one of two solvent molecules to bn^- (Figures 2-5). This indicates that bn^- preserves its identity upon solvation. The structure of $bn^-(H_2O)$ was previously investigated by Maeyama et al.[58] Using B3LYP/6-31+G(d,p) calculations, they determined the optimized cluster geometry, whereas the H_2O molecule is singly hydrogen-bound to the CN group of bn^-. The VDE of $bn^-(H_2O)$ was predicted to be 0.678 eV,[58] compared to our experimental value of 0.38 eV [Figure 2(b)].

Since no structural information concerning the oxygenated bn^- clusters exists in the literature, we attempted to optimize the $bn^-(O_2)$ cluster anion geometry using the M06-2X density functional implemented in the Gaussian 09 software package[54] paired with the aug-cc-pVDZ basis set. The functional was chosen for its proven performance for long-distance interactions in molecular complexes and clusters.[76-78] These attempts resulted in the excess charge localized predominantly on the oxygen, i.e., the O_2^-(bn) cluster motif rather than $bn^-(O_2)$. While this is not particularly surprising, since O_2 has a much larger EA than bn, this computational result contrasts the experiments, which clearly show the bn^- core anion. It is likely that the observed $bn^-(O_2)$ cluster anions are formed by attachment of O_2 to the initially formed bn^-, resulting is a local-minimum structure. Similar arguments apply to the structures of all others water and oxygen clusters of bn^- which retain the features of band A.

4.4 The Benzonitrile Dimer Anion

The experimentally determined band shifts summarized in Table 1 reveal that the

strongest solvation interactions among all the clusters studied are observed when a second bn moiety is added to bn^- or to a cluster anion already containing one moiety of benzonitrile. The interaction of bn^- with bn is stronger than with any other solvent studied, including water, which usually exhibits strong binding to anions. In this sub-section, we examine the dimer anion structures that may be responsible for this effect.

Stronger-than-hydration, non-covalent effects are a hallmark of ion-π and π-π stacking interactions.[79-82] The results summarized in Table 1 are suggestive of the involvement of the π system of benzonitrile in the observed bonding. This would also be consistent with the results of nitrobenzene dimer anion,[59] as similar solvation energies in the two cases suggest that the underlying interaction is not unique the cyano- or nitro-group.

In its neutral state, benzonitrile forms a dimer complex with hydrogen bonds between the cyano-group of one molecule and the othro-hydrogen of the other in a planar C_{2h} symmetry geometry.[35,83,84] However, neutral intermolecular interactions tend to be much weaker than anion-neutral interactions and there is no reason to expect that the structure of the dimer anion should follow the neutral complex motif. Case in point, Maeyama et al. showed clearly that the $bn^-(H_2O)$ anion has a different hydrogen-bonding scheme than the neutral system.[58] Hence, we carried out exploratory calculations on several plausible $(bn)_2^-$ structures, using the M06-2X density functional.

Initially, the structures of the neutral bn molecule and the bn^- anion were optimized separately using the aug-cc-pVDZ basis set. Various plausible combinations of the optimized bn and bn^- geometries were then used as the starting points for the dimer anion calculations. Due to the size of the system, complete $(bn)_2^-$ geometry optimization

presented a challenge, which was addressed using a two-step approach. First, crude potential energy scans, consisting of single-point energy calculations with the smaller 6-311+G* basis, were carried out by changing the relative positions of the frozen bn and bn^- structures (optimized above), until an energy minimum with respect to the intermolecular coordinates was found. The resulting $(bn)_2^-$ geometry was then used as the starting point of a complete geometry optimization using the 6-311++G** basis set. This approach yielded several plausible structures of the benzonitrile dimer anion. For each $(bn)_2^-$ structure, the solvation/interaction energy was calculated as the difference between the sum of the isolated bn^- and bn energies calculated using the same theory and basis, and the $(bn)_2^-$ dimer anion energy.

Three major structural motifs have emerged. The first corresponds to a planar structure with the two bn moieties laid end to end, maintaining an overall C_{2v} symmetry in collinear sigma-bonded geometry. The corresponding optimized geometry is shown in Figure 11(a). The solvation energy for this structure is calculated to be 0.47 eV (without accounting for the zero-point vibrational energy correction or the neutral van der Waals interactions). The Milliken charge distribution (–0.07/–0.93 for the top/bottom bn moieties in the figure) indicates a predominantly ion-dipole motif and a bn^-·bn solvated-anion structure.

The second is that of a hydrogen-bonding motif, shown in Figure 11(b), with the nitrogen of the cyano- groups ~2.7 Å from the ortho-hydrogen of the other ring. This structure is very similar to that previously reported by Borst et al. for the neutral van der Waals dimer.[84] The solvation energy is estimated to be 0.32 eV, indicating a weaker interaction than in the ion-dipole motif (a). We must consider, however, that a high

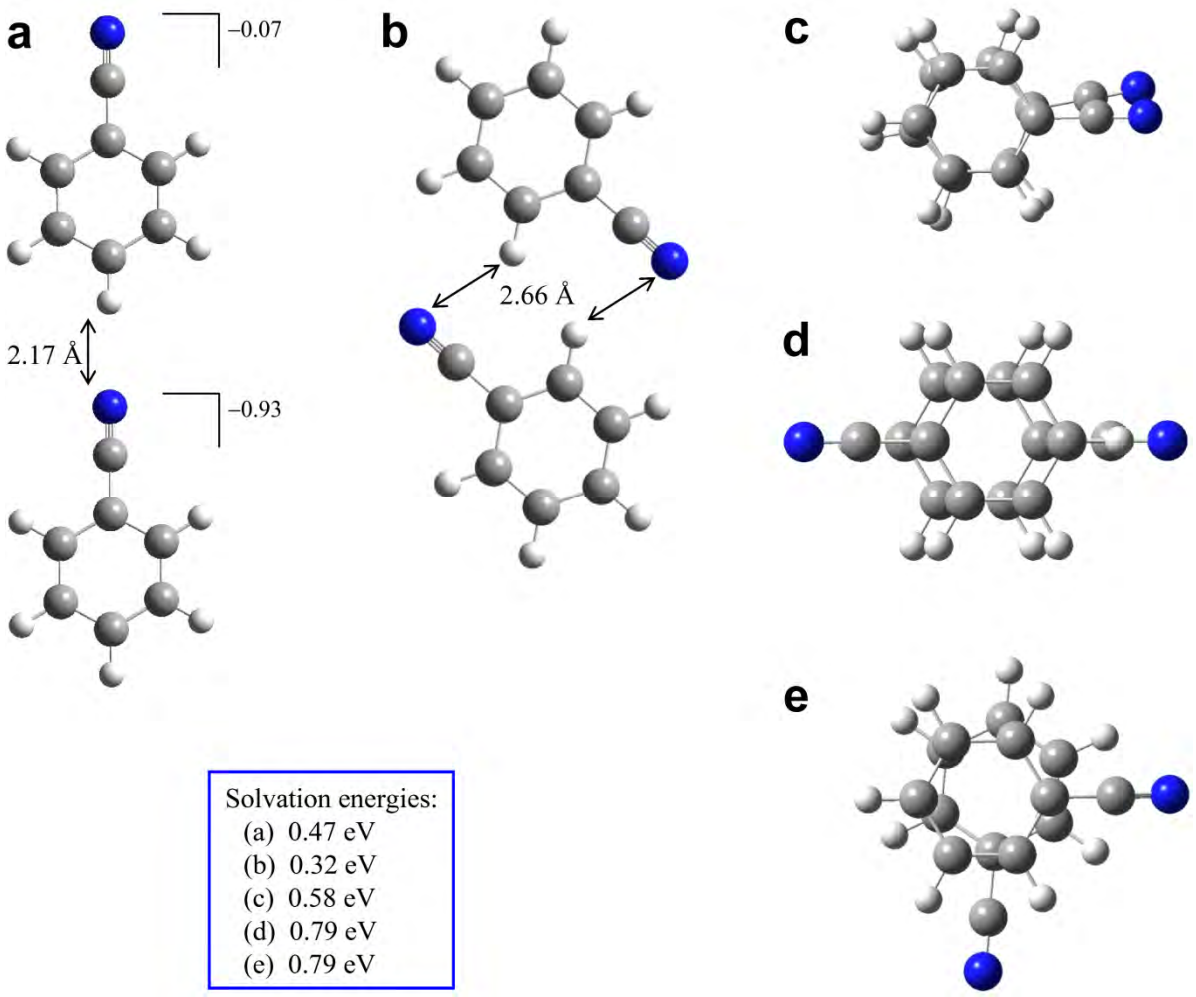

Figure 11. Five relaxed $(bn)_2^-$ structures optimized using the M06-2X functional with the 6-311++G** basis set (see the text for details). The solvation/interaction energies corresponding to each of the structures are summarized in the inset in the bottom left corner of the figure. The negative values next to the angular brackets in (a) indicate the Mulliken charges of the two bn moieties. In (b)-(e), the excess charge is approximately equally shared between the monomers. The average separation between the two moieties in the stacked geometries (c)-(e) is 3.2–3.4 Å.

degree of delocalization of the excess charge in each moiety and across the structure (Milliken analysis indicates the charge is evenly shared) mutes the benefits of an anion participating in a hydrogen bond. Secondly, the strong dipole of the neutral and anion predicted at this level of theory (4.7 and 4.4 Debye, respectively) may favor the ion-dipole interaction.

Other plausible $(bn)_2^-$ structures that were discovered involved π-π stacking interactions, with the charge shared approximately equally between two monomer moieties sandwiched approximately parallel to each other, with an inter-moiety separation in the 3.2–3.5Å range. The salient features of three stacked local-minimum structures are illustrated in Figure 11(c)-(e). The primary distinction between structures (c), (d), and (e) is in the relative orientation of the cyano-groups with respect to each other, as described by the eclipse angle. In (c), the CN groups of the two bn moieties are aligned in nearly the same direction (the eclipse angle is nearly zero). In structure (d), the CN eclipse angle is 180°, while structure (e) corresponds to an intermediate arrangement (eclipse angle ~ 90°).

Such π-π stacking structural motifs are quite common in dimers and dimer-anions of conjugated molecules. Structure (e), in particular, is reminiscent of the uracil dimer anion.[85] The respective solvation stabilization energies of structures (c), (d), and (e) in Figure 11, determined at the M06-2X/6-311++G** level of theory, are 0.58, 0.79, and 0.79 eV. While it is impossible to say definitively which $(bn)_2^-$ structure, (d) or (e), is most stable, it is clear that structure (c), corresponding to the two CN groups nearly eclipsing each other, is most unstable of the three stacked geometries (c)–(e). It has been shown that π-π stacking interactions of substituted benzenes are destabilized when the

substituents are close enough to interact directly through their local enviroment.[86] The $(bn)_2^-$ results presented here are in direct agreement with this observation. These results strongly support the importance of the π-π interactions in stabilizing the dimer anion and indicate that the corresponding structural motif favors minimizing the direct interaction between the CN substituent groups.

Similar to the water and O_2 clusters, band A of the $(bn)_2^-$ shown in Figure 6(b) has somewhat similar features to the spectrum of bare bn^-, despite the increase in the eBE. However, there is significant broadening, indicating solvent rearrangement upon $(bn)_2^-$ photodetachment. To shed light on the expected geometry changes, we optimized (M06-2X/6-311++G**) the neutral dimer structures using the anion geometries in Figure 11(d) and (e), reproduced in Figure 12(a) and (b), respectively, as the starting points. The results are shown in Figure 12, right. Both optimized neutral structures show an increase in the average distance between the moieties by 0.2–0.3 Å, compared to the anions. The structural changes of each moiety upon electron detachment from the dimer are quite small, similar to those in the detachment of bare bn^-. This result is consistent with the preservation of the overall features of band A and also with the greater broadening of the dimer-anion band compared to the mono-solvated water or oxygen clusters, since the (intermolecular) geometry change is larger for $(bn)_2^-$ than any other cluster studied.

The neutral energies corresponding to the initial and final geometries shown in Figure 12, in conjunction with the optimized anion energies, allowed for the calculation of the corresponding VDEs and EAs. The EAs corresponding to dimers structures (a) and (b) in Figure 12, right, are 0.513 and 0.514 eV respectively. This result is—again—consistent with the local substituent environment being the main factor in π-π interactions of

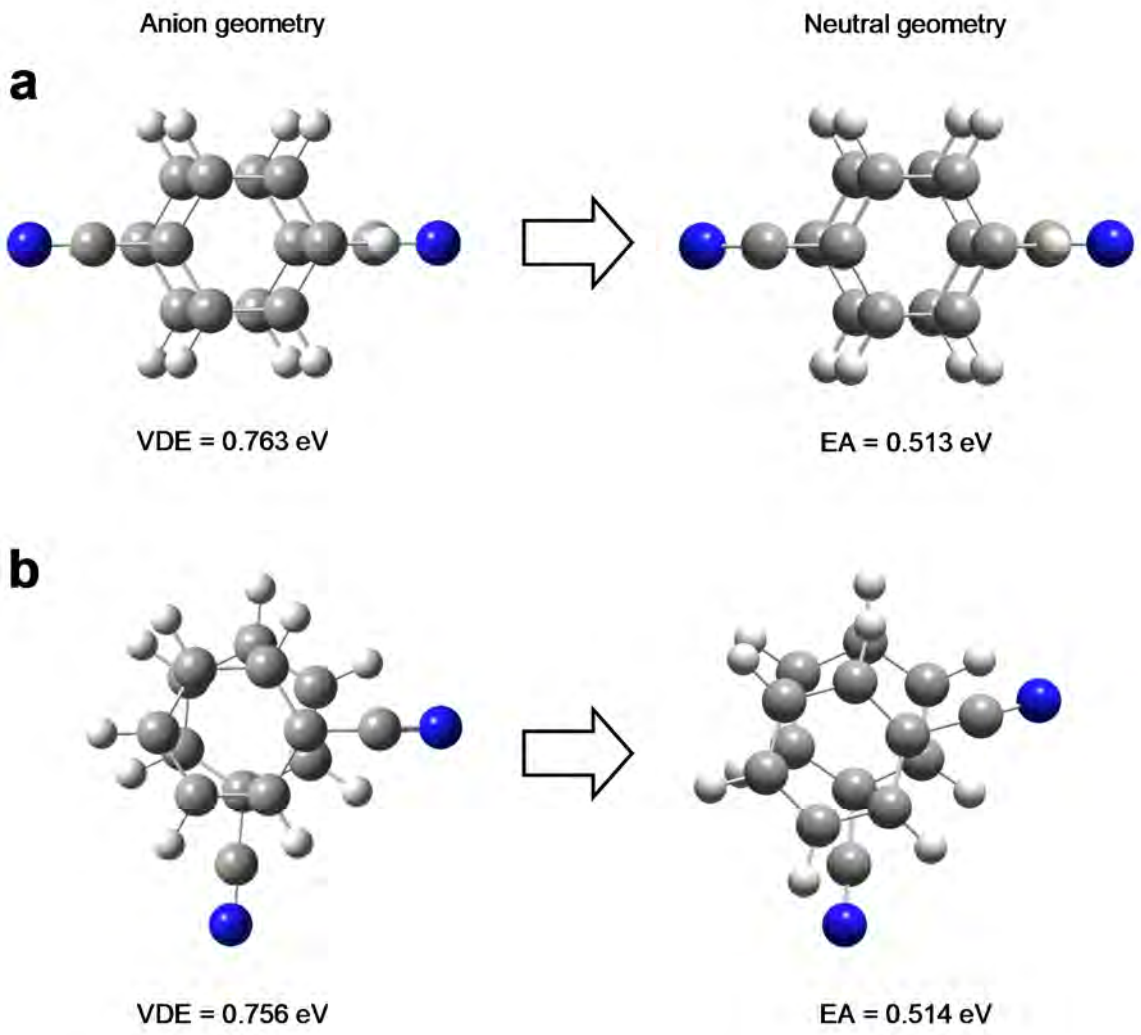

Figure 12. Left, (a) and (b): The $(bn)_2^-$ dimer anion structures reproduced from Figures 10(d) and (e), respectively. Right, (a) and (b): The neutral structures obtained by M06-2X/6-311++G** optimization using the anionic structures on the left as respective starting points. The average separation distance between the neutral stacked moieties is 3.4–3.6 Å.

substituted benzenes. The predicted VDEs of dimer anions (d) and (e) in Figure 11, corresponding to Figure 12(a) and (b), left, are 0.763 eV and 0.756 eV, respectively. Although the agreement between the predicted solvent stabilization energies and the experimental band shifts in the dimer anion (Table 1) is not perfect, it can hardly be expected given the limitations of the M06-2X functional and the limited size of the basis set used. Charge sharing between the two monomer moieties is clearly advantageous from the dimer bonding perspective. It effectively contributes covalent character to what otherwise would be a purely electrostatic interaction.

5. Summary

We have reported a negative-ion photoelectron imaging study of benzonitrile and several of its hydrated, oxygenated, and homo-molecularly solvated cluster anions. Benzonitrile is found to have a very small electron affinity. The photodetachment transition from the ground state of the anion to the $\tilde{X}^1A_1$ state of the neutral peaks at a VDE = 58 ± 5 meV. This transition is assigned to the $^2B_1$ valence anion, but the existence of a dipole-bound state of similar energy and geometry cannot be excluded and is in fact likely.[39] The above VDE value is also assigned as the upper bound of adiabatic EA of benzonitrile, improving over previous indirect methods. The EA of the first excited electronic state, the $\tilde{a}^3A_1$ state, was determined to be 3.41 ± 0.01 eV. The next excited state, the open-shell singlet $\tilde{A}^1A_1$, corresponds to an anion VDE = 4.45 ± 0.01 eV. These experimental results are in good agreement with the predictions of ab initio calculations. The step-wise and cumulative solvation energies of benzonitrile anions by several types of species were also determined. The strongest intermolecular interactions are observed between two benzonitrile moieties. The magnitude of these homo-molecular interactions

exceeds the hydration or oxygenation energies. Theoretical modeling of the benzonitrile dimer anion using density functional theory predicts that the dimer anion favors a stacked structural motif, capitalizing on the π-π interactions between the two benzonitrile moieties.

Chapter 4: The Unusual Solvent-Anion Pairing of O_2^- Solvated by Ethylene

Overview

Ethylene has been shown to be a degradation product following the 1-e^- attachment to ethylene carbonate. This ethylene product was not detected in isolation, but as a solvent molecule for O_2^-. Our photoelectron imaging study shows a relatively small solvation energy of ≤ 0.24 eV for the expected π-π interaction in the $O_2^-(C_2H_4)$ cluster anion. This result is supported by computations and MO analysis. EOM-IP-CCSD for $O_2^-(C_2H_4)$ results confirm 3 transitions expected of the O_2^- core anion, showing relatively little perturbation by the ethylene solvent. The EA of the $O_2(C_2H_4)$ cluster was measured at 0.69 ± 0.01 eV, while the $X\,^3A'' \leftarrow X\,^2A''$ photodetachment transition shows a 1400 ± 100 cm^{-1} vibrational progression in the 1064 nm spectrum.

1. Introduction

Ethylene carbonate is a key component in Li-ion battery technology as a non-aqueous solvent.[87] Its degradation, a topic of active research and development, [88-93] is a subject of numerous studies focused on the oxidation and reduction pathways. While many studies examine this decomposition in the condense phase and under practical electrolyte conditions, considerably less has been done to understand the changes to ethylene carbonate in the gas-phase. We report here the results of our investigation using ethylene carbonate as a solid sample. While we initially expected to observe the dipole-bound anion, we instead have indirectly detected a 1-e^- dissociative product, ethylene.[73]

Ethylene has been experimentally observed as a decomposition product of electrolyte solution by gas chromatography, with two major proposed mechanisms which explain its formation. However, these mechanisms and experiments occur at electrolyte-anode interfaces. The conditions in our home-built plasma source involve mostly isolated species. Additionally, two-e^- reduction is not possible due to electrostatic repulsion and the slow secondary-electron attachment process. However, at least one study has shown ethylene to be a dissociation product in the gas phase.[94]

The resulting ethylene here is detected as a solvent, associated with the O_2^- core anion. We report a photoelectron imaging and computational study on the mass-to-charge 60 anion which confirms the identity of the solvent as ethylene. Computations show a solvation interaction which is the result of a weak π-π bonding. This confirmation shows that ethylene is indeed a product of 1-e^- reduction of ethylene carbonate in the gas phase.

2. Experimental

Photoelectron imaging of the $O_2^-(C_2H_4)$ cluster anion was performed using the home-built anion photoelectron velocity-map imaging spectrometer described in detail in Chapter 2. Ethylene carbonate was purchased from Tokyo Chemical industries Co Ltd and used without further purification. The solid was kept refrigerated until being placed in the sample holder, where it was left at room temperature (~20 °C). The sample holder was heated to ~100 °C during experiments. Carrier gas composition was a particularly sensitive requirement to the formation of the target cluster. The primary carrier gas used was argon, however a small oxygen contamination was found to be absolutely necessary to the formation of the cluster. To this end, oxygen was used as a carrier gas for up to 10 seconds. Afterwards, argon was used and the spectrum monitored until cluster formation occurred. After cluster formation decreased, oxygen could be run again to return signal intensity. Using both oxygen as a carrier gas, and argon without the addition of trace oxygen both failed to form the cluster ion. The sample vapor and carrier gas were introduced to the high-vacuum source chamber by a pulsed General Valve Series 9 gas nozzle operating at 50 Hz, to match the laser system. The supersonic expansion was ionized to plasma by a culminated continuous beam of ~1 kV electrons. Ions were formed by slow secondary-electron attachment to the cluster.

Anions were extracted in the Wiley-McLauren TOF mass spectrometer region by a pusher plate using a -950 V pulse and were accelerated to a final potential of 3.5 kV. Ions of mass-to-charge 60 were interrogated by linearly-polarized laser pulses, with detached electrons velocity-mapped in the perpendicular direction to both the ion beam and laser electric field polarization direction. The 1064 (fundamental), 532 (second

harmonic), 355 (third harmonic), and 266 (fourth harmonic) nm laser light was produced using a SpectraPhysics LAB-130-50 Nd:Yttrium laser. Photoelectron signal were recorded using a position-sensitive dual-MCP detector coupled to a P43 phosphor screen; light produced was collected using a CoolSnap Myo thermoelectrically-cooled CCD. Typical images were collected for ~1 x 10^6 experimental cycles. Images were reconstructed using the inverse Abel transformation,[17] implemented in the BASEX program.[51] Radial distributions were converted to binding energy spectra, calibrated to the well-known EA of atomic oxygen.[52,53]

Geometry optimization and electronics structure calculations were performed using the Gaussian09 software.[54] Electron affinity (EA) was calculated as the difference in electronic energy of the anion and the neutral, each at their respective optimized geometry. Vertical detachment energy was calculated as the difference in electronic energy of the anion and neutral, both at the optimized geometry of the anion. Normal mode analysis was performed on the optimized structures to ensure the system was at a minimum. EOM-IP-CCSD was performed with the aug-cc-pVTZ basis on the optimized anion structure using the anion reference wavefunction, as implemented in Q-Chem 4.0.[25]

3. Results

3.1 Photoelectron Imaging of m/z 60 Anions

The results of the photoelectron imaging of the mass-to-charge 60 anion are shown in Figure 1. At 1064 nm (Fig. 1A), the first transition (labeled A) is visible, starting at 0.69 ± 0.01 eV. This first peak is labeled as the EA of this system. A broad but resolved vibrational progression is observed, with a frequency of 1400 ± 100 cm^{-1}.

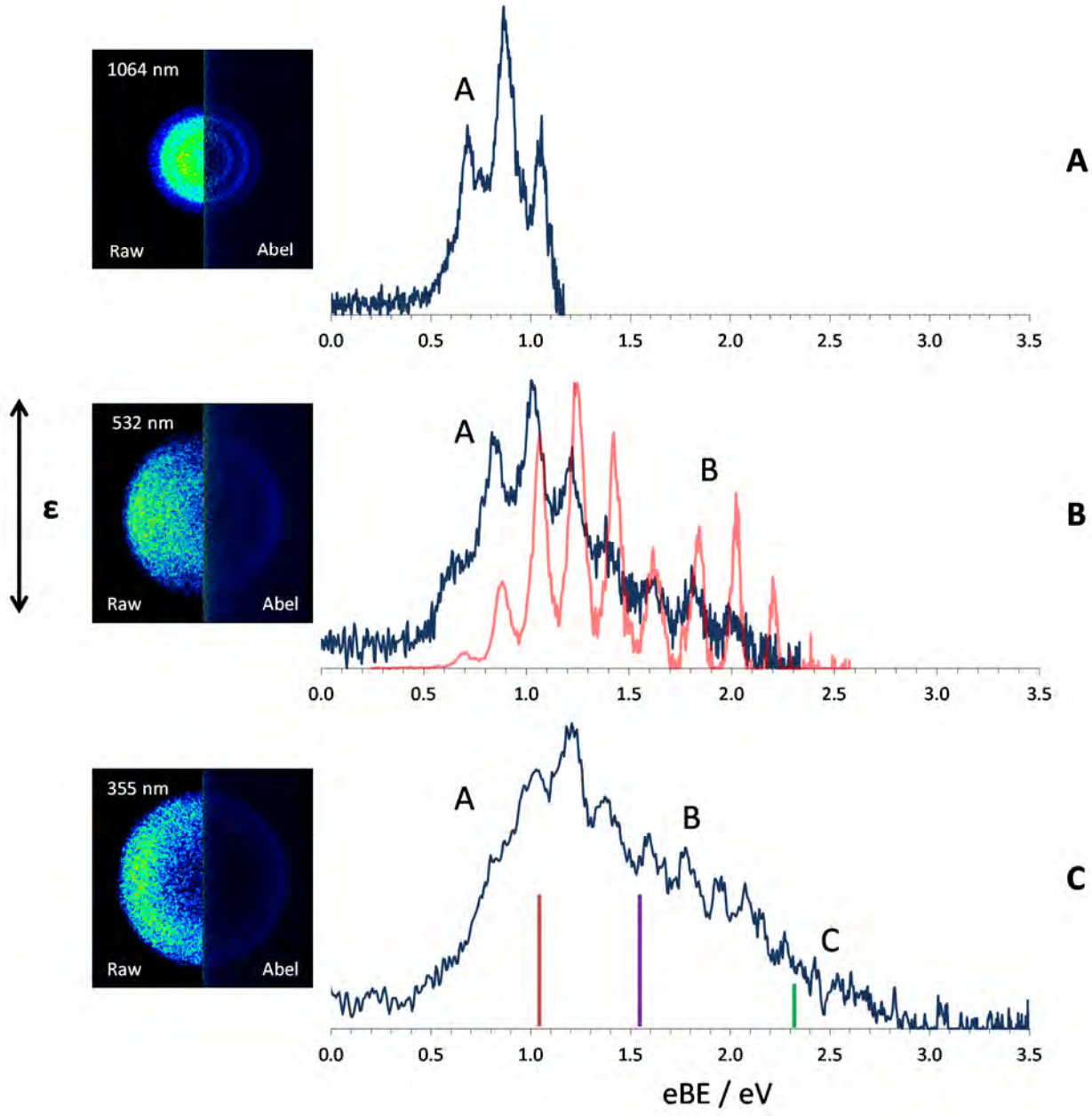

Figure 1. The photoelectron spectra obtained for m/z 60 anions are shown in black. The double-sided arrow indicates the direction of electric field polarization. Bands A, B, and C are identified as the ground-state triplet, closed-shell singlet, and open-shell singlet transitions respectively. The red spectrum is that of O_2^- shifted to higher eBE by 0.24 eV. The colored sticks indicate the EOM-IP-CCSD results in Table 1.

Increasing the photon to 2.34 eV (Fig. 1B), a second feature (labeled B) is observed, centered at about 1.77 eV. The profile of the spectrum indicates two Gaussian-like features, while the examination of the image shows that the PAD of these features is significantly different. Based on this empirical examination, we assign B to a second electronic transition to the neutral cluster.

The spectra obtained agree very well with those obtained for O_2^- under similar experimental conditions.[64,67] The solvent-broadened vibrational progression agrees with that of O_2^- detachment, which has a fundamental frequency of ω_e of 1580 cm^{-1}.[95] The relative positions and profiles of bands A and B, a separation of 0.75 eV using 532 nm, are an excellent match for the two low-lying electronic transitions from O_2^-.[67] The broadened profiles and increased binding energies are consistent with a solvated system with an O_2^- core anion. Further increasing the photon energy to 3.54 eV (Fig. 1C) causes a loss in resolution due to higher eKE. While unresolved, a weak increase in signal intensity around 2.4 eV binding energy is consistent with an expected excited singlet. This region is labeled as band C, but is done so only based on previous results as the band is unresolved.

Without the knowledge of the solvent, we can approximate the solvation energy for the system. For this we use the following formula,

$$E_{Solvation} \leq EA_X - EA_{X \cdot M} \qquad (1)$$

where the principle assumption is that the solvent-neutral interaction is significantly weaker. While a good assumption in many cases, the determined value is strictly an upper bound for the solvation energy. Using the determined value of this cluster, 0.69 ± 0.01

eV, and the most recent determination of the electron affinity of O_2, 0.4480 ± 0.0060 eV,[60] the $E_{Solvation}$ is determined as ≤ 0.24 eV.

3.2 Nature of the m/z 60 Cluster Anion

To determine the identity of the solvent, the number of possible species was narrowed by mass (28 amu) and by composition. Two possibilities remained: carbon monoxide (CO) and ethylene (C_2H_4). Both were used for a comprehensive theoretical investigation using the M06-2X density functional and the aug-cc-pVDZ basis set. Numerous geometries and configurations were attempted with both solvents. O_2^-(CO) was found to have a global minimum as the carbonate anion, CO_3^-. The calculated EA, along with the very nature of the anion, does not match the experimentally-determined EA or the spectral profile.

Ethylene was found to have an unexpected global minimum with the O_2^- anion, corresponding to the structure pictured in Figure 2, with C_s symmetry and the O_2 unit interacting predominantly with a single hydrogen. For this cluster geometry, CCSD/aug-cc-pVDZ predicts the EA at 0.522 eV, which is fairly reasonable when compared to the experimental result of 0.69 ± 0.01 eV. The EA predicted for unsolvated O_2 at the same level of theory is 0.189 eV, so any shortcomings in agreement between theory may be due to the limited basis set employed. This might also indicate that the first resolved peak is in fact not the 0-0 transition. Continuing with this geometry, EOM-IP-CCSD was performed for the C_S cluster at the anion geometry and reference wavefunction. In this way, the results will reflect the experimental VDEs. The results are shown in Table 1, and

despite an inconsistent match with the EA result, the EOM-IP calculation matches very well with the experiment.

The lowest energy transition is from the β-14a′ orbital, forming the ground-state triplet configuration. The predicted VDE matches quite well with the position of the maximum around band A. The second highest excitation is from the α-3a″ orbital and results in the closed-shell singlet configuration, which matches the first excited state of O_2, $^1\Delta_g$, and makes a reasonable fit to band B. An exact match would be in the realm of a Franck-Condon overlap simulation of the band, but this is outside the scope of this work. The third highest transition confirms that a third transition at about 2.4 eV is predicted for this system and is matched to band C.

Table 1. EOM-IP-CCSD/aug-cc-pVTZ results using the CCSD/aug-cc-pVDZ anion geometry and the $X\ ^2$A″ reference state.

Nominal detachment orbital	Neutral state	Predicted VDE / eV	Observed transition
β-14a′	$X\ ^3$A″	1.045	Band A
α-3a″	$a\ ^1$A′	1.553	Band B
α-14a′	$b\ ^1$A″	2.318	Band C[a]
β-15a′	$A\ ^3A''$	5.423	-

[a] Band C is totally unresolved

The fourth highest transition is well outside of the energy window of 355 nm, but is an excited triplet configuration. The 3 lowest energy transitions are marked in Figure 1C as vertical bars.

4. Discussion

Based on mass spectra for different carrier gas, the efficient production of the $O_2^-(C_2H_4)$ cluster anion from ethylene carbonate requires only a small amount of oxygen, but does indeed require external oxygen. Too little oxygen in the carrier gas mixture does not produce a sufficient number of clusters; presumably, pure oxygen causes oxidation of the ethylene carbonate vapor.

This leaves the production of ethylene to come from ethylene carbonate. Thermal degradation of the sample could be one source; however, this possibility seems somewhat unlikely compared to a complete combustion. Further, experimental work shows that degradation of the dry solid occurs slowly at temperatures above 200 °C, and the compound is stable in the presence of water at 100 °C.[96] A more likely possibility is a dissociative electron attachment with ethylene carbonate vapor, as there is no stable *valence* ion of ethylene carbonate.[97] While much of the focus of ethylene carbonate is on its stability and decomposition as part of Li-ion battery solvent, at least one theoretical study shows that ethylene is indeed a product of one-electron attachment.[94] While this is not shown to be the only possible product, it clearly is produced in detectable amounts for our experiment.

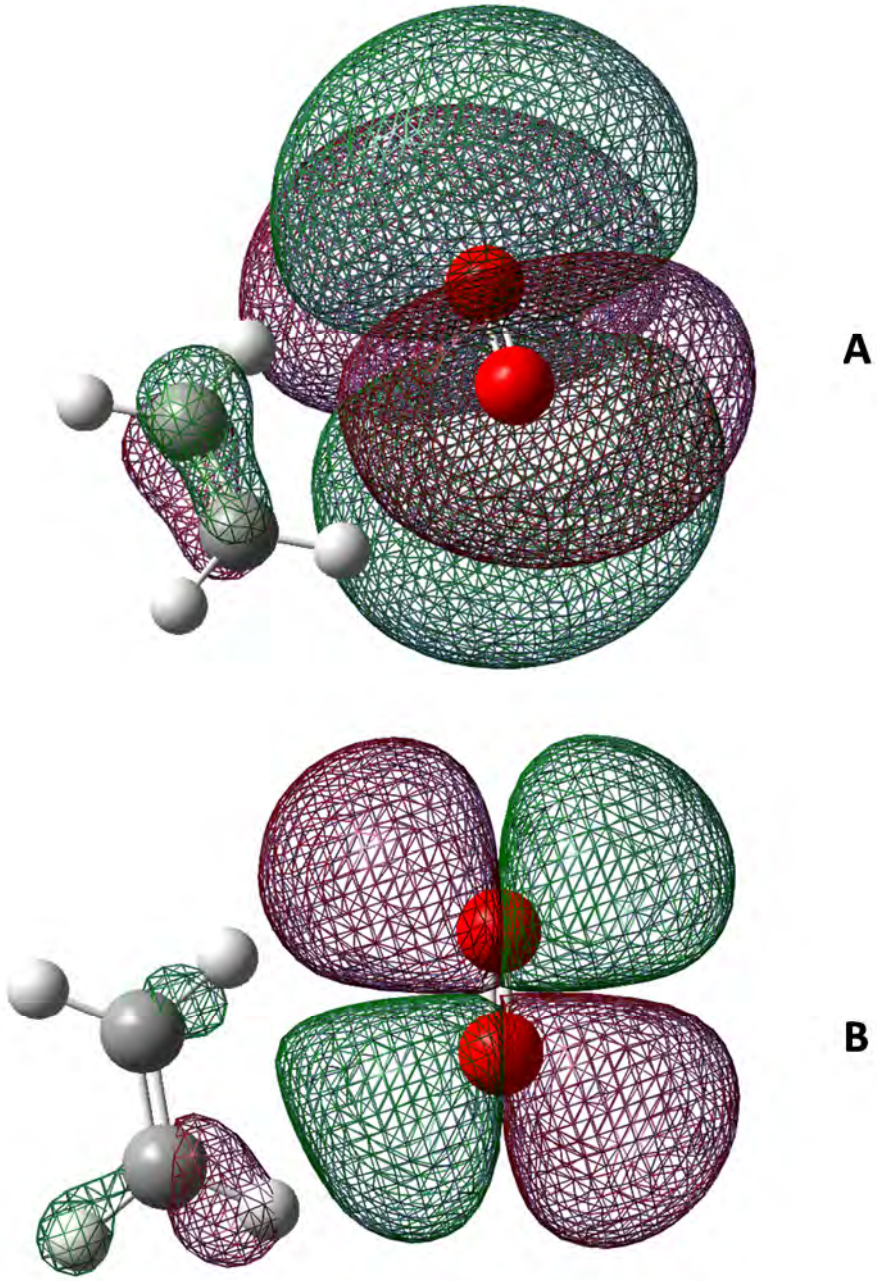

Figure 2. (A) shows the HOMO α-3a″ orbital with a π-orbital interaction between the O_2^- core and the C_2H_4 solvent. (B) shows the HOMO-1 α-14a′ orbital with a σ-like interaction. Iso-surface values are adjusted for clarity.

Despite having a π orbital with which to interact seemingly directly with the *d*-like HOMO of the O_2 anion (a π-π stacking like the bn_2^- system in Chapter 3), the low-energy geometry involves the interaction of a single hydrogen. This preference is intuitive upon closer examination. The HOMO of O_2^- is well-known to be antibonding; the π-bond of ethylene is instead bonding. This produces a poor overlap between any possible phases of the ethylene π-bond. Molecular orbital analysis at the CCSD/6-311++G** level shows that the HOMO of the system is indeed the antibonding orbital of O_2^-. Only lobes of one oxygen overlap with the density located in ethylene, resulting in a very weak π-interaction. This result agrees well with the expectation of a π-bond, but has a low solvation energy for the type of interaction (compared to bn_2^- in Chapter 3 for example). The odd position of O_2 relative to ethylene is likely driven by sterics. The HOMO-1 shows the 14a′ orbital interacting very weakly through a σ-type interaction. With the oxygen orbital lobes in-plane with ethylene, little favorable overlap with the orbitals of ethylene is available. Likewise, linear arrangement between the carbon and oxygen atoms can produce favorable overlap only between the ethylene π-bonding and either the HOMO or HOMO-1 of O_2^-

5. Summary

The mass-to-charge 60 ion was determined to be a core O_2^- species with the unusual solvent of ethylene. The ethylene is hypothesized to be produced under the thermal decomposition of ethylene carbonate under weakly aerobic conditions. The ethylene solvation energy was determined to be ≤ 0.24 eV. While this value may appear small for what appears to be a π-π interaction, analysis of the molecular orbitals shows

that the overlap between the O_2^- core and the solvent is limited by the bonding-antibonding orbital overlap.

Chapter 5: Heterogeneously Substituted Carbenes - Photoelectron Imaging of the $FCCN^-$ and Comparison to $ClCCN^-$

Overview

This work continues our studies of heterogeneous substitution effects in cyanohalo-radicals and carbenes. Negative-ion photoelectron imaging was used to investigate the substituted carbene derivative of fluoroacetonitrile. We report a closed-shell singlet ground state for the cyanofluorocarbene, FCCN, with an adiabatic electron affinity EA = 2.081 ± 0.002 eV and a singlet-triplet gap of $\Delta E_{S\text{-}T}$ = 0.42 ± 0.04 eV. The open-shell singlet $^1A''$ state was also observed experimentally. The results are discussed in comparison with the previously reported fluoro- and cyano-substituted carbenes, as well as in light of our recent work on the radical and carbene derivatives of chloroacetonitrile. We find that the experimentally measured $\Delta E_{S\text{-}T}$ of FCCN agrees well with the general trend of similar carbenes.

1. Introduction

Carbenes are reactive intermediates that play important roles in chemical reactions. The properties of carbenes are largely determined by the two non-bonding electrons distributed between the nearly-degenerate σ and π orbitals localized (nominally) on a carbon center. The two electrons in two orbitals motif allows for close-lying …$\sigma^2\pi^0$ and …$\sigma^1\pi^1$ electron configurations.[10] The substituent groups affect the stability of the orbitals and, therefore, the energetic ordering of the singlet and triplet states,[98] as well as the magnitude of the singlet-triplet splitting, $\Delta E_{S\text{-}T.}$ The splitting dictates the reactivity of the carbene, as reactions mechanisms often vary for the singlet and triplet species.[99,100]

Anion photoelectron imaging is a uniquely useful tool for examining these highly reactive molecules. The negative ions of carbenes can be formed in the gas phase by H_2^+ abstraction reactions of a closed-shell precursor with O^- produced in situ.[101,102] The anions of both singlet and triplet ground-state carbenes are radical anions with the same canonical …$\sigma^2\pi^1$ electron configuration.[10] In photodetachment, a photon of sufficient energy can access the singlet (…$\sigma^2\pi^0$) or the triplet (…$\sigma^1\pi^1$) states of the carbene by removing an electron from the respective π or σ orbitals of the anion. Detachment from the σ orbital can additionally access the higher-lying open-shell singlet (…$\sigma^1\pi^1$) state.

Due to different characters and/or symmetry properties of the π and σ orbitals, the respective photodetachment processes are, in general, characterized by distinct photoelectron angular distributions (PAD). The PADs are thus instrumental in spectroscopic assignments and may assist in a straightforward determination of the ground-state multiplicity of a neutral carbene.

Many substituents involved in π and σ interactions have been studied

previously.[103,104] Halogens act as strong σ withdrawers and π donors; the cyano-group is often described as a pseudo-halogen for its similarly strong σ withdrawing properties, but acts as π acceptor rather than π donor. Both types of substituents, in general, increase radical stability. However, with regard to the singlet-triplet splitting in the corresponding carbenes the halogen and CN substituents are known to act in opposition, with most halogens (F, Cl, and Br) favoring singlet ground states[105,106] and the CN stabilizing the triplet.[10,107,108]

Among the many carbene species that have been studied previously, most have been homogeneously substituted, i.e. :CR_2, where R is a halogen[106,109,110] or CN.[108] The work reported here continues our group's recent interest in heterogeneously substituted species, with one halogen and one cyano-substituent. We have recently investigated one particular case of such species, derived from the chloroacetonitrile (CH_2ClCN) precursor.[111] The corresponding carbene was found to have nearly degenerate singlet and triplet states. Continuing this theme, fluoroacetonitrile was used as a precursor in the presented work. Fluorine has a significantly higher σ withdrawing power compared to chlorine and, because of the size of its 2*p* orbitals, significantly stronger π donation effect. The fluoro- and difluoro- carbenes show significantly destabilized triplet states.[105,112]

We report our findings for cyanofluorocarbene using anion photoelectron imaging spectroscopy. We report a singlet ground state for the FCCN carbene with a significant $\Delta E_{S\text{-}T}$. The results for the carbene species are compared to the singly and homogenously double-substituted methyl species, as well as the previous results for ClCCN anion.

2. Experimental and Theoretical Methods

Photoelectron imaging experiments were carried out using a custom-built time-of-flight mass-spectrometer coupled with a velocity-map imaging assembly, described in detail in Chapter 2. N_2O carrier gas was flowed over fluoroacetonitrile (CH_2FCN) and the resulting mixture was introduced into the source chamber using a pulsed supersonic nozzle (General Valve 9) operated at a repetition rate of 20 or 50 Hz, to match that of the laser. Atomic oxygen radical anions were formed by slow secondary electron dissociative attachment to the carrier gas, and ions of interest were produced through the well-documented H_2^+ abstraction reaction.[101,102] The resulting anions were extracted into the Willey-McLauren time-of-flight mass-spectrometer, where they were further accelerated to 3.5 keV and separated by the mass-to-charge ratio. The ion beam was intersected by a pulsed, linearly polarized laser beam, timed to interact only with ions of a mass-to-charge ratio of 56. The second, third, and forth harmonics of a Spectra Physics, Inc. Quanta Ray Nd:YAG laser (50 Hz repetition rate) was used to produce 532 (4 mJ/pulse) nm, 355 nm (2 mJ/pulse), and 266 nm (800 μJ/pulse) radiation by doubling, tripling, or quadrupling the fundamental output. A Continuum, Inc. ND6000 dye laser pumped by a Surelite II Nd:YAG (20 Hz) was used with Rhodamin 590 to produce 612 nm light, which was frequency-doubled to produce 306 nm (6 mJ/pulse).

Photoejected electrons were projected by a series of velocity-map imaging[15] electrodes onto a position-sensitive dual-microchannel plate detector coupled to a P43 phosphor screen and the resulting images were recorded by a charge-coupled device (CCD) camera. Typical raw images were collected over ~10^6 experimental cycles. The complete three-dimensional photoelectron distribution was reconstructed[17] using the

inverse Abel transformation, implemented in the BASEX program.[51] The energy scale was calibrated using the well-known[52,53] photodetachment transition of O^-.

Electronic structure calculations with geometry optimization at the CCSD level of theory were carried out with the Gaussian 09 software package.[54] After optimizing the geometries for the anion and neutral ground and excited states, the normal-mode analysis was used to confirm that the optimized structures corresponded to true potential minima. Equation-of-motion (EOM) ionization potential (IP) and spin-flip (SF)[25,113-115] calculations included diagonal triples (dT)[116] corrections for CCSD energy and were performed for the optimized geometries using the Q-Chem 4.0 software package.[26]

3. Results and Analysis

3.1 Experimental Analysis

Photoelectron images of the anion of cyanofluorocarbene, $FCCN^-$, were collected at 532 nm, 355 nm, 306 nm and 266 nm. The images and corresponding spectra are shown in Figure 1.

At 532 nm (Figure 1a), the photon energy is just above the detachment threshold of the anion. The photoelectron spectrum consists of two prominent well-resolved peaks, separated by approximately 1800 cm^{-1}. The outermost band in the image, corresponding to the lowest-eBE (electron binding energy) spectral peak, is assigned to the vibrational origin of the photodetachment transition, allowing for a robust and precise determination of the adiabatic electron affinity of FCCN, EA = 2.081 ± 0.002 eV. The uncertainty range is narrower than the 0-0 band width; it was determined as the standard deviation of the peak position for several independent experimental runs.

At 355 nm (Figure 1b), two transitions are apparent in the image, with the inner

transition displaying a hint of a vibrational progression. The outer (lower-eBE) transition displays a prominent perpendicular anisotropy with respect to the laser polarization direction, while the inner (higher-eBE) transition has a notable parallel anisotropy. Qualitatively similar anisotropy properties of the two transitions persist at 306 nm (Figure 1c) and 266 nm (Figure 1d), with an additional, third transition appearing in the center of the image at the latter wavelength.

Previous examples of photoelectron imaging have shown that the assignment of the singlet and triplet carbene states can be aided by the anisotropy of the corresponding photodetachment transitions. The canonical electron configuration of a ground-state carbene anion is $^2A''$: $\ldots\sigma^2\pi^1$, where σ and π are the nominal sp^2 and p nonbonding orbitals of the carbene center, respectively. The transition to the singlet carbene ($^1A'$: $\ldots\sigma^2\pi^0$) removes an electron from the out-of-plane π orbital. Likewise, a transition to the triplet ($^3A''$: $\ldots\sigma^1\pi^1$) requires the detachment from the σ orbital, which lies in the plane of the molecule and has partial *s* character. As such, it is expected that the singlet transition will display a predominantly perpendicular anisotropy within a moderate eKE regime, in contrast to the triplet, which is expected to be parallel or nearly isotropic.[117,118]

The anion of cyanofluorocarbene provides an excellent illustration of these general predictions. Two transitions with distinct anisotropy properties are clearly seen in each of the 355 nm, 306 nm, and 266 nm photoelectron images. The outermost transition in each case is notably perpendicular, while the next higher-eBE transition is predominantly parallel. Based on this observation, we assign the outer, lower-eBE transition to $^1A'$ state of the carbene, while the inner, higher-eBE transition is assigned to the $^3A''$ state.

The above determination of the adiabatic EA = 2.081 ± 0.002 eV (from Figure 1a)

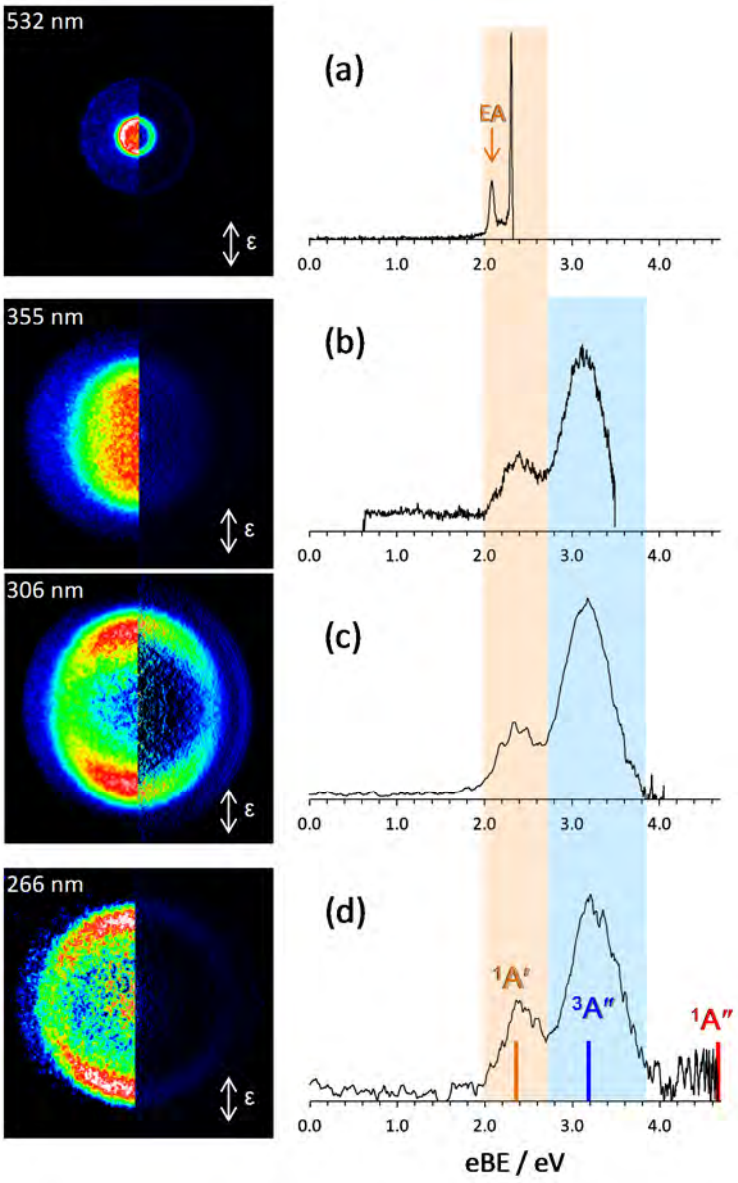

Figure 1. Photoelectron images and reconstructed spectra of $FCCN^-$ obtained at (a) 532 nm, (b) 355 nm, (c) 306 nm, and (d) 266 nm. Double-sided arrows (ε) indicate the laser polarization direction. The left halves of the composite images are raw data, while the right halves are the corresponding Abel-inverted results. The stick plot in (d) shows the EOM-IP/SF-CCSD(dT)/aug-cc-pVTZ energies of the vertical transitions from the anion to the closed-shell singlet (^{1}A′), triplet (^{3}A″), and open-shell singlet (^{1}A″) states of the neutral.

thus corresponds to the $^1A'$ singlet state carbene. Since the lower binding energy side of the triplet state transition overlaps with the singlet transition, the unambiguous determination of that band's onset is not possible from the data and hence the exact value of ΔE_{S-T} cannot be determined directly from the experiment.

The vertical detachment energy, VDE, is an important property that can be derived from the experiment for comparison with theoretical predictions. Based on the positions of the singlet band maxima in the 355 nm, 306 nm and 266 nm spectra (Figure 1b-d), we estimate the VDE of $FCCN^-$ corresponding to the singlet neutral state as 2.40 ± 0.01 eV. The VDE of the triplet transition is similarly determined from the 306 nm and 266 nm spectra as 3.20 ± 0.04 eV.

The additional weak transition at the center of the 266 nm image is a high binding energy feature with an onset at about 4.2 eV. The open-shell singlet state, $^1A''$: $\ldots\sigma^1\pi^1$, similar to the one observed in other carbenes, is a likely candidate for the assignment of this higher-energy band.

3.2 Theoretical Investigation

The optimized geometries of the cyanofluorocarbene anion and the singlet and triplet states of the neutral, derived from CCSD/aug-cc-pVTZ calculations, are displayed in Figure 2. In line with other carbenes, the bond angle at the central carbon is similar in the $FCCN^-$ anion and singlet FCCN (105.7° vs. 107.2°), while the triplet state is characterized by a more open carbene angle (128.3°). These geometric properties are consistent with the states' nominal electron configurations. The double occupancy of the in-plane lone-pair σ orbital in the anion and the singlet favors the similarly sharp bond

angles in these species, while the single-occupancy of this orbital in the triplet allows for a less constrained geometry. The π orbital population, on the other hand, has no significant effect on the carbene angle. The main geometric difference between the anion and the singlet is in the respective C–F bond lengths, 1.427 Å vs. 1.298 Å. This property does not change notably from the singlet to the triplet carbene. The high electronegativity of fluorine is responsible for its large effective charge in the $FCCN^-$, significantly weakening the anionic C–F bond.

Table 1. Energetic parameters (in eV) obtained from the electronic structure calculations on cyanofluorocarbene and its anion.

Method [a]	Adiabatic EA		VDE		ΔE_{S-T}
	Singlet ($^1A'$)	Triplet ($^3A''$)	to Singlet ($^1A'$)	to Triplet ($^3A''$)	
CCSD	2.093	2.462	2.391	3.097	0.369
EOM-IP/SF-CCSD(dT)	2.045 [b]	2.470 [b]	2.351 [c]	3.168 [c]	0.425 [d]
Experiment	2.081(2)	2.50(4) [e]	2.40(2)	3.20(4)	0.42(4) [f]

[a] All calculations used the aug-cc-pVTZ basis set.

[b] Calculated by combining the relevant energy gaps, determined from the EOM-SF-CCSD(dT) calculations, with the anion VDE, determined using the EOM-IP-CCSD(dT) method. Specifically, EA($^1A'$) = VDE – (Singlet relaxation energy); EA($^3A''$) = EA($^1A'$) + ΔE_{S-T};

[c] Calculated using the EOM-IP-CCSD(dT) method.

[d] Calculated using the EOM-SF-CCSD(dT) results for the singlet and triplet geometries (Figures 2b and 2c).

[e] Estimated using Eq. (1), the experimental VDE of the triplet, and the results of the EOM-SF-CCSD(dT) calculations.

[f] Calculated using the experimentally determined EA($^1A'$) = 2.081 ± 0.002 eV, and the estimated value of EA($^3A''$) = 2.50 ± 0.04 (see footnote [e] above).

Because of the shortening of the C–F bond upon photodetachment to the singlet, accompanied by a small change in the FCC bond angle, we expect the corresponding vibrational modes to be excited in the singlet band. The CCSD/aug-cc-pVDZ calculations predict 1183 cm^{-1} and 597 cm^{-1} harmonic frequencies for the C–F stretch and the bending vibrational modes of the singlet carbene, respectively. Neither of these frequencies matches the ~1800 cm^{-1} spacing between the two dominant peaks in the 532 nm spectrum, but a combination of these modes is a good match.

The CCSD/aug-cc-pVTZ calculations were also used to predict the VDEs of the anion corresponding to the detachment to the singlet and triplet carbene species, as well as the adiabatic EAs of the neutral states. The results are summarized in the first row of Table 1. The VDE was determined as the electronic energy difference between the target neutral state and the anion, both at the optimized geometry of the anion. The EA is defined as the difference in electronic energy of the geometry-optimized neutral and that of the anion. The results are in reasonably good agreement with the experimental values (also included in Table 1), particularly for the singlet band.

The VDEs of the anion were also determined using the EOM-IP-CCSD(dT) methodology[25,116] (IP, for brevity). In these calculations the singlet ($^1A'$: $\ldots\sigma^2\pi^0$) and triplet ($^3A''$: $\ldots\sigma^1\pi^1$) states of the neutral carbene were accessed by removing electrons from the $\pi\alpha$ or $\sigma\beta$ spin-orbitals of the anion ($^2A''$: $\ldots\sigma^2\pi^1$) reference. The VDEs predicted using the IP method are included in Table 1, and indicated as by the respective orange and blue sticks in Figure 1d. As seen from the figure, the agreement between the theory predictions and the experimentally observed positions of the singlet and triplet band maxima is very good.

The diradical motif of carbenes' electronic structure gives rise to several close-lying electronic states with inherently multi-configurational wavefunctions. To describe the multi-configurational nature of the low-lying electronic states of FCCN, we employed the EOM-SF-CCSD(dT) method[25,116] (SF, for brevity), based on the spin-flip methodology, originally proposed by Krylov.[113] In these calculations, the robust high-spin (M_S = 1) triplet state reference (^{3}A″: …$\sigma^1\pi^1$) and one-electron spin-flip excitation operators were used to produce several electronic configurations, which were then combined to yield low-energy solutions with the appropriate symmetry of the target states. Consistent with our past investigation of chlorocyanocarbene[111] and based on Krylov's recommendation,[119] the low-spin (M_S = 0) component of the triplet was used to determine the singlet-triplet energy gaps.

The results of the SF calculations on FCCN are summarized in Figure 2, where the relative energies of the closed-shell singlet (^{1}A′), the triplet (^{3}A″), and the open-shell singlet (^{1}A″) states are indicated for three different molecular geometries, corresponding to the CCSD/aug-cc-pVTZ optimized structures of (a) the $FCCN^-$ anion, (b) the ^{1}A′ neutral FCCN, and (c) the ^{3}A″ neutral FCCN. The numeric energy values for each vertical manifold are given relative to the lowest state at that geometry. The adiabatic energy differences between the lowest states at different geometries, i.e. the singlet relaxation energy from geometry (a) to geometry (b) and the adiabatic singlet-triplet splitting $\Delta E_{S\text{-}T}$ (b-c), are also indicated.

The results for the anion geometry (Figure 2a) can be directly compared to the experimental band positions in Figure 1. The 266 nm photoelectron spectrum is reproduced on the left-side margin of Figure 2 to illustrate the correspondence of the

spectral peak positions to the corresponding state energies. The vertical gap between the $^1A'$ and $^3A''$ states at the anion geometry (not to be confused with the adiabatic singlet-triplet splitting, $\Delta E_{S\text{-}T}$) is 0.815 eV, per SF calculations, which agrees very well with the experimental spectra, as well as the IP result of VDE($^3A''$) – VDE($^1A'$) = 0.817 eV.

The relaxation energy of the singlet carbene from the anion geometry (accessed in a vertical photodetachment process) to the equilibrium structure is determined to be 0.306 eV (per SF). Combined with the VDE($^1A'$) = 2.351 eV (IP), this result places the fully relaxed singlet at 2.045 eV above the anion. The adiabatic singlet-triplet splitting is determined to be $\Delta E_{S\text{-}T}$ = 0.425 eV (per SF).

The EA of the triplet carbene could not be determined directly in the experiment because the onset of the triplet band in Figure 1 overlaps the singlet. However, it can be estimated using a combination of experimental results and theoretical predictions. Since the relaxation energy of the triplet state of FCCN from the anion geometry to the equilibrium structure equals the difference between the corresponding VDE and the triplet-state EA, the latter can be estimated by the relationship:

$$EA_{est} = VDE_{exp} - \Delta E_{rel,} \quad (1)$$

where ΔE_{rel} = 0.696 eV, as determined from the SF calculations, and VDE_{exp} = 3.20 ± 0.04 eV is the experimental VDE value corresponding to the triplet band. Using Eq. (1), we estimate the affinity of the triplet as $EA_{est}(^3A'')$ = 2.50 ± 0.04 eV (Table 1). The uncertainty range of the estimated EA only reflects that of the experimentally determined VDE. Further, using the experimental EA value of the singlet and estimated EA value of the triplet, the singlet-triplet splitting of the carbene can be calculated as $\Delta E_{S\text{-}T}$ = 0.42 ± 0.04 eV, in agreement with the SF result of $\Delta E_{S\text{-}T}$ = 0.425 eV. Thus, cyanofluorocarbene

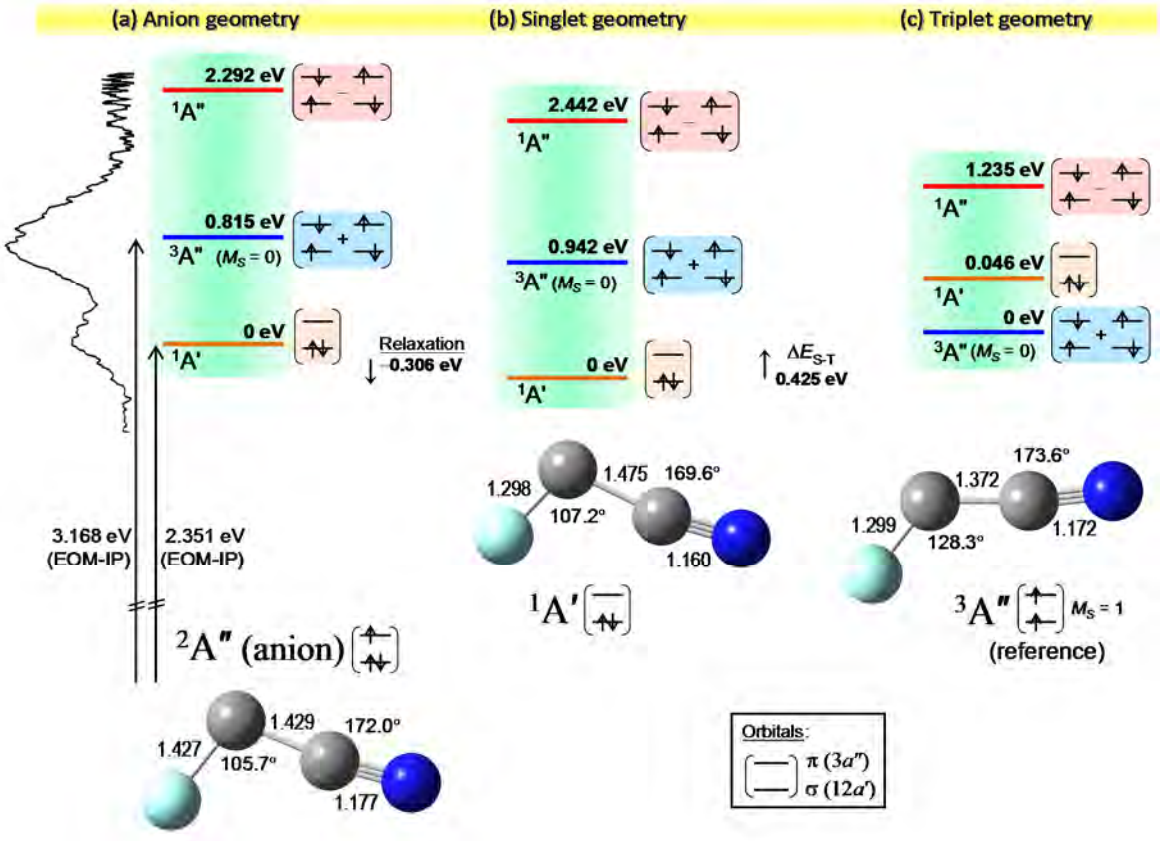

Figure 2. Manifolds of the low-lying electronic states of neutral FCCN calculated using the EOM-SF-CCSD(dT)/aug-cc-pVTZ method for the equilibrium geometries of (a) the anion, (b) the singlet (^{1}A′) neutral, and (b) the triplet neutral. The geometries were optimized at CCSD/aug-cc-pVTZ level of theory. The bond lengths are given in Angstroms. For each of the three geometries, the vertical ordering of the ^{1}A′, ^{3}A″ (M_S = 0), and ^{1}A″ states is indicated, with the energies given relative to the lowest state *at that geometry*. The dominant electron configurations for each of the target states are also indicated, with the orbitals shown corresponding to the non-bonding carbene orbitals, 12*a*′ (σ) and 3*a*″ (π). The spectrum shown along the left side of the figure is the 266 nm experimental spectrum reproduced from Figure 1d.

has a singlet ground state, by a wide margin.

In comparison to ClCCN, where the singlet and the triplet states are effectively degenerate, the singlet state of FCCN lies significantly lower in energy than the triplet. This is in agreement with the trend observed in HCCl and HCF, where the F-substituent stabilizes the singlet over the triplet by 0.46 eV more than Cl. The $\Delta E_{S\text{-}T}$ determined here for FCCN is, on the other hand, smaller than that of HCF (0.65 ± 0.02 eV),[105,112] indicating that indeed, as discussed in the Introduction, the cyano-group stabilizes the triplet configuration and narrows the energy gap between the states.

The SF calculations also predict that at the anion geometry the open-shell singlet $^1A''$ state of FCCN lies 2.292 eV above the closed-shell singlet, $^1A'$ (Figure 2a). Using the experimental value of 2.40 ± 0.02 eV for the singlet-band VDE, we estimate the VDE of the $^1A''$ state to be around 4.69 eV (red stick in Figure 1d), just above the 266 nm photon energy (4.66 eV). This prediction is consistent with the appearance of a weak band at the center of the 266 nm photoelectron image in Figure 1d.

The open-shell singlet comes much closer in energy to the triplet state at the triplet geometry (Figure 2c), suggesting that the relaxed geometry of the open-shell singlet is more similar to the triplet geometry than that of the anion or the closed-shell singlet. This is not surprising, since the $^1A''$ and $^3A''$ states arise from the same nominal electron configuration ($\ldots\sigma^1\pi^1$). It can be further predicted that, similar to the triplet band, the open-shell singlet transition should have a broad Frank-Condon envelope.

4. Effects of Heterogeneous Substitution

Both halogens and the cyano-group are strong σ withdrawers. In relation to the carbene, σ withdrawal from both types of substituents stabilizes the singlet state, since

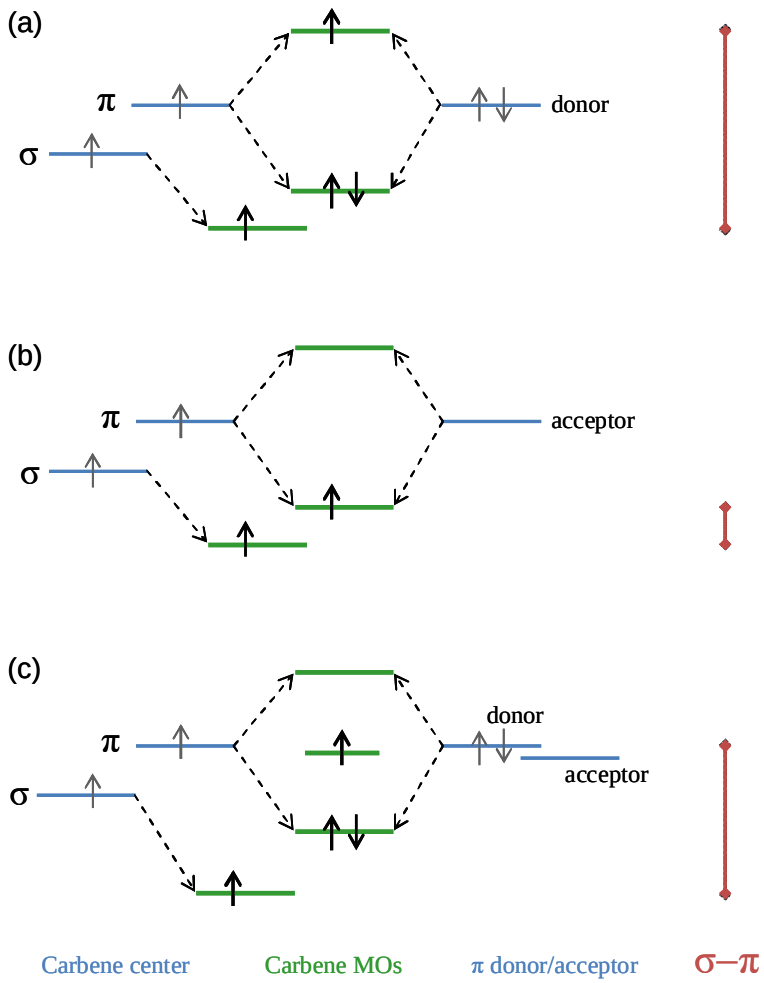

Figure 3. Schematic molecular orbital diagrams illustrating the interaction of the π and σ orbitals on the carbene center with different types of substituents: (a) π donor, (b) π acceptor, (c) π donor and π acceptor (heterogeneous double-substitution). The double-sided arrows on the right in each case indicate the resulting splitting between the carbene σ orbital and lowest available π vacancy. The MO populations shown correspond to a triplet carbene.

paring both electrons in the carbene σ orbital contributes more electron density to the σ orbital system than the triplet configuration does.

In the π system, any appropriate π orbitals of a substituent will mix with the nonbonding $2p(\pi)$ orbital on the carbene center. Molecular orbital diagrams for carbenes with different types of substituents are shown in Figure 3, with the orbital populations shown corresponding to the triplet state.[10] Since halogens act as π donors, the resulting π orbitals of the carbene molecule must contain the two π electrons of the halogen. The lower energy orbital of this mixed pair is therefore occupied in any configuration, and the non-bonding electron of the carbene may only occupy the higher energy orbital of the pair, as illustrated in Figure 3a. This increases the gap between the σ and the lowest vacant π orbital, having the effect of raising the energy of the triplet state and increasing the $\Delta E_{S\text{-}T}$. By contrast, the cyano-group is a π acceptor. It has a π system like a halogen, but adds no additional electrons. The mixing, therefore, has the effect of creating a lower energy π orbital for a non-bonding carbene electron (Figure 3b), lowering the energy of the triplet state and decreasing the $\Delta E_{S\text{-}T}$.

When both a π accepting (CN) and a π donating (halogen) substituent are present in a heterogeneously substituted carbene, there are three distinct π interactions (acceptor-carbene center, donor-carbene center, and donor-acceptor) and therefore three mixed π orbitals (Figure 3c). In general then, the triplet state cannot be destabilized as much as with only the π donating group. Thus, $\Delta E_{S\text{-}T}$ is expected to be intermediate between the cases of either substituent alone.

5. Summary

Cyanofluorocarbene, FCCN, has a singlet ground state with an adiabatic EA = 2.081 ± 0.002 eV and a singlet-triplet splitting $\Delta E_{S\text{-}T}$ = 0.42 ± 0.04 eV. A third photodetachment transition, with an onset of approximately 4.2 eV is attributed to the open-shell singlet state of the carbene. These results are in excellent agreement with the theoretical predictions. The measured $\Delta E_{S\text{-}T}$ of FCCN agrees well with the general trend of similar carbenes.

Chapter 6: First Spectroscopic Investigation of the Singlet-Triplet Gap in Mixed Phenylcarbenes

Overview

We report preliminary results on the photoelectron imaging of phenylcarbene, cyanophenylcarbene, and chlorophenylcarbene anions. Triplet phenylcarbene is observed to have an EA of ≤ 0.83 eV, considerably lower than the previously indirectly-determined value. Transitions to the singlet and triplet ground state of both cyanophenylcarbene and chlorophenylcarbene are observable, though unidentified bands make full assignment difficult. Cyanophenylcarbene is found to have a triplet ground-state, with a tentative EA of 2.04 eV. Chlorophenylcarbene is found to have a singlet ground-state. The phenyl-group is found to favor the singlet state slightly. While clearly a π-conjugating substituent the π-accepting behavior of the phenyl-ring is counteracted by the aromaticity, which disfavors additional electron density in the ring.

1. Introduction

Carbenes, $:CR_1R_2$, are an important class of reactive intermediates. The interesting properties of carbenes can be attributed in large part on the two non-bonding electrons distributed between the nearly-degenerate σ and π orbitals localized (nominally) on a carbon center. The two electrons in two orbitals of similar energies creates close-lying $\ldots\sigma^2\pi^0$ and $\ldots\sigma^1\pi^1$ electron configurations.[10] We will refer to these configurations as the 'singlet' and 'triplet' for brevity, although the later configuration also corresponds to the 'open-shell singlet' state. The substituent groups, R_1 and R_2 affect the stability of the orbitals and thus the energetic ordering of the singlet and triplet states[98] and the magnitude of the singlet-triplet splitting, $\Delta E_{S\text{-}T.}$ The splitting dictates the reactivity of the carbene, as reactions mechanisms often vary for the singlet and triplet species.[99,100]

Anion photoelectron imaging is a uniquely useful tool for examining these often short-lived molecules (particularly those with triplet ground-states)[120]. The negative ions of carbenes can be formed in the gas phase by H_2^+ abstraction reactions of a closed-shell precursor with O^- produced in situ.[101,102] The anions of both singlet and triplet ground-state carbenes are radical anions with the same canonical $\ldots\sigma^2\pi^1$ electron configuration.[10] In photodetachment, a photon of sufficient energy can access the singlet ($\ldots\sigma^2\pi^0$) or the triplet ($\ldots\sigma^1\pi^1$) states of the carbene by removing an electron from the respective π or σ orbitals of the anion. Detachment from the σ orbital can additionally access the higher-lying open-shell singlet ($\ldots\sigma^1\pi^1$) state. Since the two lowest-lying states involve different orbitals of significantly different character, the respective photodetachment processes are, in general, characterized by distinct photoelectron angular distributions (PAD). The

PADs are thus instrumental in spectroscopic assignments and may assist in a straightforward determination of the ground-state multiplicity of a neutral carbene with a simple qualitative examination of the photoelectron images.

Many substituents involved in π and σ interactions have been studied previously.[103,104] Halogens act as strong σ withdrawers and π donors; the cyano-group is often described as a pseudo-halogen for its similarly strong σ withdrawing properties, but acts as π acceptor rather than π donor. Both types of substituents, in general, increase radical stability. However, with regard to the singlet-triplet splitting in the corresponding carbenes the halogen and CN substituents are known to act in opposition, with most halogens (F, Cl, and Br) favoring singlet ground states[105,106] and the CN stabilizing the triplet.[10,107,108]

A class of substituents which is of great interest is those which are highly conjugated rings or fused rings. The phenyl-group is the prototypical example of this class. Oddly however, some of the key properties of the phenyl-substituent itself still remain unknown. In particular, there is no direct determination of the ΔE_{S-T} of phenylcarbene. The best available estimate, ΔE_{S-T} = -0.10 eV (the negative sign is shown here to indicate a triplet ground state),[121] was measured using laser flash photolysis.[122] There is a singular, indirectly measured value by CIDC of the electron affinity, EA = 1.207 ± 0.030 eV.[9]

Anion photoelectron imaging is an attractive method to refine both of these values spectroscopically. Additionally, the phenyl-substituent and its properties can be indirectly examined by studying heterogeneously-substituted carbenes, like chlorophenylcarbene and cyanophenylcarbene. These additional substituents act significantly different enough as to give some insight into the effects of the phenyl-group.

In this chapter, the preliminary results of the photoelectron imaging of the anions of phenylcarbene, cyanophenylcarbene, and chlorophenylcarbene are present. While the conclusions are limited due to difficulties with the spectra, some general conclusions about the phenyl-group are made. In particular, the phenyl-group is a clear π-accepting substituent, but the aromatic nature of the species creates an energetic preference for the singlet state.

2. Experimental

Photoelectron imaging experiments were carried out using a custom-built time-of-flight mass-spectrometer coupled with a velocity-map imaging assembly, described in detail in Chapter 2. N_2O carrier gas was flowed over the precursor sample (toluene, benzyl chloride, or benzyl cyanide) and the resulting mixture was introduced into the source chamber using a pulsed supersonic nozzle (General Valve 9) operated at a repetition rate of 50 or 71 Hz, to match that of the laser. Atomic oxygen radical anions were formed by slow secondary electron dissociative attachment to the carrier gas, and ions of interest were produced through the well-documented H_2^+ abstraction reaction.[101,102] The resulting anions were extracted into the Willey-McLauren time-of-flight mass-spectrometer, where they were further accelerated to 3.5 keV and separated by the mass-to-charge ratio. The ion beam was intersected by a pulsed, linearly polarized laser beam, timed to interact only with ions of interest. The second and third harmonics of a Spectra Physics, Inc. Quanta Ray Nd:YAG laser (50 Hz repetition rate) was used to produce 532 (4 mJ/pulse) and 355 nm (2 mJ/pulse) radiation by doubling or tripling the fundamental output. A Spectra Physics, Inc. regeneratively-amplified Ti:sapphire laser system was used to produce 808 nm light (<1 mJ/pulse) and was linked to the experiment

by a signal divider, triggering the experiment at one fourteenth the rate of the 1 kHz laser (~71 Hz).

Photoejected electrons were projected by a series of velocity-map imaging[15] electrodes onto a position-sensitive dual-microchannel plate detector coupled to a P43 phosphor screen and the resulting images were recorded by a charge-coupled device (CCD) camera. Typical raw images were collected over ~10^6 experimental cycles. The complete three-dimensional photoelectron distribution was reconstructed[17] using the inverse Abel transformation, implemented in the BASEX program.[51] The energy scale was calibrated using the well-known[52,53] photodetachment transition of O^-.

Electronic structure calculations with geometry optimizations with the B3LYP density functional and the coupled-cluster method with single and double excitations using the augmented Dunning's correlation-consistent basis of double and triple-ζ quality were carried out with the Gaussian 09 software package.[54]

3. Results

3.1 Phenylcarbene

The photoelectron images of phenylcarbene anion are shown with the resulting spectra in Figure 1A and 1B. The image at 532 nm displays two different anisotropies. The outer parts (lower-eBE) of the signal region are approximately isotropic. At higher eBE, closer to the center of the image, the angular distribution is predominantly perpendicular. Additionally, a rise in intensity near 0 eKE indicates the possibility of a third transition.

The presence of 3 low-lying transitions is not at all unexpected. Based on previous examples,[108,111,123] the singlet ground state signature is a perpendicular angular

distribution, reflecting the detachment from the nominally π orbital of the anion. Likewise, a more parallel distribution is a much better fit to the triplet transition. As is known, the ground state of phenylcarbene is a triplet, which the position of the transitions reflects, ie the isotropic distribution appears at lower-eBE. The third transition at much higher eBE is a good candidate for the open-shell singlet transition.

The 808 nm image is qualitatively very similar to that at 532 nm, though it does not access higher-eBE. The spectra are difficult to interpret. Namely, the spectra are significantly convoluted. At 808 nm, low laser power creates a noisy spectrum due to low signal intensity. At 532 nm is much better, but the lower energy resolution (due to higher eKE) adds additional difficulty in a very dense spectrum. Still, there are some very apparent features. At 808 nm, the first feature is discernable at ~0.83 eV. Based on the anisotropy assignments, this can tentatively be assigned to the upper bound of the electron affinity (EA) of phenylcarbene. Additional features are visible at ~1.0 and ~1.2 eV, but their assignment requires more detail. Likewise, the 532 nm spectrum contains numerous transitions. At a qualitative glance, there appears to be two vibrational progressions, one which has noticeably sharp peaks and is first discernable at 1.2 eV, and another which is associated with considerably broader peaks.

3.2 Cyanophenylcarbene

The 532 and 355 nm spectra of cyanophenylcarbene anion are shown in Figure 2A and 1B, along with the accompanying photoelectron images. Despite being somewhat noisy, the 532 nm spectrum is quite promising. A very small feature at ~2.04

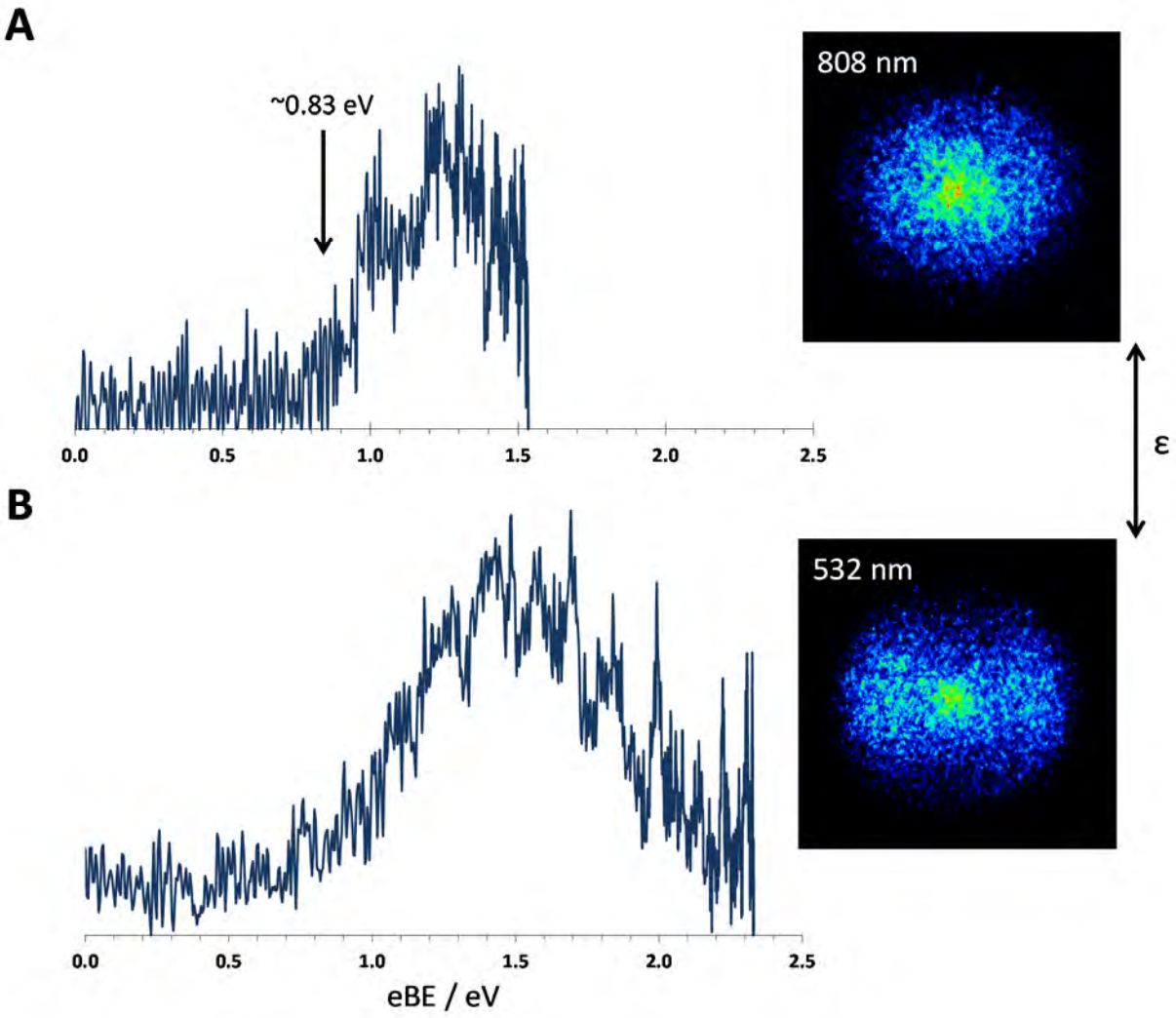

Figure 1. The photoelectron images and spectra for the phenylcarbene anion at (A) 808 nm and (B) 532 nm. The direction of electric field polarization is indicated by the double-sided arrow. The black arrow indicates the position of the first discernable feature of the 808 nm, which is the tentatively assigned EA of triplet phenylcarbene.

eV is distinguishable and will be discussed later. The majority of the spectrum is a single, very near 0 eKE feature that rises very sharply. While possibly autodetachment, this feature moves away from 0 eKE at higher photon energies, though there are other problems associated with the assignment.

At 355 nm, the spectrum bears only little resemblance to that at 532 nm. Around the cutoff of the 532 nm photon energy, what we will call Band A is now resolved. Examination of the image and of the spectrum around 2.5 eV shows two peaks, ~2.4 and ~2.6 eV respectively, distinguishable by different anisotropy. Band A (2.4 eV) has a slightly isotropic distribution, while the newly visible Band B (2.6 eV) has a distinct parallel anisotropy. Upon further examination of the image, Band B, whose peak intensity lies at ~2.6 eV, actually ends to lower eBE and perhaps even lower than the onset of Band A. Examination of the center of the image indicates the possibility of another transition a high eBE based on signal intensity. This region, though it has few distinguishing features in the spectrum, will be labeled as Band C to refer to eBEs of 3 to 3.5 eV. Referring to previous studies of carbenes[108,111,112,123] and the anion nominal electronic structure, the obvious parallel distribution of Band A allows for a qualitative assignment of the singlet transition. The more parallel anisotropic distribution of Band B would be consistent with an assignment of the triplet transition. More so, a third low-lying transition would be consistent with previous examples of an ‘open-shell’ singlet. This assignment is much less compelling and much more tentative.

The difficulty in the examination of this data occurs are *lower* eBE than Band A. The 532 nm spectrum has no obvious features below 2 eV. At 355 nm, a broad feature (0.5 – 1.8 eV) and a sharper, brighter feature at ~2.0 eV will be labeled Band D and E

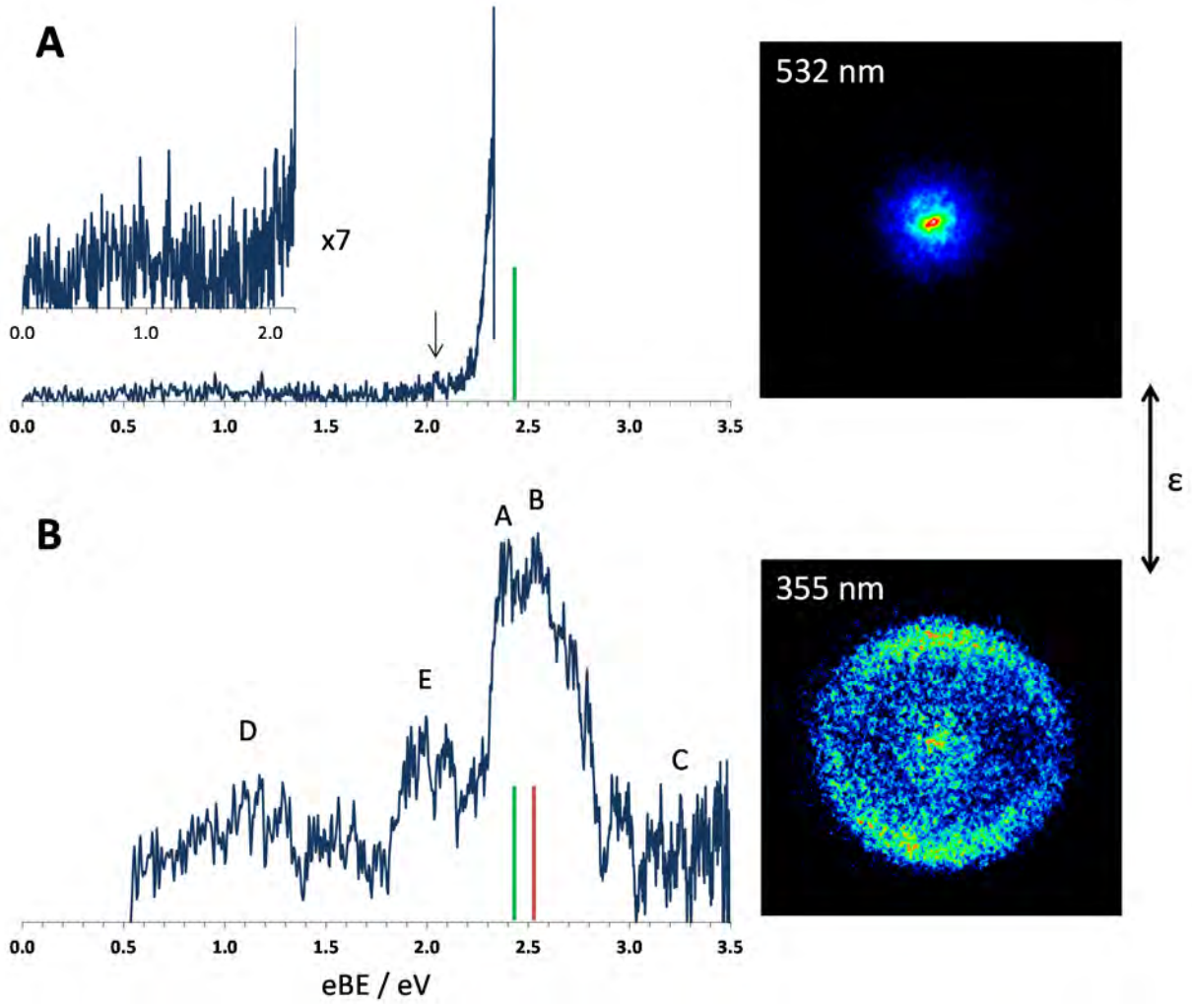

Figure 2. The photoelectron images and spectra of cyanophenylcarbene anion at (A) 532 nm and (B) 355 nm. The double-sided arrow indicates the direction of electric field polarization. A 7x magnification of the 532 nm spectrum between 0 and 2.02 eV eBE is included in (A). The black arrow indicates the position of the first discernable feature in the 532 nm spectrum. The green and red vertical bars indicate the VDE results of the singlet and triplet transitions at the B3LYP/aug-cc-pVTZ level of theory respectively. Band A and B are assigned to the transitions $X\,^2\mathrm{A}'' \rightarrow a\,^1\mathrm{A}'$ and $X\,^2\mathrm{A}'' \rightarrow X\,^3\mathrm{A}''$. Band C is tentatively assigned to a transition to the open-shell singlet. Bands D and E are unassigned. See text for details.

respectively. A blow up of the Band D eBE region in the 532 nm is included in Fig. 1A. With some hesitation, there is a very slight intensity rise in this region. While not definitive, there is a hint that Band D is visible due to some kind of resonant enhancement at 355 nm. Band E on the other hand has no such counterpart in the 532 nm spectrum.

3.3 Chlorophenylcarbene

The photoelectron images and spectra are even more congested than those of cyanophenylcarbene. To complicate things further, the presence of a chlorine atom allows an isotopologue which has a near identical electronic structure. For additional insight, these spectra have been included. Figure 3A and 2B show the 355 nm spectra of the $PhC^{35}Cl$ and $PhC^{37}Cl$ anions respectively. The significant noise and congestion require that we consider what is the shared and what is different to make any real assignments. Band F, G, and H have been labeled in the spectra as shared features. Coincidently, they are also the obvious features in the corresponding images. Band F has a visually-resolved isotropic to perpendicular distribution. Using the same arguments that apply to cyanophenylcarbene anion, Band E can be assigned to the singlet transition. Likewise, Band G has a significantly parallel distribution which can be assigned to the triplet transition. Unlike cyanophenylcarbene anion, Band H is likely autodetachment as it varies severely in intensity and is not separated from 0 eKE.

While initially these assignments are promising, their usefulness is limited due to a similar issue encountered with cyanophenylcarbene anion. Band I is a low-eBE

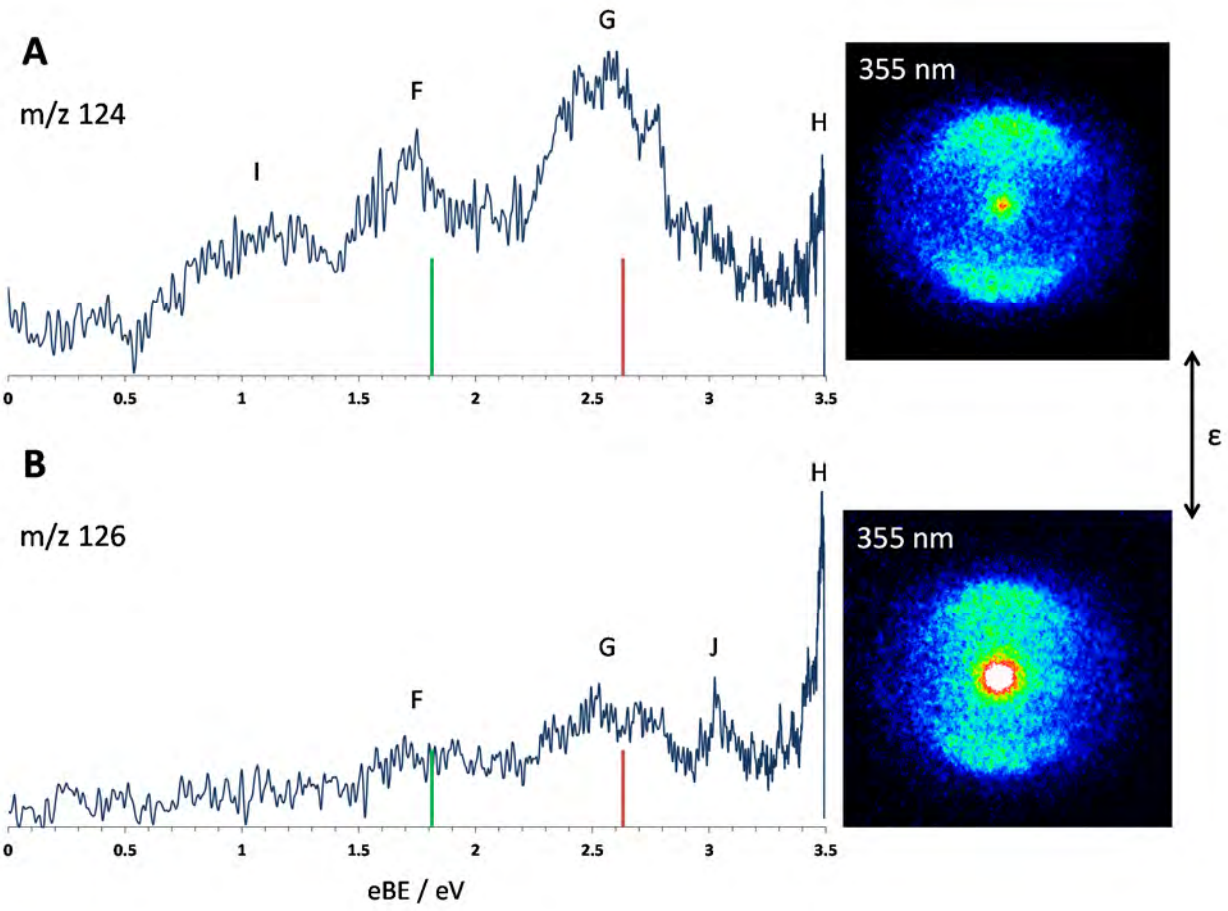

Figure 3. The photoelectron images and spectra of chlorophenylcarbene anion isotopologues (A) ^{35}Cl and (B) ^{37}Cl at 355 nm. The double-sided arrow indicates the direction of electric field polarization. The green and red vertical bars indicate the VDE results of the singlet and triplet transitions at the B3LYP/aug-cc-pVTZ level of theory respectively. Band F and G are assigned to the transitions $X\ ^2\mathrm{A}'' \rightarrow X\ ^1\mathrm{A}'$ and $X\ ^2\mathrm{A}'' \rightarrow a\ ^3\mathrm{A}''$. Band H is assigned to autodetachment. Bands I and J are unassigned. See text for details.

transition in Figure 3A ($PhC^{35}Cl^-$) that extends from 0.5 eV to where it convolutes with Band F at ~1.4 eV. It has no pair in Figure 3B ($PhC^{37}Cl^-$). Likewise, a very sharp band in the Figure 2B spectrum at ~3.0 eV, labeled Band J, has no pair in Figure 3A. Band J, while sharp and tempting to assign to a solvated chloride ion, is lower in eBE by about 0.5 eV than the unsolvated ion.

4. Discussion

4.1 Phenylcarbene

To assist in the assignment of the spectra, calculations were carried out on the anion, singlet, and triplet phenylcarbene species up to the CCSD/aug-cc-pVDZ level, with the geometries shown in Figure 4 and the calculated values in Table 1. The electron affinities are, calculated as the difference in energy between the neutral and anion at the respective optimized geometries, and vertical detachment energies (VDE) as the difference in energy between the neutral and anion species both at the anion optimized geometries. Noticeable right away, the triplet is the ground-state of phenylcarbene based on its lower calculated EA of 0.910 eV. This result is in fairly decent agreement with the first discernable transition in the 808 nm spectrum. We can now confidently assign the EA of the triplet as ≤0.83 eV. This value is differs from the previously reported value of 1.207 ± 0.030 eV by CIDC.[9] Additionally, the VDE is predicted at 1.396 eV and is in general a good match to the peak intensity in the 532 nm spectrum. The EA of the singlet is predicted as 1.163 eV. Previous work has determined the $\Delta E_{S\text{-}T}$ as -0.10 eV, a value lower in magnitude than that predicted by CCSD/aug-cc-pVDZ, 0.253 eV. It is not surprising that standard electronic structure methods do not perfectly replicate a complex multi-configurational problem, if the current experimentally-determined value holds.

Detailed analysis will require a Franck-Condon simulation to attempt to identify the vibrational progressions observed.

Table 1. Calculate values for phenylcarbene at the CCSD/aug-cc-pVDZ level of theory in eV and without ZPE correction.

Associated State	$^3A''$	$^1A'$
EA	0.910	1.163
VDE	1.396	1.238

Based on the calculated structures, we might infer the general spectral features. The central carbon bond angle is shown in Figure 4. As with previous carbenes, the double occupation of the nominal σ orbital in both the anion and singlet state creates similar angles. This would imply a much more narrow transition for the singlet than the triplet, which undergoes a change in bond angle of over 26° upon photoelectron detachment versus ~0 in for the singlet. Reexamining the spectra, this may perhaps indicate that the singlet transition might be fully visible in the 808 nm spectrum while the long vibrational progressions both belong to the triplet. Further investigation is certainly much warranted.

4.2 Similarities of Phenyl Carbene Spectra

The low-eBE transitions in Figure 2B and 2A and labelled Band D and H may not be entirely coincidental. The similarity of these features may indicate similar origins.

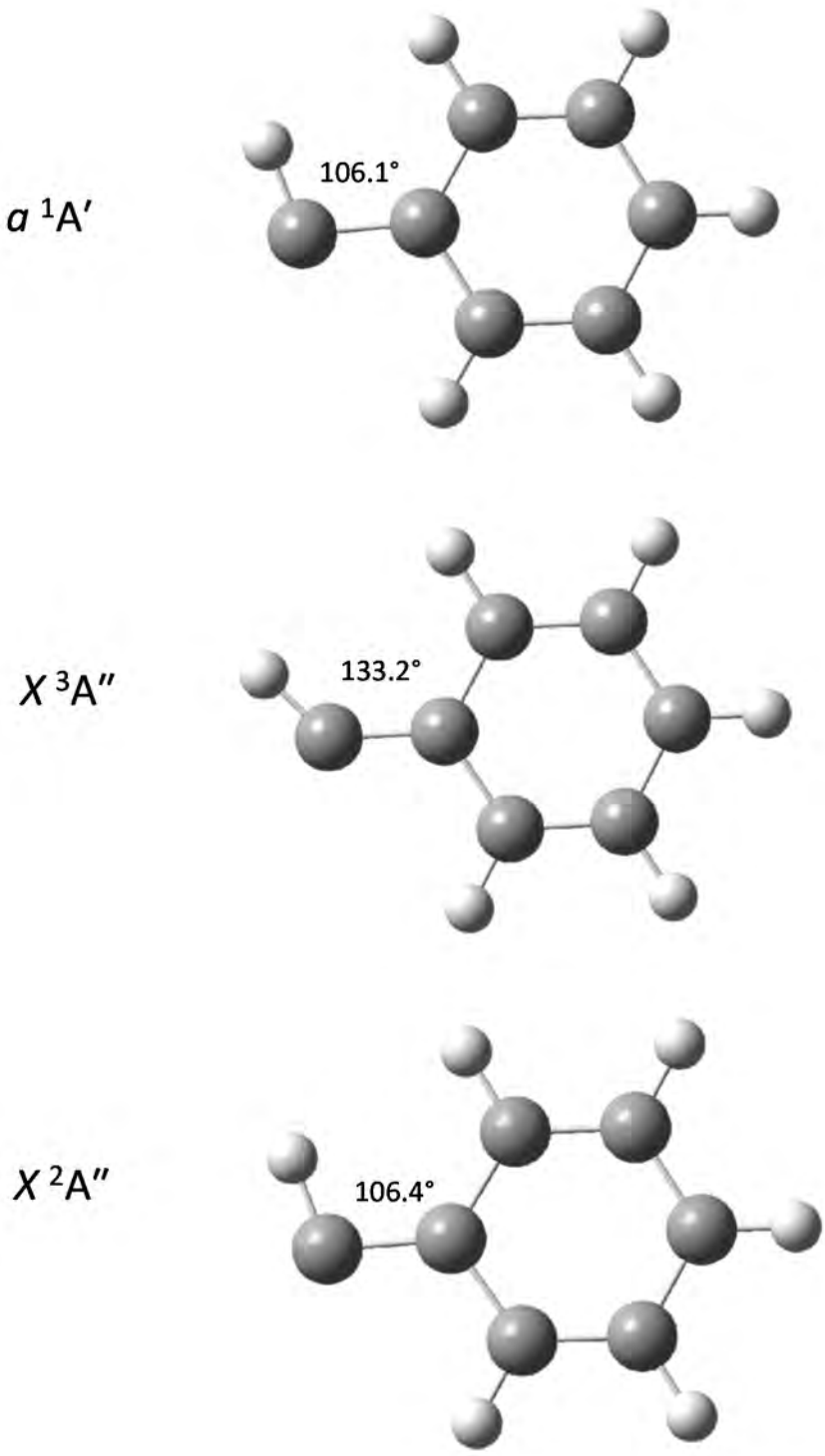

Figure 4. The optimized structures for phenylcarbene anion and neutral electronic states at the CCSD/aug-cc-pVDZ level of theory. Central carbon bonds are indicated.

Both experiments implement N_2O carrier gas, which would provide similar solvents and ions. Further, both precursors contain the benzyl-functionality ($PhCH_2$), leading to the possibility that this may provide the offending signals. A two-photon process or an ion formed during the supersonic expansion may also be responsible. The lack of a similar feature in $PhC^{37}Cl^-$ spectrum in Figure 3B and at 532 nm for $PhCCN^-$ in Figure 2A might suggest that this process is photon-dependent and related to the common motif. However, this issue requires significant investigation for an assignment. Significant intensity changes with wavelength or photon flux would be helpful, as would background spectra for this m/z region.

4.3 Theoretical Investigation of the Assignable Transitions: Cyanophenylcarbene

Due to the considerable size of the system and the limited spectral information, preliminary theoretical investigations were carried out using the B3LYP DFT functional and the aug-cc-pVTZ basis. While the augmented basis set works well to capture the typically diffuse

nature of anionic systems, B3LYP is not the preferred choice in theoretical method. However, it is better suited for larger systems. The results are listed in Table 2. The optimized geometries are pictured in Figure 5A. The key central carbon bond angle is noted in Figure 5.

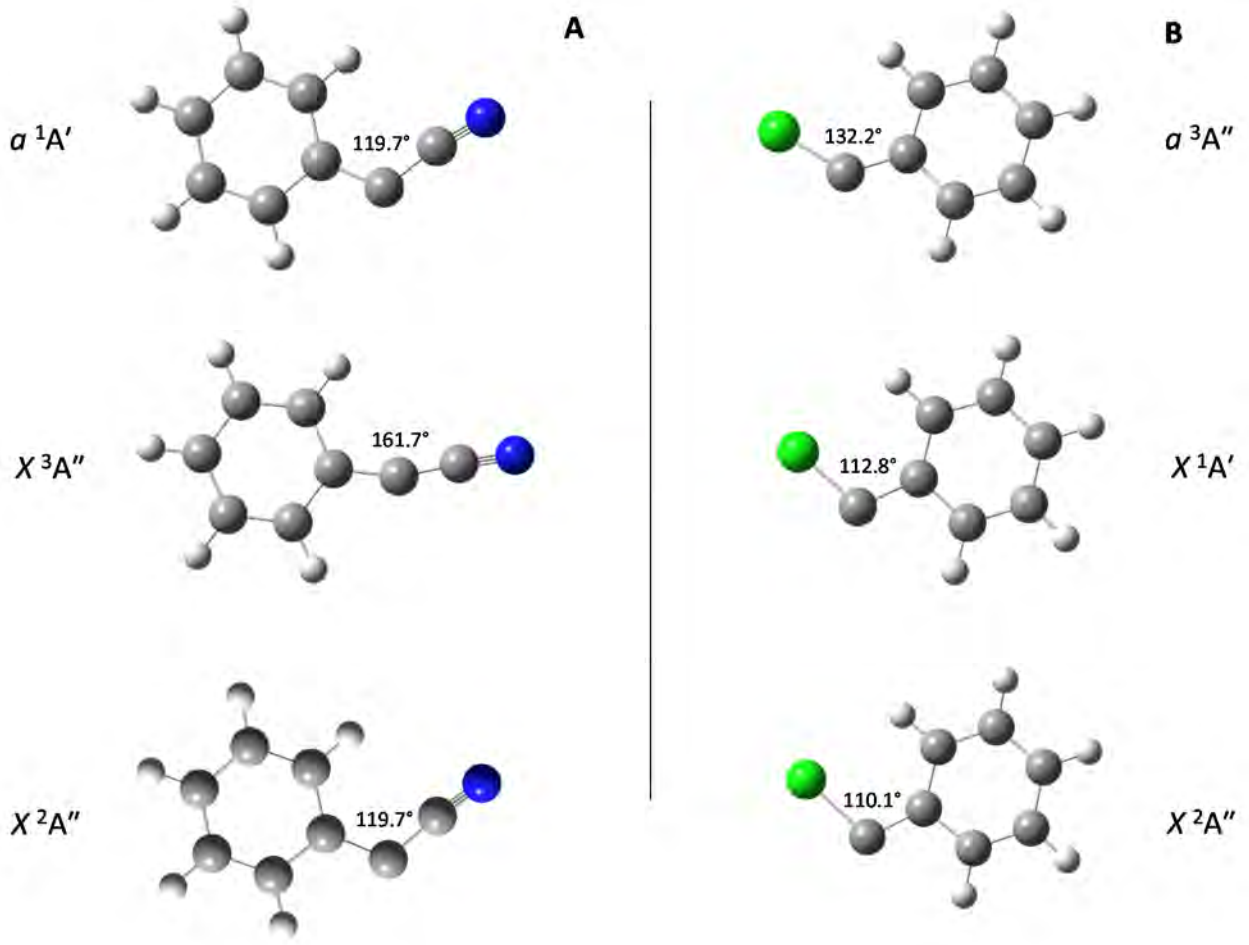

Figure 5. Optimized structures for the anion and neutral electronic states for (A) cyanophenylcarbene and (B) chlorophenylcarbene at the B3LYP/aug-cc-pVTZ level of theory. Central carbon bond angles are indicated.

Table 2. Calculate values for cyanophenylcarbene at the B3LYP/aug-cc-pVTZ level of theory in eV and without ZPE correction.

Associated State	$^1A'$	$^3A''$
EA	2.396	2.073
VDE	2.435	2.512

Despite the relatively low level of theory, the B3LYP results do qualitatively agree very well with the experimental observations for the assignable singlet and triplet transitions. Firstly, the order and the relatively small spacing between the VDEs of the singlet and triplet match well. Band A, assigned to the singlet, is a good fit for the predicted 2.435 eV peak position. The triplet VDE is predicted to be just 0.1 eV higher, which is in good agreement with the position of Band B with respect to Band A. Like many other carbenes, the triplet transition is predicted to be considerably wide based on the difference between the EA and VDE,[108,111,123] even when the ground state is the triplet. This is consistent with Band B extending considerably. Likewise, it is predicted that the transition corresponding to the singlet is much narrower, in line with Band A. While the predicted values of the EAs are likely suspect, the singlet-triplet splitting, ΔE_{S-T}, is more reliable based on the subtraction of errors. The predicted ΔE_{S-T} = -0.323 eV, the negative value indicating that the triplet is more stable than the singlet and is the ground-state. Again, while the predicted EAs are not very rigorous, the small feature discernable at 2.04 eV now comes into play as a possible real transition to the triplet state. If the sharp rise into Band A at ~2.26 eV is considered as the 0-0 singlet transition, this gap is ~0.2 eV and on the correct order for the predicted ΔE_{S-T}. More detailed work,

like a Franck-Condon simulation of both bands, would be extremely valuable in this confirmation.

The geometry of all the calculated species agrees well with geometries of previous species and the spectra. The ground-state triplet, like HCCN and NCCCN, has a near-linear central carbon bond angle of 161.7°. Likewise, the singlet and anion geometry are much more similar, given the double occupation of the nominal σ orbital. The nearly identical central carbon angle indicates a very narrow transition, like that observed for Band A.

4.4 Theoretical Investigation of the Assignable Transitions: Chlorophenylcarbene

Likewise, initial calculations on the chlorophenylcarbene were carried out with the B3LYP/aug-cc-pVTZ level of theory. The results are listed in Table 3, while the geometries are shown in Figure 5B. Like the results for cyanophenylcarbene, the predicted values are in good qualitative agreement with the assigned bands of the spectra. In particular, the absolute values for the predicted VDEs are not quite accurate with positions of highest intensity for Bands E and F; they are shifted to higher eBE. However, the separation of 0.788 eV matches the experimental separation of ~0.8 eV very well. The predicted ΔE_{S-T} = 0.238 eV indicates that the singlet is the ground state. The experimental evidence leaves much desired for a quantitative assessment of this prediction, and will also likely benefit from a Franck-Condon simulation analysis.

Table 3. Calculate values for chlorophenylcarbene at the B3LYP/aug-cc-pVTZ level of theory in eV and without ZPE correction.

Associated State	$^1A'$	$^3A''$
EA	1.650	1.888
VDE	1.847	2.635

The calculated geometries of the anion, singlet, and triplet species are consistent with other carbene species, namely the triplet geometry being considerably different than that of the anion. This is reflecting in the large difference in calculated EA and VDE for the triplet when compared to the singlet. Being a ground-state singlet like HCX (X=F, Cl, Br, and I), the triplet bond angle is much smaller and reflects the weaker π-accepting ability of halogens over the cyano- group. Similar to some extent to the predicted singlet state of PhCCN, the central bond angle of the singlet (112.8° is very close to that of the anion (110.1°) but indicates a slightly broader transition.

4.5 Lessons about Phenylcarbene from Related Species

Halocarbenes, based on the π-donating features of halogens, stabilize the singlet ground state to ensure an empty π-like orbital on the central carbene.[105] Likewise, cyanocarbenes were found to have more stable triplet states; the π-accepting property of the cyano-group also for the same π-like orbital of the central carbon to lower considerably in energy.[107,108] This in turns brings it low enough to make the triplet configuration energetically preferred over pairing the two valence electrons. Previously

regarding the 'mixed' chlorocyanocarbene and fluorocyanocarbene, it was found that substituent pairs with π-accepting and π-donating properties create a carbene with mixed properties.[111,123] That is at a first pass, the effect of each substituent can be described as an effect of that substituent alone. Compared to the unsubstituted carbene, CH_2, the change in ΔE_{S-T} and other properties upon single-substitution with X or CN can be roughly quantified and tagged to the substitution.

The properties of a 'mixed' carbenes were then found to be roughly additive. For instance the ΔE_{S-T} of the CH_2 is -0.394 ± 0.004 eV;[124] the ΔE_{S-T} of HCCN and HCCl are -0.516 ± 0.017 and 0.18 ± 0.11 eV respectively.[105,107] These differences are roughly -0.1 and +0.5 eV from the unsubstituted case, thus we might predict that the total change to ΔE_{S-T} would be +0.4 eV. Indeed, the determined ΔE_{S-T} of CCl(CN) is ~0.01 eV (-0.394 eV + 0.4 eV). This case does not apply when the substituent groups are in the same class, ie two π-accepting CN groups does not produce a significantly more stable triplet. However, it does drive some properties like central bond angle to the further extremes. For example again, the dicyanocarbene triple has a quasilinear central carbon bond angle of 168.4° compared to the cyanocarbene's 143.1°. EA is also found to increase in a very similar, additive way.

Using this general trend, examination of the properties of PhCCN and PhCCl gives insight into the effects of the phenyl- group on the energetics and electronic structure of the unsubstituted carbene. For simplicity in these crude predictions, we will simply subtract the change associated with the singularly substituted carbenes from that of the PhCCN and PhCCl, and average the difference. Based on the EA of the ground-state of CH_2 and HCCN, the cyano- substitution increases EA by ~1.3 eV. The chloro-

substitution does so by ~0.5 eV. Based now on the calculated EAs of the ground-states of PhCCN and PhCCl, the phenyl- group increases EA by ~0.0 to ~0.4 eV. While a broad range, it likely places the EA of ground-state PhCH just under 1 eV (0.67 + ~0.2 eV), which is in good agreement with the spectrum in Figure 1A.

Examining related methyl radicals, it was shown that the phenyl- group acts a good π-acceptor within the M.O. framework.[111,123,125] This assertion suggests that the estimation of the $\Delta E_{S\text{-}T}$ would indicate a slightly more negative value, meaning a more stable triplet state. As shown in Figure 6, this is not the case. In fact, the phenyl- group is associated instead with a slight positive change in $\Delta E_{S\text{-}T}$ compared to CH_2, indicating a more stable *singlet*. The predicted value, -0.26 eV, is an average of the changes associated with the phenyl-group upon substitution of HCCN and HCCl respectively. It is in surprisingly good agreement with the value predicted by CCSD/aug-cc-pVDZ. Even with the understanding that this prediction is crude, the phenyl-group clearly tracks with a slight preferential stabilization of the singlet state. This is counter-intuitive to the results from phenymethyl radicals.

To reconcile this prediction, we must consider that the phenyl-group is an *aromatic π-acceptor*, emphasizing a property unique to it over the cyano-group. Unlike –CN, the π*orbitals of the phenyl-ring are tied very strongly to the π-bond system of the substituent. This is perhaps nothing more than a way of stating the phenyl-group is aromatic, while –CN is not. While the unoccupied π* orbitals of both groups are available to central carbon for interaction, the effect of doing so with an aromatic system mean that essentially, an additional electron is added to the 6 π electrons of the ring (the central carbon is not considered as a new edition to the ring for obvious reasons). This in turn

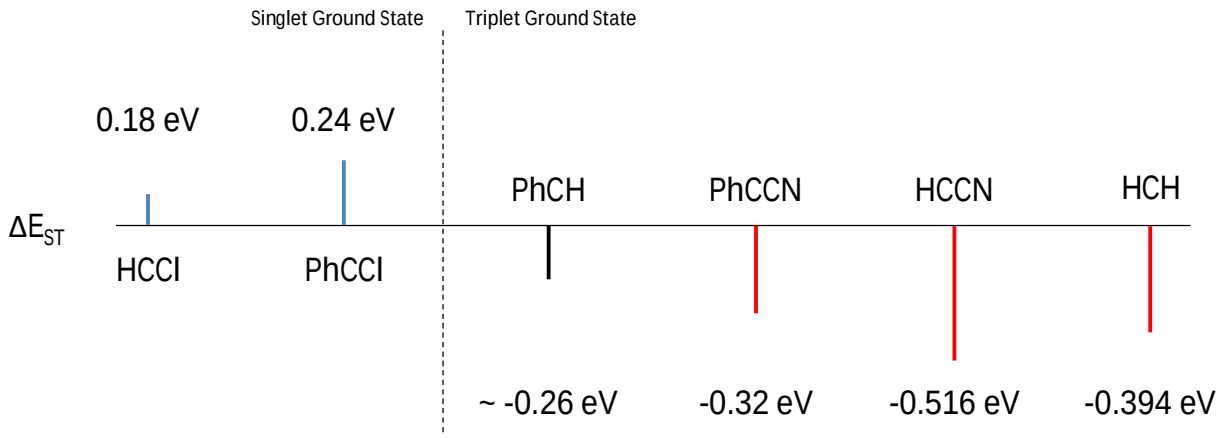

Figure 6. An illustration of $\Delta E_{S\text{-}T}$ for several related carbenes including methylene (CH_2),[124] chlorocarbene (HCCl),[105] and cyanocarbene (HCCN).[107] Negative value indicates a ground-state triplet. The value for cyanophenylcarbene and chlorophenylcarbene are those predicted by B3LYP/aug-cc-pVTZ, while the value for phenylcarbene is estimated. See Section 4.5 for details.

makes the new phenyl- group slightly *less aromatic* by Hückel's Rule of 4n+2. Six and ten π electrons are aromatic, eight is anti-aromatic, and 7 and 9 are not aromatic. While such a rule cannot be strictly applied to a phenylcarbene, we believe that the general concept rings true.

The phenyl-group has energetic preference for the singlet configuration not for a lack of π* orbitals to conjugate nor the presence of π-donation, but because the singlet configuration preserves the aromatic nature of the ring. The phenyl-group does act as a π-acceptor based on the results of 'mixed' phenylmethanes, but the only low-lying state is a doublet where the σ-orbital is a fully-occupied bonding orbital. In the carbene, we may than conclude that the triplet state is indeed stabilized compared to CH_2, simply not as much as the singlet state is due to the loss in aromaticity. This effect has been thoroughly investigated computationally[122] and agrees with the assessment made here. Further, while the experimental determination of ΔE_{S-T} is smaller than that predicted by CCSD/aug-cc-pVDZ, both values are indeed more positive than the splitting for CH_2, ΔE_{S-T} = -0.394 eV.

5. Conclusions

While the definitive quantitative results of these preliminary studies are limited, worthwhile conclusions can be drawn. Of immediate importance is the apparent EA of phenylcarbene, determined as ≤ 0.83 eV. This value is in decent agreement with the CCSD/aug-cc-pVDZ results and is significantly different than the previously determined value. While the ΔE_{S-T} is not readily determined from the 532 nm spectrum, partially resolved vibrational structure gives hope that a Franck-Condon analysis may be extremely valuable. Cyanophenylcarbene and chlorophenylcarbene transitions have been

successfully observed, though complex interference in the spectra makes fully assigning all features challenging. Follow-up experiments to isolate these features are required, as is more advance theoretical treatment when prudent. Otherwise, results are in good agreement with values predicted by DFT calculations, and ground-states can be assigned well within reason. The phenyl-group is a π-accepting substituent, which but ironically stabilizes the singlet over the triplet in carbenes due to the aromatic nature of the group.

Chapter 7: Substituted Methyl Radicals - Study of π-Electron Effects through Radicals with Mixed Substituent Types

Overview

This work continues our studies of heterogeneous substitution effects in methyl radicals. The cyanofluoromethyl radical, FC(H)CN, was estimated to have an EA of 1.53 ± 0.08 eV, by a combination of experimental and theoretical results.. With similar methodology, we report the adiabatic electron affinity of the cyanobenzyl radical, EA(PhCHCN) = 1.90 ± 0.01 eV, and assign an upper limit of the EA for the chlorobenzyl radical, EA(PhCHCl) ≤ 1.12 eV. These values were used to estimate the C–H bond dissociation energy (BDE)s for these substituted methanes. Fluoroacetonitrile was found to have a BDE of DH_{198} = 90.7 ± 2.8 kcal mol^{-1}. The C–H bond dissociation energies at the benzyl-α sites of the phenylmethanes are determined as 80.9 ± 2.3 kcal mol^{-1} for benzyl nitrile and an upper limit of 84.2 kcal mol^{-1} for benzyl chloride. These results are discussed in terms of substituent interactions in a simple MO framework and in relation to other similar molecules, including recently reported results for chloroacetonitrile.

1. Introduction

Organic radicals are important intermediates in a myriad of chemical reactions. Radicals, which have a single unpaired electron, are players in atmospheric reactions, photochemical systems, catalysis, and in biological systems. Often, the impact of these radicals can be tied closely to their abundance and lifetime in the system. This in turn is linked to the stability of the radical. One way to view this stability is with respect to the parent molecule by the bond dissociation energy (BDE), since (in the case of simple organic molecule) the RH → R + H reaction enthalpy is negatively correlated with the stability of the product radical.[126,127] The lower the BDE, the more stable the radical.

The effects of substituent group on the stability of the radical are reflected directly in the BDE of the parent species. This is perhaps best understood in the context of a substituted methane, $CHR_1R_2R_3$ (where R is a hydrogen, halogen, cyano-group, etc). Interactions involving π-electrons are of strong importance in this example; the parent is a nominally closed-shell molecule while the radical has a canonical p-orbital electron. In general, both π-accepting and π-donating substituent groups tend to stabilize radicals[126] while electron withdrawing effects destabilize radicals with respect to the parent species.[110,126,127] In a molecular-orbital picture, the stabilization by the π-accepting cyano and unsaturated hydrocarbon groups is due to interaction of the unpaired electron on the radical carbon center with the unoccupied π orbitals of the substituent. In the case of π-donating halogens (F, Cl, Br), the stabilization results from the interaction of the radical-center orbitals with the non-bonding electron pairs of the substituents.[128] In homogenously substituted radicals with several substituent groups of the same type (i.e. $\cdot CHR_2$, and $\cdot CR_3$, where R is a halogen[110], CN[108]), substitutions beyond the first tend to

have diminishing effects on the radical stability and, therefore, the BDE of the corresponding closed-shell molecule. In the extreme case of fluorine substituents, the radicals are actually destabilized beyond the first substitution.[129]

This well-studied group of mono- and homogeneously-substituted methanes begs the question about 'mixed' substitutions. That is, doubly and triply substituted methanes of both different substituents and those with differing π-interaction types (donating and accepting). We have recently investigated one particular case of such species, derived from the chloroacetonitrile (CH_2ClCN) precursor.[111] The BDE, calculated with the newly determined EA using the electron affinity gas-phase acidity cycle (an application of Hess's Law), was found to be exceptionally low compared to similar chloro- and cyanomethanes. This defies the trend set by homogenous substitutions. Rather than a saturation effect, the combination of π-donating and π-accepting groups appears synergistic. To further expand on this newly-studied class of methanes, we turn to radicals produced from fluoroacetonitrile, benzyl nitrile, and benzyl chloride. We find that, analogous to chloroacetonitrile, the BDEs of the mixed species fluoroacetonitrile and benzyl chloride are lower than predicted from similar methanes. In contrast, benzyl nitrile acts like similar homogenously-substituted methanes. These results are examined within simple molecular orbital theory framework which accounts for the synergistic (captodative) stabilization.

2. Experimental Methods

The experiments were performed using a custom-built anion photoelectron velocity-map imaging spectrometer, described in detail in Chapter 2 of this work. The benzyl nitrile, benzyl chloride, or fluoroacetonitrile precursor was brought into the gas phase by

flowing carrier gas, either O_2 or N_2O, over a liquid sample at room temperature. The resulting gas mixture was introduced to the high-vacuum ion-source chamber through a pulsed supersonic nozzle (General Valve Series 9) operated at 20 or 50 Hz to match the laser system used. The supersonic expansion was crossed with a continuous 1 keV electron beam. The O^- ions were formed by dissociative attachment of slow secondary electrons to the carrier gas, while the anions of interest were formed through the well-known deprotonation reactions of O^- with the precursor molecules.[101,102] The anions were pulse-extracted into a Wiley-McLaren time-of-flight mass spectrometer and detected using a dual microchannel-plate detector with a metal anode. A representative anion mass-spectrum obtained in one of the experiments described in this paper, specifically for the benzyl chloride precursor seeded in oxygen, is presented in Figure 1. As expected, the mass-spectrum is dominated by hydrated oxygen cluster anions. The anion of interest, $PhCHCl^-$, corresponds to the 125 a.m.u. peak marked with a red arrow.

The mass-selected anions were interrogated by linearly-polarized laser pulses, timed to interact only with ions of a specific mass. Photoelectrons were velocity-mapped[15] in the direction perpendicular to the ion and laser beams and projected onto a 40 mm diameter dual microchannel-plate detector, coupled to a P43 phosphor screen. Photoelectron positions were recorded by a thermoelectrically cooled charge-coupled-device camera. Images were typically accumulated for ~10^6 experimental cycles. The complete three-dimensional photoelectron distribution was reconstructed via an inverse Abel transformation[17] implemented in the BASEX program.[51] The resulting radial distributions were converted into the electron kinetic energy (eKE) domain using the appropriate Jacobian transformation. The photoelectron spectra were plotted versus

electron binding energy (eBE), defined as eBE ≡ $h\nu$ – eKE, where $h\nu$ is the photon energy. The spectra were calibrated using the well-known photodetachment transitions of O^-.[52,53]

Two laser systems were used in this work. A Spectra-Physics LAB-130 Nd:YAG laser operating at 50 Hz was used to produce 1064, 532, and 355 nm laser light as the fundamental output (5 mJ/pulse), the second harmonic (3 mJ/pulse), and third harmonic (2 mJ/pulse) respectively. The 612 nm (10 mJ/pulse) light was produced as the fundamental output of a Continuum ND6000 dye laser running Rhodamine 590 dye and pumped by the second harmonic (532 nm) of a Continuum Surelite II (20 Hz) Nd:YAG laser.

Electronic structure calculations with geometry optimization at the B3LYP and CCSD level of theory were carried out with the Gaussian 09 software package.[54] After optimizing the geometries for the anion and neutral ground and excited states, the normal-mode analysis was used to confirm that the optimized structures corresponded to true potential minima. Adiabatic electron affinities (EA) were calculated as the difference in the electronic energy for the anion and neutral species at their respective fully optimized geometries. Vertical detachment energies (VDE) were calculated as the difference in electronic energy for the anion and neutral species, both at the optimized geometry of the anion.

3. Experimental Results

3.1. Cyanofluoromethyl Radical

The photoelectron image and the corresponding spectrum of $FC(H)CN^-$ obtained

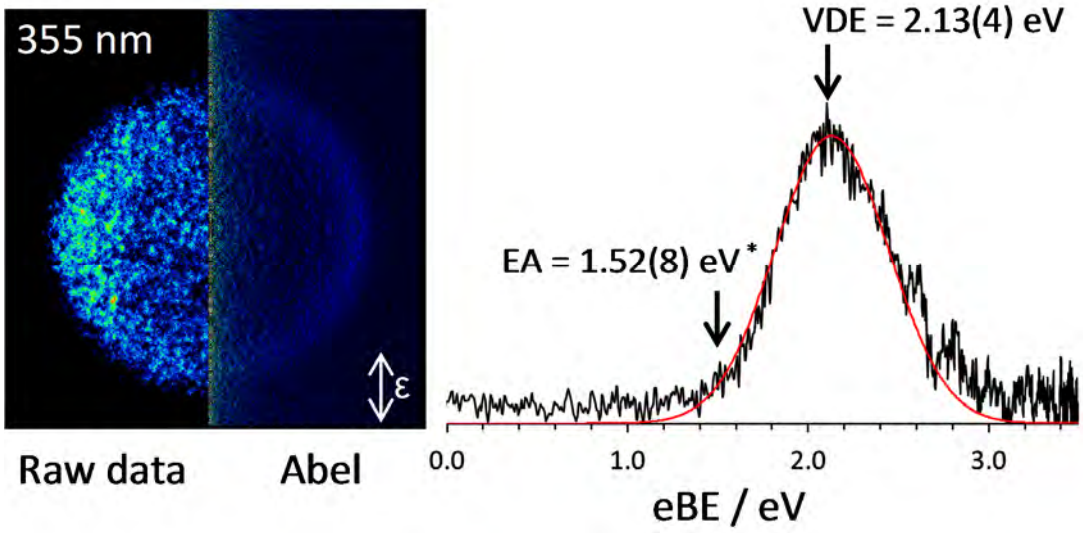

Figure 1. Photoelectron image and spectrum of $FC(H)CN^-$ at 355 nm. The double-sided arrow (ε) indicates the direction of laser polarization. The red curve superimposed with the experimental spectrum is the scaled Gaussian function fitted to the spectrum.

at 355 nm is presented in Figure 1. The image displays slightly negative photodetachment anisotropy with respect to laser polarization direction. The photoelectron spectrum consists of a single broad, vibrationally unresolved band, similar to that observed for the anion of the chlorocyanomethyl radical, ClC(H)CN$^-$. In both cases, the broad band indicates a large geometry change between the anion and the neutral. The FC(H)CN$^-$ photoelectron band in Figure 1 was fitted with a scaled Gaussian function including a eKE$^{1/2}$ pre-factor to account for the low-eKE behavior of the photodetachment cross-sections.[130,131] The VDE = 2.13 ± 0.04 eV was determined from the fit, corresponding approximately to the position of the band maximum. While no clear band onset is discernable, we estimate EA ~ 1.5 eV corresponding to the spectral region where the signal-to-noise ratio increases sharply to ~3.

The geometries of the anion and neutral radical species were optimized at the CCSD level using the aug-cc-pVTZ basis set. The resulting structures are shown in Figure 2, with the quantitative structural parameters summarized in the figure and its caption. Similar to chlorocyanomethylide, the relaxed geometry of FC(H)CN$^-$ is trigonal pyramidal, while that of the neutral radical, FC(H)CN, is trigonal planar. The large geometry difference between FC(H)CN$^-$ and FC(H)CN is consistent with the broad photoelectron band in Figure 1. The same calculations predict an adiabatic EA = 1.410 eV, which is in good agreement with the above experimental estimation. Similarly, the predicted VDE = 2.015 eV is close to the experimental value of 2.13 ± 0.04 eV (Figure 1).

An adiabatic EA cannot be determined unambiguously directly from the vibrationally unresolved spectrum in Figure 1. However, it can be estimated from the experi-

mental VDE and the theoretically determined relaxation energy of the neutral radical from the anion geometry to the equilibrium structure, ΔE_{rel}. Since ΔE_{rel} equals the difference between the VDE and EA, the EA can be estimated using the relationship: $EA_{est} = VDE_{exp} - \Delta E_{rel}$.[110,111] In the absence of a direct experimental value, this approach is more advantageous than direct calculation of the EA, because it uses theory only to estimate the relatively small correction from the experimental VDE value (VDE_{exp}). This method naturally accounts for some of the inaccuracy in the calculation of VDE and EA by subtraction of errors. We use the following equation with the experimental VDE value and a relaxation energy, ΔE_{rel} = VDE – EA, determined from ab initio (CCSD) calculations.

$$EA_{exp} = VDE_{exp} - \Delta E_{rel} \qquad (1)$$

Per the results summarized in Table 1, the calculated ΔE_{rel} values, depending on the basis set used, all fall within a 0.06 eV wide range. Substituting the relaxation energy result for the largest basis set (aug-cc-pVTZ), ΔE_{rel} = 0.605, and VDE_{exp} = 2.13 ± 0.04 eV into Eq. (1), we estimate the EA of the FC(H)CN radical as 1.53 ± 0.08 eV. The above error range is a combination of the 0.04 eV uncertainty in the experimental VDE value and an empirical spread encompassing the calculated ΔE_{rel} values; it is not a rigorously determined value.

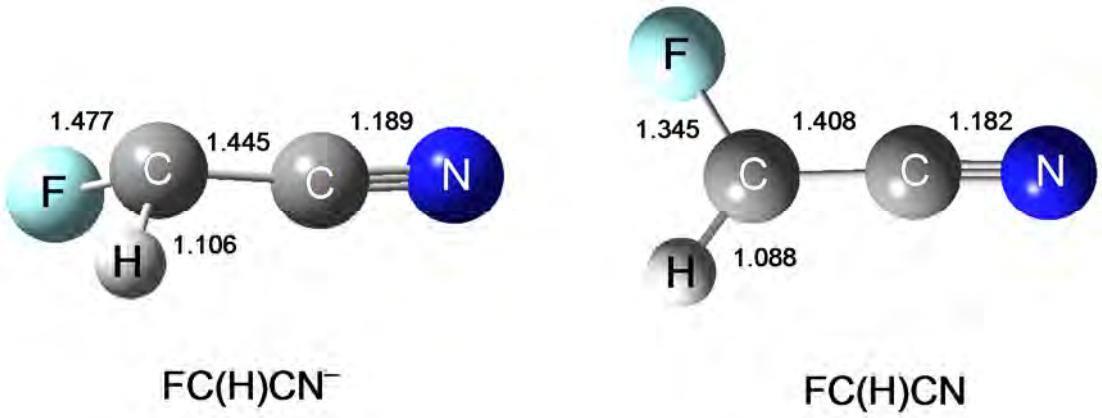

Figure 2. CCSD/aug-cc-pVTZ optimized geometries of $FC(H)CN^-$ and FC(H)CN. The anion has a trigonal pyramidal structure, while the neutral radical is planar. The bond lengths are indicated in Angstroms. Other optimized structural parameters are as follows. Anion: ∠F–C–C = 108.0°, ∠C–C–H = 109.8°, ∠C–C–N = 173.3°, Dihedral(F–C–C–N) = 123.8°, Dihedral(H–C–C–N) = –122.3°. Neutral (planar): ∠F–C–C = 118.5°, ∠C–C–H = 125.2°, ∠C–C–N = 178.2°, Dihedral(F–C–C–N) = 180°.

Table 1. Energetic parameters (in eV) obtained from the electronic structure calculations on cyanofluoromethyl radical and its anion. [a]

Method / Basis set	**EA**	**VDE**	ΔE_{rel} [b]
CCSD/6-311++G**	1.226	1.859	0.633
CCSD/aug-cc-pVDZ	1.393	2.058	0.665
CCSD/aug-cc-pVTZ	1.410	2.015	0.605
Experimental	1.53(8) [c]	2.13(4)	

[a] Values are calculated from electronic energy only.

[b] Defined as $\Delta E_{rel} = VDE_{calc} - EA_{calc}$.

[c] Determined from the experimentally determined VDE in conjunction with the CCSD/aug-cc-pVTZ results using Eq (1).

3.2. Cyanobenzyl Radical

The photoelectron imaging results for deprotonated benzyl nitrile, i.e. the $PhCHCN^-$ anion (116 a.m.u.), are presented in Figure 3. A single band with an onset at about 1.9 eV is observed in the 532 nm image and the corresponding photoelectron spectrum. The maximum position at eBE = 1.941 ± 0.003 eV (determined from the average of several independent runs) is assigned as the VDE of $PhCHCN^-$. The slightly negative anisotropy observed in the image is consistent with detachment from the canonical π (2*p*) orbital centered on the radical carbon center.

Geometry optimization and electronic structure calculations using the B3LYP density-functional theory method and a variety of basis sets were carried out for the $PhCHCN^-$

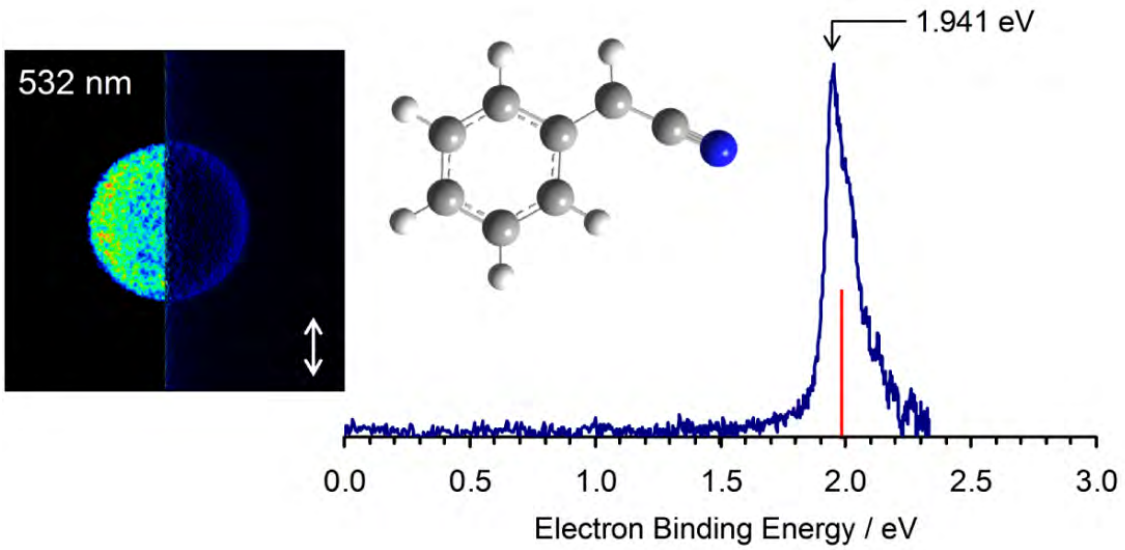

Figure 3. Photoelectron image and corresponding spectrum of the cyanobenzyl anion, $PhCHCN^-$, at 532 nm. The red vertical line in the spectrum indicates the VDE value determined from the B3LYP/aug-cc-pVQZ calculations.

Table 2. The adiabatic electron affinity (EA) of cyanobenzyl radical and the vertical detachment energy (VDE) of $PhCHCN^-$ calculated at the B3LYP level of theory (in eV).[a]

Basis Set	EA	VDE	ΔE_{rel} [b]
aug-cc-pVDZ	1.954	1.991	0.036
aug-cc-pVTZ	1.948	1.985	0.037
aug-cc-pVQZ	1.950	1.988	0.038
Experiment	1.90(1) [c]	1.941(3)	-

[a] Values are calculated from electronic energy only.

[b] Defined as $\Delta E_{rel} = VDE_{calc} - EA_{calc}$.

[c] Determined from the experimentally determined VDE in conjunction with the B3LYP/aug-cc-pVQZ results using Eq (1).

anion and the corresponding neutral radical in the respective ground electronic states. From these calculations, the adiabatic EA of PhCHCN and the VDE of the anion were determined and summarized in Table 1. The VDE = 1.988 eV, corresponding to the largest basis set used in this study (aug-cc-pVQZ), is also indicated as a red vertical bar in the experimental spectrum in Figure 3. The calculated properties are in good agreement with the experimental results.

The neutral radical and anion geometries optimized with the aug-cc-pVQZ basis are presented in Figure 4 (A and B). Only the key structural parameters are indicated in the figure, while the complete geometries are provided in Appendix II. The neutral radical is strictly planar, while the anion has a minor (0.07°) out-of-plane puckering of the cyano-group indicated by the calculations. Since the energetic barrier at the strict planarity, associated with this distortion, is orders of magnitude smaller than the zero-

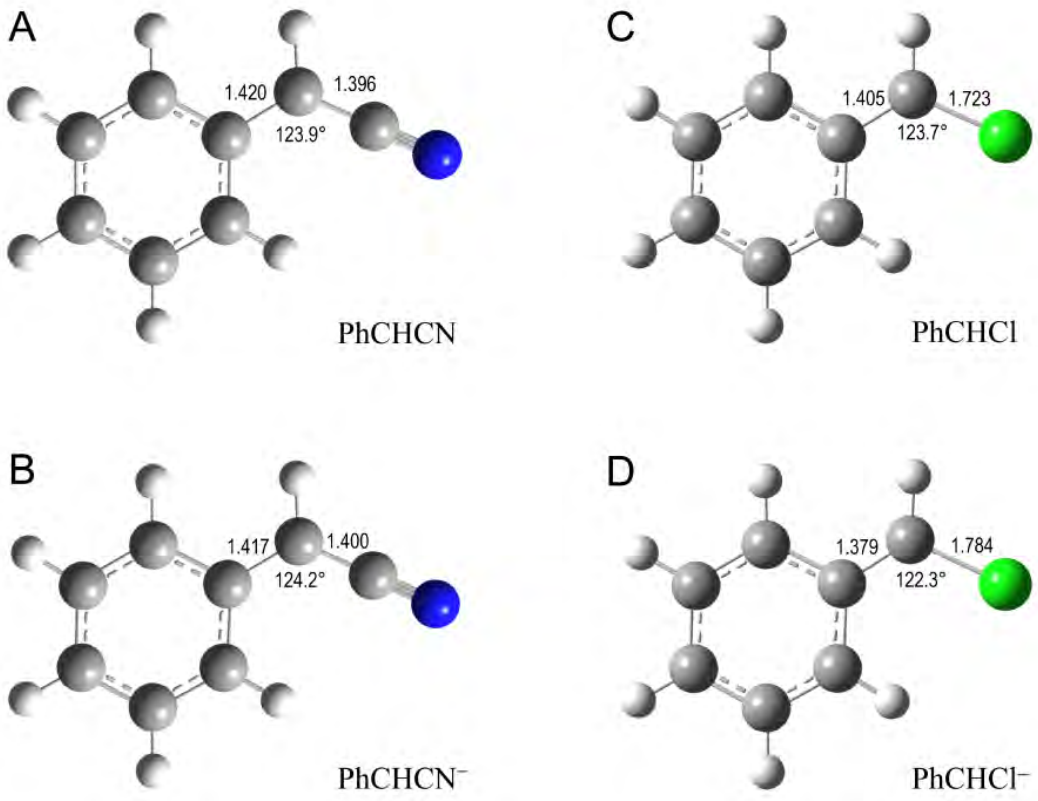

Figure 4. The optimized geometries of (A) the cyanobenzyl radical, (B) the cyanobenzyl anion, (C) the chlorobenzyl radical, and (D) the chlorobenzyl anion. The geometries were optimized at the B3LYP level of theory. Calculations on cyanobenzyl employed the aug-cc-pVQZ basis set, while the chlorobenzyl calculations used the aug-cc-pVTZ basis. Only the key structural parameters are indicated in the figure (bond lengths in – Angstroms, bond angles – in degrees).

point vibrational energy, we view this quasi-planar anion structure as effectively planar.

Beyond this, there exist only minor differences in the key bond lengths and angles. The very similar anion and neutral geometries, as well as the small difference between the calculated VDE and EA values (Table 2) are consistent with the relatively narrow band observed in the photodetachment (Figure 3).

The EA of cyanobenzyl radical cannot be determined directly from the unresolved spectrum in Figure 3, though it can be estimated using the same method which was applied to cyanofluoromethyl anion, namely Eq. (1). Using VDE_{exp} = 1.941 ± 0.003 eV (Figure 1) and ΔE_{rel} = 0.038 eV (the B3LYP/aug-cc-pVQZ result in Table 2), we estimate EA(PhCHCN) = 1.90 ± 0.01 eV. The uncertainty reflects the range of relaxation energies from different calculations. This EA value agrees well with the approximate band origin in the experimental spectrum in Figure 3.

3.3. Chlorobenzyl Radical

The photoelectron imaging results for the low-abundance 125 a.m.u. anion (the mass of $PhCHCl^-$) are presented in Figure 5. At 1064 nm only a weak, low-eKE signal is observed (Figure 4A). The spectral feature rises above the noise level at eBE ≈ 1.1 eV. Two partially overlapping features (a) and (b) are apparent in the 612 nm image and the corresponding spectrum (Figure 4B). Modeling the spectrum with a sum of two Gaussians indicates that bands (a) and (b) are centered at eBE = 1.20 and 1.43 eV, respectively, with (a) being significantly narrower than (b).

The geometries of the neutral chlorobenzyl radical and its anion, optimized at the B3LYP/aug-cc-pVTZ level, are shown in Figure 4 (C and D), with a complete summary

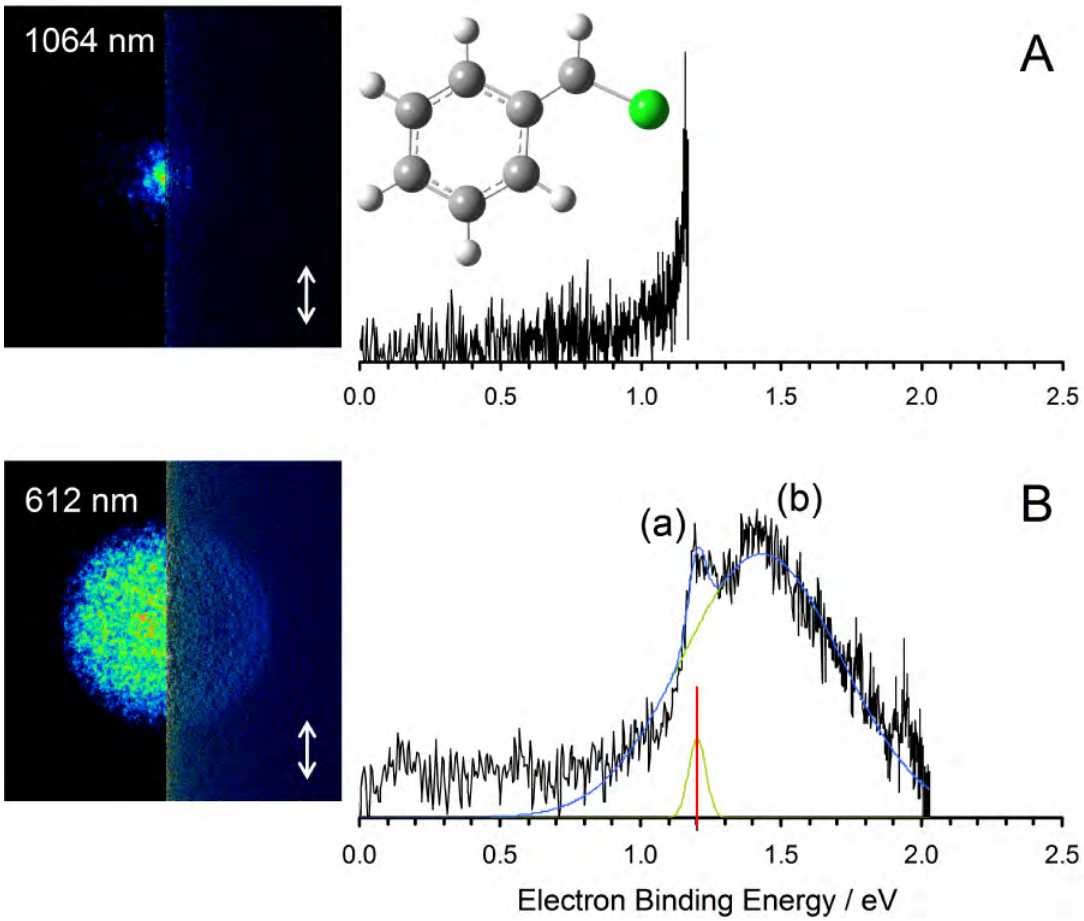

Figure 5. Photoelectron images and corresponding spectra of the 125 a.m.u. anions, obtained at (A) 1064 nm and (B) 612 nm. All signal in (A) and band (a) in (B) are assigned to the chlorobenzyl anion, $PhCHCl^-$, while band (b) in (B) corresponds to a different anion of the same mass, plausibly the monohydrated methoxyphenide anion, $C_7H_7O^-\cdot H_2O$. The VDE of $PhCHCl^-$, calculated at the B3LYP/aug-cc-pVTZ level of theory, is indicated in (B) with a vertical red line. A global spectral fit with a sum of two Gaussian functions in (B) is shown as a blue curve. The individual Gaussian components (a) and (b) are shown as light-green curves.

Table 3. The adiabatic electron affinity (EA) of the chlorobenzyl radical and the vertical detachment energy (VDE) of $PhCHCl^-$ calculated at the B3LYP level of theory (in eV).[a]

Basis Set	EA	VDE	ΔE_{rel} [b]
6-311++G**	1.107	1.204	0.097
aug-cc-pVDZ	1.120	1.212	0.092
aug-cc-pVTZ	1.110	1.201	0.091
Experiment	≤ 1.12	1.20(2)	–

[a] Values are calculated from electronic energy only.

[b] Defined as $\Delta E_{rel} = VDE_{calc} - EA_{calc}$.

of the structural parameters is given in Appendix II. Similar to cyanobenzyl, the equilibrium geometry change expected in the photodetachment of $PhCHCl^-$ is small. Again, the neutral is strictly planar, while the anion is effectively planar, with the out-of-plane puckering even smaller than in the cyanobenzyl anion. We do note, however, the 0.03 Å lengthening of the C–Ph bond and the 0.06 Å shortening of the C–Cl bond expected upon the detachment of $PhCHCl^-$. Based on these similar geometries, we expect a relatively sharp $PhCHCl^-$ photodetachment feature, qualitatively similar to that observed for $PhCHCN^-$ in Figure 3.

The EA values calculated for PhCHCl using three different basis sets (Table 3) agree well with the onset of the transition observed in the low eKE regime at 1064 nm (Figure 5A), as well as with the low-energy wing of band (a) in the 612 nm spectrum (Figure 5B). The VDE values calculated for the anion agree well with the maximum position for band (a). The B3LYP/aug-cc-pVTZ VDE value, 1.201 eV, is indicated in the

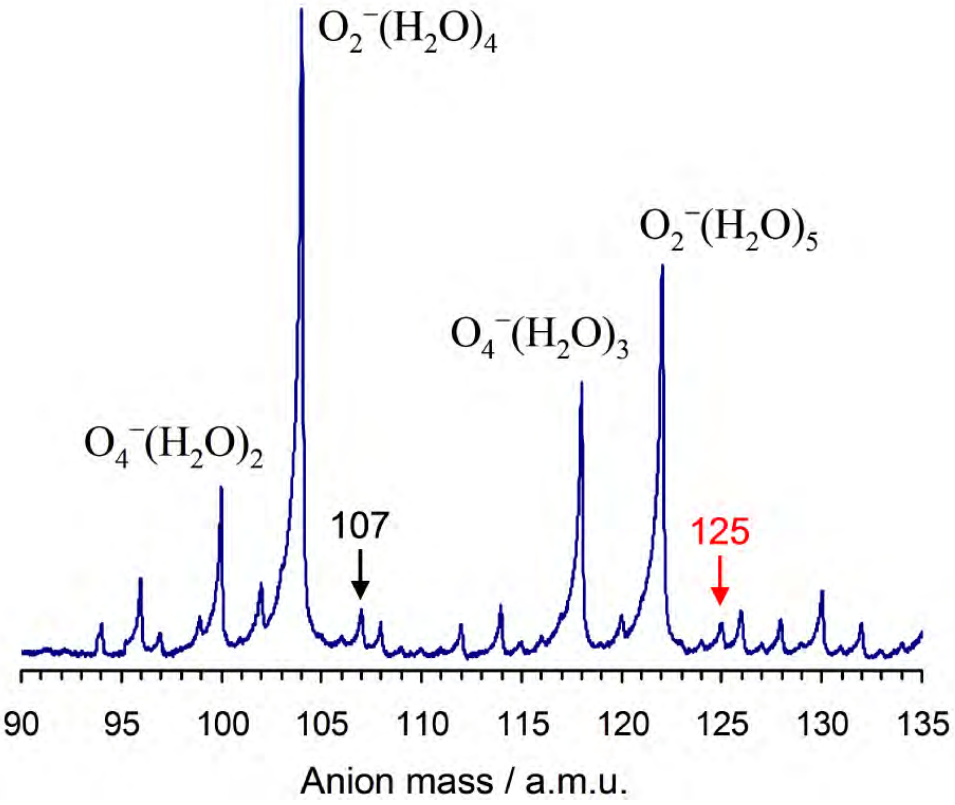

Figure 6. A representative anion mass-spectrum recorded using the benzyl chloride precursor seeded in oxygen, with water impurities present in the gas delivery lines. The anion of interest, $PhCHCl^-$, corresponds to the 125 a.m.u. peak, marked with a red arrow. Other ions of the same mass may include the monohydrated methoxyphenide cluster anion, $C_7H_7O^-\cdot H_2O$. The 107 a.m.u. peak, marked with a black arrow, is plausibly assigned to unsolvated $C_7H_7O^-$.

spectrum with a vertical red line, which agrees essentially perfectly with the peak position of the corresponding Gaussian fit at 1.20 ± 0.02 eV. Therefore, we assign feature (a) to the detachment from $PhCHCl^-$. Transition (b), which does not fit any of the predicted properties of $PhCHCl^-$, is attributed to the photodetachment of a different anion of the same mass. Calculations at the B3LYP/aug-cc-pVTZ level of theory of the phenide anions and respective neutrals of α-chlorotoulene, deprotonated at the o-,m-, and p-positions, indicated clearly they were not responsible for band (b).

To understand the origin of band (b) in Figure 5B, we turn to the parent-ion mass-spectrum shown in Figure 6. The spectrum is quite congested in the 120-130 a.m.u. region and several alternative ions can account for mass 125 a.m.u., besides $PhCHCl^-$. With the abundance of water clusters in the spectrum and the presence of oxygen anions in the ion source, another plausible assignment for the 125 a.m.u. peak in Figure 6 is the cluster of the methoxyphenide anion (deprotonated methoxybenzene, also known as anisole) with water, $C_7H_7O^-\cdot H_2O$. This hypothesis is supported by two observations.

First, a 107 a.m.u. peak, plausibly assigned to $C_7H_7O^-$, is also observed in Figure 6. The 107 and 125 a.m.u. peaks are both marked in the figure with arrows. The two peaks are of comparable intensity, consistent with a sizable $C_7H_7O^-\cdot H_2O$ contribution at 125 a.m.u. Second, the electron affinity of the methoxyphenyl radical has been previously determined through the acidity of methoxybenzene as $EA(C_7H_7O)$ = 1.12 ± 0.19 eV and 1.25 ± 0.19 eV for the *meta*- and *ortho*- isomers, respectively.[95,132] Accounting for additional stabilization by hydration, band (b) in Figure 5B is consistent with the photodetachment of $C_7H_7O^-\cdot H_2O$.

The above assignment band (b) in Figure 5B to the photodetachment of

$C_7H_7O^- \cdot H_2O$ is admittedly not very robust, but the methoxyphenide anion or its clusters are not the focus of this work. The presented hypothesis merely gives a plausible explanation for the additional band in the photodetachment of 125 a.m.u. anions that is not consistent with the predicted properties of the target anion, $PhCHCl^-$. Thus, from here on, we focus only on the properties of band (a).

Similar to the cyanobenzyl case, the EA of chlorobenzyl radical cannot be determined unambiguously directly from the vibrationally-unresolved data in Figure 5. Due to the overlap of spectral features, the VDE is also subject to scrutiny. Therefore, we can safely assign only an upper bound of the EA, as the eBE value where the spectral feature observed at 1064 nm rises sharply above the noise level, i.e. EA(PhCHCl) ≤ 1.12 eV.

4. The C-H Bond Dissociation Energy of 'Mixed' Methanes

From the known EA of the product radical, the corresponding C–H bond dissociation energy of the parent closed-shell molecule can be determined through the general gas-phase acidity/electron affinity thermodynamic cycle[127]:

$$D\mathit{H}_{298}(R–H) = \Delta_{acid}\mathit{H}_{298}(RH) + EA(R) – IE(H) + [\text{thermal corrections}], \quad (2)$$

Per this equation, the BDE of the close-shell molecule RH, formally defined as $D\mathit{H}_{298}$(R–H), is equal to the corresponding enthalpy of deprotonation (acidity), $\Delta_{acid}\mathit{H}_{298}$(RH), plus the electron affinity of the radical, EA(R), minus the ionization energy of the hydrogen atom, IE(H) = 13.60 eV.[133] The thermal corrections contributing to Eq. 2 are typically small (< 0.3 kcal mol^{-1}) and can be neglected in light of much larger errors associated with some of the other terms.[134]

The gas-phase acidity of all three methanes in this work have been previously measured. Using the determined EAs (or upper bound in the case of chlorophenylmethyl radical), we determine the R-H BDEs. The enthalpy of the reaction $CH_2FCN \rightarrow H^+ +$ CHFCN at room temperature, known to be 369.0 ± 2.1 kcal mol^{-1},[135] EA(R) = 1.53 ± 0.08 eV is the EA of the radical determined above in 3.1., and the IE(H). Using these values, the first C–H BDE of fluoroacetonitrile is determined to be DH_{298} = 90.7 ± 2.8 kcal mol^{-1}, with the uncertainty of the combined experimental and theoretical results taken into consideration. Using the EA of cyanobenzyl radical, determined in this work, EA(CHPhCN) = 1.90 ± 0.01 eV, the known acidity for the benzyl-α site of benzyl nitrile, $\Delta_{acid}H_{298}(PhCH_2CN)$ = 1467 ± 9.6 kJ mol^{-1},[95,136] we calculate the BDE corresponding to the formation of the cyanobenzyl radical from benzyl nitrile: DH_{298}(H–CHPhCN) = 80.9 ± 2.3 kcal mol^{-1}. Applying the same procedure to the experimentally determined upper limit of 1.12 eV for the EA of chlorobenzyl radical, and the benzyl-α site acidity of benzyl chloride, $\Delta_{acid}H_{298}(PhCH_2Cl)$ = 1556 ± 8.8 kJ mol^{-1},[95,136] we determine the upper limit of the BDE of $PhCH_2Cl$, corresponding to the formation of chlorobenzyl radical, DH_{298}(H–CHPhCl) ≤ 84.2 kcal mol^{-1}.

All of these values represent relatively low BDEs. To put these values in a context, the BDEs of several related species are summarized in Table 4. For the ease of comparison, the radical stabilization energy (RSE) of each species has been calculated as the corresponding BDE relative to that of methane: RSE(R–H) = $DH_{298}(CH_3–H)$ – DH_{298}(R–H).[142] A greater RSE value indicates a weaker R–H bond and a more stable radical R.

Table 4. Bond dissociation energies of select substituted methanes (in kcal mol^{-1}).

Compound	DH_{298}	Reference	RSE[a]
CH_4	104.9 ± 0.4	[127]	0
Fluoro-methanes:			
CH_3F	103.2 ± 1.0	[129]	1.7 ± 1.1
CH_2F_2	106.4 ± 0.7	[129]	–1.5 ± 0.8
CHF_3	106.7 ± 1.0	[129]	–1.8 ± 1.1
Chloro-methanes:			
CH_3Cl	100.1 ± 0.6	[137]	4.8 ± 0.7
CH_2Cl_2	95.7 ± 0.5	[137]	9.2 ± 0.6
$CHCl_3$	93.8 ± 0.6	[137]	11.1 ± 0.7
Cyano-methanes:			
CH_3CN	94.2 ± 2.0	[138,139]	10.7 ± 2.0
$CH_2(CN)_2$	88.7 ± 2.1	[111,139]	16.2 ± 2.1
Phenyl-methanes:			
CH_3Ph	89.8 ± 0.5	[140]	15.1 ± 0.6
CH_2Ph_2	81.3 ± 3.1[b]	[95,141]	23.6 ± 3.1
Cyano-halo-methanes:			
CH_2ClCN	87.0 ± 2.7	[111]	17.9 ± 2.7
CH_2FCN	90.7 ± 2.8	this work	14.2 ± 2.8
Benzyl nitrile (cyanophenylmethane):			
$PhCH_2CN$	80.9 ± 2.3 [c]	this work	24.0 ± 2.3 [c]
Benzyl chloride (chlorophenylmethane):			
$PhCH_2Cl$	< 84.2	this work	< 20.7

[a] Radical (R) stabilization energy, defined as RSE = DH_{298}(CH_3–H) – DH_{298}(R–H)

[b] Value calculated with EA and $\Delta_{acid}H_{298}$ from Ref. using Eq. 1.

[c] Value and error estimated from experimental and theoretical results, see the text for details.

Among the mono-substituted methanes listed in Table 4, toluene ($PhCH_3$) has the largest RSE = 15.1 ± 0.5 kcal mol^{-1}.[140] This indicates that among Ph, F, Cl, and CN, phenyl is the most stabilizing substituent, which may be responsible for most of the RSE magnitudes for α-chloro- and α-cyano- toluenes ($PhCH_2Cl$ and $PhCH_2CN$, respectively), determined in the present study. In general, the RSE action of a substituent may be attributed to effects within the σ and π electron systems of the closed-shell parent molecule and the corresponding radical. Both halogens and CN are strong σ withdrawers lowering the energy of the entire molecule (relative to methyl radical) through the σ orbital system. However in relation to the BDE, it must be considered that the closed-shell parent molecule is also affected by strong σ withdrawing effects. Furthermore, since the parent molecule has an additional bond to hydrogen (with 2 more σ electrons), the energy of the parent molecule is lowered *more* than that of the radical with the same substitution (F, Cl, CN). Thus, the energy difference between the parent and radical is larger, leading to a greater BDE. In general, BDE is larger for more strongly σ withdrawing substituent groups and greater numbers of them in the absence of other effects.[143] As a σ withdrawing group, phenyl ranks low compared to F, Cl, or CN. For this reason, although it stabilizes the closed-shell parent molecule more than the corresponding radical, the effect of the σ withdrawing ability of Ph on the parent molecule's BDE is limited. The large RSE of Ph is attributed mainly to its π system, which acts as a net π electron acceptor in the extended molecule. This is consistent with the changes observed in acidity for conjugated acids with phenyl substituents.[144]

One way to consider the results in a larger context is to consider whether or not the mixed pair of substituents is synergistically stabilizing a radical or if the effects are

saturated. To do so, we will consider the mono-substituted systems' RSE. We might naively consider that the RSEs from a single substitution can be attributed uniquely to the R-group. Further, if one assumes the absence of any substituent-substituent interactions, then two substitutions would have the effect of an additive RSE. This is of course not the case, but it does establish a baseline. Now we may compare a doubly-substituted specie's RSE to the expected additive RSE, a ΔRSE. A positive value indicates synergy between substitutions; a negative value indicates the more likely saturation effect. For example, the RSE of CH_3CN is 10.7 ± 2.0 kcal mol^{-1}, while for $CH_{2(}CN)_2$ the RSE is 16.2 ± 2.1 kcal mol^{-1}. The ΔRSE is -5.2 ± 3.5 kcal mol^{-1}, indicating that well within error the net effect between substituents is saturating. In comparison, the ΔRSE of chloroacetonitrile, fluoroacetonitrile, and benzyl chloride are all positive: 2.4 ± 3.4, 1.8 ± 3.6, and > 0.8 kcal mol^{-1}. Despite the relatively large error, it is clear that these radicals enjoy a non-saturation of the π-interactions. Conversely, the ΔRSE of benzyl nitrile is -1.8 ± 3.4 kcal mol^{-1}; the negative value indicates saturation, as expected for any homogenously-substituted system. Therefore we can be certain that is the type of π-interaction, not the identity of the substituent which is the defining factor.

To understand this, we turn to a simple molecular orbital picture. The effect of π acceptance from the cyano- or phenyl- group in the substituted radical is easily understood. As illustrated in Figure 7, the mixing of the radical's π orbital with a π-acceptor substituent lowers the radical electron's energy. Since this interaction lowers the energy of the radical (and not of the parent molecule, which has no π orbitals), it lowers the parent molecule's BDE. The π donating effect of a halogen is also very similar in this simple picture. However, the substituent orbital is now fully occupied. For this reason,

there are always three electrons in the π donating group's interaction. From a simple molecular orbital picture though, this interaction still has a net 1 electron stabilization as compared to unmixed orbitals. This, like a π-accepting effect, lowers the energy of the radical and thus lowers the BDE. Adding a second substituent introduces a third orbital to the mixing. In our picture, if we add this new substituent interaction to the mon-substituted system, this produces a new molecular orbital within the manifold that is essentially un-impactful on the energy. If this new system is donor-donor, the 5 electron system is still stabilized by a net ~1 e^- interaction. While the effect is greater, it is smaller change than the initial interaction scheme. If the system is acceptor-acceptor, we have an identical 1 net e^- stabilization. Now, the synergy of a donor-acceptor species is obvious. In our simple MO picture, the synergy comes from the 3 MOs having only 3 e^-. The lowest energy MO is fully occupied, and the radical electron now occupies only an intermediate energy MO. This picture is admittedly very simple, but it does capture the basis of the stabilizing effects present in a methyl radical, providing a framework to understand multiple substituent effects on radical centers.

5. Summary

The VDE of the cyanofluoromethylide is 2.13 ± 0.04 eV. Although the corresponding band origin is not directly observable, the adiabatic EA was estimated to be 1.53 ± 0.08 eV. Using the estimated EA, the first C–H BDE of fluoroacetonitrile was determined through the general electron affinity/gas-phase acidity thermodynamic cycle, DH_{298} = 90.7 ± 2.8 kcal mol^{-1}. We have reported the EA for the cyanobenzyl radical, EA(PhCHCN) = 1.90 ± 0.01 eV, and assigned the upper limit of EA for the chlorobenzyl radical, EA(PhCHCl) ≤ 1.12 eV.

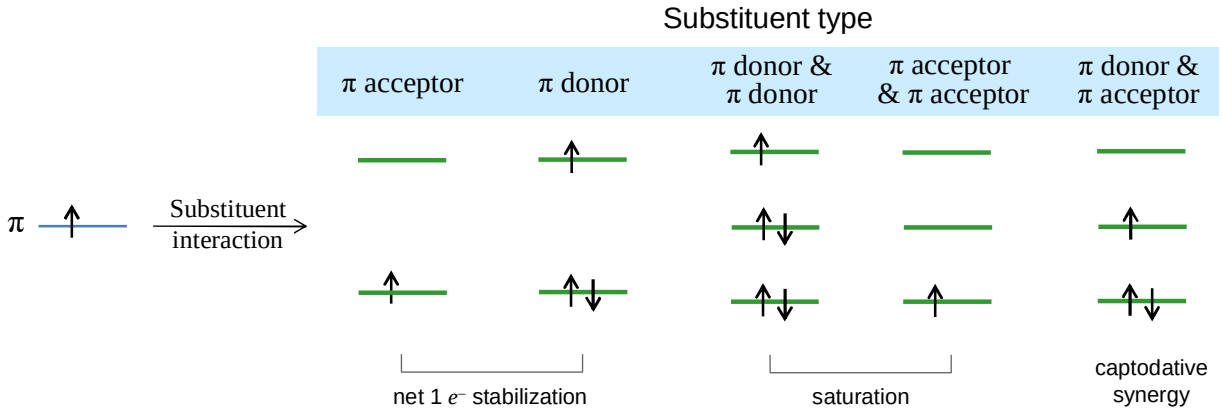

Figure 7. Schematic energy diagram illustrating the effects of interaction between the non-bonding 2*p* (π) electron of the central carbon and substituents of different types in substituted methyl radicals. See the text for details.

The C–H BDE of benzyl nitrile at the benzyl-α site was found to be: DH_{298}(H–CHPhCN) = 80.9 ± 2.3 kcal mol^{-1}, while the corresponding BDE of benzyl chloride was assigned an upper bound of DH_{298}(H–CHPhCl) ≤ 84.2 kcal mol^{-1}. These determinations fall in line with the previous studies of homogeneously substituted radicals, which exhibiting saturation of the substituent effects on the RSE, and the more recent studies of heterogeneously substituted species, which sometime display a synergistic (captodative) interaction of π donating and π accepting substituents. These effects were described by a simple MO framework.

Chapter 8: Photoelectron Imaging Spectroscopy of the Glyoxal and Methylglyoxal Radical Anions

Overview

We report a photoelectron imaging study of the glyoxal and methylglyoxal radical anion. The 532 nm photoelectron spectrum provides the first direct spectroscopic determination of the adiabatic electron affinity of glyoxal, EA = 1.10(2) eV. This assignment is supported by a Franck-Condon simulation of the experimental spectrum that successfully reproduces the observed spectral features. The vertical detachment energy of the glyoxal radical anion is determined as VDE = 1.30(4) eV. The EA of methylglyoxal is determined as $\leq$ 0.8 eV based on the signal-to-noise ratio of the $X\ ^1A' \leftarrow X\ ^2A''$ transition, with a VDE = 1.28(4) eV. The EA of the $a\ ^3A'' \leftarrow X\ ^2A''$ and $A\ ^1A'' \leftarrow X\ ^2A''$ transitions are determined as 3.28(3) eV and 3.614(5) eV respectively.

1. Introduction

Small dicarbonyls play important roles in atmospheric chemistry. The simplest of these molecules is glyoxal (OHCCHO), shown in Figure 1. Although glyoxal and methylglyoxal are a minor component of the atmosphere, their contributions to the chemistry of volatile organic compounds make them important to the modeling of atmospheric processes. [145-148] Glyoxal uptake into aqueous systems, such as aerosols, creates significant risks for the environment. Specifically, glyoxal and its derivatives can be oxidized, hydrolyzed, and oligomerized through heterogeneous reactions to form dimers and larger complexes.[149-151] The oligomers in particular are known to be a source of oxidizing radicals and secondary organic aerosols (SOA).[152-154] Although the effect of glyoxal oligomers on the modeling of SOAs has not been quantified, laboratory experiments suggest their importance.[155] Methylglyoxal displays orientation preference at air-water interfaces which can alter the surface chemistry of atmospheric particles.[156] Perhaps most significantly, glyoxal and other dicarbonyls can form light-absorbing imidazoles, photosensitizing the growth of organic aerosols.[157-160] In addition, very recently glyoxal has emerged as a precursor for several small reactive intermediates with interesting properties, such as the OCCO diradical [161] and the OHCCO and HOCCO radicals.[162] It is in fact these species that motivated our initial interest in the anionic chemistry of glyoxal, in general, and the glyoxal radical anion in particular.

Despite its importance, some of the most fundamental properties of the glyoxal molecule and its anion remain unknown or poorly defined. In particular, the electron affinity (EA) of glyoxal has not been measured. The value appearing in contemporary databases, EA = 0.62 ± 0.26 eV, is an indirect estimate determined from the enthalpies of

formation of the anion and the neutral in a study of ethylene carbonate [155]. This indirect result is inconsistent with the Gaussian-3 (G3MP2B3) method predicting ca. 1.0 eV.[163] No attempts to experimentally determine the EA of methylglyoxal have been made to our knowledge, though one group has made the estimate based on their calculation of glyoxal.[164] While the methodology leaves the absolute value suspect, the estimation is that methylglyoxal was proposed to have an EA of 0.2 eV less than glyoxal base on similar substitutions with methyl groups.

The photochemistry of neutral glyoxal has received more attention. It was studied using fluorescence and UV-visible spectroscopy, while computational studies have focused on dimerization,[165] dissociation,[166] and hydrolysis.[167] Laser-induced fluorescence (LIF) measurements located the lowest-excited singlet state 2.728 eV above the ground state.[168] The lowest triplet state was also observed just below the singlet transition, at 2.381 eV[169] and the singlet-triplet coupling has been studied using level-anti-crossing spectroscopy. [170-172] Of particular interest to atmospheric chemistry is glyoxal dissociation.[166,173] In one of the known channels, photoexcited OHCCHO forms two CHO radicals,[174] while most famous is the "triple whammy" dissociation into two CO molecules and H_2.[175]

Methylglyoxal shares much of the same electronic structure. LIF shows the triplet state to be 2.414 eV above the ground state,[169] while the lowest-lying excited singlet is 2.743 eV.[168] The singlet-triplet coupling event in glyoxal has been extensively studied by Level-Anticrossing spectroscopy.[170-172] Like glyoxal, methylglyoxal will undergo unimolecular dissociation events to form OHC.[176]

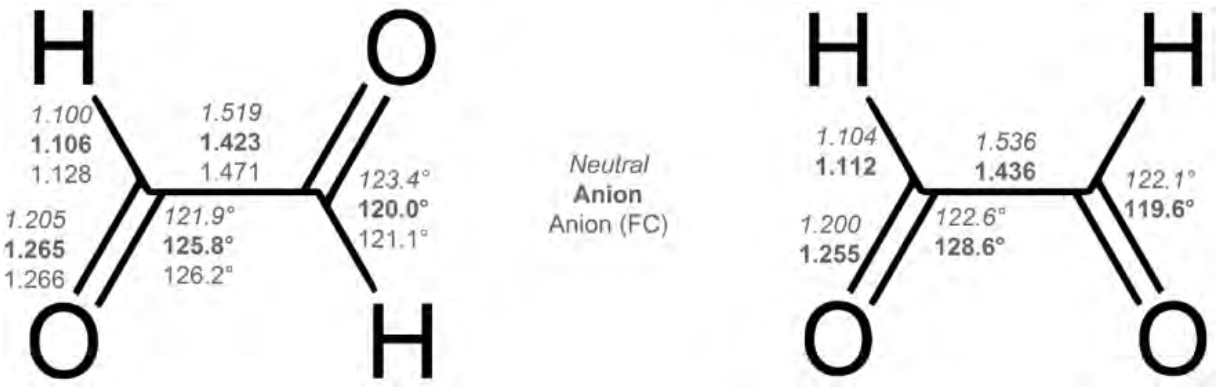

Figure 1. The C_{2h} (left) and C_{2v} (right) structures of the neutral and anion species of glyoxal optimized at the CCSD/aug-cc-pVTZ level of theory. The optimized geometric parameters for the neutral and the anion are given in italics and in bold, respectively. The C_{2h} anion parameters adjusted as part of the Franck-Condon simulation of the experimental spectrum are shown in plain font.

The height of the internal rotation barrier between the C_{2h} and C_{2v} isomers of glyoxal was investigated experimentally, with the results varying from 1770 ± 60 cm^{-1} by from During, Bucy and Cole in 1975 [177] to 2077 cm^{-1} by Butz in 1990.[173] Theoretical predictions of the barrier height vary from 1960 cm^{-1}, as determined by Scuseria and Schaefer in 1989,[178] to 2400 cm^{-1} by Kakumoto in 1987.[179] Theoretical evidence from the previous as well as present work also clearly shows that the C_{2h} symmetry isomer (Figure 1, left) corresponds to the global minima of both the neutral and anion glyoxal species. Likewise, methylglyoxal is also trans- with respect to the carbonyl groups. Calculations show and experiments agree that a fairly significant energy difference for the methyl group conformers exists, ~7 kcal mol^{-1} in the eclipsed conformer with respect to the staggered conformer, which makes staggered the dominate conformer in the ground state.[180]

We report the first direct experimental determination of the electron affinities and vertical detachment energies (VDE) of the glyoxal and methylglyoxal radical anions using anion photoelectron imaging spectroscopy. The experimental results, supported by additional theoretical calculations and Franck-Condon simulations, provide new insight into the electronic structure of glyoxal and methylglyoxal, both neutral and anionic systems.

2. Experimental and Theoretical Methods

The experiments were performed using a custom-built anion photoelectron imaging spectrometer described previously.[22,49] The glyoxal and methylglyoxal solutions (40% by weight in water) were first partially dehydrated using a ~1:1 volume ratio of 3 Å molecular sieves for at least 24 hours until the solutions were yellowish rather than

colorless and transparent. The glyoxal solution was then extracted from the sieve mixture using methanol,[50] while the methylglyoxal solution did not require any solvent and was simply decanted. The resulting glyoxal solution was heated to 70-85 ºC in order to raise its vapor pressure; methylglyoxal had sufficient vapor pressure at room temperature. Sample vapor was seeded into an N_2O carrier gas with a backing pressure of 20 psi. The mixture was expanded into the source chamber through a pulsed supersonic nozzle (General Valve, Inc., Series 9) operated at a repetition rate of 50 Hz. The expansion was crossed with a collimated beam of 1 keV electrons from an electron gun. Anions were formed by attachment of slow secondary electrons in the electron-impact ionized plasma.[50]

Anions were interrogated by linearly polarized laser pulses. The 532 nm light was obtained by frequency doubling the fundamental output a Spectra Physics LAB-130-50 Nd:YAG laser. The 612 and 306 nm lines were obtained using a Continuum Surelite II Nd:YAG with a ND6000 dye laser, fed with Rhodamine 590 . The laser pulses were timed to interact only with the ions of a mass-to-charge ratio m/z = 58 and 72 respectively. Photoelectrons were velocity-mapped[15] in the direction perpendicular to the ion and laser beams and projected onto a 40 mm diameter dual microchannel-plate detector, coupled to a P43 phosphor screen. Photoelectron impact positions were recorded by a thermoelectrically cooled charge-coupled-device camera. Images were typically accumulated for ~10^6 experimental cycles. The complete three-dimensional photoelectron distribution was reconstructed via an inverse Abel transformation[17] implemented in the BASEX program.[51] The resulting radial distributions were converted to photoelectron spectra using the well-known O^- photodetachment transitions for

calibration.[52,53]

Electronic structure calculations and geometry optimizations were performed using the GAUSSIAN 09 software package.[54] Geometry optimizations using the coupled-cluster method with single and double excitations (CCSD) with Dunning's augmented correlation-consistent basis of triple-ζ quality (aug-cc-pVTZ). Optimization was performed for both the anion and neutral species of glyoxal, yielding both the C_{2h} and C_{2v} symmetry equilibrium structures. The resulting structures were used in the calculations of adiabatic electron affinities (EA) and vertical detachment energies (VDE). The EAs were calculated as the difference in the electronic energy for the anionic and neutral species at the respective optimized geometries (C_{2h} or C_{2v} with respect to glyoxal). The VDEs were calculated as the energy difference for the anion and the neutral species, both at the optimized geometry of the anion. Zero-point vibrational energy corrections were determined using harmonic frequency calculations performed on the CCSD/aug-cc-pVTZ optimized geometries.

Several of the CCSD/aug-cc-pVTZ optimized geometries and vibrational frequencies were also used for the normal mode analysis as part of the Franck-Condon (FC) simulations This included the singlet glyoxal transitions geometries (C_{2h} or C_{2v}) and the triplet methylglyoxal transition. These simulations were carried out using the PESCAL 2010 software, with the normal modes treated as uncoupled harmonic oscillators with full Duschinsky rotation using the Chen method.[55,181]

3. Results and Analysis

3.1 Photoelectron Imaging of Glyoxal Anion

The raw photoelectron image of glyoxal anion collected at 532 nm is shown in

Figure 2 along with the corresponding spectrum. The spectrum is plotted versus electron binding energy: eBE = *hv* – eKE, where *hv* is the photon energy and eKE is the kinetic energy of the photoelectrons. The image indicates slightly negative photoelectron anisotropy with respect to the laser polarization direction, along with some limited vibrational resolution discernable in the spectrum.

The spectrum consists of the main intense band labeled A with partial vibrational resolution and a weak shoulder (B) extending from under the major feature A towards lower eBEs. Later in this Section, band A will be assigned to the $X\ ^1A_g \leftarrow X\ ^2A_u$ photodetachment transition in the glyoxal radical anion (C_{2h} isomer). The anion VDE is defined approximately by the position of the overall band A maximum. It was determined as VDE = 1.30 ± 0.04 eV by fitting a broad Gaussian envelope to the entire band.

The maximum of the first peak (marked '0' in Figure 2) corresponds to the adiabatic EA of glyoxal, determined as EA = 1.10 ± 0.02 eV. This directly determined value is significantly different from the previous indirectly obtained result EA = 0.62 ± 26 eV[155], presently cited in databases. On the other hand, the new spectroscopic determination is in a much better agreement with the G3MP2B3 theory prediction of EA ≈ 1.0 eV.[163]

3.2 Photoelectron Imaging of Methylglyoxal Anion

The photoelectron spectra of methylglyoxal at 612 and 306 nm are shown in Figure 3A and B respectively. In Figure 3A a single transition labeled C, partially vibrationally-

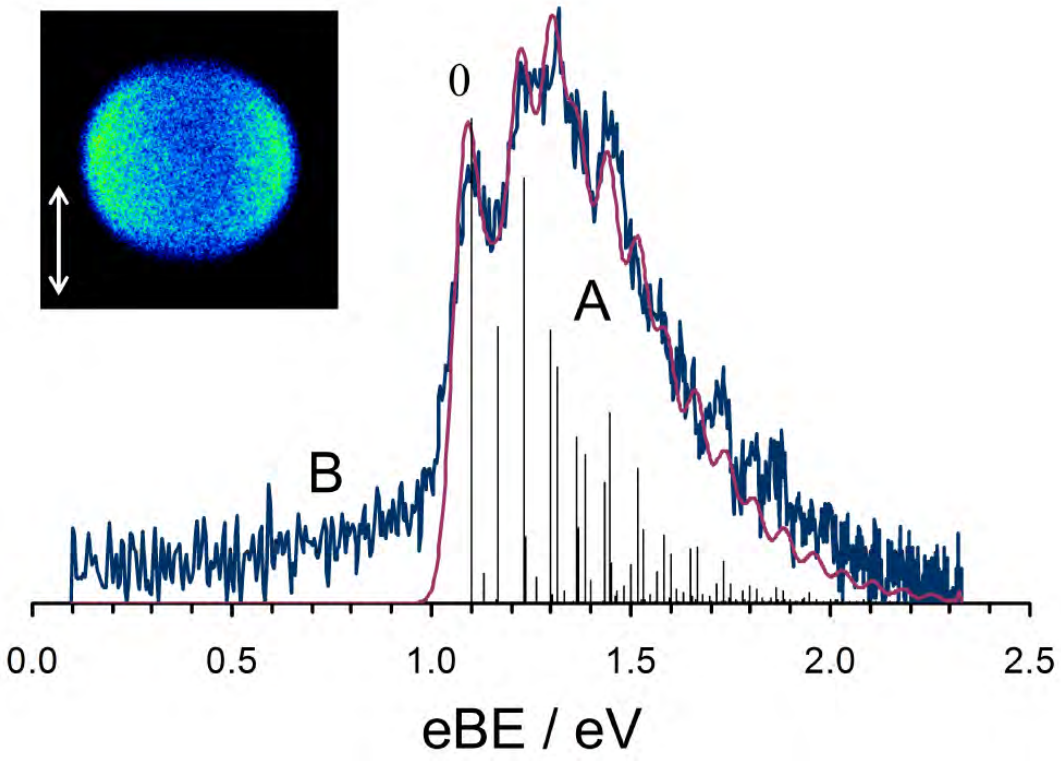

Figure 2. The 532 nm photoelectron image and the corresponding photoelectron spectrum of the glyoxal anion. Vertical double arrow indicates the laser polarization direction. The experimental spectrum is superimposed with the Frank-Condon simulation obtained as described in the text.

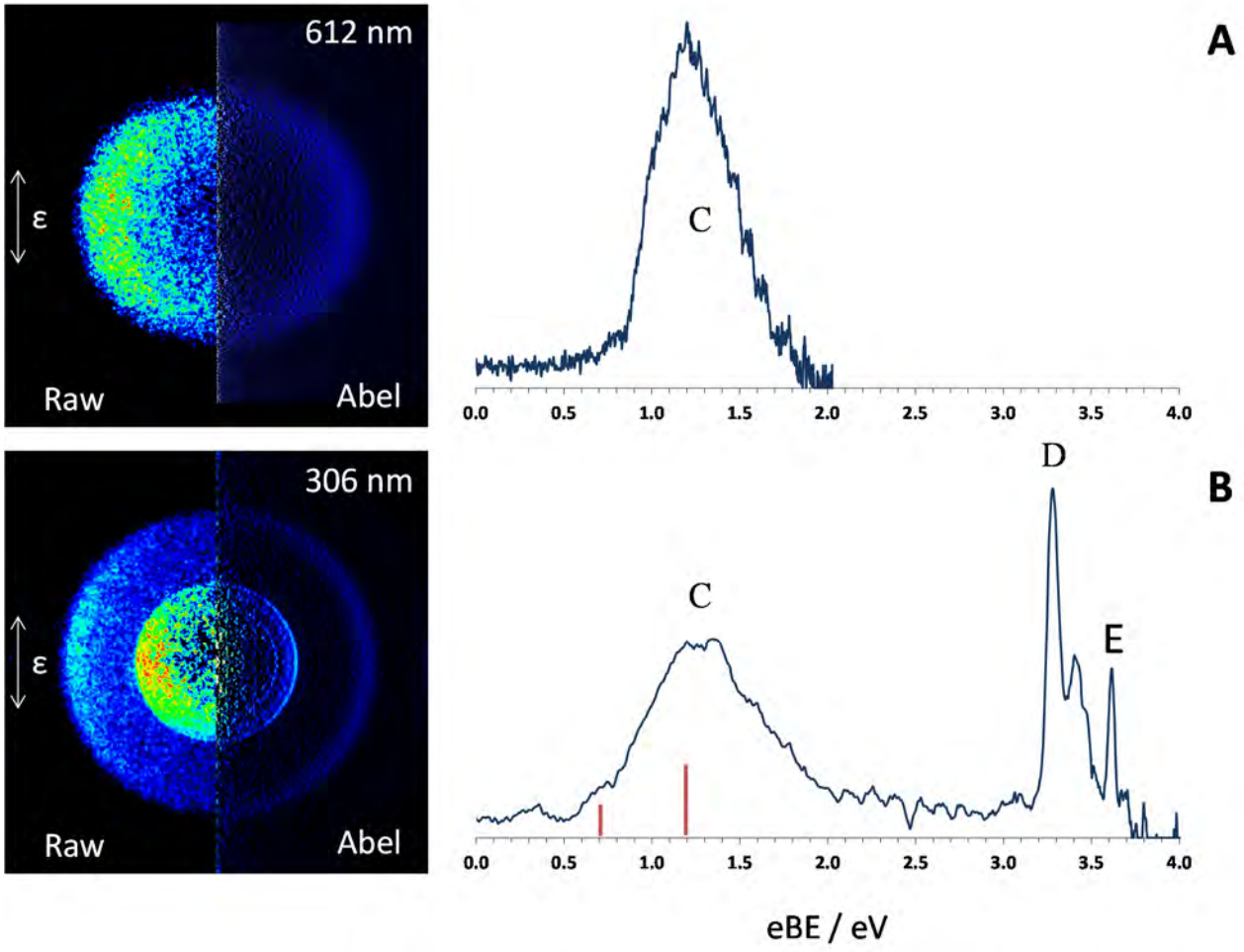

Figure 3. The 612 (A) and 306 (B) nm photoelectron images and corresponding spectra of the methylglyoxal radical anion. Band C is assigned to the ground-state singlet transition, band D is assigned to the lowest-lying triplet, and band E is assigned as the first excited singlet. The red vertical bars indicated the EA (short bar) and the VDE (long bar) calculated for the methylglyoxal singlet transition at the CCSD/aug-cc-pVTZ level of theory.

resolved, is observed to have a negative anisotropy, with an onset of ~0.8 eV, where signal rises to 3 times the background noise. This feature is assigned to $X\ ^1\mathrm{A}' \leftarrow X\ ^2\mathrm{A}''$ transition to the ground state of methylglyoxal. At 306 nm (Figure 3B) this feature is now fully energetically accessible, though the higher electron kinetic energy reduces the energetic resolution. Two new transitions, justified in section 4.2, are visible at higher eBE. The more intense feature, labeled D, is assigned to the triplet $a\ ^3\mathrm{A}'' \leftarrow X\ ^2\mathrm{A}''$. transition. The first vibrational transition of this feature is identified as the 0-0 transition, indicating an EA = 3.28 ± 0.03 eV. The weaker feature at higher-eBE, labeled E, is assigned to the excited singlet $A\ ^1\mathrm{A}'' \leftarrow X\ ^2\mathrm{A}''$ transition. The lone feature is assigned to the 0-0 transition with an EA = 3.614 ± 0.005 eV.

4. Discussion

4.1 Glyoxal

To aid in the detailed analysis of the photoelectron spectrum, the geometries of both the neutral and anion species of glyoxal were optimized at the CCSD/aug-cc-pVTZ level, for both the C_{2v} and C_{2h} symmetry isomers. The optimized geometric parameters are included in Figure 1 (in bold for the anion and in italics for the neutral). The calculated EAs and VDEs of the respective neutral and anion species are summarized in Table 1. The position of the 0 peak in the experimental spectrum (Figure 2) matches well with the C_{2v} EA value, but the experimental VDE is a better match for the corresponding C_{2h} prediction. Clearly, additional analysis is required for a consistent interpretation of the data.

For both the anion and the neutral, the C_{2h} structures are more stable than their C_{2v} counterparts. Indeed, the previous studies established that the most stable structure of

Table 1. The EA and VDE values calculated with the CCSD/aug-cc-pVTZ methodology for glyoxal (anion), compared to the experimental determinations. The calculated values include the zero-point vibrational energy corrections determined at the same level of theory, but with the smaller aug-cc-pVDZ basis set.

Isomer	Transition	EA / eV	VDE / eV
C_{2h}	$X\,^1A_g \leftarrow X\,^2A_u$	0.901	1.256
C_{2v}	$X\,^1A_1 \leftarrow X\,^2B_1$	1.089	1.450
Experiment		1.10 ± 0.01	1.30 ± 0.02

neutral glyoxal corresponds to the C_{2h} isomer (Figure 1, left), with a C_{2h} to C_{2v} internal rotation (isomerization) barrier of 2077 cm^{-1}.[173] This barrier height is compared to the 1688 cm^{-1} energy difference between the two isomers, determined by dispersed fluorescence spectroscopy.[173] The electronic structure calculations described above indicate that the additional electron in the anion occupies an a_u molecular orbital, which has a bonding π character with respect to the C–C bond. As a consequence, there is noticeable shortening of the C–C bond from neutral glyoxal to the anion (see Figure 1). Given the additional π bonding character, we infer that the internal-rotation barrier in the anion must be higher than that in the neutral and hence the dominant isomer of the anions generated by electron attachment to C_{2h} glyoxal molecules should follow the same structural motif.

The photoelectron spectrum expected in the photodetachment of the C_{2h} anion was simulated using the PESCAL program.[55,181] The energy of the 0-0 photodetachment transition was set to 1.10 eV, matching peak 0 in Figure 2 and the starting *ab initio* anion

geometry shown in Figure 1 (left) was adjusted to match the experimental spectrum (band A). The adjustment was done by treating the displacements along the neutral normal modes as adjustable parameters in order to match the final FC simulation to the experimental spectrum. In the process, the calculated FC intensities were multiplied by an $eKE^{3/2}$ pre-factor, accounting for the Wigner-like[182] scaling of the electronic part of the photodetachment cross-section.[111] The scaled FC stick spectrum is included in Figure 2, while the adjusted geometric parameters of the anion are included in Figure 1 (left) in plain font for direct comparison to the *ab initio* predictions in bold.

The stick spectrum was convoluted with an instrumental resolution function. The convolution was carried out in the speed domain and the resolution function was taken to be a Gaussian of a FWHM = 2×10^4 m/s, as determined from O^- photodetachment under similar experimental conditions. The convoluted spectrum was then transformed into the eBE domain using the appropriate Jacobian. The result is shown in Figure 2 in purple, overlaid with the experimental spectrum.

The agreement between the FC simulation and the experimental spectrum leaves little doubt about the robustness of the adjusted geometric parameters of the glyoxal anion included in Figure 1. A similar simulation was attempted for the C_{2v} anion isomer, but it failed to reproduce the observed spectral features, providing additional confirmation that the data in Figure 2 (band A) do indeed correspond to the C_{2h} isomer of the anion.

The minor feature, band B appearing as a broad low-eBE tail in the spectrum, cannot be accounted for by one-photon detachment of the glyoxal anion. Possible explanations for it are, therefore: hot bands, a two-photon process, or a coincident mass-

to-charge species. The feature extending > 0.5 eV below the adiabatic EA is unlikely to be a hot band of the same species. A two-photon process is possible, but the signal intensity was insufficient to determine band A's scaling with laser power.

In the absence of conclusive proof, we are nonetheless fairly certain that band A corresponds to a coincident species with the same mass-to-charge ratio as the glyoxal anion, *m/z* = 58. The most likely candidate is the solvated anion of methylene, $CH_2^-{\cdot}N_2O$. In preparation of the glyoxal sample, the dehydrated glyoxal solution was extracted from the sieve mixture using methanol, as described in Section 2. The methylene anion could be produced in our ion source from the residual methanol present in the sample. Supporting this hypothesis, an *m/z* = 31 species, corresponding to the methoxide anion, was also observed in low abundance in the primary ion mass-spectrum. The electron affinity of CH_2 is 0.652 eV,[124] while the solvation energy by N_2O is expected to be ~0.2 eV, making the $CH_2^-{\cdot}N_2O$ cluster anion, whose mass is nominally coincident with that of glyoxal, a viable candidate for the origin of the weak B band observed in Figure 2.

4.2 Methylglyoxal

The anion and neutral structures (singlet and triplet) of methylglyoxal were optimized at the CCSD/aug-cc-pVTZ level of theory and basis; the results are shown in Figure 4. While overall the structures are similar, the ground state singlet has a staggered conformation of the methyl group and the aldehyde functionality. Conversely, both the anion and triplet have eclipsed geometry with respect to the methyl group. This is

consistent with LIF results that show the triplet transition has a characteristic vibrational progression, indicating a 60° rotation of the methyl group,[168,169] and the triplet and anion having the same nominal orbital occupation of ……a'^1a''. Qualitatively, we expect a broader transition in the spectra to the singlet ground-state, and a sharper transition for the excited triplet. This is completely consistent with the experimental spectrum taken at 306 nm; band C is a wide and vibrationally-unresolved transition while band D (justified below) has an intense 0-0 transition indicating limited structural changes upon detachment.

The EA of the ground state singlet of methylglyoxal is calculated at 0.710 eV, which is in fairly good agreement with the approximate onset of the singlet transition, C, observed at 612 nm. The change in structure, the rotation of the methyl-group, is in good agreement with the observed broad transition.

The separation between the calculated EA and VDE, 0.486 eV, is an excellent match the observed value of ~0.5 eV, giving confidence to the experimental determination of the EA of the singlet. While the comparison between the calculated and theoretical values for the triplet transition leaves much room for improvement, the excited singlet state being so close in energy (justified below) could easily interfere in the single-reference calculation and offers an explanation for the poor result.

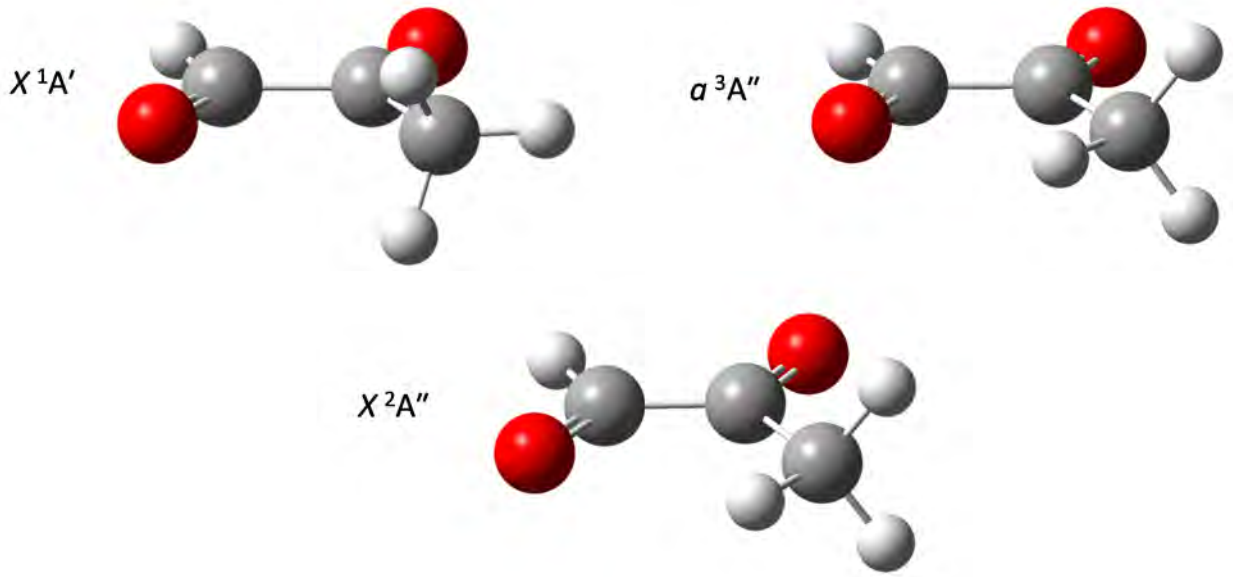

Figure 4. The geometry optimization results for methylglyoxal anion, singlet, and triplet states at the CCSD/aug-cc-pVTZ level, illustrating the rotation of the methyl-group.

Table 2. The EA and VDE values calculated with the CCSD/aug-cc-pVTZ methodology for methylglyoxal (anion), compared to the experimental determinations. The calculated values include the zero-point vibrational energy corrections determined at the B3LYP/aug-cc-pVDZ level of theory and basis set.

Transition	Calc. EA / eV	Exp. EA / eV	Calc. VDE / eV	Exp. VDE / eV
$X\ ^1\mathrm{A}' \leftarrow X\ ^2\mathrm{A}''$	0.710	~0.8	1.196	1.28(4)
$a\ ^3\mathrm{A}'' \leftarrow X\ ^2\mathrm{A}''$	3.220	3.28(3)	3.412	-
$A\ ^1\mathrm{A}'' \leftarrow X\ ^2\mathrm{A}''$	-	3.614(5)	-	-

To facilitate a complete assignment of the higher-eBE features, a Franck-Condon simulation was performed for the triplet $a\ ^3\mathrm{A}'' \leftarrow X\ ^2\mathrm{A}''$ transition. The technique used was identical to that of glyoxal, though no further fitting of the simulation parameters was performed or required. The results are shown in Figure 5. The simulation clearly accounts for two major features visible in the spectrum, and indicates the first peak is the 0-0 transition of the $a\ ^3\mathrm{A}'' \leftarrow X\ ^2\mathrm{A}''$ transition.

The identification of band E as the 0-0 $A\ ^1\mathrm{A}'' \leftarrow X\ ^2\mathrm{A}''$ transition is now justified. Firstly, the simulation of the triplet transition does not account for this feature. Secondly, the nominal orbital occupation of the anion, triplet, and excited singlet is the same, …$\mathrm{a}'^1\mathrm{a}''^1$, which suggests that the geometry of both the triplet and excited singlet is like that of the anion, with the methyl-group in the eclipsed conformation. The geometry optimization results of the triplet at the CCSD/aug-cc-pVTZ level, as well as the Franck-

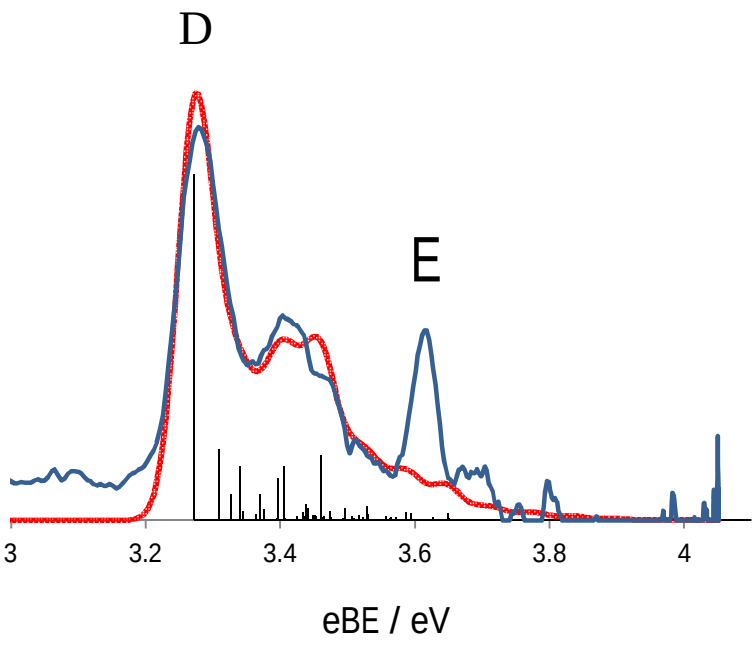

Figure 5. The blue spectrum is a magnified region of the 306 nm spectrum of methylglyoxal radical anion shown in Figure 3(B). The results of the Franck-Condon simulation for the triplet transitions are shown in black as discrete transitions, while the red spectrum is the simulation convoluted with a Gaussian function representing instrument resolution. See text for details.

Condon simulation, are in agreement with this assessment for the triplet. Finally, the position of this feature is in good agreement with the previously determined energy gap between the ground and excited singlet state. The excitation energy was reported as 2.743,[168] with the experimentally-determined separation as 2.8 eV.

5. Summary

Using photoelectron imaging spectroscopy, we have measured the photoelectron spectrum of the glyoxal anion and obtained the first direct spectroscopic determination of the adiabatic electron affinity of glyoxal, EA = 1.10(2) eV. The vertical detachment energy of the glyoxal radical anion is determined as VDE = 1.30(4) eV. Franck-Condon simulations indicate several vibrational modes activated upon electron photodetachment and successfully reproduce the observed spectral features.

The first 3 low-lying states of methylglyoxal were observed with photoelectron imaging spectroscopy. The EA of methylglyoxal is determined as ≤ 0.8 eV; this is based on the eBE at which the signal-to-noise ratio of the $X\ ^1\mathrm{A}' \leftarrow X\ ^2\mathrm{A}''$ transition rises above 3. Despite the relatively crude method that was used to predict the difference in EA between glyoxal and methylglyoxal,[164] the predicted 0.2 eV value is in surprisingly good agreement with the experimental results. The ground-state transition was observed with a VDE = 1.28(4) eV, the large offset from the EA reflecting the internal rotation of the methyl-group. The EA of the $a\ ^3\mathrm{A}'' \leftarrow \mathrm{X}\ ^2\mathrm{A}''$ was confirmed by Franck-Condon analysis to be 3.28(3) eV. The first excited singlet state transition, $A\ ^1\mathrm{A}'' \leftarrow X\ ^2\mathrm{A}''$, was observed to have similar qualities to that of the triplet transition. This indicates that the excited singlet also has an eclipsed conformation of the methyl-group, like the anion and triplet. The EA of the $A\ ^1\mathrm{A}''$ is determined as EA = 3.614(5) eV.

Chapter 9: Spectroscopy of Ethylenedione (OCCO)

Overview

The long sought-after, intrinsically short-lived ethylenedione molecule (OCCO) was definitively observed and investigated using anion photoelectron spectroscopy. The adiabatic electron affinity of its $^3\Sigma_g^-$ ground state is 1.936(8) eV. The vibrational progression with a 417(15) cm^{-1} frequency observed within the triplet band corresponds to a trans-bending mode. Several dissociative singlet states are also observed, corresponding to two components of the $^1\Delta_g$ state and the $^1\Sigma_g^+$ state. The experimental results are in agreement with the theory predictions and constitute the first spectroscopic observation and characterization of the elusive ethylenedione molecule.

1. Introduction

We report a spectroscopic characterization of ethylenedione (OCCO). This report follows a century-long history of controversy and failed attempts to observe this deceptively simple molecule.[183] Its history dates back to 1913, when the reaction of oxalyl bromide with mercury to form CO was postulated to include an "OC:CO" intermediate.[184] In the 1940s, "O=C=C=O" was claimed to be the active formula of glyoxylide, a wonder-drug purported to be an antidote for a long list of afflictions, but classified as fraud by the U.S. Food and Drug Administration.[185]

For decades, OCCO continued to be pursued as a synthetic target,[186-189] but all past experimental studies[183,186,189-191] failed to provide conclusive evidence of the existence of this "exceedingly coy molecule".[183] To this day, OCCO has not been observed, not only as a substance, but even as a transient species. Its mysteriously elusive nature conflicts with the convincing theoretical evidence of a stable covalent OCCO minimum on the C_2O_2 potential energy surface.[189,192,193] To deepen the controversy, its sulfur analogs OCCS and SCCS, and even the selenium analog SeCCSe have both been observed and studied experimentally,[194-196] but not OCCO.

Despite the straightforward closed-shell Kekulé structure (O=C=C=O), the ground state of OCCO is a linear-geometry triplet with the unpaired electrons occupying two degenerate π orbitals.[183,192,193,197] This motif puts OCCO in the same class as O_2. Although the triplet is bound, it is theorized to undergo a crossing to the nearby singlet, which in turn dissociates rapidly to two CO molecules.[189,192,198] This process is exothermic by several electron-volts,[192,193] hence the unstable nature of the molecule. However, the triplet-singlet crossing is predicted to occur on a nanosecond timescale,[189]

making triplet OCCO a spectroscopically long-lived species with no good reason to evade detection.

It is against this backdrop that we report the first direct spectroscopic observation and characterization of OCCO. Forgoing the neutral-based strategies, we accessed its low-lying states via the photodetachment of the stable anion, $OCCO^-$ [199,200] where the neutral states ethylenedione can be accessed with less regard of their lifetime. The photoelectron spectra are in excellent agreement with the theory predictions, leaving no doubt that the observed states belong to OCCO. Although the equilibrium structure of the anion corresponds to a trans-bent C_{2h} geometry,[199,200] the relaxed vibrational state of linear ethylenedione is accessed in the experiment.

2. Experimental

The photoelectron velocity-map imaging spectrometer used for this work has been described in detail in Chapter 2 of this dissertation. The refrigerated glyoxal precursor (40% wt/wt, aq) was dried over 3 Å molecular sieves (~1:1 volume of sieves to glyoxal solution) for 24 hours and then decanted. This process not only reduces water, but may also reduce the formation of glyoxal oligomers present in the commercial solution. The dried solution was placed in a sample holder connected to the carrier gas line and mildly heated (~50 °C) to increase vapor pressure. The mixture was introduced to the instrument by a pulsed supersonic nozzle (General Valve 9), crossed perpendicularly with a continuous ~1 kV electron beam. The reaction of glyoxal with O^- was performed in the electron-impact ionized supersonic expansion of the precursor vapor seeded in N_2O. The mass-56 anions were photodetached using the second (532 nm) or third (355 nm) harmonics of a SpectraPhysics LAB-130-50 Nd:yittrium aluminum garnet laser.

Photoejected electrons were projected by a series of velocity-map imaging[15] electrodes onto a position-sensitive dual-microchannel plate detector coupled to a P43 phosphor screen and the resulting images were recorded by a charge-coupled device (CCD) camera. Typical raw images were collected over ~10^6 experimental cycles. The complete three-dimensional photoelectron distribution was reconstructed[17] using the inverse Abel transformation, implemented in the BASEX program.[51] The energy scale was calibrated using the well-known[52,53] photodetachment transition of O^-.

Electronic structure calculations with geometry optimization at the CCSD level of theory were carried out with the Gaussian 09 software package.[54] After optimizing the geometries for the anion and neutral ground and excited states, the normal-mode analysis was used to confirm that the optimized structures corresponded to true potential minima. Equation-of-motion (EOM) ionization potential (IP) and spin-flip (SF)[25,113-115] calculations included diagonal triples (dT)[116] corrections for CCSD energy and were performed for the optimized geometries using the Q-Chem 4.0 software package.[26]

Optimized geometries and frequencies at CCSD/aug-cc-pVTZ level were also used with the FCFGaus09a program to create input for the PESCAL Franck-Condon simulation program.[55] To simplify the treatment of the non-linear to linear geometry relaxation of the anion minimum to that of the neutral, the CCSD/aug-cc-pVTZ normal modes were calculated for neutral OCCO with a distorted structure. In this case, the oxygen atoms were moved so that the ∠CCO angle was equal to 179.6° to create a C_{2h} symmetry. This prevents the loss of a normal mode, and produces normal modes which agree well with the minimized linear structure, sans the 6th mode generated by reducing the symmetry. Along with the optimized anion geometry and frequencies, these results

were used to simulate a photoelectron velocity stick spectrum, calculated assuming independent, uncoupled harmonic oscillators with full Duschinsky rotation, in the Sharp-Rosenstock-Chen method. The 0-0 transition was set to the center of the first peak as determined by a global fit of the S_1-subtracted spectrum (see discussion), and the stick spectrum was convoluted with Gaussian functions of a FWHM of 20,000 m/s, an approximate width determined by the photodetachment transition of O^- taken under similar experimental conditions.

3. Results

3.1 The Photoelectron Imaging of $OCCO^-$

The 532 nm spectrum of $OCCO^-$ is presented in Figure 1A. It consists of a vibrational progression (T_0), riding on top of a broad pedestal (S_1). The spectral structure suggests the involvement of two types of neutral states: a long-lived state that gives rise to the progression and another responsible for the pedestal. The latter may be dissociative or involve a large geometry change relative to the anion. Another indication of two electronic transitions is based on the photoelectron anisotropy parameter (β).[118] The values for the T_0 peaks are shown in Figure 1A as open circles, while the average for the S_1 tail is displayed as a filled circle. The discontinuity in the trend between the filled and open symbols, observed despite the cross-contamination between the bands, suggests that they correspond to different transitions.

Based on these qualitative observations, we assign the vibrational progression in Figure 1A to the bound triplet state of OCCO, while the broad pedestal is assigned to a

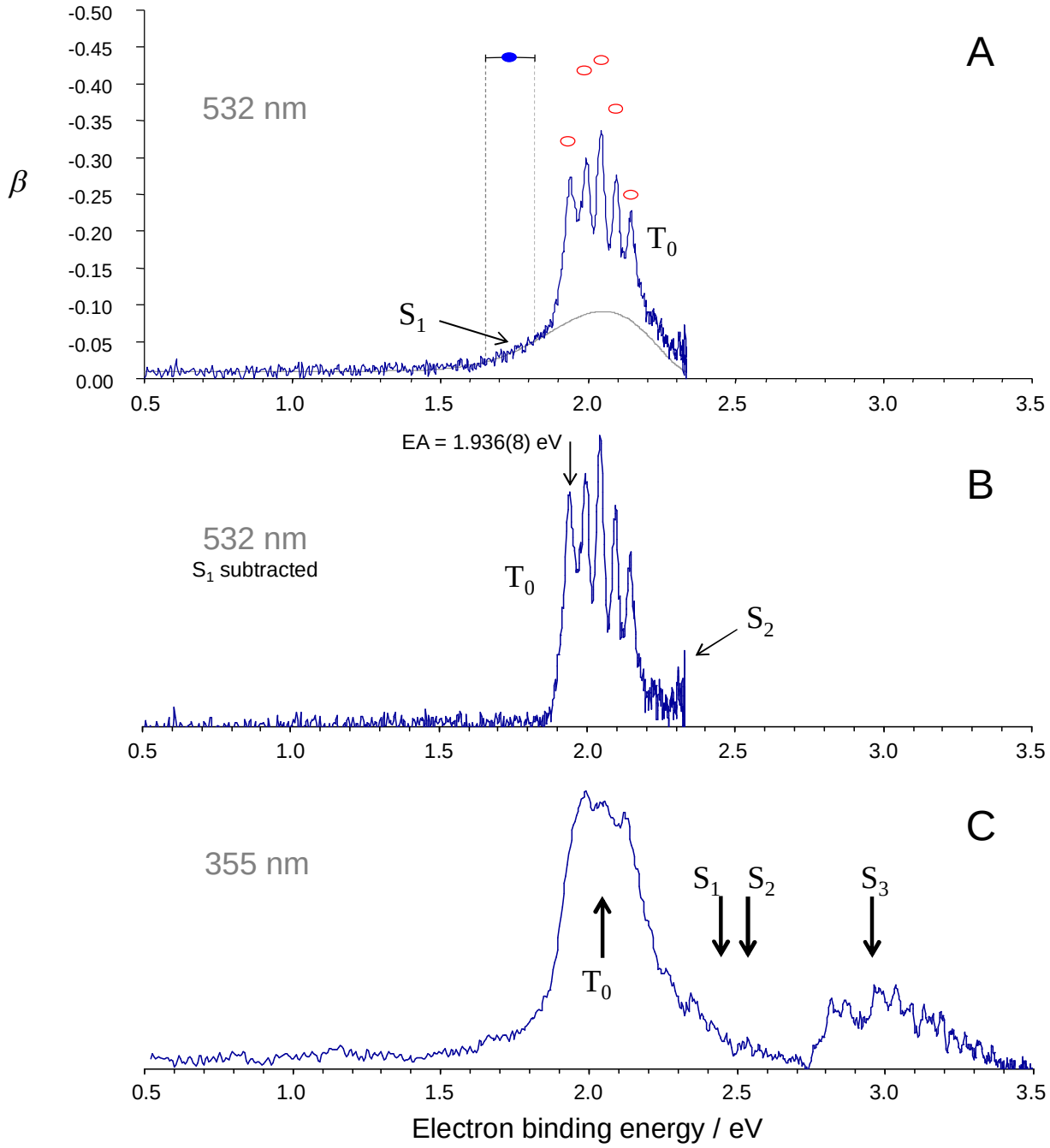

Figure 1. Figure 1A shows the photoelectron binding energy spectrum of $OCCO^-$ at 532 nm. The closed and open circles indicate the measured anisotropy parameter, β, for the indicated features. Figure 1B shows the S_1-subtracted 532 nm spectrum, and Figure 1C shows the spectrum of $OCCO^-$ taken at 355 nm.

dissociative singlet. The quantitative analysis that follows supports these assignments. The adiabatic electron affinity (EA) of triplet ethylenedione is determined based on the first T_0 peak: EA = 1.936(8) eV. The observed T_0 progression is consistent with the geometry difference between the anion and the linear OCCO triplet. The average spacing of 417(15) cm^{-1} is close to the 396 cm^{-1} frequency predicted for the trans-bending mode of the $^3\Sigma_g^-$ state of OCCO by the MCSCF/cc-pVTZ calculations.[192] The S_1 pedestal extends lower in energy than the triplet EA value, because of the dissociative nature of the singlet. The adiabatic minimum of the singlet surface corresponds to the CO($^1\Sigma^+$) + CO($^1\Sigma^+$) limit, which lies some 2.55 eV below the triplet OCCO equilibrium.[200] The dissociation limit has no measurable Franck-Condon overlap with the $OCCO^-$ anion, but the spectral tail in Figure 1A reflects the downhill structure of the singlet surface.

3.2 Theoretical Investigation of the Photodetachment

The OCCO neutral and its anion have been the subjects of many theoretical studies.[189,192,193,200] The configurations of the relevant states involve two nearly-degenerate orbitals, $6b_u$ and $2a_u$ (at the C_{2h} geometry of the anion), shown schematically in Figure 2A. At linearity, these orbitals turn into the degenerate $2\pi_u$ orbitals and their population by two electrons gives rise to the $^3\Sigma_g^-$, $^1\Delta_g$, and $^1\Sigma_g^+$ states of OCCO, as indicated in Figure 2B (right). The energy gaps shown for the neutral OCCO are from the MRCI/cc-pVTZ//B3LYP/6-311+G(2df) calculations by Talbi and Chandler.[192] While the singlets dissociate to CO($^1\Sigma^+$) + CO($^1\Sigma^+$) this channel cannot be accessed on the triplet surface. All other dissociation channels lie significantly higher in energy.

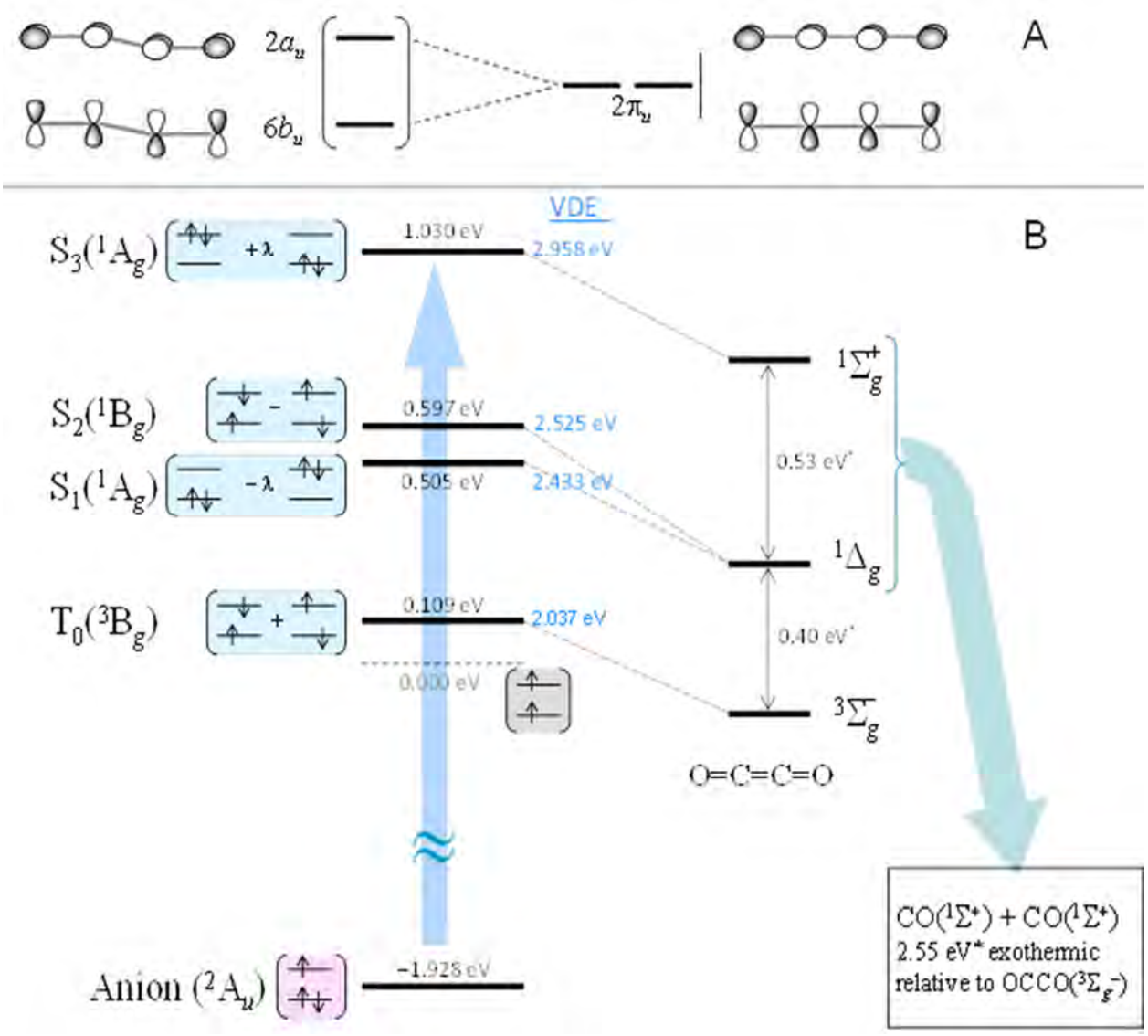

Figure 2. Figure 2A shows the transformation of the $2a_u$ and $6b_u$ molecular orbitals of the anion into the doubly-degenerate $2\pi_u$ orbitals of the linear neutral triplet. Figure 2B shows the combined EOM-IP and EOM-SF results for photodetachment from the anion, while the right shows the calculated energy gaps for the linear neutral triplet by Talbi and Chandler.[192]

To complement the experimental results, we carried out calculations specifically targeting $OCCO^-$ photodetachment. To meet the needs of these calculations, the anion geometry was optimized[54] at the CCSD level with the aug-cc-pVTZ basis set. The results are shown in Figure 3B and the geometric parameters calculated *ab initio* are shown in normal text. In accord with the past studies,[200] the optimization yielded an $OCCO^-$ structure of C_{2h} symmetry, with CO and CC bond lengths of 1.240 and 1.281 Å, respectively, and a CCO angle of 161.2°. This geometry was used for the calculations employing the EOM-IP and EOM-SF methods,[25] combined with the coupled cluster theory, using Q-Chem 4.0.[26] This methodology was used to describe the multi-configurational nature of the OCCO diradical states.

First, the vertical detachment transitions at the anion geometry were explored with the EOM-IP-CCSD method. The neutral states were accessed from the ^2A_u: $\ldots(6b_u)^2(1a_u)^1$ reference. In particular, removal of the beta-spin $6b_u$ electron results in the high-spin (M_S = 1) ^3B_g: $\ldots(6b_u)^1(1a_u)^1$ triplet configuration, indicated in Figure 2B. The corresponding excitation energy of 1.928 eV will be used in what follows as the estimated gap between the anion and the high-spin triplet reference.

Second, the EOM-SF-CCSD calculations were performed for the same anion geometry, using the high-spin triplet configuration as a reference. Combinations of one-electron SF excitations yielded the low-spin (M_S = 0) component of the $T_0(^3B_g)$ state and three singlet states (S_1, S_2, and S_3). The $T_0(^3B_g)$ state energy in Figure 2B corresponds to the low-spin (M_S = 0) component, as recommended by Krylov.[119] Included in the figure are the state labels, dominant configurations, and energies relative to the triplet reference (all at the anion geometry).

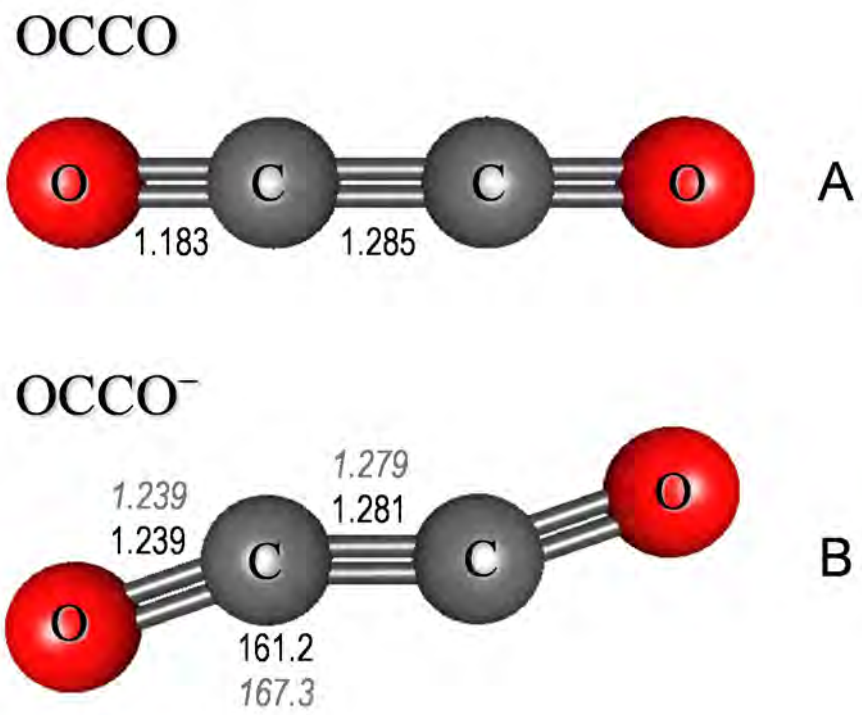

Figure 3. Optimized parameters of OCCO neutral and anion structures. Results from CCSD/aug-cc-pVTZ calculations are shown in normal text; italicized text indicates the optimized parameters of the anion from the Franck-Condon simulation implemented in the PESCAL 2010 software.

Combining the IP energy for the anion with the SF energies of the neutral, the VDEs for the formation of different OCCO states were determined. The results are indicated in blue-color font in Figure 2B. The predicted VDE = 2.037 eV for the T_0 transition is in excellent agreement with the most intense peak in Figure 1A. The first singlet state $S_1(^1A_g)$ corresponds to a theoretical VDE = 2.433 eV, which is slightly above the 532 nm photon energy used to collect the data in Figure 1A. This state dissociates to $CO(^1\Sigma^+)$ + $CO(^1\Sigma^+)$, as discussed above. Thus, although it lies above T_0 at the anion geometry, its adiabatic minimum is much lower in energy than the T_0 equilibrium. The down-slope shape of the potential manifests as the low-energy tail of the S_1 pedestal in Figure 1A that extends below the T_0 EA. In addition to the T_0 band, the S_1-subtracted spectrum in Figure 1B (see Section 4) shows additional signal marked S_2 near the photon-energy cut-off. Although this assignment is not definitive, we attribute this extra signal, possibly including a hint of another vibrational progression, to the $S_2(^1B_g)$ state, predicted slightly above S_1, at an anion VDE of 2.525 eV (see Figure 2B).

Finally, Figure 1C shows the spectrum collected at 355 nm. Despite its lower resolution, the T_0 peak does show the low- and high-energy shoulders attributed to the singlet states S_1 and S_2. The spectrum shows an additional band, whose position is in agreement with the VDE predicted for the ^1A_g state (S_3). The vertical arrows in Figure 1C indicate the VDEs corresponding to all four neutral states, taken from the results in Figure 2B. The 355 nm spectrum is completely consistent with the predicted OCCO properties, just like the 532 nm spectrum.

4. Modelling of the $OCCO^-$ Detachment Profile

The final simulation result is shown in Figure 4A, where the simulated spectrum

(black) is overlaid with the 532 nm experimental spectrum reproduced from Figure 1A. The simulated spectrum is a sum of the triplet (T_0) vibrational progression and the lowest dissociative-singlet (S_1) bands. The separated T_0 and S_1 components of the simulation are shown in Figure 4B.

The calculated VDE from the combined results of the EOM-IP/SF calculations allows us to model the S_1 band, as shown by the grey curve in Figure 1A. The simulation assumes a Gaussian envelope centered at the VDE = 2.433 eV. To account for the photon-energy cut-off and the eKE dependence of the cross-section, the envelope is scaled with a Wigner-like[182] pre-factor assuming an (intermediate) 3/2 effective exponent.[111] Subtracting the model curve from the experimental data, yields the spectrum in Figure 1B, clearly showing the T_0 vibrational progression with the origin at EA = 1.936(8) eV and the most intense peak at VDE = 2.04(2) eV.

The T_0 band was modeled as follows. The fundamental harmonic vibrational frequencies of the triplet neutral and the anion were calculated at the CCSD level with the aug-cc-pVTZ basis set, the results of which are shown in Figure 3, with *ab initio* parameters in normal text. To avoid issues with the differing numbers of vibrational degrees of freedom of the linear neutral and trans-bent anion, the neutral structure was perturbed from its equilibrium geometry by setting ∠CCO to 179.6°, thus reducing its symmetry from $D_{\infty h}$ to C_{2h}. The Franck-Condon (FC) factors were calculated using the PESCAL program,[55] assuming independent uncoupled harmonic oscillators with full Duschinsky rotation using the Chen method.[181] The origin (0-0) transition was set to

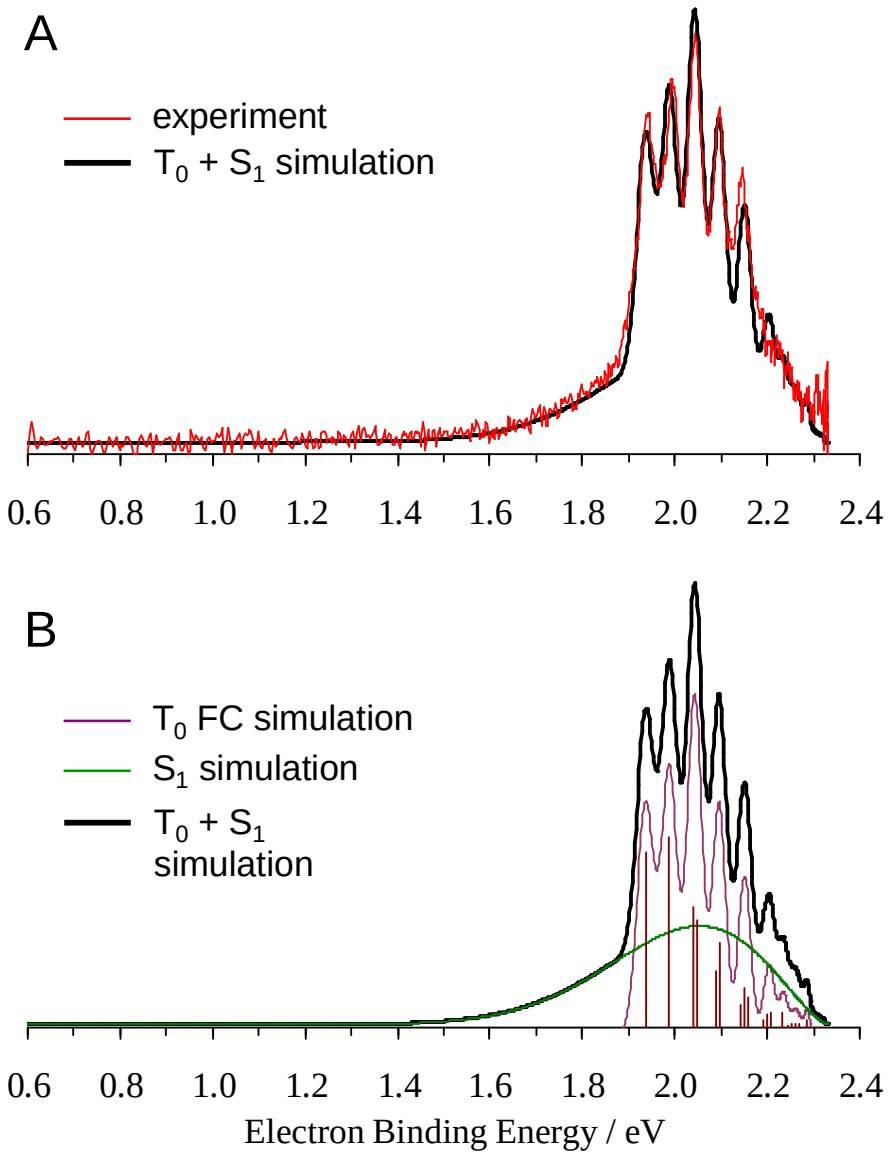

Figure 4. In 4A, the result of the 532 nm photodetachment of $OCCO^-$ is shown in red, with the sum of the simulations (see text for details) is shown in black. Fig. 4B shows the results of the simulated component spectra and their sum. The vertical bars correspond to the simulated Franck-Condon transitions, while the purple spectrum corresponds to the simulated transitions convoluted with the approximate instrument resolution and a Wigner-like prefactor. The green spectrum is the simulated S_1 spectrum with the same prefactor. See text for full details

coincide with the maximum of the first vibrational peak of the observed triplet band using the S_1-subtracted spectrum shown in Figure 1B and the starting *ab initio* anion geometry was adjusted to match the experimental spectrum. This adjustment occurs by fitting the displacements along the neutral normal mode coordinates to match the experimental spectral profile, which then correspond to the adjusted initial geometry of the anion. The calculated FC intensities were multiplied by an $eKE^{3/2}$ pre-factor, accounting for the expected Wigner-like[182] scaling of the electronic part of the photodetachment cross-section and identical to the modeling of the S_1 band. The final scaled FC stick spectrum is included in Figure 4B and the adjusted geometric parameters of the anion are included in Figure 3B in *italics* for direct comparison to the *ab initio* predictions.

The stick spectrum was convoluted with an instrumental resolution function. The convolution was carried out in the scalar velocity (speed) domain, which corresponds directly to the radial distributions derived from the Abel-inverted photoelectron images. The resolution function was taken to be a Gaussian of a FWHM = 2×10^4 m/s, as determined from O^- photodetachment under similar experimental conditions. The resulting speed-spectrum was transformed into the eBE domain using the appropriate Jacobian. The result is shown in Figure 4(b) in purple. Figure 4(a) compares the simulation to the experimental photoelectron spectrum of $OCCO^-$ and we conclude that the analysis presented here is completely consistent with the experimental results.

5. Summary

We conclude that the photoelectron spectra presented in this work reflect the low-lying electronic states of the elusive OCCO molecule. The electron affinity of the quasi-bound $^3\Sigma_g^-$ state of OCCO is 1.936(8) eV, while the vertical detachment energy of the

$OCCO^-$ anion is 2.04(2) eV. In addition, two singlet states were directly observed, with a plausible assignment of a third. The photoelectron spectrum of OCCO has been further examined by the simulation of the spectral profile. The S_1 is shown to be well-represented by a smooth Gaussian-like profile combined with a Wigner-like prefactor. The vibrationally-resolved T_0 band is simulated under the Franck-Condon approximation and the same prefactor. The simulated profile matches the observed 532 nm spectrum excellently, giving no doubt that it can be assigned to the photodetachment of $OCCO^-$.

These results pave the way for time-resolved studies of transient OCCO by means of anion-neutral-cation charge-reversal spectroscopy.[201] The photodetachment of $OCCO^-$, as described in this work, launches the dynamics on the neutral surfaces, with a predicted ~0.5 ns lifetime for the triplet.[189] These dynamics and the appearance of the $CO(^1\Sigma^+)$ products, can be probed by delayed photoionization.

Chapter 10: HOCCO versus OCCO - Comparative Spectroscopy of the Radical and Diradical Reactive Intermediates

Overview

Two glyoxal derivatives related to the ethylenedione anion ($OCCO^-$), ethynediolide ($HOCCO^-$) and glyoxalide ($OHCCO^-$), were studied. These anions provide access to the corresponding neutral reactive intermediates: the HOCCO and OHCCO radicals. Contrasting the straightforward deprotonation pathway expected to yield glyoxalide ($OHCCO^-$) in the reaction of O^- with glyoxal (OHCCHO), $OHCCO^-$ is shown to be a minor product, with $HOCCO^-$ being the dominant observed isomer of m/z = 57 anion. In the HOCCO/OHCCO anion photoelectron spectrum, we identify several electronic states of this radical system and determine the adiabatic electron affinity of HOCCO as 1.763(6) eV. This result is compared to the corresponding 1.936(8) eV value for ethylenedione (OCCO), reported in our recent study of this transient diradical [A. R. Dixon, T. Xue, and A. Sanov, Angew. Chem. Int. Ed. **54**, 8764-8767 (2015)]. Based on the comparison of the $HOCCO^-$/$OHCCO^-$ and $OCCO^-$ photoelectron spectra, we discuss the contrasting effects of the hydrogen connected to the carbon framework or the terminal oxygen in OCCO.

1. Introduction

Anion photodetachment provides access to the ground and excited states of neutral molecules without regard for their transient or stable nature. Moreover, states of different multiplicities can be probed at the same time, provided the photon energy used is sufficient and there is sizable Franck-Condon overlap between the anion equilibrium and the neutral states of interest.

This feature of anion photoelectron spectroscopy has been used to study a variety of exotic neutral species, including transient molecules, reactive intermediates, and even transition states, all of which are challenging to access using other methods.[23,202-205] Here, we present a comparative analysis of three previously unstudied glyoxal derivatives, the OHCCO radical, the HOCCO radical and OCCO diradical. The spectroscopy of HOCCO is reported for the first time, while the discussion of OCCO builds upon our recent brief report[161] of the discovery of this molecule.

The spectroscopic characterization of the ethylenedione molecule, OCCO, was accomplished recently[161] against the backdrop of a century-long history of failed attempts to detect this species. Despites its apparent (yet deceptive) simplicity, manifested in the straightforward O=C=C=O Kekulé structure, ethylenedione is a short-lived reactive intermediate.[183,189] Its existence was first proposed in 1913,[184] but all previous experimental strategies tried ever since had failed to produce conclusive evidence that OCCO really existed.[183,186-191] The molecule was at long last found in 2015,[161] via the photodetachment of its stable[199,200] anion. The results shed light on the manifold of low-lying electronic states of OCCO,[161] confirming the past predictions of its electronic structure.

In short, the ground (bound) state of OCCO is a triplet with linear geometry, with two unpaired electrons occupying two degenerate π orbitals.[161,183,192,193,197,206] This motif puts OCCO into the same diradical class as O_2, but there are significant differences. Promoted by the bending motion which distorts OCCO from its linear equilibrium geometry, the triplet undergoes an intersystem crossing (ISC) to a nearby singlet, which promptly dissociates to two CO fragments.[189,192,198] Although the CO + CO asymptote lies > 2 eV lower than the triplet OCCO minimum,[192,193] the enabling ISC takes about half a nanosecond to occur,[189] giving OCCO a spectroscopically long lifetime. In this work, we continue the analysis of the OCCO anion photoelectron spectrum, present its detailed Franck-Condon analysis, which reinforces our initial findings and conclusions,[161] and put it in the context with the spectroscopy of a related radical species, HOCCO.

The photoelectron spectrum of $HOCCO^-$ emerged quite unexpectedly from the experiment intended to target $OHCCO^-$ (glyoxalide). The ions were generated using a variation of the same O^- chemistry that leads to the formation of $OCCO^-$,[101,102] only instead of H_2^+ abstraction it involves a single deprotonation of the glyoxal precursor. For clarity and for historical reasons, we note that *glyoxalide* ($OHCCO^-$) should not be confused with g*lyoxylide*. The former is the deprotonated-glyoxal ion (glyoxal-ide), while glyoxylide is the name given to an infamous homeopathic wonder-drug from the 1940s, long ago classified as fraud by the U.S. Food and Drug Administration.[185] Ironically, the active ingredient of glyoxylide was claimed to be "O=C=C=O",[185] i.e. ethylenedione, a molecule whose transient nature is now well-established.[189] Although both OCCO (the molecule) and glyoxalide (the $OHCCO^-$ ion) are investigated here, glyoxylide (the drug) has no connection to the present work.

Although single deprotonation of glyoxal was expected to yield glyoxalide, the observed product proved to be a mixture of $OHCCO^-$ and $HOCCO^-$, with glyoxalide being the minor species. The dominant isomer, $HOCCO^-$ (ethynediolide), is the conjugate base of ethynediol (acetylenediol), which is a popular addition to anionic surfactant mixtures.[167] Ethynediol has been detected directly by infrared spectroscopy,[207] and its cation has been observed by mass-spectrometry.[208,209] Similar works exist on the singularly-substituted ethynol (hydroxyacetylene),[210,211] but $HOCCO^-$ and the corresponding neutral radical, have not been studied previously. In our experiment, $HOCCO^-$ could, in principle, be formed as a product of glyoxalide rearrangement, $OHCCO^- \rightarrow HOCCO^-$, but the analysis shows that this is unlikely to be the case. Instead, we propose an alternative mechanism for $HOCCO^-$ formation in the O^- reaction with glyoxal.

The presence of the two anion isomers, $OHCCO^-$ and $HOCCO^-$, creates an opportunity to study the corresponding radical species, HOCCO and OHCCO, by themselves, in comparison to each other, and in comparison to OCCO. The comparison to OCCO, in particular, allows us to draw conclusions about the relative degrees of the distortion of the ethylenedione framework due to the addition of an extra hydrogen atom bound to a carbon or an oxygen.

The analysis of the experimental results presented in this work relies of the electronic structure calculations for both the anions and the corresponding neutral radicals and diradicals. Such species are often described by dense manifolds of low-lying states with inherently multi-configurational electronic wavefunctions and present considerable challenges for calculations. We address these challenges using the equation-of-motion

(EOM) ionization-potential (IP) and spin-flip (SF) methods, in conjunction with the coupled-cluster theory (CCSD).[25,113,119,212,213]

2. Experimental and Theoretical Methods

The photoelectron imaging spectrometer and the experimental procedures used for this work have been described in detail elsewhere.[49,161] Briefly, commercial glyoxal solution (Acros Organics, Inc., 40 wt. % in water) was dehydrated for ~12 hours using a 1:1 volume ratio of 3 Å molecular sieves. The solution was then decanted and transferred to the sample holder of the instrument, where it was heated to ~50°C to increase the vapor pressure. The vapor was seeded in an N_2O carrier gas at ~25 psi. The resulting mixture was pulsed into the high-vacuum ion-source chamber using a General Valve, Inc. Series 99 supersonic valve, operating at 50 Hz to match the repetition rate of the laser system.

The supersonic expansion was crossed at a right angle with a continuous ~1 keV electron beam to create plasma. Dissociative electron attachment to N_2O produced O^- anions, which further reacted[101,102,214] with glyoxal to produce mass-to-charge 56 and 57 anions. Anions were extracted into the time-of-flight mass spectrometer using a repeller plate pulsed from 0 to –950 V, and further accelerated to ~3.5 kV total potential.[49] 532 or 355 nm laser pulses from a Spectra Physics, Inc. LAB-130-50 Nd:YAG laser were timed to interact with the desired mass-to-charge anion packets within the velocity-map[15] imaging[13] assembly.[49] Photoelectrons were projected upward by a series of velocity-mapping electrodes in the mutually perpendicular direction to the ion and laser beams. Photoelectrons were detected by a position-sensitive dual-MCP detector in a Chevron configuration, coupled to a P43 phosphor screen. The photoelectron images were

recorded using a thermoelectrically-cooled CCD (Photometrics, Inc., CoolSnap Myo). Raw images were collected typically for ~1×10^6 experimental cycles, and reconstructed using the inverse Abel transformation[17] implemented in BASEX.[51] Radial distributions were calibrated using the well-known electron affinity of atomic oxygen.[52,53]

Theoretical geometry optimizations and harmonic frequency calculations for the HOCCO and OHCCO neutral and anionic species were carried out at the CCSD/aug-cc-pVTZ level using the Gaussian 09 software package.[54] Normal mode analysis was performed on the fully optimized structures and further used for Franck-Condon simulations. These simulations were carried out using the PESCAL 2010 software, with the normal modes treated as independent uncoupled harmonic oscillators with full Duschinsky rotation using the Chen method.[55,181] EOM-XX-CCSD calculations, where XX = SF or IP, were performed using the Q-Chem 4.0 software package,[26] using geometries optimized at the CCSD/aug-cc-pVTZ level as described above.

3. Experimental Results

We begin with comparative spectroscopy of HOCCO and OCCO. Figure 1 presents the 532 and 355 nm photoelectron spectra of the *m/z* = 57 ($HOCCO^-$) and *m/z* = 56 ($OCCO^-$) anions. The spectra are plotted versus electron binding energy (eBE), defined as eBE = $h\nu$ – eKE, where eKE is electron kinetic energy. The $HOCCO^-$ spectra are new, obtained in this work, while the $OCCO^-$ results were reported recently in our initial report on the discovery of the ethylenedione molecule.[161] Despite some revealing similarities between the *m/z* = 57 and *m/z* = 56 spectra, their comparison confirms that they are indeed unique and correspond to distinct species. In support of this conclusion, there was no overlap between the *m/z* = 57 and *m/z* = 56 peaks in the parent-ion mass-spectrum.

The intensities of the respective mass-peaks were in an approximately 1:2 ratio, therefore there can be only a minor contribution of ^{13}C substituted $OCCO^-$ at *m/z* = 57 (2% of $OCCO^-$ intensity).

The bulk of *m/z* = 57 anions may include two distinct isomers: $OHCCO^-$ (deprotonated glyoxal) and the rearrangement product $HOCCO^-$ (conjugated base). The analysis in Section IV suggests that the observed spectra correspond predominantly to $HOCCO^-$, with only a minor contribution attributed to $OHCCO^-$. The corresponding band assignments are presented in Figure 2. For clarity, the $HOCCO^-$ spectra in Figure 2 are reproduced from Figure 1 without overlay with the $OCCO^-$ results. Also included in Figure 2 are the raw and Abel-inverted photoelectron images.

The 532 nm $HOCCO^-$ spectrum in Figure 2(a) includes two main features: a broad low-intensity band A, with an apparent onset at eBE ≈ 1 eV, and a significantly more intense band B that rises sharply at eBE ≈ 1.7 eV and includes a hint of a partially resolved vibrational progression. In Section IV.B we show that band A corresponds to the $OHCCO^-$ isomer, while the more intense band B, as well as C [in Figure 2(b)], to $HOCCO^-$. The first peak of band B (labeled 1) is observed at 1.763(6) eV, as indicated in Figure 1(a), compared to the first peak in the triplet OCCO progression, which is observed at 1.936(8) eV. Partially resolved peaks 1, 2, and 3 [Figure 2(a)] belong to the dominant vibrational progression with a fundamental frequency of 430(10) cm^{-1}. Additional lower-frequency modes are excited too, contributing to the satellite peaks to the right of peaks 1, 2, and 3.

Band B's vibrational structure is also discernable in the 355 nm spectrum [Figure2(b)], although the decreased absolute resolution (due to higher eKEs)

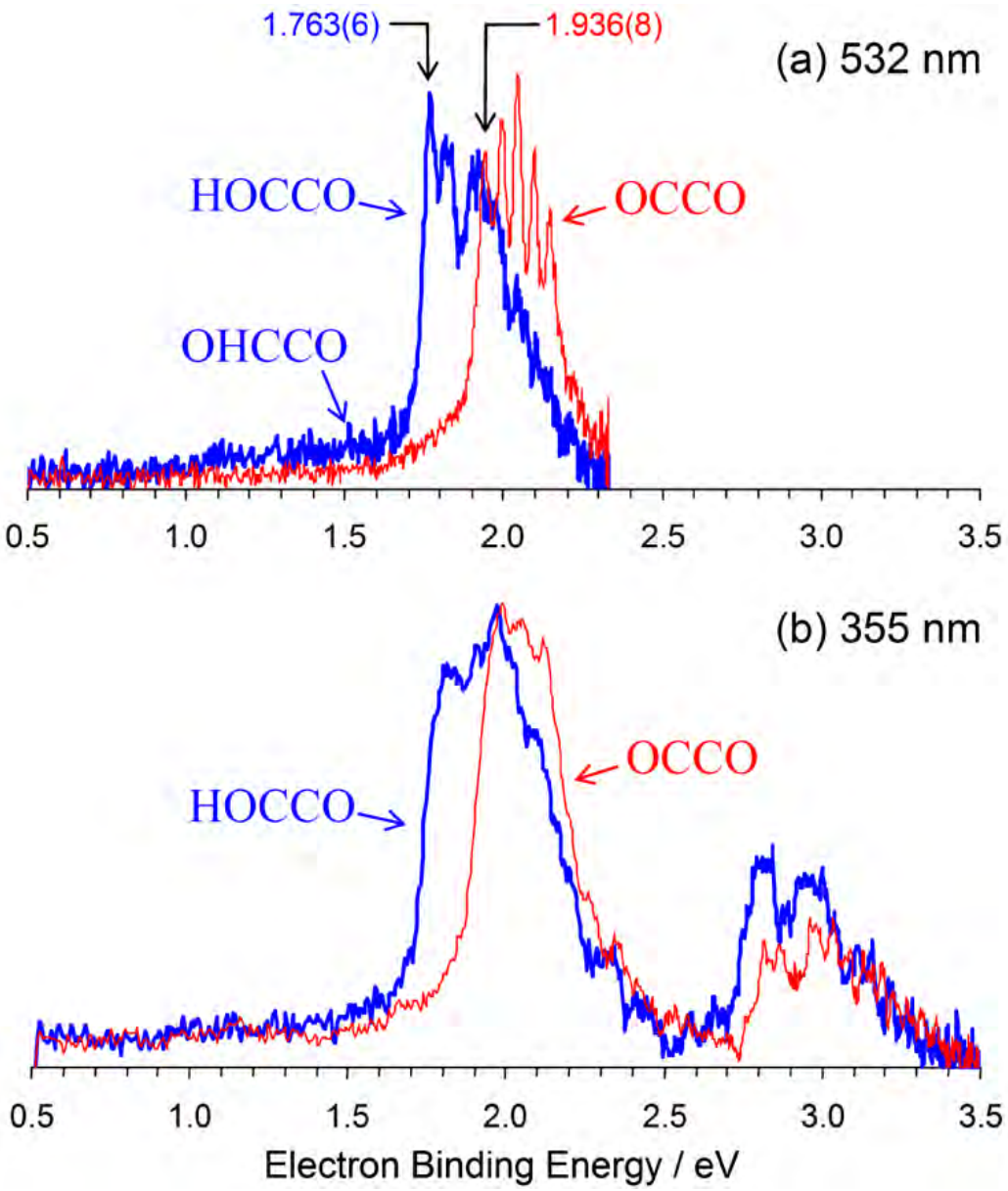

Figure 1. Comparison of the 532 nm (a) and 355 nm (b) photoelectron spectra of $OCCO^-$ (in red) and $HOCCO^-$/$OHCCO^-$ (in blue). Electron affinities for the indicated bands are given in eV.

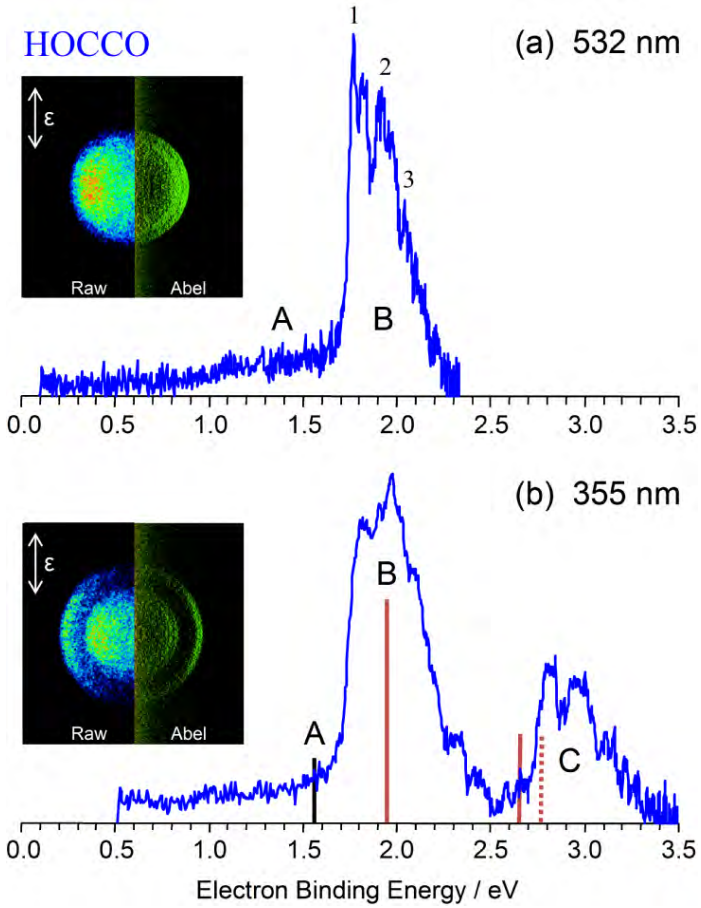

Figure 2. The 532 nm (a) and 355 nm (b) anion photoelectron spectra of the HOCCO/OHCCO radical system, along with the corresponding photoelectron images. Spectral band A corresponds to detachment from $OHCCO^-$, while Band B and C are attributed to $HOCCO^-$ (see section 4.1 for details). The solid vertical bars indicate the computed EOM-IP-CCSD/aug-cc-pVTZ vertical detachment energies for the $OHCCO^-$ (A) and $HOCCO^-$ (B and C) species. The dashed bar (C) indicates the combined EOM-IP/SF-CCSD result for $HOCCO^-$. The photoelectron images are shown on a split scale, representing the raw (left halves) and Abel-inverted (right halves) data, using different arbitrary color schemes chosen for presentation clarity. The direction of laser polarization is indicated by the double-sided arrows.

prevents detailed analysis of the corresponding features. Fitting the envelope of band B in Figure 2(b) with a single Gaussian function places the vertical detachment energy (VDE) at 1.93(4) eV. Band A is weak, but also discernable at 355 nm. An additional spectral band C appears at a higher energy, with a maximum at approximately 2.8 eV. It bears a partially resolved vibrational progression with a ~ 1300 cm^{-1} spacing between the first two prominent peaks.

In the photoelectron images included in Figure 2, all three bands A, B, and C exhibit strong negative anisotropies with respect to laser polarization direction.

4. Discussion

4.1 HOCCO/OHCCO Radicals via the $HOCCO^-$/$OHCCO^-$ System Photodetachment

The *m/z* = 57 anion, whose spectra are shown in blue in Figures 1 and 2, can be ascribed two distinct isomers: (i) the glyoxalide anion $OHCCO^-$, obtained by single deprotonation of the glyoxal molecule; (ii) $HOCCO^-$, the conjugate base of 1,2-ethynediol (acetylenediol), HO–C≡C–OH. A possible mechanism for the formation of $HOCCO^-$ from glyoxal in our experiment is proposed in Section IV.C.

The structures of $OHCCO^-$, $HOCCO^-$, and the corresponding neutral radicals OHCCO and HOCCO were optimized at the CCSD level of theory with the aug-cc-pVTZ basis set. The resulting equilibrium geometries are shown in Figure 3. For OHCCO, the neutral structure (a) is planar, while the anion is not. The non-planar $OHCCO^-$ is shown in two different projections, (b) and (b′). The OHCCO and $OHCCO^-$ geometries also differ considerably along the O1-C1-C2 dangling angle: 179.3° in the neutral (a) vs. 148.7° in the anion (b′). The HOCCO (c) and $HOCCO^-$ (d) geometries, on the other

hand, are significantly more similar to one another.

Single-point EOM-IP-CCSD/aug-cc-pVTZ calculations were performed on the optimized $OHCCO^-$ and $HOCCO^-$ geometries shown in Figure 3(b) and (d). The respective closed-shell singlet anion configurations were used as wavefunction references. EOM-IP is non-conserving method with respect to the number of electrons, as it removes one electron from the reference to form target states. When applied to anions, it nominally corresponds to vertical detachment transitions, provided that the target state can be described from the anion reference used. We previously used the same methodology for the ethylenedione system.[161]

According to the EOM-IP calculations for $OHCCO^-$ photodetachment, the two lowest transitions (which nominally correspond to the removal of an electron from the respective HOMO and HOMO–1 of the anion) are found at 1.559 eV and 3.855 eV. The next transition (corresponding to HOMO–2 detachment), is much higher in energy, at 6.360 eV. The energy of the lowest predicted transition (VDE = 1.559 eV) is indicated with the vertical bar next to labeled A in Figure 2(b). It does not match particularly well the position of band B in the experimental spectra in both Figures 2(a) and 2(b). It is, however, consistent with the weak band A, appearing as the lower-eBE tails in both spectra. Moreover, the onset of this tail, appearing just above 1 eV, is consistent with the adiabatic electron affinity (EA) of OHCCO, calculated as EA = 1.034 eV at the CCSD/aug-cc-pVTZ level, while the very gradual nature of the band's onset is consistent with the large geometry change between $OHCCO^-$ and the corresponding neutral equilibrium [Figure 3(a) and (b)]. Hence, band A, rather than band B, is the more likely candidate for the lowest photodetachment transition of the glyoxalide anion, leaving band

B to be explained by something else. Similarly, none of the $OHCCO^-$ (glyoxalide) → OHCCO transitions predicted by the EOM-IP method can explain band C in the 355 nm spectrum in Figure 2(b).

To explain the origin of the dominant spectral bands B and C in Figure 2, we momentarily return to the comparison of the $OCCO^-$ and $HOCCO^-$/$OHCCO^-$ anion photodetachment in Figure 1. The qualitative parallels between the two spectra suggest that perhaps the addition of hydrogen to an *oxygen* in $OCCO^-$ to form $HOCCO^-$, rather than to a carbon to form $OHCCO^-$, could explain the results, since the former would be a weaker perturbation of the $OCCO^-$ framework compared to glyoxalide.

The structural properties of the $HOCCO^-$ anion (the conjugate base of ethynediol) have not been studied at all, although the neutral acid has been identified in the gas phase.[207] Similarly, no information is available thus far about the corresponding neutral radical species, HOCCO. To shed light on these species, we analyzed the HOCCO radical using the same theoretical procedures as described above for OHCCO.

Turning to Figure 3, the relative similarity of the HOCCO (c) and $HOCCO^-$ (d) structures, as opposed to the dissimilar OHCCO (a) and $OHCCO^-$ (b) geometries, is consistent with the narrow and even partially vibrationally resolved structure of Band B in Figure 2. The lowest photodetachment transitions, predicted by the EOM-IP-CCSD/aug-cc-pVTZ calculations at the $HOCCO^-$ geometry using the closed-shell anion reference, are found at VDE = 1.929 eV (HOMO detachment) and 2.656 eV (HOMO–1), corresponding to a ground–excited state splitting of 0.728 eV. The next neutral state is predicted to lie much higher, at a VDE > 7 eV.

The energies of the two lowest predicted transitions are indicated with solid vertical

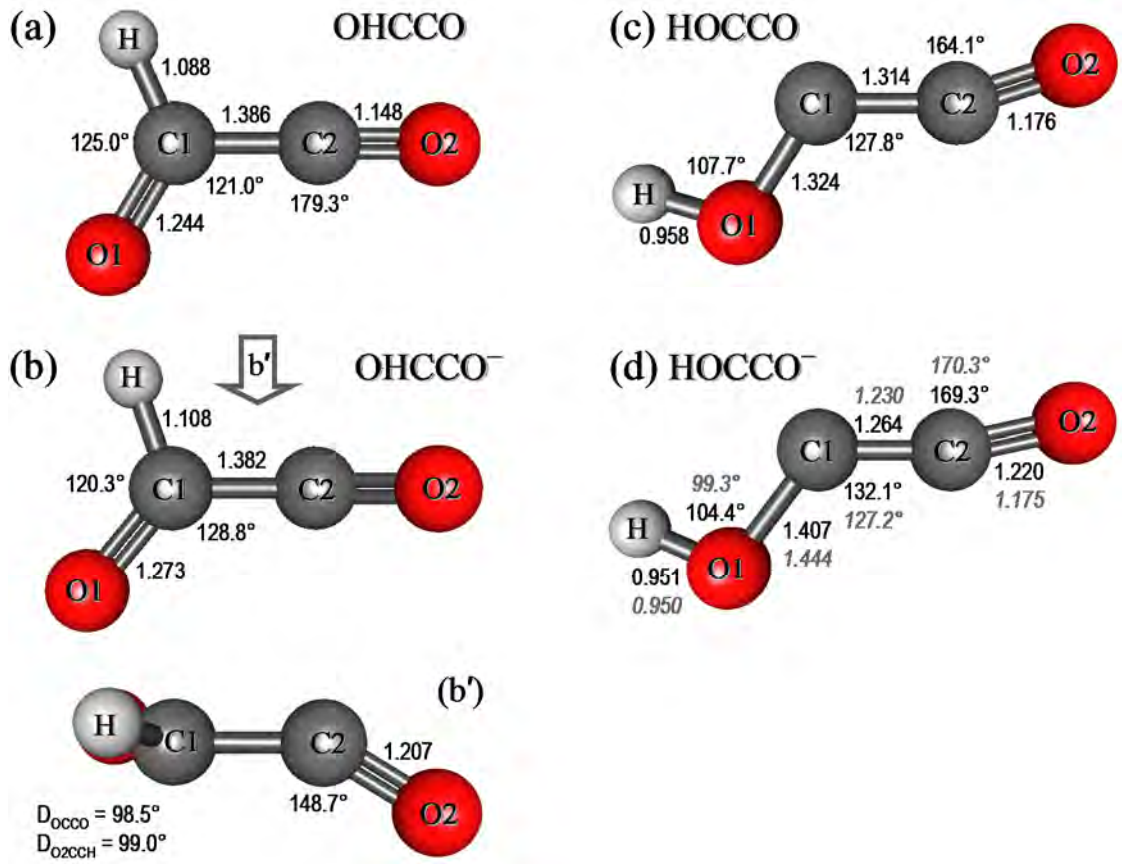

Figure 3. Optimized structures of (a) OHCCO, (b, b') $OHCCO^-$, (c) HOCCO, and (d) $HOCCO^-$. Bond lengths (in Angstroms) and bond angles from CCSD/aug-cc-pVTZ calculations are shown in plain font; italicized values are the adjusted parameters for $HOCCO^-$ from fitting the Franck-Condon simulation to the experimental data.

bars B and C in Figure 2(b). The first is in perfect agreement with the experimental VDE of band B, 1.93(4) eV. The second transition, predicted by the EOM-IP calculations to have a VDE of 2.656 eV, coincides with the observed onset of band C in Figure 2(b). Its agreement with the position of band C's maximum (at ~2.8 eV) seems adequate, but leaves more to be desired.

To explore the possibility that the slight discrepancy between the predicted and experimental VDEs to the first excited state of HOCCO is due to non-negligible contributions of electron configurations that are not adequately described by the EOM-IP method with the closed-shell anion reference, we performed additional calculations using the EOM-SF-CCSD methodology. Unlike EOM-IP, spin-flip (SF) is an electron conserving method and hence it cannot describe photodetachment directly. However, it allows access to a variety of doublet configurations starting from the high-spin quartet (triradical) reference,[213] giving a more complete description of the energy splitting between the neutral states.

At the same $HOCCO^-$ anion geometry, the EOM-SF-CCSD/aug-cc-pVTZ calculations predict the lowest excited state of the neutral HOCCO radical (a doublet) to lie at 0.837 eV above the ground state (also a doublet). This state splitting is slightly greater than that predicted by the EOM-IP (0.728 eV), so the SF description of the two states accounts perfectly for the slight EOM-IP discrepancy noted above. By adding the 0.837 eV EOM-SF splitting to the EOM-IP VDE corresponding to the ground HOCCO state (1.929 eV), we predict the VDE to the first excited state to be 2.766 eV, in excellent agreement with the experimental maximum of band C (~2.8 eV). The combined EOM-IP/SF result for the first excited state is indicated in Figure 2(b) by the dashed vertical

bar.

We also performed a Franck-Condon simulation of the lowest-energy photodetachment transition of $HOCCO^-$ (band B in Figure 2), using the same methodology as described in Section IV.A for $OCCO^-$. The harmonic vibrational frequencies of the neutral and anion species of HOCCO were calculated using the CCSD/aug-cc-pVDZ level of theory in Gaussian and were used to generate the $HOCCO^-$ photodetachment spectrum using the PESCAL 2010 program. The output was optimized using the same procedures followed for OCCO, where the 0-0 peak was set to match the first resolved peak of band B in Figure 2(a). The final simulation result is displayed in Figure 4, while the adjusted $HOCCO^-$ structural parameters are included in Figure 3(d) in *italics*, for comparison with the starting CCSD/aug-cc-pVTZ values. Overall, only minor adjustments were needed compared to the *ab initio* structure. Similar to Section IV.A, the stick spectrum shown in Figure 4 has been scaled with a Wigner pre-factor. It was then convoluted with an experimental broadening function, yielding the smooth spectrum shown in the figure. For comparison, the simulated spectrum is overlaid with the experimental result reproduced from Figure 2(a).

Overall, the quality of the fit in Figure 4 and the agreement of the theoretical VDE predictions with the experiment leave little doubt that band B and Band C belong to detachment from $HOCCO^-$. Based on the combination of the experimental and FC simulation results, we assign the EA of the X $^2A''$ state of HOCCO as 1.766(3) eV, with a VDE of 1.93(4) eV. The splitting between the first two partially resolved vibrational peaks of band B is assigned to the in-plane carbon wagging mode of 430(10) cm^{-1}.

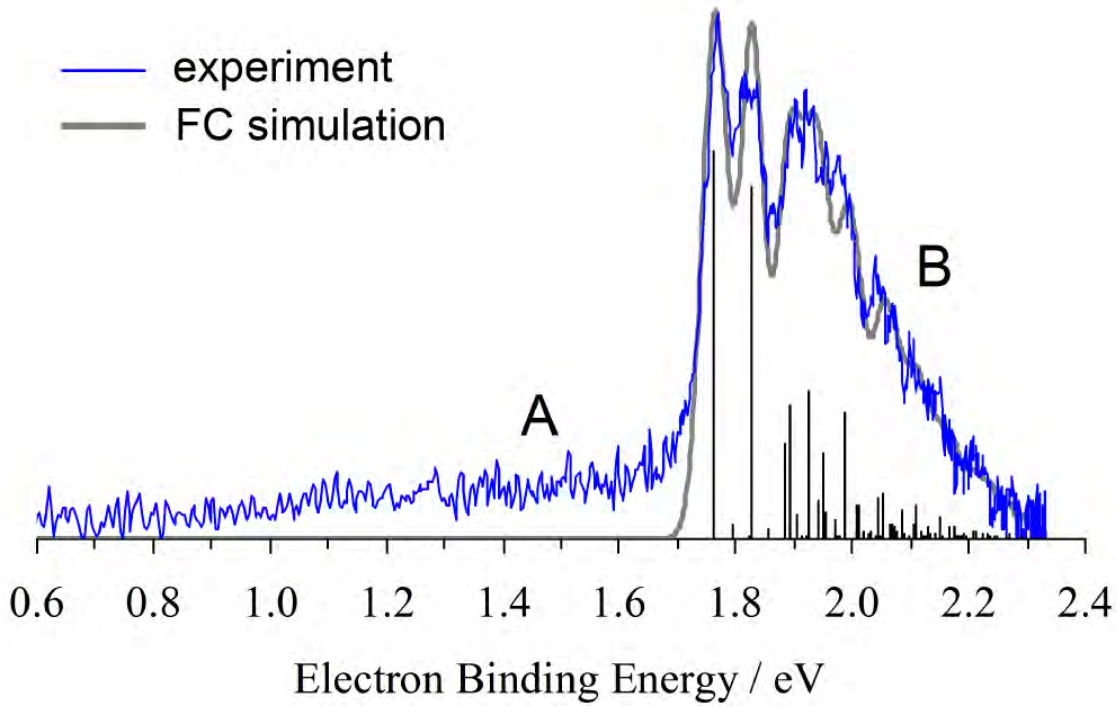

Figure 4. Simulated Franck-Condon spectrum of $HOCCO^-$ (grey), compared to the 532 nm experimental photoelectron spectrum of the $HOCCO^-/OHCCO^-$ system (blue), reproduced from Figure 2(a). The black vertical bars represent the individual Franck-Condon transitions, while the smooth grey spectrum is obtained by convolution with the instrumental resolution function. See text for details.

4.2 Formation of Ethynediolide, $HOCCO^-$

The unambiguous assignment of bands B and C in the photoelectron spectra of the *m/z* = 57 anion (Figure 2) to the conjugate-base isomer $HOCCO^-$ (ethynediolide) raises the question of this ion's origin in our experiment.

Ethynediol, HOCCOH is not present in the precursor expansion. While it is a metastable tautomer of glyoxal, it is 46.8 kcal mol^{-1} less stable at the CCSD(T)/cc-pVTZ level,[215] so it is unreasonable to expect such a rearrangement in the precursor. The glyoxal tautomerization to ethynediol is predicted to involve the hydroxyketene intermediate,[207] but this species would probably form the glyoxalide anion $OHCCO^-$ more readily than $HOCCO^-$ via the loss of hydrogen from the hydroxyl group rather than the carbon. We conclude that ethynediolide observed in our experiment is not likely to be formed via a tautomerization reaction involving ethynediol or hydroxyketene.

On the anion surface, $HOCCO^-$ can potentially be formed from glyoxal via two distinct mechanisms. First is a two-step sequential process, whereas the glyoxalide anion is formed first via the expected single deprotonation of glyoxal:

$$OHCCHO + O^- \rightarrow OHCCO^- + OH \quad (1a)$$

followed by the glyoxalide → ethynediolide rearrangement:

$$OHCCO^- \rightarrow HOCCO^- \quad (1b)$$

However, ethynediolide is 12.4 kcal mol^{-1} less stable than glyoxalide (at the CCSD/aug-cc-pVTZ level), making interconversion of nascent $OHCCO^-$ to $HOCCO^-$ unfavorable. Under this mechanism, we would expect a dominant presence of the $OHCCO^-$ anions (responsible for band A in Figures 2 and 4), compared to the less favorable rearrangement product $HOCCO^-$ (responsible for bands B and C).

Instead, we hypothesize that $HOCCO^-$ is formed in an attempted, but failed H_2^+ abstraction from glyoxal, whereas the failure to abstract both hydrogen nuclei creates ethynediolide, rather than glyoxalide, because of a steric rather than energetic propensity:

$$OHCCHO + O^- \rightarrow HO + H\cdots OCCO^- \rightarrow H_2O + OCCO^- \quad (2a)$$

$$\rightarrow HO + HOCCO^- \quad (2b)$$

Here, $HOCCO^-$ is formed along the same reaction path that leads to $OCCO^-$. The reaction proceeds via an $H\cdots OCCO^-$ complex, from which most trajectories lead to the $OCCO^-$ product (2a above). Indeed, the $OCCO^-$ ion peak was observed to be significantly more intense than the *m/z* = 57 anion in the parent ion mass-spectrum. Those reaction trajectories that do not possess enough energy to complete path 2a terminate in the "half-way" $HOCCO^-$ product along path 2b. The planar OCCO skeleton of glyoxal is a better match to that in $HOCCO^-$ than in $OHCCO^-$. $HOCCO^-$ is also planar, while the OCCO group in relaxed glyoxalide has a significant out-of-plane distortion [Figure 3(b)]. Therefore, when the almost abstracted second hydrogen returns to the $OCCO^-$ skeleton along path 2b, it tends to form ethynediolide rather than glyoxalide, because of the comparatively small rearrangement of the heavy atoms required in this case.

By the same reasoning, formation of glyoxalide by single deprotonation of glyoxal is unfavorable due to the large geometry change needed to equilibrate the new structure. However, some $OHCCO^-$ may be formed via this mechanism or a subsequent $HOCCO^- \rightarrow OHCCO^-$ rearrangement to explain the presence of the weak band A in the spectra in Figures 2 and 6.

4.3 HOCCO Versus OCCO

Finally, we comment on the parallels between the properties of $OCCO^-$ and $HOCCO^-$, as well as the corresponding neutral species. The qualitative similarity of the photoelectron spectra in Figure 1 is striking, but not surprising, The calculated electron affinities of HOCCO and OCCO differ by only 0.17 eV, in agreement with the experimental data in Figure 1. The first excited state of HOCCO [band C in Figure 2(b)] and the S_3 state of OCCO differ in VDE by a similarly small amount [see Figure 1(b)]. In the anion state, both $HOCCO^-$ and $OCCO^-$ have similar trans-bent geometries of the OCCO skeleton [Figures 5(d) and 3(b), respectively]. Both species undergo a contraction of the O-C bonds upon electron detachment, with HOCCO also experiencing a significant elongation of the C-C bond relative to the anion, much more pronounced than in OCCO. By far the greatest difference between the OCCO and HOCCO structures is the overall similarity of the HOCCO geometry to its anion. $OCCO^-$ changes from trans-bent to linear upon photodetachment to the ground (triplet) state of the neutral diradical, while the HOCCO radical retains the trans-bent configuration of its anion.

Considering the calculated energetics and geometries, OCCO is much more similar to HOCCO than to OHCCO. This observation supports our assignment of the m/z = 57 ions as predominantly $HOCCO^-$, rather than $OHCCO^-$. Qualitatively, the addition of a hydrogen to an oxygen in OCCO can be thought of as a relatively minor perturbation, compared to H bonding to one of the carbon atoms. As seen in Figure 3, the formation of a C–H bond significantly distorts the heavy-atom skeleton of the molecule, especially in the anion, much more so than the formation of an O–H bond at one of the terminal atoms.

5. Summary and Future Directions

We presented a comparative anion photoelectron imaging study of a family of exotic glyoxal-derived species, including the OCCO diradical and the radical species HOCCO and OHCCO. The main spectral features can be summarized as follows. The 532 nm photoelectron spectrum of $OCCO^-$ [Figure 1(a)] features a vibrational progression assigned to the (quasi-) bound triplet state of OCCO.[161] Detailed analysis of the spectrum in Chapter 9, including the Franck-Condon simulation of the triplet-state vibrational progression, confirms the previously determined EA of triplet OCCO, EA = 1.936(8) eV. The broad spectral pedestal underlying the progression is assigned to the dissociative singlet state of OCCO, while the higher-energy band observed in the 355 nm spectrum at eBE ~ 3 eV is assigned to a higher-lying singlet state.[161]

The photoelectron spectra of the *m/z* = 57 anion are found to include contributions of the $OHCCO^-$ (glyoxalide) and $HOCCO^-$ (ethynediolide) isomers of the anion, with $HOCCO^-$ being the dominant species. Similar to OCCO, the 532 nm spectrum [Figures 1(a) and 2(a)] also features a partially-resolved vibrational progression [band B in Figure 2(a)]. With the aid of the Franck-Condon analysis, it is assigned to the ground state of the HOCCO radical, which come as a surprise, because direct deprotonation of the glyoxal precursor was expected to yield the glyoxalide anion, $OHCCO^-$. The adiabatic EA of the HOCCO radical is determined to be 1.763(6) eV, slightly smaller in magnitude than that of quasi-bound triplet OCCO. The spectrum also shows a weak, but broad low-eBE tail (band A in Figure 2), which is similar in appearance to the dissociative-state pedestal in the OCCO spectrum. In contrast to OCCO, this tail is attributed to a different isomer of the anion, $OHCCO^-$, rather than to a dissociative neutral state. Thus, band A is

the only observed signature of the direct deprotonation product of glyoxal, $OHCCO^-$, while all other spectral features are attributed to $HOCCO^-$ and the resulting neutral radical. The higher-energy band observed in the 355 nm $OHCCO^-$/$HOCCO^-$ spectrum, also (as in OCCO) at eBE ~ 3 eV, is attributed to an excited state of the HOCCO radical.

Although for the reason explained in section 4.2 the dominance of the $HOCCO^-$ bands in the spectra was unexpected, the analysis, supported by FC simulations and electronic-structure calculations, leaves little doubt that $HOCCO^-$ is indeed the major *m/z* = 57 anion product observed in the reaction of glyoxal with O^-. We proposed a mechanism for this reaction, which involves a *failed* abstraction of H_2^+ (en route to the $OCCO^-$ product) that terminates in H^+ (rather than H_2^+) abstraction and favors the formation of $HOCCO^-$ over $OHCCO^-$ due to geometric constraints. Further theoretical study of this reaction, possibly using transition-state theory and semi-classical trajectory calculations, could lead to a more complete understanding of the origins of the $HOCCO^-$ anion, and preliminary discussions of such calculations are currently under way. Moreover, the qualitative mechanism proposed here may prove to be more general, with implications to a broader class of organic reactions. On the experimental side, measurements of anionic fragmentation products, provided such pathways exist, could also help unambiguously differentiate between the $HOCCO^-$ and $OHCCO^-$ isomers. Isotopically substituted glyoxal, glyoxal-d_2, or the addition of D_2O to the sample mixture may provide some insight into possible formation mechanisms. Inhibition of $HOCCO^-$ formation or a change in relative photoelectron intensity between $HOCCO^-$ and $OHCCO^-$ would be illuminating, and make a good companion to the aforementioned theoretical approach.

The parallels between the anion photoelectron spectra of the HOCCO radical and the OCCO diradical result from the relatively minor perturbation caused by the hydrogen addition to an oxygen in OCCO. Conversely, the addition of a hydrogen to the carbon frame results in the much a more severe perturbation and a large geometry change predicted for OHCCO and the corresponding anion. The low-lying states of OHCCO and HOCCO remain largely unexplored, although their reactivity may prove important to atmospheric and combustion chemistry, due to the ubiquitous nature of glyoxal. We reiterate[161] that future experiments targeting the lifetime of OCCO and the energy exchange in its unimolecular decomposition, will provide insight into the fundamental properties of this intriguing molecule.[183,189]

Chapter 11: Dicyanoacetylene Anion - A Possible Target of Astrochemical Interest

Overview

Initial attempts were made to detect and observe the dicyanoacetylene anion, $NCCCCN^-$, by photoelectron imaging. While it is believed the experimental design path of H_2^+ abstraction from fumaronitrile is sound, no spectral signature can be assigned to $NCCCCN^-$. Calculations targeting the low-lying transitions from the anion indicate that the molecule should have a significantly positive electron affinity and at least the ground state should be accessible with the currently available laser sources. The cluster ion $O_2(N_2O)^-$ of the same nominal mass as $NCCCCN^-$ is identified as an interfering ion and ideas are proposed for resolving this difficulty.

1. Introduction

Dicyanoacetylene (NC_4N or NCCCCN) is a member of a class of reduced carbon chains which are predicted to play a significant role in interstellar chemistry.[216-221] In particular, evidence for the existence of solid dicyanoacetylene ice has been found on Saturn's moon Titan, though to date no evidence of the pure vapor form has been found.[222,223] Laboratory experiments show that dicyanoacetylene vapor can be partly responsible for the formation of the yellowish haze observe on the moon, [224] providing a possible sink for the vapor. Detection of linear dicyanoacetylene by rotational spectroscopy is made impossible by its lack of a dipole, but at least one attempt has been made to assign a diffuse interstellar band (DIB) to NC_4N^+.[216]

The electronic structure of dicyanoacetylene has been studied rather extensively.[225] Observed phosphorescence in cryogenic noble gas mediums indicates an efficient intersystem crossing from the first excited singlet to the lowest-energy triplet state.[226] There are several experiments and studies of the anionic resonances which indicate electron attachment to isolated NCCCCN can result in a stable anion of the title molecule or several anionic fragments.[227,228] This makes dicyanoacetylene, and other reduced carbon-chain molecules, important sources for chemically active species in the interstellar medium.

The electron affinity of dicyanoacetylene is not known, this important property would be vitally important to the study of the molecule and its role. While the electronic structure is well studied, additional insights might be offered in examining the electron detachment process, either energetically or perhaps band profiles through Franck-Condon simulations.

2. Experimental and Theoretical Methods

The details of the velocity-map imaging spectrometer used for this experiment have been described elsewhere.[49,229] Briefly, a commercial sample of fumaronitrile was heated to 40-50° C and vapor was seeded into a N_2O carrier gas. This gas was pulsed into the vacuum chamber by a General Valve Series 9 gas nozzle, operating at 50 Hz to match the laser system. The supersonic expansion of the gas was crossed perpendicularly with a continuous ~1 keV beam of electrons produced by an electron gun to form plasma. Atomic oxygen anions were formed from the dissociative attachment of electrons to N_2O. The target anion of dicyanoacetylene, $NCCCCN^-$, is formed by the H_2^+ abstraction of fumaronitrile by O^-.[101] Anions were extracted in the Wiley-McLauren TOF mass spectrometer region by a pusher plate using a -950 V pulse and were accelerated to a final potential of 3.5 kV. Ions of mass-to-charge 76 were integrated by linearly-polarized laser pulses, with detached electrons velocity-mapped in the perpendicular direction to both the ion beam and laser electric field polarization direction. 1064 (fundamental), 532 (second harmonic), and 355 (third harmonic) nm laser light was produced using a SpectraPhysics LAB-130-50 Nd:Yttrium laser. Photoelectron signal were recorded using a position-sensitive dual-MCP detector coupled to a P34 phosphor screen; light produced was collected using a CoolSnap Myo thermoelectrically-cooled CCD. Typical images were collected for ~1 x 10^6 experimental cycles. Images were reconstructed using the inverse Abel transformation,[17] implemented in the BASEX program.[51] Radial distributions were converted to binding energy spectra, calibrated to the well-known EA of atomic oxygen.[52,53]

Theoretical optimizations of the dicyanoacetylene species at the CCSD/aug-cc-

pVTZ level of theory were done using the Gaussian 09 software.[54] EOM-IP-CCSD/aug-cc-pVTZ investigations were carried out using Q-Chem 4.0[26] using the structures optimized in Gaussian 09.

3. Experimental Results

Photoelectron images were collected for the mass-to-charge (m/z) 76 anion packet at 1064, 532, and 355 nm; the images along with the resulting binding energy spectra in Figure 1. Electron binding energy is defined as, eBE =hν – eKE, where hν is photon energy and eKE is electron kinetic energy. In Fig. 1A, the small energy window of 1064 nm does reveal two peaks, one at ~0.82 eV and another at ~1.00 eV. In Fig 1B, more of this transition is revealed with several decently-resolved lines. Even spacing of approximately 1300 cm^{-1} suggests that this is a vibrational progression, and we now label the feature as Band A. At 355 nm, Fig. 1C, a significant loss of resolution occurs due to the increase in eKE. However, 3 features are now visible. The lowest eBE feature is Band A. A new transition, labeled Band B is apparent at ~2 eV. Autodetachment is also visible and is labeled as Band C, and can be identified as the sharp increase in signal at 0 eKE.

4. Discussion

4. 1 Consideration of the Spectral Components

The m/z 76 anion packet was identified hopefully as the anion of dicyanoacetylene, NCCCCN. However, this m/z also overlaps with the ion cluster $O_2^-(N_2O)$. Based on the ~1300 cm^{-1} spacing of the vibrational progression in Band A, it is quite clear that this Band can be assigned almost assuredly to this cluster ion. The shift in the 0.4480 ± 0.0060 eV 0-0 transition for O_2^-, ~0.38 eV based on the spectrum

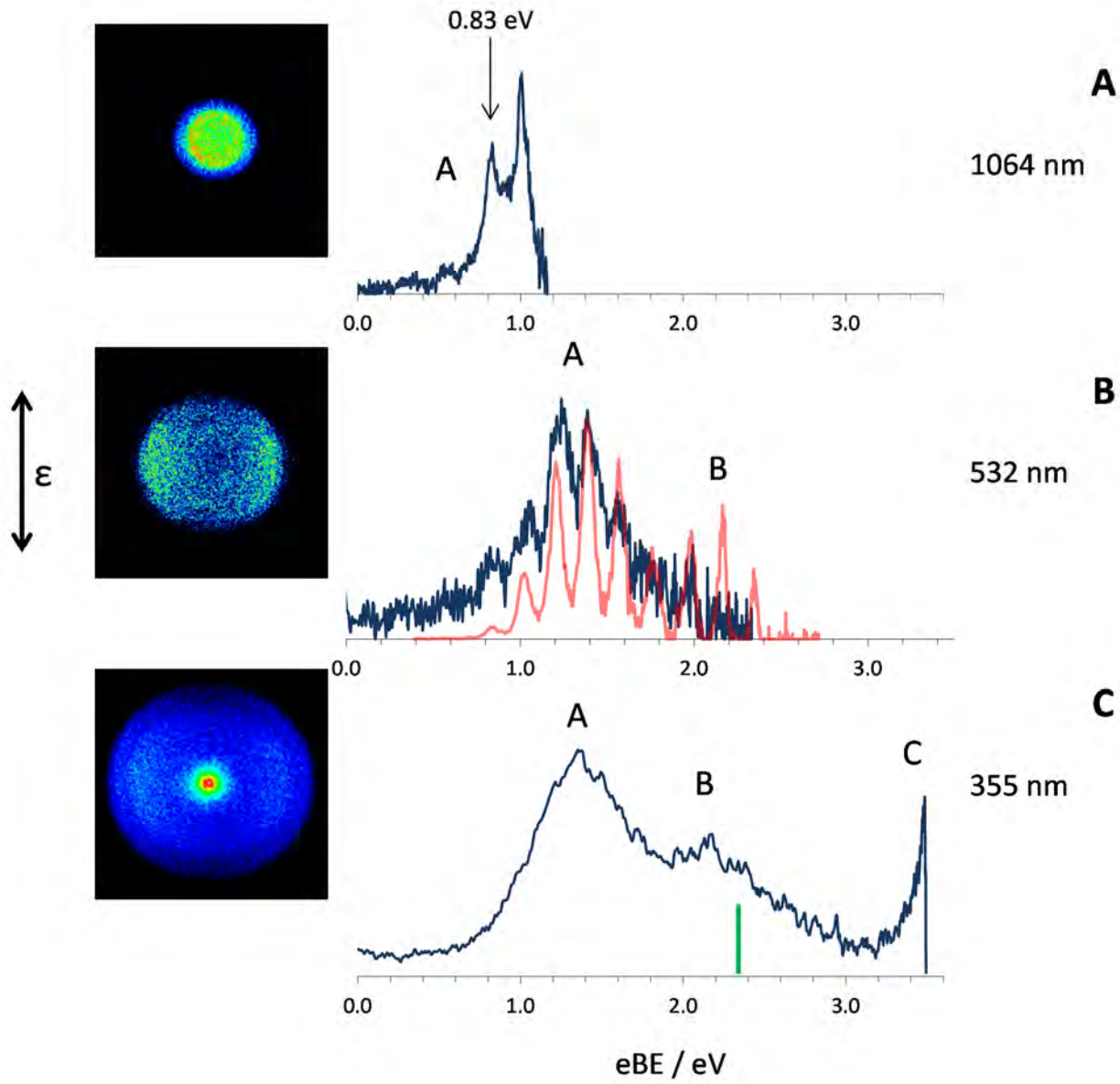

Figure 1. The photoelectron images and corresponding spectra for the m/z 76 anion packet. The double-sided arrow indicates the direction of electric field polarization. Band A and B correspond to transitions of $O_2^-(N_2O)$, while Band C is assigned to autodetachment. The red spectrum in (B) is spectrum obtained for O_2^- and shifted by 0.38 eV to higher eBE. The vertical green bar indicates the EOM-IP-CCSD/aug-cc-pVTZ result for detachment from the α-$9a_g$ orbital of $NCCCCN^-$. See text for details.

overlap, is a reasonable value for the approximate solvation energy of N_2O to the O_2 core anion, where

$$E_{Solvation} \leq EA_X - EA_{X \cdot M} \qquad (1).$$

While some lower-eBE features are visible in the 1064 and 532 nm spectra, these can very likely be attributed to detachment from O_2^- following the loss of solvent by photoexcitation.

With this qualitative assignment, the identify of Band B likely falls to the transitions of the two lowest singlet states of the $O_2(N_2O)$ neutral cluster. However, the presence of autodetachment in the 355 nm spectrum has not been observed previously for O_2^- or any of its cluster ions. This does present a possibility that some other species is present. To make any assignment unambiguous, particularly any assignment related to dicyanoacetylene, one key experimental change should be made to reduce any sources of contamination. The unfortunate overlapping of the $O_2^-(N_2O)$ cluster ion must be resolved to obtain any spectral information about $NCCCCN^-$.

Perhaps the most straightforward solution is the isotopic substitution of carbon in the fumaronitrile precursor. While fumaronitrile is not currently commercially available with carbon-13 substitution, it can done in principal using either carbon-13 substituted acetylene or nitrile feedstock in a Rosenmund–von Braun synthesis of fumaronitrile.[230] This would shift the nominal mass of $NCCCCN^-$ by 2 amu, resulting in a mass-to-charge ratio of 78.

Secondly, the presence of the O_2^- ion can be resolved by scrubbing oxygen from the carrier gas. Molecular oxygen is present as an impurity in the N_2O carrier gas.

Materials do preferentially adsorb oxygen for gas chromatographs and similar systems. A column containing such material could be placed just before the inlet to the source chamber to greatly reduce the amount of oxygen present. In turn, the abundance of the cluster ion would be reduced, as would its spectral contribution. This is perhaps the most practical change in methodology. A third option would be a complete change to the carrier gas, where O^- can be formed by another reaction besides the dissociative electron attachment to N_2O, which would remove the cluster ion altogether. Molecular oxygen is (perhaps ironically) a possible choice for this application as it would remove N_2O from the possible solvent molecules.[231]

4.2 Theoretical Investigation

The electronic structures of neutral and anionic dicyanoacetylene are well-studied.[227,232] Particularly, 4 excited neutral states have been spectroscopically observed, including the lowest-lying triplet, observed at 3.18 eV above the ground-state. The stable anion of NCCCCN is by comparison under-studied. To understand the photodetachment process from $NCCCCN^-$, calculations were performed to specifically capture this process. The anionic, singlet neutral, and triplet neutral species were optimized at the CCSD/aug-cc-pVTZ level of theory. The geometries of the optimized species are shown in Figure 2, while the calculated values are shown in Table 1. Electron affinity (EA) is calculated as the electronic energy of the neutral minus that of the anion at their respective geometries.

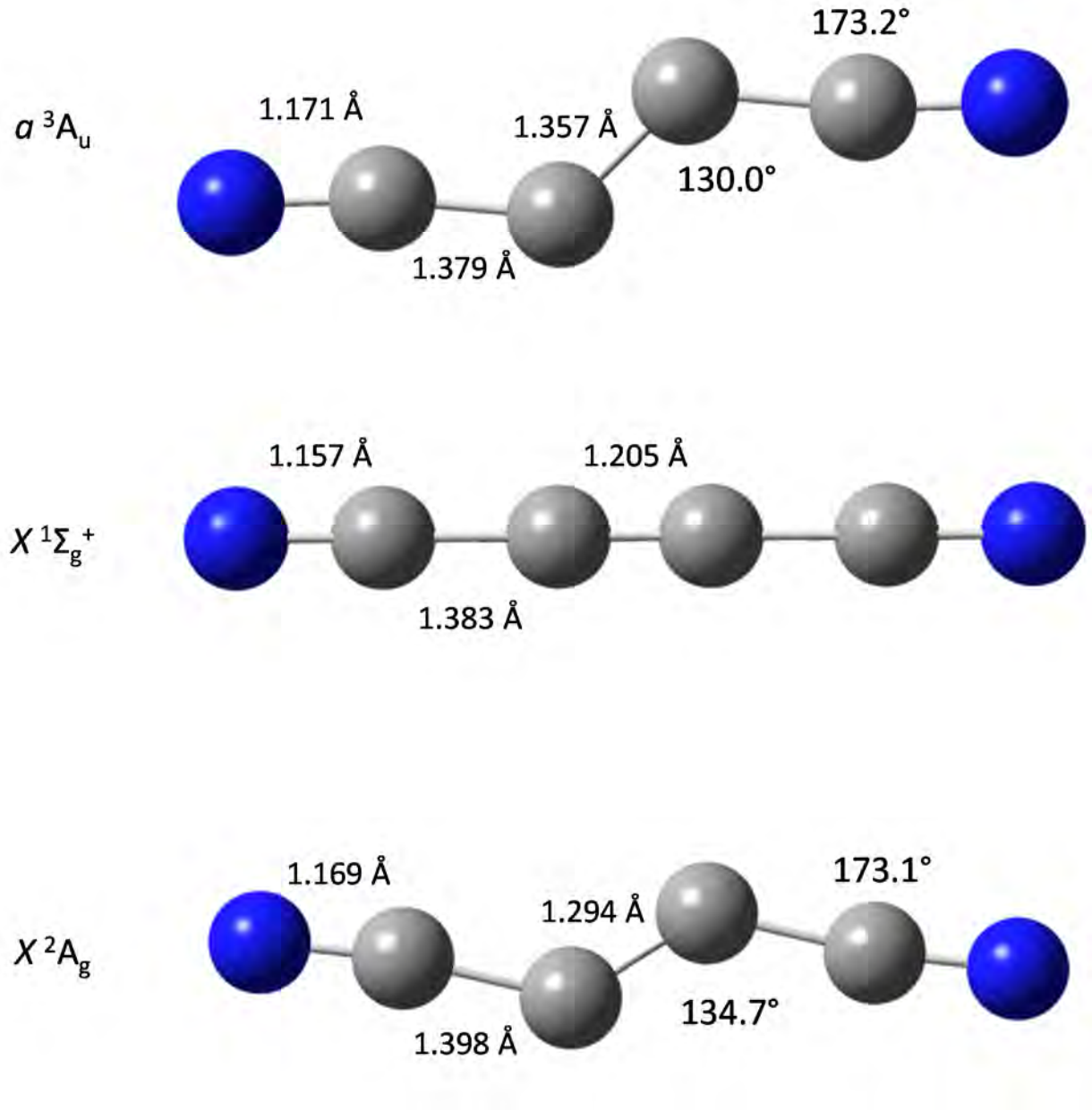

Figure 2. The geometries of the anion and low-lying neutral states of dicyanoacetylene, optimized at the CCSD/aug-cc-pVTZ level of theory and basis.

Vertical detachment energy (VDE) is calculated as the electronic energy of the neutral minus that of the anion, both at the anion geometry. As found before, the ground-state of neutral dicyanoacetylene is linear, while the lowest-lying triplet has a trans-geometry of C_{2h} symmetry. The ground-state anion also has a C_{2h} symmetry. Compared to the triplet geometry, the anion has slightly more bonding character between the two acetylene

Table 1. Calculated EA and VDEs for NCCCCN species in eV, without ZPE corrections, at CCSD/aug-cc-pVTZ

	$X\ ^1\Sigma_g^+$	$A\ ^3A_u$
EA	1.156	4.983
VDE	2.229	5.110

carbons. The singlet state is characterized by the shortest bond distances observed for any species pictured.

The EA calculated for the singlet is 1.156 eV, indicating a fairly stable anion and suggesting that observing the anion-singlet transition could be done with the 532 nm light used in Figure 1B. Conversely, the calculated EA of the triplet is 4.983 eV, well above the 266 nm spectral window. This value is however in discrepancy with the observed separation of 3.18 eV between the singlet and triplet, which was by phosphorescence.[233] Testing the calculated value based on photodetachment with 266 nm would be valuable. In any case, at least one transition should be observable. The VDE calculated for the

singlet transition is 2.229 eV, which is in good agreement with the very large geometry change expected upon detachment. A combination of symmetric stretching and bending modes can be expected to be important for describing the detachment profile based on the calculated geometries, leading likely to a highly congested band. The triplet has a calculated VDE of 5.110 eV; the small difference in calculated EA and VDE suggests a very sharp band and is consistent with the triplet geometry being very similar to that of the anion.

To further capture the photodetachment, equation-of-motion ionization potential (EOM-IP) calculations were carried out on the anionic reference wavefunction ($\ldots b_u^2 a_u^2 a_g^1$) and geometry to determine the VDE. The results for the lowest-lying transitions are shown in Table 2. Symmetry labels correspond to the anion geometry, not the global minimum geometry for each state.

Table 2. EOM-IP-CCSD/aug-cc-pVTZ results for the anionic wavefunction and optimized geometry of NCCCCN.

Nominal Detachment Orbital	Corresponding Neutral State	Predicted VDE / eV
α-9a_g	$X\ ^1A_g$	2.3404
β-8b_u	$a\ ^3B_u$	5.0204
β-2a_u	$b\ ^3A_u$	5.3728
α-2a_u	$A\ ^1A_u$	5.6526

The EOM-IP-CCSD results for both the ground-state and the lowest-lying triplet are in good agreement with values determined by the electronic energies. A third transition is predicted in very close proximity to the triplet, but still well outside the 266 nm photon energy window. The dominate reference produced is a triplet, but this may be a component of the $^1\Delta_u$ electronic state observed for linear, neutral NCCCCN. The first excited-state singlet is very similar in energy, and is consistent with the observed intersystem crossing.[226] No new transitions are predicted between the ground-state singlet and triplet.

5. Conclusions

While the first attempt in observing the dicyanoacetylene anion is inconclusive, the O^- abstraction route to its formation is promising. The spectra for m/z 76 show a clear O_2^- core anion signature; several suggestions have been made to avoid this interference. Calculations show that dicyanoacetylene should form a stable anion with an EA of 1.16 eV, accompanied by a significantly broad band for the singlet transition. The lowest-lying triplet is outside the current photon energy window available, but shares a very similar geometry to the anion.

Further photofragmentation experiments should also be attempted pending successful detection of $NCCCCN^-$, though in practice they could be performed without taking into account the interfering $O_2^-(N_2O)$ ion. Dissociative electron attachment forming CN^- and $CCCN^-$ has been observed at or above an eKE of 3 eV, and been attributed to metastable resonances of $NCCCCN^-$.[228] Detection of these fragments

following the photoexcitation of $NCCCCN^-$ at 355 nm should be possible, enlightening, and aid in the definitive assignment of ion.

Chapter 12: Summary and Future Research

Overview

The previous chapters have shown that anion photoelectron velocity-map imaging spectroscopy is an extremely powerful technique to investigate chemical between electrons and molecules, and the electronic structure of novel and elusive intermediates. This chapter contains a broad summarization of the main conclusions and possible future directions for study.

The following sections for this chapter are given for a more complete review of the topics covered in the main body of this work. The application of anion photoelectron velocity-map imaging spectroscopy to studying the nuances of chemical bonding and electronic structure is extremely fruitful. The simultaneous detection of both energetic and angular information provides for, in many cases, unambiguous assignment of spectral features. This has been applied to great effect in the study diradicals and solvent clusters, as well as a number of intermediate species. The technique is shown to be flexible and powerful in these investigations, and promises a great deal of future work.

1. Solvent Interactions Mediated by Electrons

1.1 Benzonitrile

The study of benzonitrile revealed that the bare neutral molecule binds an additional electron very weakly. The weak negative anisotropy is not the expected result of a dipole-bound electron, and the preservation of the limited vibrational resolution with solvation suggests a valence electron. This vibrational profile was confirmed with a Franck-Condon overlap simulation of the detachment from valence-bound benzonitrile anion. However, the magnitude of the EA, just 60 meV, in the range expected for a dipole-bound system.[40,73,75,234] Currently unpublished work by the Adamowicz group shows the existence of a stable dipole-bound benzonitrile anion with a binding energy of 18.5 meV.[235] The similar energies suggest that this dipole-bound state should play a role in the benzonitrile anion system. One possibility is that this dipole-anion state acts as a gateway state; the large 4.5 Debye dipole could efficiently capture slow electrons in a dipole state, offering a long time window for interconversion to bind the electron to the

valence of the molecule. Additionally, a benzonitrile anion may exist both or convert back and forth between these distinctively different states.

While the electronic structure of benzonitrile (baring possible dipole-bound states) has been well-examined, there exists a plethora of anisotropy data for the bare anion and many solvated species. This data has yet to be analyzed in depth, and may offer some insight into the dipole/valence-bound system. The primarily *s* character of the extremely diffuse dipole-bound state orbital should give primarily positive anisotropy. If the valence-bound orbital detachment can be properly modelled, the anisotropy data may show discrepancies showing the dipole-bound state contribution.

The benzonitrile dimer anion and other homo-molecularly solvated anions of benzonitrile are among the most interesting results. While benzonitrile has been observed to form neutral dimers, the geometry of these systems does not match the π-π stacking of the bn_2^- system. This interaction, explored with DFT, matches the large ~0.5 eV shift in VDE, and matches similar changes in electronic structure observed with nitrobenzene dimers. While the shift indicates a significantly-stabilized anion, the preservation of band profiles and the appearance of a second state shifted from the triplet transition by a similar ~0.4 eV shows a primarily non-covalent interaction. That is, the system is primarily a benzonitrile core anion. Solvation energy calculations indicate that this dimer is also significantly stable in the neutral form, though less than the anionic system.

1.2 Fumaronitrile Dimer

This benzonitrile system differs immensely from the previously observed fumaronitrile dimer anion, fn_2^-. [56] Even though fumaronitrile is a heavily conjugated system like benzonitrile, this dimer appears distinctly different than the monomer. Unlike the π-π stacking interaction, fumaronitrile forms a covalent dimer with a shift in electron affinity of 0.94 eV from the monomer. This dimer reflects a pair of triplet fumaronitrile neutral molecules forming a fused singlet ground-state by the direct interaction of two radical centers. The previously published 532 nm and unpublished 355 nm spectrums show a single, unresolved band. These results are shown in Figure 1. Previous calculations on this structure were carried out with the M06 DFT functional and the aug-cc-pVTZ basis, which should provide reasonable geometries. However, the electronic structure method EOM-IP-CCSD, which was immensely successful for benzonitrile and numerous other diradical species (carbenes, OCCO), was employed with the very limited 3-21G basis. EOM-SF-CCSD, used with great success in complex electronic structures common to radicals, was not employed at all, due to the calculation expenses at the time.

Preliminary results for the EOM-IP-CCSD/3-21G indicate 3 transitions at 2.02, 2.16, and 3.09 eV.[56] While the lower-eBE transitions, the ground-state singlet and lowest-lying triplet respectively, could be indistinguishable or difficult to observe, there is no mistaking that the 355 nm spectrum in Fig. 1B does not show any substantial transitions at or near 3.09 eV. This may be a failure in prediction due to the small basis employed, or the diradical nature of the neutral fumaronitrile dimer creates a complex electronic structure more suited to the spin-flip methodology. The photoelectron cross-section may

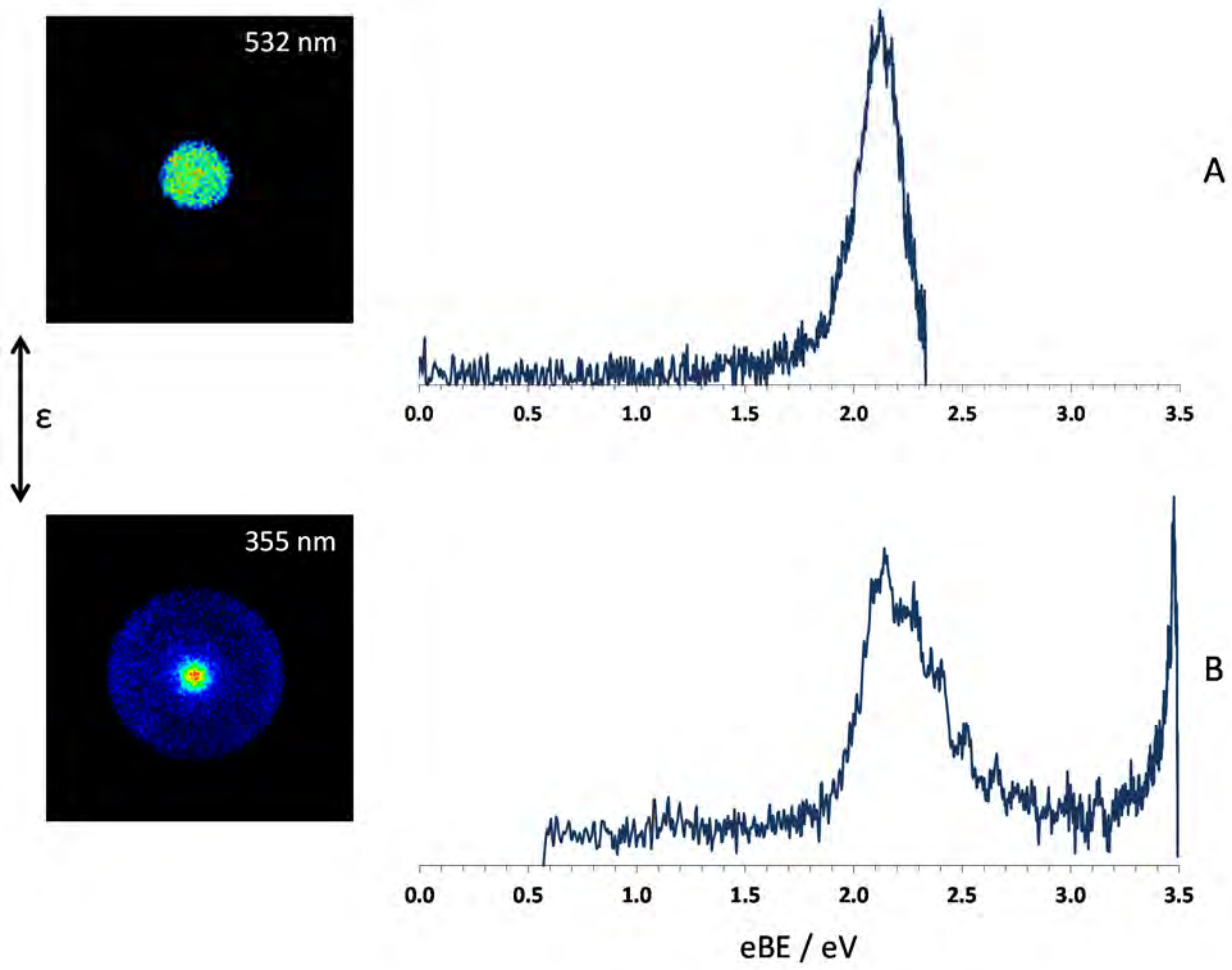

Figure 1. The photoelectron spectra of the fumaronitrile dimer anion at 532 (A) and 355 nm (B). No transitions are fully assigned, see text for details.

simply be too low to observe in the current spectrum. Further, though the system is complex, a Franck-Condon simulation of the singlet and high-spin triplet transition would be very illustrative of the nature of the single feature present in the 355 nm spectrum. While the method employed to calculate normal modes for benzonitrile was M06-2X/aug-cc-pVTZ on the CCSD/aug-cc-pVDZ geometries, the result was very useful in examining the band profile. A similar level of theory applied to the fumaronitrile dimer should achieve some success in de-convoluting the single band at 355 nm into contributions from the singlet and triplet. Additionally, the spin-flip methodology should give much more reliable predictions for electronic transitions when employed with a larger basis.

The fumaronitrile dimer is in a class of 'triplet-based' dimers including $(OCS)_2^-$ and $(CS_2)_2^-$, where dimers are built by the bonding of 2 triplet neutral monomers. Conversely both bn_2^- and CO_2^- are formed from singlet building blocks. For the latter, the energetic cost of forming triplet neutrals is not recovered by forming the anionic dimer while the in the previous systems it is. Conceptually, benzonitrile could form a triplet-based dimer if the electron affinity was substantially higher or the ΔE_{S-T} was smaller. This suggests that molecules with low ΔE_{S-T} are more likely to form anionic dimers based on triplet monomers. TCNE, ΔE_{S-T} = ~1 eV,[57] and TCNQ, ΔE_{S-T} = ~2.0 eV[236] are two potential molecules for which this process seems likely. TCNE is a direct substation to fumaronitrile, able to undergo geometry change like rotation about the central ethylene bond, while the aromatic of TCNQ maintains a planar structure like benzonitrile. Dimers may be observable for both species, either covalent or based on the π-π interactions.

1.3 Ethylene Solvent Molecule

In contrast to all of the strong interactions observed for radical-radical and π-π interactions, the solvation interaction in the $O_2^-(C_2H_4)$ cluster is much weaker. Despite both molecules having prominent π-orbitals, the interaction energy is a ≤0.24 eV. Compared to similar systems, N_2O manages a solvation energy of ~0.3 eV when paired with O_2^-. This initial expectation of a strong π-π is of course incorrect upon further examination. The excess electron of O_2^- occupies a π* while the HOMO of ethylene is a bonding π-orbital. There is no favorable π-orbital overlap for this pair. Instead, the interaction is to reduce unfavorable overlap, resulting in the unexpected planar geometry. This allows for an asymmetric interaction between the core anion and solvent HOMOs. While certainly not as striking as bn_2^-, the solvent cluster shows that there is more to π-π interactions than simply having valence π-orbitals. Despite this the ethylene does stabilize the superoxide anion, a process made possible by the diffuse excess electron allowing for weaker, longer range interactions. Ethylene as a solvent in the gas phase represents an interesting molecule. It is perhaps the simplest example of a molecule which has a bonding π-HOMO. Presumably, a number of anions may have weak interactions like O_2^-, but many more might have strong interactions with the proper overlap.

2. Carbene and Methyl Radical Substituent Effects

The substituent effects observed in carbenes and radicals are, in an intramolecular sense, structure-activity relationships. Though the interactions studied are more nuanced than any model proposed in this thesis, the observed trends provide an attractive model framework to start from.

2.1 Carbene Substituents

The two nominally non-bonding electrons on the carbene center are particularly sensitive to local substituent effects, which in turn determine the $\Delta E_{S\text{-}T}$ which is so important in describing the chemistry of carbenes. In particular, the study of the heterogeneously-substituted chlorocyanocarbene and fluorocyanocarbene has shown some very interesting insights into how multiple substituents interact. In the studied carbenes, the heterogeneous substitutions include different functionalities, but also different π-interactions with the nominal *p*-orbital on the carbene center. Halogens act as π-donating groups while the cyano-group, sometimes referred to as a pseudo-halogen, acts as a π-accepting group. To a first approximation these pairs largely *do not* affect each other, at least in this case of small substituents. This is to say that the substitution effects on the prototypical methylene species by one of the substituents are added to the effects of the other in the mixed species.

The result of this has predictive value; combinations of different π-interactions can be estimated by examining the mono-substituted carbenes. In examining the preliminary data for two 'mixed' phenylcarbenes, this apparent property is used to make some predictions for the properties of phenylcarbene. Firstly, the prediction for the EA of less than 1 eV is so far in good agreement with the first spectroscopic result of ~0.83 eV.[121] Additionally, the $\Delta E_{S\text{-}T}$ as predicted to be slightly more in favor of the singlet ground-state, in good agreement with all the available experimental and theoretical work on the species.[9,121,237-239]

2.2 π-Interactions with the Carbene Center

In Chapter 5, a molecular-orbital framework was put forth which gives a simplified view of the carbene-substituent interactions. To summarize, there are 3 basic interactions which determine the energy of nominal σ orbital and the lowest available π orbital for the non-bonding electrons of the carbene. This in turn determines the stability of the triplet state configuration $\ldots\sigma^1\pi^1$, as compared to the singlet, $\ldots\sigma^2\pi^0$. Firstly is the stabilization of the nominal σ-orbital by what can be referred to as electron-withdraw (or donation). In this case halogens, the cyano-, and phenyl-group are all some level of σ-withdrawing. Thus, they all stabilize this orbital by interacting through the σ-orbital molecular framework. This interaction makes the singlet configuration more stable.

The second type of interaction is the mixing of π-orbitals from the carbene and substituents. Halogens and cyano-groups both interact with the nominal *p*-orbital of carbene primarily through a single orbital, using non-bonding *p*-orbitals or π* orbitals respectively. The phenyl-group is more complex, and at least 6 π-orbitals come into play. This provides a rather dense set of molecular orbitals within the framework. These orbital mixing interactions determine the stabilization of these orbitals, but the final 'interaction' is addressing the number of π-electrons present. This is what sets halogens apart from the cyano-group. The cyano-group donates no electrons to the framework; the π* orbital is empty. When considering the triplet configuration of the carbene, the unpaired π-electron occupies the lowest energy π-orbital. In contrast, a halogen donates 2 electrons, and the unpaired electron must occupy a much higher energy antibonding orbital. It is this unpaired electron's energy which determines the triplet energy. While both the singlet and triplet configurations involve the nominal σ-orbital, the π-orbitals of

the carbene only play a role in the triplet configuration. If the lowest energy orbital available for an unpaired electron is sufficiently low, than the energy to pair the electron is larger and the triplet configuration is the ground-state. In the case of a higher energy π-orbital, for instance with halogen substitutions, than the pairing energy is lower than the energy cost of the triplet configuration and a singlet ground-state occurs. Thus the number and occupation of the π-orbitals drives the electronic structure in the examined mixed carbenes.

The phenyl group is an interesting substituent because it provides 6 π-orbitals and 6 π-electrons. This means that while the group has a strong π-interaction, the first available orbital to an unpaired electron is quite likely a relatively high-energy orbital. Despite have an extensive conjugated ring, the triplet configuration is slightly less favored than the singlet configuration. This can be thought of as a preservation of aromaticity, as mentioned in Chapter 6.

Substituents which have no significant π-interactions will only affect the σ-orbital energy, and likewise so will changes to the electron-withdrawing character of a substituent. Substituents of the formula $C(CX_3)$ or $Ph(CX_3)$ for example could be used to tune the electron-withdrawing (X=F) or donating (X=H) character without strongly affecting π-interactions. Substituted amines and ethers also make interesting targets with which to examine σ-effects, although additional acidic hydrogen does make the formation of carbene anions by H_2^+ less straightforward.

2.3 Relationship of π-Interactions in Carbenes to Methyl Radicals

Methyl radicals have a similar molecular orbital framework to carbenes. They are actually simpler in this sense that there is only one significant orbital to consider, the nominally singly-occupied π-orbital located in the carbon center. Rather than the ΔE_{S-T} defining the reactivity, a methyl radical is considered with respect to the parent methane through the BDE. The lower the BDE, the more stable the radical is. The key in stabilizing the radical is the π-orbital, which does not exist in the parent methane. Therefore, any π-interactions are likely to stabilize the radical and reduce the BDE. Further, since there is only one electronic state, the nominal doublet, the electronic configuration does not come into play for the reactivity.

Like the molecular orbital frame work, methyl radical stability can be explained with the two π-interactions of mixing orbitals and filling them with electrons. The 'mixed' methyl radicals of chlorocyanomethane and fluorocyanomethane both show that the combination of a π-donating and π-accepting substituent also for a very favorable combination of orbitals and total electrons in stabilized orbitals. As a result, these species showed an exceptionally low BDE. This was also characterized by the lack of 'saturation' in substituent effects. For all homogenously-substituted methanes, (IE. CH_3X, CH_2X_2, CHX_3) the effect of successive substitutions is less than the initial substitution. This can be seen in the molecular orbital framework as additional empty or full orbitals in the interaction create smaller changes to the energy of the final π-orbitals. This is mitigated in 'mixed' methanes by adding both empty and full π-orbitals, providing both a number of stabilized molecular orbitals and the electrons to occupy them. This creates a

synergistic stabilization which was noted by a radical stabilization which was greater than the sum of the individual substituent effects.

In this picture, the phenyl-group simply contributes 6 π-electrons which become stabilized after bond dissociation and mixing with the nominal π-orbital of the radical center. The result is that while the group slightly favors singlet carbene ground-states, the BDE of the parent phenylmethanes is exceptionally low. Despite this the comparison of chlorophenylmethane and cyanophneylmethane is not clear. While chlorophenylmethane displays synergistic stabilization of the radical, cyanophneylmethane does not. While this was addressed as viewing the phenyl-group as a π-accepting functionality, it is clear that the numerous interacting π-orbitals of a phenyl-ring make a straightforward picture impossible. One might consider that the difference in saturation versus synergy maybe be the proper overlap between the π-orbital of the substituent and those of the phenylmethyl radical. A proper test of this would be the BDE fluorophenymethane. If the phenyl-group acts primarily as a π-acceptor in methyl radicals, than this species should display synergistic stabilization in the BDE. If not, than the effects of the phenyl-group are more complex than π-accepting and donating. This in turn will need to be reflected in the effect on the carbene center. The electron-withdrawing ability of the ring may instead be the primary cause of the slight difference in $\Delta E_{S\text{-}T}$ from methylene, favoring a singlet ground-state

2.4 Future Work in Carbenes and Methyl Radicals

As stated above, the determination of the BDE for fluorophenylmethane would be extremely illuminating to the molecular orbital framework. The examined

phenylcarbenes are promising species where only experimental difficulties prevent definitive claims. In particular, applying the EOM-IP-CCSD and EOM-SF-CCSD where possible could very much aid in the positive identification of spectral features beyond what has been done. This is particularly important for the case of phenylcarbene, whose spectra indicate convoluted singlet and triplet transitions. Higher levels of calculation, combined with the Franck-Condon simulation of both transitions should offer much more than the initial observations.

3. Ethylenedione and Perturbation by Hydrogen

3.1 The Future of OCCO

The investigation of ethylenedione through anion photoelectron spectroscopy is for the most part complete. One shortcoming was the identification of the S_2 transition, which was only plausibly visible in the 532 nm spectrum, shown in Chapter 9. Certainly, further investigation of this binding energy region can be performed to definitively observe this transition.

The glaring questions left for the OCCO system are of course those revolving around the expected short lifetime of neutral triplet ethylenedione and the corresponding dissociation. Ultrafast spectroscopy of ethylenedione, prepared perhaps in the ground or first excited vibrational state of the Π_g wagging mode from the anion, could monitor the evolution of the OCCO population by photoionization or some other sensitive spectroscopic technique. Additionally, photoelectron-photofragment coincidence spectroscopy as developed by the Continetti group[240] would be immensely useful in

monitoring the energy flow from photoelectron detachment to the carbon monoxide fragments produced by the S_1 transition.

3.2 Differing Perturbations of OCCO by H and the Relationship to Glyoxal

The investigation of the radical HOCCO and OHCCO makes an interesting parallel to OCCO and glyoxal, $(OHC)_2$. On one hand OHCCO is the direct radical product formed from H• abstraction from glyoxal. This product is likely relatively unstable, similar the OCCO, since the neutral can be described as a stable formyl radical and carbon monoxide. The heavily distorted geometry as compared to glyoxal or OCCO does set this species apart from the related compounds. However, the electron affinity can be determined as approximately <1 eV, meaning that if a gas-phase acidity can be determined for glyoxal then Hess's Law can determine the BDE.

In another view, HOCCO and OHCCO are products of binding a H• radical to the ethylenedione diradical, OCCO. For HOCCO, the resulting perturbation is relatively small. The hydrogen bonding to the oxygen disrupts the degeneracy of the two π-orbitals which are oriented orthogonally in OCCO. However, there remains a degree of conjugation similar to the trans-geometry of ethylenedione anion. Like the carbenes and methyl radicals derived from the same parent molecules, adding hydrogen simplifies the electronic structure. When moving from carbene to methyl radical, the low-lying singlet and triplet states are replaced with a doublet ground-state. While ethylenedione diradical has a very dense manifold, the effect is rather similar; the 4 low-lying states become 2 doublet states. Interestingly, the new doublet and excited doublet states have parallels to

the primary electronic configurations determined by EOM-SF-CCSD for OCCO at the anion geometry. Considering the HOMO and HOMO-1 of both systems, the ground-state triplet of OCCO and the ground-state doublet both have a single electron occupation in the HOMO. We might consider than the HOMO-1 is the perturbed π-orbital which the addition of hydrogen affects directly. This occupation is also 'identical' to the ethylenedione anion and can be linked to the preservation of the trans-geometry of the O-C-C-O frame. The excited-state doublet of HOCCO has a doubly-occupied HOMO which parallels the S_3 excited singlet configuration of OCCO. Further, the position of these bands is very similar and very much like the comparison of the ground-states. This parallel is rather striking and further highlights the relatively minor perturbation induced to OCCO by the terminal hydrogen.

In stark contrast, the addition of hydrogen to the carbon frame of OCCO disrupts the molecule severely. Unlike the highly-conjugated ethylenedione, the OHCCO ground-state is more reminiscent of a radical center localized on a single carbon. As a result, the geometry change this carbon of trigonal pyramidal to trigonal planar has much more in common with many of the methyl radicals examined in Chapter 7. The only likely direct comparison to OCCO is to the dissociative singlet state, based on the broad and unresolved band visible in the 532 nm spectrum in Chapter 10. This major perturbation is what characterizes OHCCO as the direct radical of glyoxal more than any analogue of OCCO.

3.3 Further Work

The most direct analogs to OCCO are those which substitute oxygen for sulfur, OCCS and SCCS, of which both have been experimentally observed.[183] Sulfur-substituted glyoxals exist for both of these compounds, making them very probably targets for anion formation by H_2^+ abstraction by O^-. While isoelectronic to OCCO, the electronic structure should be sufficiently interesting. As a possible analog, dicyanoacetylene shares a similar motif to ethylenedione. Particularly in the anionic state, both species have a trans-geometry. However, due to the cyano-group, the singlet has the linear geometry, not the triplet. While the $\Delta E_{S\text{-}T}$ is considerable and limits the number of transitions which are accessible given the current photon energies, dicyanoacetylene is an important and interesting species in its own right.

The curious fact that $HOCCO^-$ seems to be the dominate species in the m/z 57 anion packet rather than $OHCCO^-$ has yet to be explored beyond speculation. Certainly, this chemistry is important to the overall reactivity of glyoxal. Additionally, choosing a target molecule which primarily forms $OHCCO^-$ would be of value to study the electronic structure of this 'true' radical of glyoxal.

4. Other Future Areas of Interest

Radicals and diradicals represent a massively large class of molecules which are very applicable to study by anion photoelectron velocity-map imaging. In particular, the O^- abstraction of H^+ and H_2^+ are extremely useful in preparing anions of numerous, unstable or fleeting radical species. Small molecules containing amines or substituted amines in particular offer chances to form species which contain nitrogen without the

cyano-group common to many molecules in this thesis. Phosphorous and sulfur are other atoms which are underrepresented. The phosphorous analogs of CN and CCN are of astrochemical interest, and should be simple targets in the gas-phase, as would many small phosphorous-containing molecules. The carbon monophosphide group as a replacement for the cyano-group in cyanocarbene, dicyanocarbene, cyanomethyl radical, etc would be interesting to examine and should have similar experimental methodologies to their counterparts.

An area which may be accessible would be other homo-molecularly solvated substituted aromatics. Given dimers have been observed for benzonitrile and nitrobenzene,[59] it is logical to attempt a search for the dicyano- and dinitrobenzene dimers in addition to other those of other substituted benzenes. While it is has been shown computationally that stacked benzene rings avoid local substituent interactions,[86] there is still much to test in this theory and to perhaps find substituents or substituent pairs which defy this expectation.

Appendix I: Structures and Electronic Energies of Systems Discussed in Chapter 3

Table of Contents:

A. Fully relaxed geometry of the benzonitrile (bn) neutral species, optimized in Q-Chem 4.0 at the CCSD level theory and the aug-cc-pVDZ basis set. The total electronic energy, without ZPE correction, is reported in Hartrees.

1 C
2 C 1 1.40990
3 H 2 1.09230 1 119.759
4 C 2 1.40291 1 119.415 3 -180.000 0
5 H 4 1.09270 2 119.711 1 -180.000 0
6 C 4 1.40574 2 120.161 1 0.00000 0
7 H 6 1.09305 4 119.901 2 -180.000 0
8 C 6 1.40574 4 120.198 2 0.00000 0
9 H 8 1.09270 6 120.128 4 -180.000 0
10 C 8 1.40291 6 120.161 4 0.00000 0
11 H 10 1.09230 8 120.826 6 -180.000 0
12 C 1 1.45395 2 119.675 3 0.00000 0
13 N 12 1.17147 1 180.000 2 0.00000 0

Total Electronic Energy: -323.613498083 au

B. Fully relaxed geometry of the bn^{-} (valence) species, optimized in Q-Chem 4.0 at the CCSD level theory and the aug-cc-pVDZ basis set. The total electronic energy, without ZPE correction, is reported in Hartrees.

1 C
2 C 1 1.41451
3 N 2 1.18940 1 180.000
4 C 1 1.45436 2 121.428 3 0.00000 0
5 H 4 1.09537 1 119.085 1 0.00000 0
6 C 4 1.38599 1 120.792 1 0.00000 0
7 H 6 1.09737 4 118.671 1 0.00000 0
8 C 6 1.43394 4 121.908 1 0.00000 0
9 H 8 1.09334 6 121.272 1 0.00000 0
10 C 8 1.43394 6 117.456 1 0.00000 0
11 H 10 1.09737 8 119.421 1 0.00000 0
12 C 10 1.38599 8 121.908 1 0.00000 0
13 H 12 1.09537 10 120.123 1 0.00000 0

Total Electronic Energy: -323.605741882 au

C. Total electronic energies without ZPE correction for the fully relaxed neutral and anionic bn species at the M06-2X/6-311++G** level of theory and basis, implemented in the Gaussian 09 software.

Anion: -324.4396368 au
Neutral: -324.4377007 au

D. Fully relaxed geometry of the (a) dimer at the M06-2X/6-311++G** level of theory and basis, implemented in the Gaussian 09 software. The total electronic energy, without ZPE correction, is reported in Hartrees.

Center Number	Atomic Number	Atomic Type	Coordinates (Angstroms) X	Y	Z
1	6	0	0.000000	0.000000	-3.675902
2	6	0	0.000000	0.000000	-6.532238
3	6	0	0.000000	1.229924	-4.428115
4	6	0	0.000000	-1.229924	-4.428115
5	6	0	0.000000	-1.212404	-5.801085
6	6	0	0.000000	1.212404	-5.801085
7	1	0	0.000000	2.158334	-6.335704
8	1	0	0.000000	0.000000	-7.614527
9	1	0	0.000000	-2.158334	-6.335704
10	1	0	0.000000	-2.172257	-3.891378
11	1	0	0.000000	2.172257	-3.891378
12	6	0	0.000000	0.000000	-2.282925
13	7	0	0.000000	0.000000	-1.110487
14	6	0	0.000000	0.000000	4.932792
15	6	0	0.000000	0.000000	2.143045
16	6	0	0.000000	1.213047	4.235424
17	6	0	0.000000	-1.213047	4.235424
18	6	0	0.000000	-1.203670	2.847984
19	6	0	0.000000	1.203670	2.847984
20	1	0	0.000000	2.139573	2.302203
21	1	0	0.000000	0.000000	1.055084
22	1	0	0.000000	-2.139573	2.302203
23	1	0	0.000000	-2.145059	4.787821
24	1	0	0.000000	2.145059	4.787821
25	6	0	0.000000	0.000000	6.367939
26	7	0	0.000000	0.000000	7.520029

Total Electronic Energy: -648.8941104 au

E. Fully relaxed geometry of the (b) dimer (Figure 10) at the M06-2X/6-311++G** level of theory and basis, implemented in the Gaussian 09 software. The total electronic energy, without ZPE correction, is reported in Hartrees.

Center Number	Atomic Number	Atomic Type	Coordinates (Angstroms) X	Y	Z
1	6	0	4.710876	-0.051040	-0.000135
2	6	0	3.826318	-1.109853	-0.000084
3	6	0	2.427721	-0.867854	0.000191
4	6	0	1.964548	0.473456	0.000405
5	6	0	2.867149	1.518942	0.000342
6	6	0	4.249053	1.277513	0.000082
7	1	0	5.777259	-0.251496	-0.000303
8	1	0	4.187833	-2.131615	-0.000221
9	1	0	0.903858	0.686280	0.000557
10	1	0	2.480717	2.532219	0.000454
11	1	0	4.951269	2.102047	0.000030
12	6	0	1.503325	-1.939320	0.000138
13	7	0	0.722013	-2.798939	-0.000004
14	6	0	-1.963881	-0.472697	-0.000591
15	6	0	-2.865622	-1.518978	-0.000356
16	6	0	-4.247646	-1.278612	0.000182
17	6	0	-4.710591	0.049498	0.000504
18	6	0	-3.826850	1.109041	0.000290
19	6	0	-2.428169	0.868092	-0.000265
20	1	0	-0.903073	-0.684790	-0.000967
21	1	0	-2.478293	-2.531908	-0.000547
22	1	0	-4.949206	-2.103709	0.000365
23	1	0	-5.777130	0.249077	0.000884
24	1	0	-4.189144	2.130521	0.000511
25	6	0	-1.504551	1.940380	-0.000379
26	7	0	-0.724039	2.800649	-0.000382

Total Electronic Energy: -648.8890116 au

F. Fully relaxed geometry of the (c) dimer (Figure 10) at the M06-2X/6-311++G** level of theory and basis, implemented in the Gaussian 09 software. The total electronic energy, without ZPE correction, is reported in Hartrees.

Center Number	Atomic Number	Coordinates (Angstroms) X	Y	Z
1	6	-2.508587	1.161192	-0.011525
2	6	-1.805385	1.322633	-1.216489
3	6	-0.456723	1.611031	-1.218138
4	6	0.242363	1.762232	0.005240
5	6	-0.471255	1.608798	1.220228
6	6	-1.819847	1.320573	1.201729
7	1	-3.566534	0.929674	-0.017929
8	1	-2.318636	1.191372	-2.163451
9	1	0.082701	1.717850	-2.152088
10	1	0.056892	1.714324	2.160722
11	1	-2.344390	1.187621	2.142248
12	6	1.611228	2.138032	0.013892
13	7	2.714427	2.493397	0.021463
14	6	-1.780721	-2.037177	0.001298
15	6	-1.079548	-1.910385	-1.208472
16	6	0.274955	-1.649716	-1.220442
17	6	0.984707	-1.511916	-0.002178
18	6	0.278124	-1.649276	1.217684
19	6	-1.076422	-1.909631	1.209525
20	1	-2.844981	-2.236514	0.002612
21	1	-1.610269	-1.991417	-2.151386
22	1	0.806692	-1.537946	-2.158177
23	1	0.812238	-1.537162	2.154042
24	1	-1.604679	-1.990589	2.153815
25	6	2.392083	-1.321768	-0.004313
26	7	3.545734	-1.215532	-0.006983

Total Electronic Energy: -648.8987256 au

G. Fully relaxed geometry of the (d) dimer (Figure 10c) at the M06-2X/6-311++G** level of theory and basis, implemented in the Gaussian 09 software. The total electronic energy, without ZPE correction, is reported in Hartrees.

Center Number	Atomic Number	Coordinates (Angstroms) X	Y	Z
1	6	0.606522	2.233180	-0.000113
2	6	-0.016646	1.888990	1.209065
3	6	-1.197966	1.176441	1.219819
4	6	-1.810550	0.793155	-0.000042
5	6	-1.197916	1.176234	-1.219943
6	6	-0.016591	1.888783	-1.209253
7	1	1.552958	2.758653	-0.000136
8	1	0.455273	2.148935	2.150606
9	1	-1.656167	0.882221	2.157063
10	1	-1.656074	0.881857	-2.157158
11	1	0.455370	2.148555	-2.150820
12	6	-3.014957	0.044113	-0.000001
13	7	-4.019771	-0.537725	0.000166
14	6	-0.607018	-2.232297	0.000185
15	6	0.016486	-1.888506	1.209331
16	6	1.198217	-1.176671	1.219976
17	6	1.810890	-0.793719	0.000022
18	6	1.198246	-1.176997	-1.219843
19	6	0.016513	-1.888833	-1.209037
20	1	-1.554003	-2.756775	0.000247
21	1	-0.455455	-2.148290	2.150908
22	1	1.656835	-0.882914	2.157166
23	1	1.656897	-0.883512	-2.157102
24	1	-0.455391	-2.148892	-2.150557
25	6	3.014989	-0.044234	-0.000061
26	7	4.019548	0.538056	-0.000288

Total Electronic Energy: -648.9064308 au

H. Fully relaxed geometry of the (e) dimer (Figure 10) at the M06-2X/6-311++G** level of theory and basis, implemented in the Gaussian 09 software. The total electronic energy, without ZPE correction, is reported in Hartrees.

Center Number	Atomic Number	Coordinates (Angstroms) X	Y	Z
1	6	-1.383384	1.075307	1.861806
2	6	-1.970099	0.218646	0.954897
3	6	-1.701265	0.361117	-0.432145
4	6	-0.836453	1.396975	-0.859312
5	6	-0.259439	2.244577	0.065044
6	6	-0.510547	2.089309	1.436350
7	1	-1.577812	0.938874	2.920622
8	1	-2.619927	-0.581038	1.290080
9	1	-0.604150	1.499782	-1.913179
10	1	0.428052	3.008590	-0.281614
11	1	-0.040981	2.746656	2.158177
12	6	-2.272877	-0.540066	-1.366582
13	7	-2.762847	-1.269136	-2.125636
14	6	0.841814	-1.415663	-0.821044
15	6	0.257537	-2.241710	0.118128
16	6	0.498710	-2.055479	1.487349
17	6	1.368823	-1.032288	1.896044
18	6	1.962584	-0.196698	0.974223
19	6	1.704424	-0.370989	-0.411253
20	1	0.616850	-1.542199	-1.873928
21	1	-0.427961	-3.013003	-0.216083
22	1	0.023065	-2.695748	2.220400
23	1	1.555224	-0.871475	2.952879
24	1	2.609796	0.610636	1.295844
25	6	2.284485	0.508090	-1.361336
26	7	2.781699	1.219443	-2.132394

Total Electronic Energy: -648.9064448

I. Fully relaxed geometry of the (b) dimer (Figure 13) at the M06-2X/6-311++G** level of theory and basis, implemented in the Gaussian 09 software. The total electronic energy, without ZPE correction, is reported in Hartrees.

Center Number	Atomic Number	Atomic Type	Coordinates (Angstroms) X	Y	Z
1	6	0	-1.180762	1.418200	1.857360
2	6	0	-1.733828	0.412263	1.077087
3	6	0	-1.624685	0.485522	-0.313376
4	6	0	-0.962463	1.555727	-0.920489
5	6	0	-0.404190	2.550435	-0.129734
6	6	0	-0.515237	2.483180	1.256538
7	1	0	-1.262386	1.366220	2.936419
8	1	0	-2.241405	-0.429930	1.531092
9	1	0	-0.869226	1.589892	-1.999239
10	1	0	0.130557	3.367412	-0.598077
11	1	0	-0.078810	3.262395	1.870293
12	6	0	-2.162518	-0.573054	-1.123424
13	7	0	-2.571347	-1.434168	-1.767934
14	6	0	0.968734	-1.575858	-0.877300
15	6	0	0.404400	-2.552349	-0.068351
16	6	0	0.505070	-2.453602	1.316827
17	6	0	1.166213	-1.375216	1.898262
18	6	0	1.725252	-0.387255	1.099497
19	6	0	1.626550	-0.492114	-0.289721
20	1	0	0.883572	-1.634539	-1.955664
21	1	0	-0.126944	-3.379770	-0.522002
22	1	0	0.063954	-3.218686	1.944844
23	1	0	1.239758	-1.298725	2.976442
24	1	0	2.229538	0.465051	1.538035
25	6	0	2.170747	0.547714	-1.119561
26	7	0	2.584778	1.393767	-1.780489

Total Electronic Energy: -648.8875517 au

J. Fully relaxed geometry of the (d) dimer (Figure 13) at the M06-2X/6-311++G** level of theory and basis, implemented in the Gaussian 09 software. The total electronic energy, without ZPE correction, is reported in Hartrees.

Center Number	Atomic Number	Atomic Type	Coordinates (Angstroms) X	Y	Z
1	6	0	0.628204	2.624039	0.000002
2	6	0	0.077419	2.202684	1.207040
3	6	0	-1.018594	1.350959	1.212768
4	6	0	-1.564264	0.922668	0.000114
5	6	0	-1.018319	1.350448	-1.212599
6	6	0	0.077690	2.202177	-1.206984
7	1	0	1.498165	3.269397	-0.000041
8	1	0	0.509826	2.530954	2.144306
9	1	0	-1.450824	1.005080	2.143943
10	1	0	-1.450344	1.004180	-2.143724
11	1	0	0.510315	2.530052	-2.144288
12	6	0	-2.675522	0.011523	0.000182
13	7	0	-3.555666	-0.729828	0.000222
14	6	0	-0.628160	-2.624091	0.000108
15	6	0	-0.077610	-2.202171	1.207054
16	6	0	1.018368	-1.350395	1.212597
17	6	0	1.564246	-0.922634	-0.000149
18	6	0	1.018529	-1.350973	-1.212769
19	6	0	-0.077449	-2.202740	-1.206969
20	1	0	-1.498094	-3.269485	0.000205
21	1	0	-0.510172	-2.530040	2.144390
22	1	0	1.450421	-1.004089	2.143695
23	1	0	1.450705	-1.005101	-2.143970
24	1	0	-0.509888	-2.531053	-2.144205
25	6	0	2.675526	-0.011516	-0.000293
26	7	0	3.555731	0.729762	-0.000436

Total Electronic Energy: -648.8875863 au

Appendix II: Structures and Electronic Energies of Phenylmethyl Radicals Discussed in Chapter 7

Table of Contents:

K. Fully relaxed geometry of cyanophenylmethyl radical optimized with the B3LYP/aug-cc-pVQZ theory and basis, implemented in the Gaussian 09 software. The total electronic energy, without ZPE correction, is reported in Hartrees.

Center Number	Atomic Number	Atomic Type	Coordinates (Angstroms) X	Y	Z
1	6	0	1.449175	1.435422	0.000011
2	6	0	0.141993	0.991808	0.000007
3	6	0	-0.146480	-0.393407	0.000000
4	6	0	0.938124	-1.301757	-0.000003
5	6	0	2.241338	-0.845905	0.000001
6	6	0	2.505853	0.523742	0.000008
7	1	0	1.653989	2.496882	0.000016
8	1	0	-0.674129	1.700765	0.000009
9	1	0	0.734195	-2.364084	-0.000008
10	1	0	3.058589	-1.553530	-0.000001
11	1	0	3.526881	0.878204	0.000011
12	6	0	-1.476452	-0.890342	-0.000004
13	1	0	-1.644258	-1.958463	-0.000010
14	6	0	-2.611457	-0.077373	-0.000006
15	7	0	-3.558262	0.592442	-0.000013

Total Electronic Energy: -363.3235103 au

L. Fully relaxed geometry of cyanophenylmethyl radical anion optimized with the B3LYP/aug-cc-pVQZ theory and basis, implemented in the Gaussian 09 software. The total electronic energy, without ZPE correction, is reported in Hartrees.

Center Number	Atomic Number	Atomic Type	Coordinates (Angstroms) X	Y	Z
1	6	0	1.474672	1.419257	0.000012
2	6	0	0.162045	0.985157	0.000005
3	6	0	-0.172389	-0.400671	-0.000010
4	6	0	0.938490	-1.293897	-0.000004
5	6	0	2.245792	-0.844853	0.000004
6	6	0	2.546152	0.520682	0.000008
7	1	0	1.672213	2.485996	0.000019
8	1	0	-0.641806	1.709985	0.000008
9	1	0	0.742447	-2.360334	-0.000007
10	1	0	3.051618	-1.571372	0.000005
11	1	0	3.570200	0.869175	0.000010
12	6	0	-1.503653	-0.884724	-0.000012
13	1	0	-1.672290	-1.953383	-0.000007
14	6	0	-2.630440	-0.071429	-0.000002
15	7	0	-3.583771	0.606115	-0.000004

Total Electronic Energy: -363.395154 au

M. Fully relaxed geometry of chlorophenylmethyl radical optimized with the B3LYP/aug-cc-pVQZ theory and basis, implemented in the Gaussian 09 software. The total electronic energy, without ZPE correction, is reported in Hartrees.

Center Number	Atomic Number	Atomic Type	Coordinates (Angstroms) X	Y	Z
1	6	0	-1.650286	-1.394444	0.000015
2	6	0	-0.320039	-1.021513	0.000013
3	6	0	0.044031	0.347676	0.000024
4	6	0	-1.000416	1.310773	0.000003
5	6	0	-2.323856	0.921388	0.000002
6	6	0	-2.662055	-0.433573	0.000017
7	1	0	-1.907855	-2.445216	0.000020
8	1	0	0.455014	-1.773742	0.000013
9	1	0	-0.745455	2.362547	-0.000005
10	1	0	-3.102506	1.672320	-0.000003
11	1	0	-3.700065	-0.735706	0.000018
12	6	0	1.373383	0.803464	0.000011
13	1	0	1.626869	1.850927	-0.000011
14	17	0	2.741731	-0.243162	-0.000032

Total Electronic Energy: -730.6505551 au

N. Fully relaxed geometry of chlorophenylmethyl radical anion optimized with the B3LYP/aug-cc-pVQZ theory and basis, implemented in the Gaussian 09 software. The total electronic energy, without ZPE correction, is reported in Hartrees.

Center Number	Atomic Number	Atomic Type	Coordinates (Angstroms) X	Y	Z
1	6	0	-1.651103	-1.387984	0.000010
2	6	0	-0.322947	-1.005734	0.000004
3	6	0	0.069499	0.379632	-0.000005
4	6	0	-1.034488	1.312312	-0.000005
5	6	0	-2.347091	0.899699	0.000000
6	6	0	-2.700317	-0.461329	0.000009
7	1	0	-1.880987	-2.449939	0.000018
8	1	0	0.450003	-1.762132	0.000005
9	1	0	-0.811069	2.374104	-0.000011
10	1	0	-3.128583	1.654424	0.000001
11	1	0	-3.735222	-0.776664	0.000016
12	6	0	1.369079	0.842292	-0.000036
13	1	0	1.664474	1.876332	0.000007
14	17	0	2.773270	-0.258203	0.000006

Total Electronic Energy: -730.691334 au

References

(1) Yang, X.; Castleman, A. W. *Journal of the American Chemical Society* **1991**, *113*, 6766.

(2) Jungwirth, P.; Tobias, D. J. *Journal of Physical Chemistry B* **2002**, *106*, 6361.

(3) Hodges, R. V.; Lee, L. C.; Moseley, J. T. *Journal of Chemical Physics* **1980**, *72*, 2998.

(4) Fehsenfeld, F. C.; Ferguson, E. E. *Journal of Chemical Physics* **1974**, *61*, 3181.

(5) Vuitton, V.; Lavvas, P.; Yelle, R. V.; Galand, M.; Wellbrock, A.; Lewis, G. R.; Coates, A. J.; Wahlund, J. E. *Planetary and Space Science* **2009**, *57*, 1558.

(6) Tulej, M.; Kirkwood, D. A.; Pachkov, M.; Maier, J. P. *Astrophysical Journal* **1998**, *506*, L69.

(7) Cogan, S.; Zilberg, S.; Haas, Y. *Journal of the American Chemical Society* **2006**, *128*, 3335.

(8) Klaboe, P. *Journal of the American Chemical Society* **1962**, *84*, 3458.

(9) Seburg, R. A.; Hill, B. T.; Squires, R. R. *Journal of the Chemical Society-Perkin Transactions 2* **1999**, 2249.

(10) Tomioka, H. *Accounts of Chemical Research* **1997**, *30*, 315.

(11) Mabbs, R.; Grumbling, E. R.; Pichugin, K.; Sanov, A. *Chemical Society Reviews* **2009**, *38*, 2169.

(12) Thoman, J. W.; Chandler, D. W.; Parker, D. H.; Janssen, M. H. M. *Laser Chemistry* **1988**, *9*, 27.

(13) Chandler, D. W.; Houston, P. L. *Journal of Chemical Physics* **1987**, *87*, 1445.

(14) Bordas, C.; Paulig, F.; Helm, H.; Huestis, D. L. *Review of Scientific Instruments* **1996**, *67*, 2257.

(15) Eppink, A. T. J. B.; Parker, D. H. *Review of Scientific Instruments* **1997**, *68*, 3477.

(16) Parker, D. H.; Eppink, A. T. J. B. *Journal Of Chemical Physics* **1997**, *107*, 2357.

(17) Heck, A. J. R.; Chandler, D. W. *Annual Review of Physical Chemistry* **1995**, *46*, 335.

(18) Cooper, J.; Zare, R. N. *J. Chem. Phys.* **1968**, *48*, 942.

(19) Cooper, J.; Zare, R. N. *J. Chem. Phys.* **1968**, *49*, 4252.

(20) Cooper, J.; Zare, R. N. Photoelectron angular distributions. In *Atomic collision processes*; Geltman, S., Mahanthappa, K. T., Brittin, W. E., Eds.; Gordon and Breach, Science Publishers: New York, London, Paris, 1968; Vol. XI-C; pp 317.

(21) Surber, E.; Mabbs, R.; Sanov, A. *J. Phys. Chem. A* **2003**, *107*, 8215.

(22) Sanov, A.; Mabbs, R. *International Reviews in Physical Chemistry* **2008**, *27*, 53.

(23) Culberson, L. M.; Wallace, A. A.; Blackstone, C. C.; Khuseynov, D.; Sanov, A. *Physical Chemistry Chemical Physics* **2014**, *16*, 3964.

(24) Khuseynov, D.; Blackstone, C. C.; Culberson, L. M.; Sanov, A. *Journal of Chemical Physics* **2014**, *141*, 124312.

(25) Krylov, A. I. *Annual Review of Physical Chemistry* **2008**, *59*, 433.

(26) Shao, Y.; Molnar, L. F.; Jung, Y.; Kussmann, J.; Ochsenfeld, C.; Brown, S. T.; Gilbert, A. T. B.; Slipchenko, L. V.; Levchenko, S. V.; O'Neill, D. P.; DiStasio, R. A.; Lochan, R. C.; Wang, T.; Beran, G. J. O.; Besley, N. A.; Herbert, J. M.; Lin, C. Y.; Van Voorhis, T.; Chien, S. H.; Sodt, A.; Steele, R. P.; Rassolov, V. A.; Maslen, P. E.; Korambath, P. P.; Adamson, R. D.; Austin, B.; Baker, J.; Byrd, E. F. C.; Dachsel, H.; Doerksen, R. J.; Dreuw, A.; Dunietz, B. D.; Dutoi, A. D.; Furlani, T. R.; Gwaltney, S. R.; Heyden, A.; Hirata, S.; Hsu, C. P.; Kedziora, G.; Khalliulin, R. Z.; Klunzinger, P.; Lee, A. M.; Lee, M. S.; Liang, W.; Lotan, I.; Nair, N.; Peters, B.; Proynov, E. I.; Pieniazek, P. A.; Rhee, Y. M.; Ritchie, J.; Rosta, E.; Sherrill, C. D.; Simmonett, A. C.; Subotnik, J. E.; Woodcock, H. L.; Zhang, W.; Bell, A. T.; Chakraborty, A. K.; Chipman, D. M.; Keil, F. J.; Warshel, A.; Hehre, W. J.; Schaefer, H. F.; Kong, J.; Krylov, A. I.; Gill, P. M. W.; Head-Gordon, M. *Physical Chemistry Chemical Physics* **2006**, *8*, 3172.

(27) Erdman, P. W.; Zipf, E. C. *Review of Scientific Instruments* **1982**, *53*, 225.

(28) Heddle, D. W. O. "Tables of Focal Properties of Three-Element Electrostatic Cyclinder Lenses," Joint Institute for Laboratory Astrophysics, 1970.

(29) Sumalekshmy, S.; Gopidas, K. R. *Journal of Physical Chemistry B* **2004**, *108*, 3705.

(30) Liu, M. S.; Jiang, X.; Liu, S.; Herguth, P.; Jen, A. K.-Y. *Macromolecules* **2002**, *35*, 3532.

(31) Giacalone, F.; Segura, J. L.; Mart, N.; Ramey, J.; Guldi, D. M. *Chemistry-A European Journal* **2005**, *11*, 4819

(32) Mishchenko, A.; Zotti, L. A.; Vonlanthen, D.; Burkle, M.; Pauly, F.; Cuevas, J. C.; Mayor, M.; Wandlowski, T. *Journal of the American Chemical Society* **2011**, *133*, 184.

(33) Aguiar, A. L.; Fagan, S. B.; Silva, L. B. d.; Filho, J. M.; Filho, A. G. S. *Journal of Physical Chemistry C* **2010**, *114*, 10790.

(34) Tao, F.; Wang, Z. H.; Xu, G. Q. *Journal of Physical Chemistry B* **2002**, *106*, 3557.

(35) Okuno, Y.; Yokoyama, T.; Yokoyama, S.; Kamikado, T.; Mashiko, S. *124* **2002**, 7218.

(36) Solomun, T.; Christmann, K.; Baumgartel, H. *Journal of Physical Chemistry* **1989**, *93*, 7199.

(37) Woon, D. E. *Chemical Physics Letters* **2006**, *331*, 67.

(38) Trevitt, A. J.; Goulay, F.; Taatjes, C. A.; Osborn, D. L.; Leone, S. R. *Journal of Physical Chemistry A* **2010**, *114*, 1749.

(39) Kirnosov, N.; Adamowicz, L. *private communication*.

(40) Desfrancois, C.; Abdoul-Carime, H.; Schermann, J. P. *International Journal Of Modern Physics B* **1996**, *10*, 1339.

(41) Jordan, K. D.; Wang, F. *Annual Review of Physical Chemistry* **2003**, *54*, 367.

(42) Ziatkis, A.; Lee, C. K.; Wentworth, W. E.; Chen, E. C. M. *Analytical Chemistry* **1983**, *55*, 1596.

(43) Wentworth, W. E.; Kao, L. W.; Becker, R. S. *Journal of Physical Chemistry* **1975**, *79*, 1161.

(44) Burrow, P. D.; Howard, A. E.; Johnston, A. R.; Jordan, K. D. *Journal of Physical Chemistry* **1992**, *96*, 7570.

(45) Maus, M.; Rettig, W.; Bonafoux, D.; Lapouyade, R. *Journal of Physical Chemistry A* **1999**, *103*, 3388.

(46) Lewis, F. D.; Holman, B. *Journal of Physical Chemistry* **1980**, *84*, 2326.

(47) Hirt, R. C.; Howe, J. P. *Journal of Chemical Physics* **1948**, *16*, 480.

(48) Huang, K. T.; Lombardi, J. R. *Journal of Chemical Physics* **1971**, *55*, 4072.

(49) Velarde, L.; Habteyes, T.; Sanov, A. *Journal of Chemical Physics* **2006**, *125*, 114303.

(50) Johnson, M. A.; Lineberger, W. C. Pulsed Methods for Cluster Ion Spectroscopy. In *Techniques for the Study of Ion Molecule Reactions*; Farrar, J. M., Saunders, W. H., Eds.; Wiley: New York, 1988; pp 591.

(51) Dribinski, V.; Ossadtchi, A.; Mandelshtam, V. A.; Reisler, H. *Review of Scientific Instruments* **2002**, *73*, 2634.

(52) Neumark, D. M.; Lykke, K. R.; Andersen, T.; Lineberger, W. C. *Physical Review A* **1985**, *32*, 1890.

(53) Cavanagh, S. J.; Gibson, S. T.; Gale, M. N.; Dedman, C. J.; Roberts, E. H.; Lewis, B. R. *Physical Review A* **2007**, *76*, 052708.

(54) Frisch, M. J.; Trucks, G. W.; Schlegel, H. B.; Scuseria, G. E.; Robb, M. A.; Cheeseman, J. R.; Scalmani, G.; Barone, V.; Mennucci, B.; Petersson, G. A.; Nakatsuji, H.; Caricato, M.; Li, X.; Hratchian, H. P.; Izmaylov, A. F.; Bloino, J.; Zheng, G.; Sonnenberg, J. L.; Hada, M.; Ehara, M.; Toyota, K.; Fukuda, R.; Hasegawa, J.;

Ishida, M.; Nakajima, T.; Honda, Y.; Kitao, O.; Nakai, H.; Vreven, T.; Montgomery, J., J. A.; Peralta, J. E.; Ogliaro, F.; Bearpark, M.; Heyd, J. J.; Brothers, E.; Kudin, K. N.; Staroverov, V. N.; Kobayashi, R.; Normand, J.; Raghavachari, K.; Rendell, A.; Burant, J. C.; Iyengar, S. S.; Tomasi, J.; Cossi, M.; Rega, N.; Millam, N. J.; Klene, M.; Knox, J. E.; Cross, J. B.; Bakken, V.; Adamo, C.; Jaramillo, J.; Gomperts, R.; Stratmann, R. E.; Yazyev, O.; Austin, A. J.; Cammi, R.; Pomelli, C.; Ochterski, J. W.; Martin, R. L.; Morokuma, K.; Zakrzewski, V. G.; Voth, G. A.; Salvador, P.; Dannenberg, J. J.; Dapprich, S.; Daniels, A. D.; Farkas, Ö.; Foresman, J. B.; Ortiz, J. V.; Cioslowski, J.; Fox, D. J. Gaussian 09; Revision A.1 ed.; Gaussian, Inc.: Wallingford, CT, 2009.

(55) Ervin, K. M.; Ramond, T. M.; Davico, G. E.; Schwartz, R. L.; Casey, S. M.; Lineberger, W. C. *Journal of Physical Chemistry A* **2001**, *105*, 10822.

(56) Khuseynov, D.; Dixon, A. R.; Dokuchitz, D. J.; Sanov, A. *Journal of Physical Chemistry A* **2014**, *118*, 4510.

(57) Khuseynov, D.; Fontana, M.; Sanov, A. *Chem. Phys. Lett.* **2012**, *550*, 15.

(58) Maeyama, T.; Yagi, I.; Murota, Y.; Fujii, A.; Mikami, N. *Journal of Physical Chemistry A* **2006**, *110*, 13712.

(59) Desfrancois, C.; Periquet, V.; Lyapustina, S. A.; Lippa, T. P.; Robinson, D. W.; Bowen, K. H.; Nonaka, H.; Compton, R. N. *Journal of Chemical Physics* **1999**, *111*, 4569.

(60) Ervin, K. M.; Anusiewicz, W.; Skurski, P.; Simons, J.; Lineberger, W. C. *Journal of Physical Chemistry A* **2003**, *107*, 8521.

(61) Sherwood, C. R.; Continetti, R. E. *Chemical Physics Letters* **1996**, *258*, 171.

(62) Sherwood, C. R.; Hanold, K. A.; Garner, M. C.; Strong, K. M.; Continetti, R. E. *Journal Of Chemical Physics* **1996**, *105*, 10803.

(63) Akin, F. A.; Schirra, L. K.; Sanov, A. *Journal of Physical Chemistry A* **2006**, *110*, 8031.

(64) Goebbert, D. J.; Sanov, A. *Journal of Chemical Physics* **2009**, *131*, 104308.

(65) Mabbs, R.; Mbaiwa, F.; Wei, J.; Van Duzor, M.; Gibson, S. T.; Cavanagh, S. J.; Lewis, B. R. *Physical Review A* **2010**, *82*, 011401.

(66) Van Duzor, M.; Mbaiwa, F.; Wei, J.; Singh, T.; Mabbs, R.; Sanov, A.; Cavanagh, S. J.; Gibson, S. T.; Lewis, B. R.; Gascooke, J. R. *Journal of Chemical Physics* **2010**, *133*, 174311.

(67) Khuseynov, D.; Goebbert, D. J.; Sanov, A. *Journal of Chemical Physics* **2012**, *136*, 094312.

(68) Sommerfeld, T.; Knecht, S. *European Physical Journal D* **2005**, *35*, 207.

(69) Goebbert, D. J.; Khuseynov, D.; Sanov, A. *Journal of Chemical Physics* **2009**, *131*, 161102.

(70) Goebbert, D. J.; Khuseynov, D.; Sanov, A. *Journal of Physical Chemistry A* **2010**, *114*, 2259.

(71) Compton, R. N.; Carman, H. S.; Desfrancois, C.; Abdoulcarmine, H.; Schermann, J. P.; Hendricks, J. H.; Lyapustina, S. A.; Bowen, K. H. *Journal Of Chemical Physics* **1996**, *105*, 3472.

(72) Hendricks, J. H.; Lyapustina, S. A.; Declercq, H. L.; Bowen, K. H. *Journal Of Chemical Physics* **1998**, *108*, 8.

(73) Hammer, N. I.; Hinde, R. J.; Compton, R. N.; Diri, K.; Jordan, K. D.; Radisic, D.; Stokes, S. T.; Bowen, K. H. *Journal of Chemical Physics* **2004**, *120*, 685.

(74) Gutowski, M.; Hall, C. S.; Adamowicz, L.; Hendricks, J. H.; de Clercq, H. L.; Lyapustina, S. A.; Nilles, J. M.; Xu, S. J.; Bowen, K. H. *Physical Review Letters* **2002**, *88*, 143001.

(75) Adams, C. L.; Schneider, H.; Ervin, K. M.; Weber, J. M. *Journal of Chemical Physics* **2009**, *130*, 074307.

(76) Zhao, Y.; Truhlar, D. G. *Theoretical Chemistry Accounts* **2008**, *120*, 215.

(77) Flick, J. C.; Kosenkov, D.; Hohenstein, E. G.; Sherrill, C. D.; Slipchenko, L. V. *Journal of Chemical Theory and Computation* **2012**, *8*, 2835.

(78) Flick, J. C.; Kosenkov, D.; Hohenstein, E. G.; Sherrill, C. D.; Slipchenko, L. V. *Journal of Chemical Theory and Computation* **2014**, *10*, 4759.

(79) Hunter, C. A.; Sanders, J. K. M. *Journal of the American Chemical Society* **1990**, *112*, 5525.

(80) Sinnokrot, M. O.; Valeev, E. F.; Sherrill, C. D. *Journal of the American Chemical Society* **2002**, *124*, 10887.

(81) Dougherty, D. A. *Science* **1996**, *271*, 163.

(82) Ma, J. C.; Dougherty, D. A. *Chemical Reviews* **1997**, *97*, 1303.

(83) Schmitt, M.; Bohm, M.; Ratzer, C.; Siegert, S.; van Beek, M.; Meerts, W. L. *Journal of Molecular Structure* **2006**, *795*, 234.

(84) Borst, D. R.; Pratt, D. W.; Schaeffer, M. *Physical Chemistry Chemical Physics* **2007**, *9*, 4563.

(85) Voityuk, A. A.; Rosch, N. *Journal of Physical Chemistry A* **1997**, *101*, 8335.

(86) Wheeler, S. E.; Bloom, J. W. G. *Journal of Physical Chemistry A* **2014**, *118*, 6133.

(87) Sato, T.; Maruo, T.; Marukane, S.; Takagi, K. *Journal of Power Sources* **2004**, *138*, 253.

(88) Leung, K. *Chemical Physics Letters* **2013**, *568*, 1.

(89) Tu, W. Q.; Xing, L. D.; Xia, P.; Xu, M. Q.; Liao, Y. H.; Li, W. S. *Electrochimica Acta*, *204*, 192.

(90) Borodin, O.; Olguin, M.; Spear, C. E.; Leiter, K. W.; Knap, J. *Nanotechnology*, *26*, 15.

(91) Weber, W.; Wagner, R.; Streipert, B.; Kraft, V.; Winter, M.; Nowak, S. *Journal of Power Sources*, *306*, 193.

(92) Leung, K.; Budzien, J. L. *Physical Chemistry Chemical Physics*, *12*, 6583.

(93) Okamoto, Y. *Journal of the Electrochemical Society* **2014**, *161*, A1527.

(94) Wang, Y. X.; Nakamura, S.; Ue, M.; Balbuena, P. B. *Journal of the American Chemical Society* **2001**, *123*, 11708.

(95) *NIST Chemistry WebBook, NIST Standard Reference Database No. 69*; NIST Standard Reference Database Number 69 ed.; Linstrom, P. J.; Mallard, W. G., Eds.; National Institute of Standards and Technology: Gaitnersburg, MD, http://webbook.nist.gov/chemistry/.

(96) **John A. Riddick, W. B. B., and Theodore K. Sakano.** *Organic Solvents : Physical Properties and Methods of Purification*, 4th ed.; Wiley: New York, 1986; Vol. II.

(97) Stepanovic, M.; Pariat, Y.; Allan, M. *Journal of Chemical Physics* **1999**, *110*, 11376.

(98) Gronert, S.; Keeffe, J. R.; O'Ferrall, R. A. M. *Journal of the American Chemical Society* **2011**, *133*, 3381.

(99) Gaspar, P. P.; Whitsel, I. B. L.; Maitland Jones, J., lb; Lamber, J. B. *Journal of the American Chemical Society* **1980**, *102*, 6108.

(100) Roth, H. D. *Carbene Reaction Mechanisms* **1977**, *10*, 85.

(101) Lee, J.; Grabowski, J. J. *Chemical Reviews* **1992**, *92*, 1611.

(102) Grabowski, J. J.; Melly, S. J. *International Journal of Mass Spectrometry* **1987**, *81*, 147.

(103) Nemirowski, A.; Shreiner, P. R. *Journal of Organic Chemistry* **2007**, *72*, 9533.

(104) Mueller, P. H.; Rondan, N. G.; Houk, K. N.; Harrison, J. F.; Hooper, D.; Willen, B. H.; Liebman, J. F. *Journal of the American Chemical Society* **1981**, *103*, 5049.

(105) Gilles, M. K.; Ervin, K. M.; Ho, J.; Lineberger, W. C. *Journal Of Physical Chemistry* **1992**, *96*, 1130.

(106) Wren, S. W.; Vogelhuber, K. M.; Ervin, K. M.; Lineberger, W. C. *Physical Chemistry Chemical Physics* **2009**, *11*, 4745.

(107) Nimlos, M. R.; Davico, G.; Geise, C. M.; Wenthold, P. G.; Lineberger, W. C.; Blanksby, S. J.; Hadad, C. M.; Petersson, G. A.; Ellison, G. B. *Journal of Chemical Physics* **2002**, *117*, 4323.

(108) Goebbert, D. J.; Pichugin, K.; Khuseynov, D.; Wenthold, P. G.; Sanov, A. *Journal of Chemical Physics* **2010**, *132*, 224301.

(109) Schwartz, R. L.; Davico, G. E.; Ramond, T. M.; Lineberger, W. C. *Journal of Physical Chemistry A* **1999**, *103*, 8213.

(110) Vogelhuber, K. M.; Wren, S. W.; McCoy, A. B.; Ervin, K. M.; Lineberger, W. C. *Journal of Chemical Physics* **2011**, *134*, 184306.

(111) Khuseynov, D.; Dixon, A. R.; Goebbert, D. J.; Sanov, A. *Journal of Physical Chemistry A* **2013**, *117*, 10681.

(112) Murray, K. K.; Leopold, D. G.; Miller, T. M.; Lineberger, W. C. *Journal of Chemical Physics* **1988**, *89*, 5442.

(113) Krylov, A. I. *Chemical Physics Letters* **2001**, *350*, 522.

(114) Slipchenko, L. V.; Krylov, A. I. *Journal of Chemical Physics* **2005**, *123*, 084107.

(115) Levchenko, S. V.; Krylov, A. I. *Journal of Chemical Physics* **2004**, *120*, 175.

(116) Manohar, P. U.; Krylov, A. I. *Journal of Chemical Physics* **2008**, *129*, 194105.

(117) Sanov, A.; Grumbling, E. R.; Goebbert, D. J.; Culberson, L. M. *Journal of Chemical Physics* **2013**, *138*, 054311.

(118) Sanov, A. *Annual Review of Physical Chemistry* **2014**, *65*, 341.

(119) Slipchenko, L. V.; Krylov, A. I. *Journal of Chemical Physics* **2002**, *117*, 4694.

(120) Hirai, K.; Itoh, T.; Tomioka, H. *Chemical Reviews* **2009**, *109*, 3275.

(121) Admasu, A.; Gudmundsdottir, A. D.; Platz, M. S. *Journal of Physical Chemistry A* **1997**, *101*, 3832.

(122) Woodcock, H. L.; Moran, D.; Brooks, B. R.; Schleyer, P. V.; Schaefer, H. F. *Journal of the American Chemical Society* **2007**, *129*, 3763.

(123) Dixon, A. R.; Khuseynov, D.; Sanov, A. *Journal of Physical Chemistry A* **2014**, *118*, 8533.

(124) Leopold, D. G.; Murray, K. K.; Miller, A. E. S.; Lineberger, W. C. *Journal of Chemical Physics* **1985**, *83*, 4849.

(125) Dixon, A. R.; Khuseynov, D.; Sanov, A. *Chemical Physics Letters* **2014**, *614*, 72.

(126) Menon, A. S.; Henry, D. J.; Bally, T.; Radom, L. *Organic & Biomolecular Chemistry* **2011**, *9*, 3636.

(127) Blanksby, S. J.; Ellison, G. B. *Accounts of Chemical Research* **2003**, *36*, 255.

(128) Bernardi, F.; Epiotis, N. D.; Cherry, W.; Schlegel, H. B.; Whangbo, M. H.; Wolfe, S. *Journal of the American Chemical Society* **1976**, *98*, 469.

(129) *CRC Handbook of Chemistry and Physics*, 94 ed.; CRC Press: Boca Raton, Florida, 2013-2014.

(130) Mead, R. D.; Lykke, K. R.; Lineberger, W. C. Photodetachment Threshold Laws. In *Electronic and Atomic Collisions*; Eichler, J., Hertel, I. V., Stolterfoht, N., Eds.; Elsevier, 1984; pp 721.

(131) Surber, E.; Sanov, A. *J. Chem. Phys.* **2003**, *118*, 9192.

(132) Dahlke, G. D.; Kass, S. R. *International Journal of Mass Spectrometry* **1992**, *117*, 633.

(133) Bartmess, J. E. "Negative Ion Energetics Data". In *NIST Chemistry WebBook, NIST Standard Reference Database Number 69*; Linstrom, P. J., Mallard, W. G., Eds.; National Institute of Standards and Technology: Gaithersburg MD, 20899, http://webbook.nist.gov (retrieved Feb 25, 2014), 2009.

(134) Ervin, K. M. *Chem. Rev.* **2001**, *101*, 391.

(135) Taft, R. W. Acetonitrile, fluoro-. In *NIST Chemistry Webbook*; Progress of Physical Organic Chemistry, 1987; Vol. 16.

(136) Fujio, M.; Mciver, R. T.; Taft, R. W. *Journal of the American Chemical Society* **1981**, *103*, 4017.

(137) *CRC Handbook of Chemistry and Physics*, 95 ed.; CRC Press: Boca Raton, Florida, 2014-2015.

(138) Moran, S.; Ellis, H. B.; Defrees, D. J.; Mclean, A. D.; Ellison, G. B. *Journal of the American Chemical Society* **1987**, *109*, 5996.

(139) Goebbert, D. J.; Velarde, L.; Khuseynov, D.; Sanov, A. *Journal of Physical Chemistry Letters* **2010**, *1*, 792.

(140) Gunion, R. F.; Gilles, M. K.; Polak, M. L.; Lineberger, W. C. *International Journal of Mass Spectrometry and Ion Processes* **1992**, *117*, 601.

(141) Bartmess, J. E.; Scott, J. A.; McIver, R. T. *Journal of the American Chemical Society* **1979**, *101*, 6046.

(142) Poutsma, M. L. *Journal of Organic Chemistry* **2011**, *76*, 270.

(143) Ambili S. Menon, D. J. H., Thomas Bally and Leo Radom. *Organic & Biomolecular Chemistry* **2011**, *9*, 3636.

(144) Bartmess, J. E.; Scott, J. A.; McIver, R. T. *Journal of the American Chemical Society* **1979**, *101*, 6056.

(145) DiGangi, J. P.; Henry, S. B.; Kammrath, A.; Boyle, E. S.; Kaser, L.; Schnitzhofer, R.; Graus, M.; Turnipseed, A.; Park, J. H.; Weber, R. J.; Hornbrook, R. S.; Cantrell, C. A.; Maudlin, R. L.; Kim, S.; Nakashima, Y.; Wolfe, G. M.; Kajii, Y.; Apel, E. C.; Goldstein, A. H.; Guenther, A.; Karl, T.; Hansel, A.; Keutsch, F. N. *Atmospheric Chemistry and Physics* **2012**, *12*, 9529.

(146) Ho, K. F.; Ho, S. S. H.; Dai, W. T.; Cao, J. J.; Huang, R. J.; Tian, L. W.; Deng, W. J. *Environmental Monitoring and Assessment* **2014**, *186*, 2835.

(147) Kampf, C. J.; Corrigan, A. L.; Johnson, A. M.; Song, W.; Keronen, P.; Konigstedt, R.; Williams, J.; Russell, L. M.; Petaja, T.; Fischer, H.; Hoffmann, T. *Atmospheric Chemistry and Physics* **2012**, *12*, 6145.

(148) Vrekoussis, M.; Wittrock, F.; Richter, A.; Burrows, J. P. *Atmospheric Chemistry and Physics* **2009**, *9*, 4485.

(149) Krizner, H. E.; De Haan, D. O.; Kua, J. *Journal of Physical Chemistry A* **2009**, *113*, 6994.

(150) De Haan, D. O.; Corrigan, A. L.; Tolbert, M. A.; Jimenez, J. L.; Wood, S. E.; Turley, J. J. *Environmental Science and Technology* **2009**, *43*, 8184.

(151) Zhao, R.; Lee, A. K. Y.; Abbatt, J. P. D. *Journal of Physical Chemistry A* **2012**, *116*, 6253.

(152) Connelly, B. M.; De Haan, D. O.; Tolbert, M. A. *Journal of Physical Chemistry A* **2012**, *116*, 6180.

(153) Carlton, A. G.; Turpin, B. J.; Altieri, K. E.; Seitzinger, S.; Reff, A.; Lim, H. J.; Ervens, B. *Atmospheric Environment* **2007**, *41*, 7588.

(154) Galloway, M. M.; Powelson, M. H.; Sedehi, N.; Wood, S. E.; Millage, K. D.; Kononenko, J. A.; Rynaski, A. D.; De Haan, D. O. *Environmental Science and Technology* **2014**, *48*, 14417.

(155) Compton, R. N.; Reinhardt, P. W.; Schweinler, H. C. *International Journal of Mass Spectrometry and Ion Processes* **1983**, *49*, 113.

(156) Wren, S. N.; Gordon, B. P.; Valley, N. A.; McWilliams, L. E.; Richmond, G. L. *Journal of Physical Chemistry A*, *119*, 6391.

(157) Rossignol, S.; Aregahegn, K. Z.; Tinel, L.; Fine, L.; Noziere, B.; George, C. *Environmental Science and Technology* **2014**, *48*, 3218.

(158) De Haan, D. O.; Hawkins, L. N.; Kononenko, J. A.; Turley, J. J.; Corrigan, A. L.; Tolbert, M. A.; Jimenez, J. L. *Environmental Science and Technology* **2011**, *45*, 984.

(159) Sedehi, N.; Takano, H.; Blasic, V. A.; Sullivan, K. A.; De Haan, D. O. *Atmospheric Environment* **2013**, *77*, 656.

(160) Drozd, G. T.; McNeill, V. F. *Environmental Science-Processes & Impacts* **2014**, *16*, 741.

(161) Dixon, A. R.; Xue, T.; Sanov, A. *Angewandte Chemie-International Edition* **2015**, *54*, 8764.

(162) Dixon, A. R.; Xue, T.; Sanov, A. *Journal of Chemical Physics* **in press**.

(163) Bartmess, J. E. Negative Ion Energetics Data. In *NIST Chemistry WebBook, NIST Standard Reference Database Number 69*; Linstrom, P. J., Mallard, W. G., Eds.; National Institute of Standards and Technology: Gaithersburg MD, 20899, http://webbook.nist.gov (retrieved June 3, 2016).

(164) Rawlings, D. C.; Davidson, E. R. *Journal of Chemical Physics* **1980**, *72*, 6808.

(165) Kua, J.; Hanley, S. W.; De Haan, D. O. *Journal of Physical Chemistry A* **2008**, *112*, 66.

(166) Koch, D. M.; Khieu, N. H.; Peslherbe, G. H. *Journal of Physical Chemistry A* **2001**, *105*, 3598.

(167) Hazra, M. K.; Francisco, J. S.; Sinha, A. *Journal of Physical Chemistry A* **2014**, *118*, 4095.

(168) Gurnick, M.; Chaiken, J.; Benson, T.; McDonald, J. D. *Journal of Chemical Physics* **1981**, *74*, 99.

(169) Spangler, L. H.; Pratt, D. W. *Journal of Chemical Physics* **1986**, *84*, 4789.

(170) Peyroula, E. P.; Jost, R.; Lombardi, M.; Dupre, P. *Chemical Physics* **1986**, *102*, 417.

(171) Pebaypeyroula, E.; Jost, R.; Lombardi, M.; Pique, J. P. *Chemical Physics* **1986**, *106*, 243.

(172) Dupre, P.; Jost, R.; Lombardi, M. *Chemical Physics* **1984**, *91*, 355.

(173) Butz, K. W.; Krajnovich, D. J.; Parmenter, C. S. *Journal of Chemical Physics* **1990**, *93*, 1557.

(174) Salter, R. J.; Blitz, M. A.; Heard, D. E.; Pilling, M. J.; Seakins, P. W. *Journal of Physical Chemistry A* **2009**, *113*, 8278.

(175) Dobeck, L. M.; Lambert, H. M.; Kong, W.; Pisano, P. J.; Houston, P. L. *Journal of Physical Chemistry A* **1999**, *103*, 10312.

(176) Chen, Y. Q.; Wang, W. J.; Zhu, L. *Journal of Physical Chemistry A* **2000**, *104*, 11126.

(177) Durig, J. R.; Bucy, W. E.; Cole, A. R. H. *Canadian Journal of Physics* **1975**, *53*, 1832.

(178) Scuseria, G. E.; Schaefer, H. F. *Journal of the American Chemical Society* **1989**, *111*, 7761.

(179) Saito, K.; Kakumoto, T.; Murakami, I. *Journal of Physical Chemistry* **1984**, *88*, 1182.

(180) Profeta, L. T. M.; Sams, R. L.; Johnson, T. J.; Williams, S. D. *Journal of Physical Chemistry A*, *115*, 9886.

(181) Chen, P. In *Unimolecular and Bimolecular Reactions Dynamics*; Ng, C.-Y., Baer, T., Powis, I., Eds.; John Wiley & Sons: Chichester, 1994; pp 371.

(182) Wigner, E. P. *Physical Review* **1948**, *73*, 1002.

(183) Lewars, E. G. Ethenedione, C_2O_2. In *Modeling Marvels*; Springer, 2008; pp 131.

(184) Staudinger, H.; Anthes, E. *Berichte Der Deutschen Chemischen Gesellschaft* **1913**, *46*, 1426.

(185) Goodrich, W. W. Interview for FDA Oral History Program, 15 October 1986. Part 2; U.S. Department of Health and Human Services, Food and Drug Administration History Office: Rockville, Maryland, 1986.

(186) Berson, J. A.; Birney, D. M.; Dailey, W. P.; Liebman, J. F. In *Modern Models of Bonding and Delocalization, Molecular Structures and Energetics*; F.Liebman, J., Greenberg, A., Eds.; VCH: Weinheim, 1988; Vol. 6; pp 391.

(187) Rubin, M. B.; Patyk, A.; Sander, W. *Tetrahedron Letters* **1988**, *29*, 6641.

(188) Sulzle, D.; Weiske, T.; Schwarz, H. *International Journal of Mass Spectrometry and Ion Processes* **1993**, *125*, 75.

(189) Schröder, D.; Heinemann, C.; Schwarz, H.; Harvey, J. N.; Dua, S.; Blanksby, S. J.; Bowie, J. H. *Chemistry- A European Journal* **1998**, *4*, 2550.

(190) Surin, L. A.; Fourzikov, D. N.; Lewen, F.; Dumesh, B. S.; Winnewisser, G.; McKellar, A. R. W. *Journal of Molecular Spectroscopy* **2003**, *222*, 93.

(191) Chen, H. W.; Holmes, J. L. *International Journal of Mass Spectrometry and Ion Processes* **1994**, *133*, 111.

(192) Talbi, D.; Chandler, G. S. *Journal of Physical Chemistry A* **2000**, *104*, 5872.

(193) Trindle, C. *International Journal of Quantum Chemistry* **2003**, *93*, 286.

(194) Sülzle, D.; Terlouw, J. K.; Schwarz, H. *Journal of the American Chemical Society* **1990**, *112*, 628.

(195) Pedersen, C. T.; Wong, M. W.; Takimiya, K.; Gerbaux, P.; Flammang, R. *Australian Journal of Chemistry* **2014**, *67*, 1195.

(196) Maier, G.; Reisenauer, H. P.; Ruppel, R. *Angewandte Chemie-International Edition in English* **1997**, *36*, 1862.

(197) Raine, G. P.; Schaefer, H. F.; Haddon, R. C. *Journal of the American Chemical Society* **1983**, *105*, 194.

(198) Korkin, A. A.; Balkova, A.; Bartlett, R. J.; Boyd, R. J.; Schleyer, P. V. *Journal of Physical Chemistry* **1996**, *100*, 5702.

(199) Thompson, W. E.; Jacox, M. E. *Journal of Chemical Physics* **1991**, *95*, 735.

(200) Thomas, J. R.; DeLeeuw, B. J.; O'Leary, P.; Schaefer, H. F.; Duke, B. J.; O'Leary, B. *Journal of Chemical Physics* **1995**, *102*, 6525.

(201) Boo, D. W.; Ozaki, Y.; Andersen, L. H.; Lineberger, W. C. *Journal of Physical Chemistry A* **1997**, *101*, 6688.

(202) Ervin, K. M.; Lineberger, W. C. Photoelectron Spectroscopy of Negative Ions. In *Advances in Gas Phase Ion Chemistry*; Adams, N. G., Babcock, L. M., Eds.; JAI Press: Greenwich, 1992; Vol. 1; pp 121.

(203) Wenthold, P. G.; Lineberger, W. C. *Accounts of Chemical Research* **1999**, *32*, 597.

(204) Neumark, D. N. *Science* **1996**, *272*, 1446.

(205) Neumark, D. M. *Physical Chemistry Chemical Physics* **2005**, *7*, 433.

(206) Ma, N. L.; Wong, M. W. *Angewandte Chemie-International Edition* **1998**, *37*, 3402.

(207) Maier, G.; Rohr, C. *Liebigs Annalen* **1996**, 307.

(208) Skujins, S.; Delderfield, J.; Webb, G. A. *Tetrahedron* **1968**, *24*, 4805.

(209) Terlouw, J. K.; Burgers, P. C.; Baar, B. L. M. v.; Weiske, T.; Schwarz, H. *Chimia* **1986**, *40*, 357.

(210) Vanbaar, B.; Weiske, T.; Terlouw, J. K.; Schwarz, H. *Angewandte Chemie-International Edition in English* **1986**, *25*, 282.

(211) Hochstrasser, R.; Wirz, J. *Angewandte Chemie-International Edition in English* **1989**, *28*, 181.

(212) Szalay, P. G.; Vazquez, J.; Simmons, C.; Stanton, J. F. *Journal of Chemical Physics* **2004**, *121*, 7624.

(213) Krylov, A. I. *Accounts of Chemical Research* **2006**, *39*, 83.

(214) Dawson, J. H. J.; Jennings, K. R. *Journal of the Chemical Society-Faraday Transactions II* **1976**, *72*, 700.

(215) Vijay, D.; Sastry, G. N. *Journal of Molecular Structure-Theochem* **2005**, *714*, 199.

(216) Rice, C. A.; Maier, J. P. *Journal of Physical Chemistry A*, *117*, 5559.

(217) Graupner, K.; Merrigan, T. L.; Field, T. A.; Youngs, T. G. A.; Marr, P. C. *New Journal of Physics* **2006**, *8*, 117.

(218) Kolos, R.; Gronowski, M.; Dobrowolski, J. C. *Astrophysical Journal* **2009**, *701*, 488.

(219) Eichelberger, B.; Snow, T. P.; Barckholtz, C.; Bierbaum, V. M. *Astrophysical Journal* **2007**, *667*, 1283.

(220) Kolos, R.; Grabowski, Z. R. *Astrophysics and Space Science* **2000**, *271*, 65.

(221) DelloRusso, N.; Khanna, R. K. *Icarus* **1996**, *123*, 366.

(222) Jolly, A.; Cottini, V.; Fayt, A.; Manceron, L.; Kwabia-Tchana, F.; Benilan, Y.; Guillemin, J. C.; Nixon, C.; Irwin, P. *Icarus*, *248*, 340.

(223) Samuelson, R. E.; Mayo, L. A.; Knuckles, M. A.; Khanna, R. J. *Planetary and Space Science* **1997**, *45*, 941.

(224) Gudipati, M. S.; Jacovi, R.; Couturier-Tamburelli, I.; Lignell, A.; Allen, M. *Nature Communications*, *4*, 8.

(225) Jensen, J. O. *Journal of Molecular Structure-Theochem* **2004**, *678*, 233.

(226) Turowski, M.; Crepin, C.; Couturier-Tamburelli, I.; Pietri, N.; Kolos, R. *Low Temperature Physics*, *38*, 723.

(227) Sebastianelli, F.; Gianturco, F. A. *European Physical Journal D*, *59*, 389.

(228) Graupner, K.; Field, T. A.; Saunders, G. C. *Astrophysical Journal Letters* **2008**, *685*, L95.

(229) Habteyes, T.; Velarde, L.; Sanov, A. *Chemical Physics Letters* **2006**, *424*, 268.

(230) Koelsch, C. F.; Whitney, A. G. *Journal of Organic Chemistry* **1941**, *6*, 795.

(231) Ding, W. X.; Pinnaduwage, L. A.; Tav, C.; McCorkle, D. L. *Plasma Sources Science & Technology* **1999**, *8*, 384.

(232) Fischer, G.; Ross, I. G. *Journal of Physical Chemistry A* **2003**, *107*, 10631.

(233) Smith, A. M.; Schallmoser, G.; Thoma, A.; Bondybey, V. E. *Journal of Chemical Physics* **1993**, *98*, 1776.

(234) Hendricks, J. H.; Lyapustina, S. A.; Declercq, H. L.; Snodgrass, J. T.; Bowen, K. H. *Biophysical Journal* **1996**, *70*, 2.

(235) Adamowicz, L. *Private Communication*.

(236) Ritsko, J. J.; Brillson, L. J.; Sandman, D. J. *Solid State Communications* **1977**, *24*, 109.

(237) Polino, D.; Famulari, A.; Cavallotti, C. *Journal of Physical Chemistry A*, *115*, 7928.

(238) Schreiner, P. R.; Karney, W. L.; Schleyer, P. V.; Borden, W. T.; Hamilton, T. P.; Schaefer, H. F. *Journal of Organic Chemistry* **1996**, *61*, 7030.

(239) Nguyen, T. L.; Kim, G. S.; Mebel, A. M.; Nguyen, M. T. *Chemical Physics Letters* **2001**, *349*, 571.

(240) Johnson, C. J.; Shen, B. B.; Poad, B. L. J.; Continetti, R. E. *Review of Scientific Instruments*, *82*, 9.